ABSTRACT

Title of dissertation: ERROR ESTIMATION, GRID SELECTION AND CONVERGENCE VERIFICATION IN LARGE EDDY SIMULATION

Siavash Toosi
Doctor of Philosophy, 2019

Dissertation directed by: Professor Johan Larsson
Mechanical Engineering Department

Large eddy simulation (LES) is a modeling approach to simulation of turbulence, in which the large and energy containing eddies are directly resolved, while the smaller scales are modeled. The "coarse-graining" length scale (the length scale below which the turbulent eddies are modeled) is an important modeling parameter that is directly tied to the computational grid. As a result, the LES grid controls both the numerical and modeling errors and in most cases (given that the LES model is consistent) becomes the most important factor in determining the accuracy of the solution. The main goal of this dissertation is to enable a systematic approach to grid selection and convergence-verification in LES.

Systematic grid selection consists of five essential ingredients: (i) an "error-indicator" that identifies the regions of error generation, (ii) some knowledge of the directional structure of error generation (i.e., an anisotropic measure of error generation at each location), (iii) a model that describes the connection between the error generation and the filter/grid resolution (i.e., how it changes with a change

in the resolution), (iv) criteria that describe the most "optimal" distribution of the error-indicator in space and in direction, and (v) a robust method for convergence-verification. Items (i), (ii), (iv) and (v) are all addressed in this dissertation, while item (iii) has not been a subject of extensive research here (because of its somewhat lower importance compared to the other four).

Three error-indicators are introduced that are different in terms of their underlying assumptions, complexity, potential accuracy, and extensibility to more complex flows and more sophisticated formulations of the problem of "optimal" grid selection. Two of these error-indicators are inherently anisotropic, while the third one is only a scalar but can be combined with either of the other two to enable anisotropic error-estimation. The "optimal" distributions of these error-indicators are discussed in detail, that, combined with a model to connect the error-indicator and the grid/filter resolution, describe our "optimal" grid selection criteria. Additionally, a more robust approach for convergence-verification in LES is proposed, and is combined with error-estimation and "optimal" grid selection/adaptation to form a systematic algorithm for large eddy simulation.

The proposed error-estimation, grid selection, and convergence-verification methods are tested on the turbulent channel flow and the flow over a backward-facing step, with good results in all cases, and grids that are quite close to what is know as "best practice" for LES of these flows.

ERROR ESTIMATION, GRID SELECTION AND CONVERGENCE VERIFICATION IN LARGE EDDY SIMULATION

by

Siavash Toosi

Dissertation submitted to the Faculty of the Graduate School of the
University of Maryland, College Park, in partial fulfillment
of the requirements for the degree of
Doctor of Philosophy
2019

Advisory Committee:
Professor Johan Larsson, Chair/Advisor
Professor James D. Baeder
Professor Peter S. Bernard
Professor Kenneth T. Kiger
Professor Arnaud C. Trouvé

Dedication

To my grandpa, who passed away and I did not get to say goodbye.

And to Parizad and Kiarash. I could not be at your engagement party and I probably will not be at your wedding, but know that being there and seeing you remain to be my biggest wish.

Acknowledgments

First and foremost, I would like to thank my advisor, Prof. Johan Larsson, for his exceptional patience with me, his incredible support and continued help, his remarkable vision, and his outstanding intelligence. I could not have hoped for a better advisor. I owe this dissertation, my understanding of the field, and any research that I would do in the future to him.

I am also deeply grateful to my labmates, without whom these years were not possible. I should also thank them for their feedback on my papers, my presentations, my thesis, and almost anything else that I did during this dissertation. My special thanks go to Abishek and Pedro.

I am forever indebted to my family for their extraordinary support and understanding, for not asking me to come back even when they had every right to, and for always pushing me forward. No word can possibly express the level of my gratitude or how much I miss all of them.

I cannot name all the friends who helped me during these years, motivated me when I was tired, supported me in my plans, cheered me up when I was bored or unhappy, and made these years a joyful experience. Thanks to each and every one of them.

Many thanks to my committee members, Prof. Baeder, Prof. Bernard, Prof. Kiger, Prof. Oran, and Prof. Trouvé (in alphabetical order) for their time, their interest in the subject, and their valuable feedback.

I should also thank the sources of our funding for this project; this includes

external fundings from the Naval Air Warfare Center Aircraft Division at Pax River, MD, and the National Science Foundation, as well as internal fundings from the Graduate School, Mechanical Engineering Department, and the Burgers program at University of Maryland. The computing time has been generously provided by the University of Maryland supercomputing resources.

And lastly, I would like to thank the Spirit Airlines Inc (especially for their $150 round-trip tickets to Las Vegas), Booking.com (and the parent company, Booking Holdings), MGM Resort International, Global Hyatt, Marriott International, J.P. Morgan Chase, Greyhound Lines (as well as the parent company, FirstGroup PLC), Uber Technologies Inc, Lyft Inc, Amazon.com Inc, Hulu (owned by The Walt Disney Company and Comcast), Netflix Inc, Spotify Technology SA, YouTube (and the parent company Google LLC); they had almost no positive contribution to this dissertation, but life definitely would have been less entertaining without them.

Table of Contents

List of Tables

List of Figures

List of Abbreviations

BFS	Backward-Facing Step
DNS	Direct Numerical Simulation
DSM	Dynamic Smagorinsky Model
ILES	Implicit Large Eddy Simulation
LES	Large Eddy Simulation
MR-LES	Multi-Resolution Large Eddy Simulation
QoI	Quantities of Interest
RANS	Reynolds-Averaged Navier-Stokes
SFS	Sub-Filter Scale
SGMV	Systematic Grid and Model Variation
SGS	Sub-Grid Scale
UQ	Uncertainty Quantification
URANS	Unsteady Reynolds-Averaged Navier-Stokes
WENO	Weighted Essentially Non-Oscillatory
lhs	left-hand side
rhs	right-hand side

Chapter 1: Introduction

Turbulence is generally defined as the state of flow in which the fluid particles show unsteady and chaotic motions. It is further characterized by an efficient mixing of particles and properties like density, concentration, temperature, etc., as well as a balance between energy injection into the flow and dissipation of that energy by the molecular viscosity. Generally speaking, the injection of energy happens at the largest scales of the flow, while the dissipation happens at the smallest scales. This gives rise to the presence of a broad range of length scales in the flow, and their corresponding velocity scales, where the flow develops smaller and smaller scales as the energy injection rate increases or the kinematic viscosity decreases, so that it can keep the energy injection and dissipation in balance.

Turbulence follows the same evolution equation that governs the laminar, transitional, and other states of the flow; i.e. the Navier-Stokes equations. Therefore, its "direct" computational simulation also follows the same procedures: to generate a computational grid that covers the domain of interest and is fine enough to capture the "important" details of the flow, and to discretely solve the equations on that grid. In a "complete" simulation, called "direct numerical simulation" (DNS), almost all scales of turbulence are important. In other words, the largest scales are

important because they contain and describe the physics that are usually of engineering interest, while the smallest scales are where the energy dissipation happens and balances the energy injection. Unfortunately, it is impossible to capture the correct large scale dynamics without capturing the correct balance between the energy injection and the dissipation rate (and some of the other interactions between "large" and "small" scales of the flow).

Roughly speaking, if the computational domain is of size L and the smallest scales are of size η, the cost of a three-dimensional direct simulation is proportional to $(L/\eta)^4$. Note that L remains constant, while η will decrease as the Reynolds number increases (see Fig. 1.1), which makes the simulation cost prohibitive for moderate to high Reynolds numbers. As a result, it is actually impossible to do DNS of many flows given today's computing power (for instance, an approximate analysis by Spalart [1] suggests that the DNS of an aircraft wing requires 10^{16} grid points, and is not possible at least until year 2080). As a result, we need to employ models that aim at modeling some of the phenomena taking place in the smallest scales of size η (most prominent of which is dissipation) to break this strong scaling with η and make the computational simulation of turbulence affordable.

1.1 Large eddy simulation

Due to the complexity of turbulence, there are multiple ways in which this modeling can be done, where these models generally vary in the portion of the physics they model, their potential accuracy, and the computational cost of the

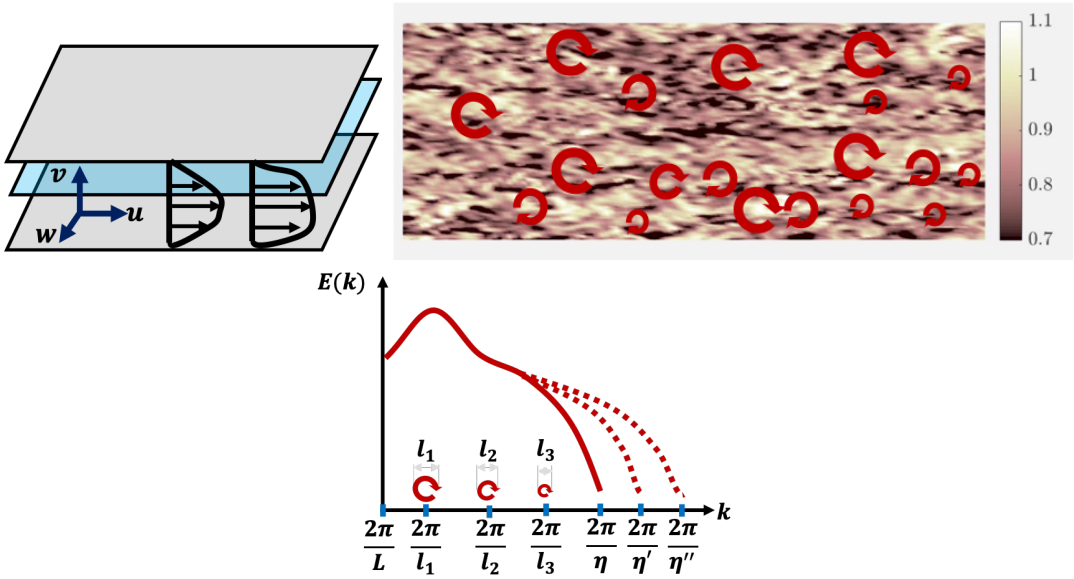

Figure 1.1: Schematic of the channel flow (top left) with a wall-parallel plane, whose instantaneous streamwise velocity is plotted in the top right panel. The circular arrows depict eddies of different sizes. The bottom panel shows the energy spectrum (in a log-log plot) where $k = 2\pi/l$ (l being the eddy size) is the wave number of the eddies (plot is not to scale). The smallest length scale η correspond to the highest wavenumber, while the domain size L correspond to the lowest value on the horizontal axis. As the Reynolds number increases $2\pi/\eta$ moves to higher and higher values (as depicted by the dotted lines), increasing the computational cost.

resulting simulation. An illustrative comparison of these models is shown in Fig. 1.2 in terms of the modeled and resolved part of the energy spectrum, and in Fig. 1.3, in terms of the modeled and resolved portion of an actual turbulent velocity field.

In the Reynolds Averaged Navier-Stokes (RANS) approach most or all of the turbulent activity is modeled. For the example of the channel flow, this modeling approach eliminates the dependence of the resolved part of the flow on the wall parallel coordinates and makes the simulation one-dimensional. This is obviously many orders of magnitude cheaper than a direct simulation of the Navier-Stokes equations on a 3D grid fine enough to resolve scales of size η. However, the problem with this modeling approach is that the largest scales of turbulence are known to

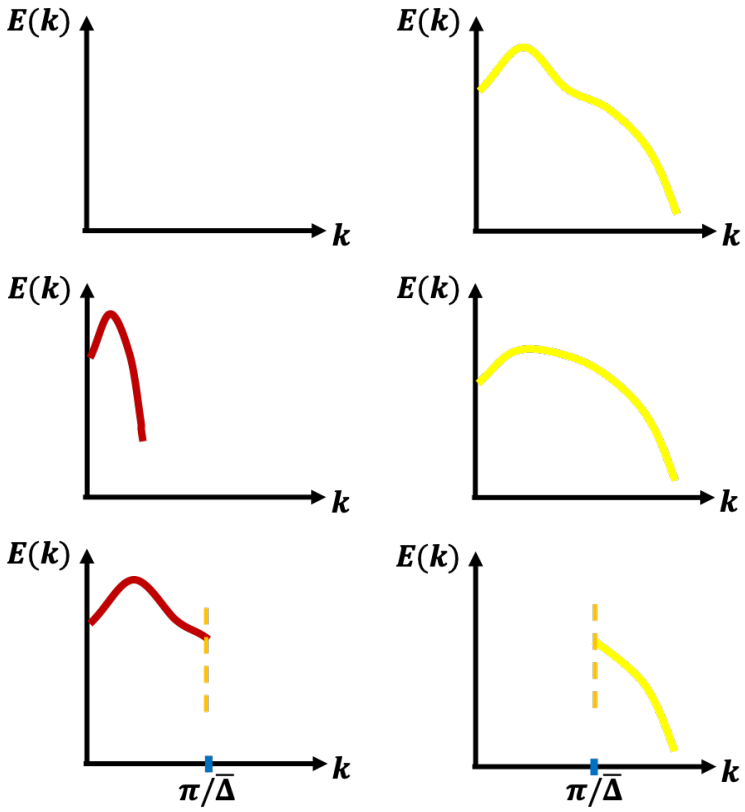

Figure 1.2: Illustration of different approaches to the modeling of turbulence. The left column shows the resolved part of the spectrum, while the right column shows the part that is handled by the model. The top and middle rows correspond to the RANS and URANS class of models, while the bottom row illustrates the approach taken in large eddy simulation (LES). Finding the "cut-off" length scale $\overline{\Delta}$ in LES is the subject of this thesis.

be flow and geometry dependent. As a result, despite the relatively sophisticated models used for RANS simulations, their accuracy is not comparable with the direct approach (DNS).

The situation is no different for the class of unsteady RANS (URANS) models that aim at directly resolving the largest unsteady, and usually non-turbulent, structures of the flow (e.g. vortex shedding, flutter, etc.) but model the rest of the turbulent scales. The modeled scales are still flow dependent and exhibit very complicated behaviors; this makes the models less effective, and the simulations are

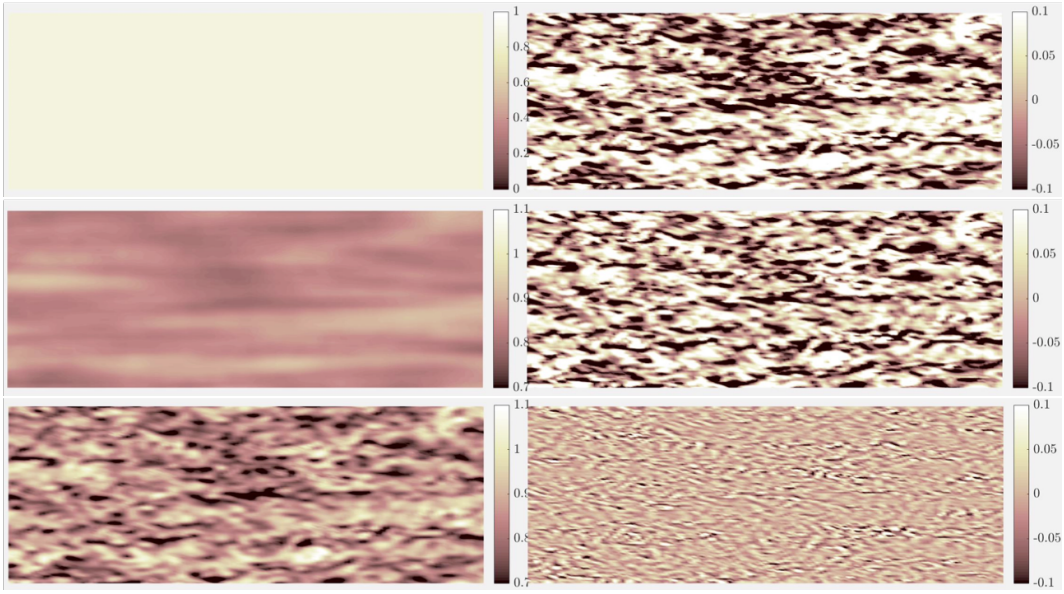

Figure 1.3: Illustration of the resolved (left column) and modeled (right column) part of the turbulent velocity field for the channel flow of Fig. 1.1 and for the modeling approaches and energy spectrums of Fig. 1.2. The first and second rows correspond to the RANS and URANS approaches that aim at modeling the entire or most of the turbulence activity. The third row corresponds to LES, where the energy containing portion of the velocity field (i.e. large turbulent "eddies") is fully resolved and only the smallest scales are modeled.

again not as accurate as DNS.

The other class of turbulence modeling, called Large Eddy Simulation (LES), is inspired by a few observations of turbulent flows. The first observation is that, contrary to the larger scales of turbulence that are flow and geometry dependent, the smaller scales become almost independent of the geometry and exhibit nearly universal behavior (e.g., see Fig. 1.4). As a result, the models used to describe them can be much more accurate and simultaneously much simpler than those used in the RANS simulations to describe the large, flow and geometry-dependent eddies. The other observation is that the amount of energy contained in the smaller length scales of the flow (higher wavenumbers in the energy spectra of Figs. 1.1 and 1.2)

drops rapidly as the length scale decreases, meaning that most of the physics that is of engineering interest is described by the larger scales of the motion. And the third observation, which is also the most important one, is that the energy transfer in turbulence (generally speaking) takes place from the larger eddies to the smaller ones; i.e., the smaller scales respond to the larger ones and not the other way around (approximately). This means that the smaller scales of turbulence do not directly affect its larger eddies, and nor does their inaccurate description, as long as the energy transfer rate (e.g., the dissipation rate) is described accurately. Therefore, if we can resolve those larger scales that are of more interest to us, and somehow model the key interactions between the larger and smaller scales of the flow accurately enough to capture the correct dynamics of the larger scales (dissipation in particular), in principle we should be able to achieve an accuracy that is not much different from a direct numerical simulation but at a much lower cost. This is why LES is so powerful and popular, and why we have decided to focus on it in this dissertation.

1.2 Importance of systematic grid selection and adaptation in LES

Even though LES is orders of magnitude cheaper than a direct numerical simulation, it is still some orders of magnitude more expensive than both the RANS and URANS approaches. As an example of this massive cost we can mention an approximate analysis by Spalart [1], who estimated that a full LES of an aircraft wing (for the least expensive LES) is not possible until year 2040 (given today's

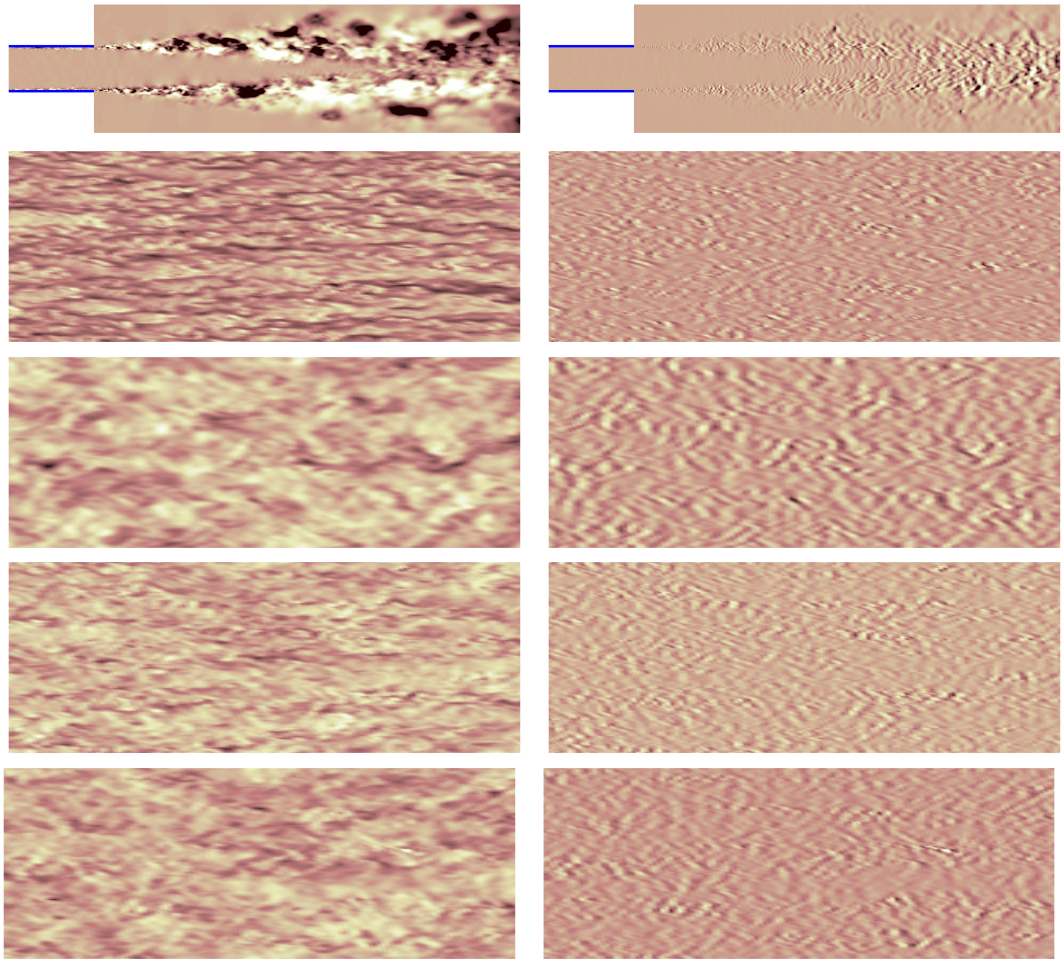

Figure 1.4: The idea behind LES. The left column shows the larger scales of the velocity field, while the right column corresponds to its smaller scales (high-pass filtered). The first row corresponds to a turbulent jet at Reynolds number of 10^6 and Mach number of 0.9 [2], while the second to last rows correspond to turbulent channel flow at different locations (y^+ of 25, 45, 65, and 135, respectively). Despite the huge difference between the larger scales of the motion, the smaller scales show a nearly universal behavior, which makes their modeling easier and more accurate.

computational power and applying Moore's law of exponential growth of the CPU power). This means that for so many of the flowfields where LES can be performed today, it is either at the edge of what is computationally possible, or at least it is very expensive. As a result, it is extremely important to be able to perform the least expensive simulation that leads to the highest accuracy of the solution.

There are a few major ways in which LES can be made more efficient: (i) by de-

veloping more accurate LES models and/or numerical schemes, and (ii) by choosing more optimal computational grids. In most cases, the choice of the computational grid is arguably at least as important as the LES model and the numerical implementation. Simply put, most LES codes and LES models produce accurate results on sufficiently "good" grids and inaccurate results on sufficiently "bad" grids. This importance of the computational grid as a significant parameter in the accuracy of LES stands in some contrast to the literature on large eddy simulation over the last half century, with many papers published on LES modeling (cf. the book by Sagaut [3]) and the influence of numerical errors (cf. [4–8] and many others) but with few studies devoted to the problem of how to optimally choose the computational grid.

The systematic and iterative process of finding this "optimal" computational grid is usually referred to as "grid-adaptation". The idea is to start from a relatively coarse and easy to generate grid, solve the governing equations on that grid, and use the solution to find a better and more optimal next grid. We then solve the equations on the new grid and see if the solution, or more formally the quantities of interest from the solution, have converged. If yes, the process is terminated, and if not, it is repeated by using the solution on the most recent grid to find an even "better" next grid, until convergence is achieved. Figure 1.5 shows a more formal representation of the grid-adaptation algorithm and the different processes involved in it.

Broadly speaking, algorithmic grid-adaptation has three different advantages compared to the kind of user-driven grid-selection that is the current standard in

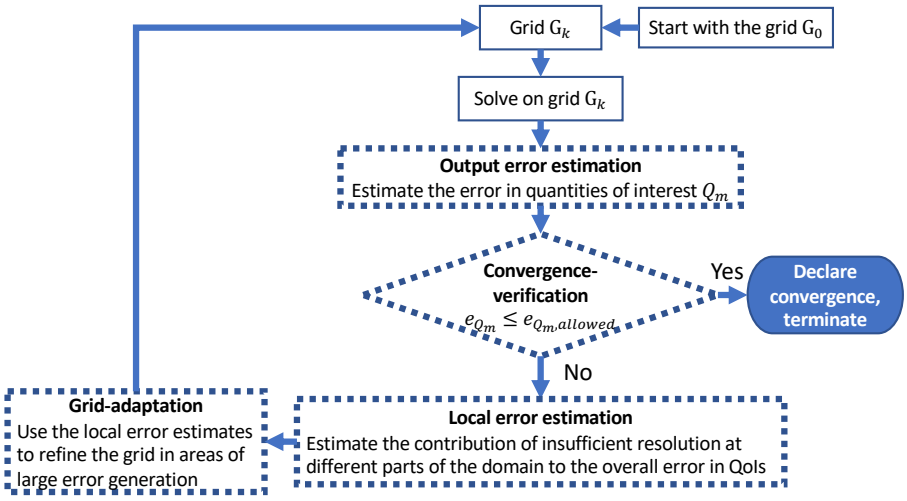

Figure 1.5: A typical grid-adaptation algorithm

LES: (i) adapted grids can be closer to "optimal", in the sense that they may produce similar accuracy with fewer cells; (ii) it can reduce the human time spent on generating grids, since the starting grids are using coarse and easy to generate, and the next grids are being automatically generated by adapting the previous grids; and, perhaps most importantly, (iii) it makes the simulation process more systematic, in that it makes it more likely that different users will end up with similar converged final results.

1.3 Motivating different parts of this dissertation

The next grid is usually found by computing an "error-indicator": a function that estimates the local sources of errors and their contribution to the overall error in the quantities of interest. The definition of a local error-indicator is relatively straightforward for computational simulations where the errors are only numerical in nature. This includes laminar and RANS simulations, as well as DNS. For such

computations the numerical errors can be estimated by computing the leading order truncation error of the numerical scheme or, almost equivalently, by estimating the numerical residuals by interpolation onto a finer grid (cf. [9]). Unfortunately, error-estimation is not as straightforward in large eddy simulation. In fact, almost none of the methods used for error-estimation in laminar, RANS, and direct simulations can be readily used for LES, due to the different nature of errors in a large eddy simulation.

The grid resolution in LES not only determines the significance of numerical errors in the resolved fields (like any other computational simulation), but also dictates the resolved part of the turbulence spectrum, and accordingly the modeled portion of it (turbulent scales below twice the grid resolution cannot possibly be resolved due to the Nyquist cut-off). If the grid is too coarse, we may model scales that are no longer in the universal regime, introducing large modeling errors into the solution (see Fig. 1.6). More importantly, no model is perfect, meaning that any large eddy simulation is essentially contaminated by the modeling errors. It is interesting to point out that in an LES the numerical errors may be avoided (we discuss this in more detail later), but there is no way of avoiding the modeling errors. Therefore, the errors in LES are either purely of modeling nature, or there is a combination of modeling and numerical errors with significant contribution from the modeling errors. This means that the existing error-indicators that target the numerical errors fail at finding the true sources of errors in LES, and we need to define new indicators with the aim of (at least partially) targeting the modeling errors.

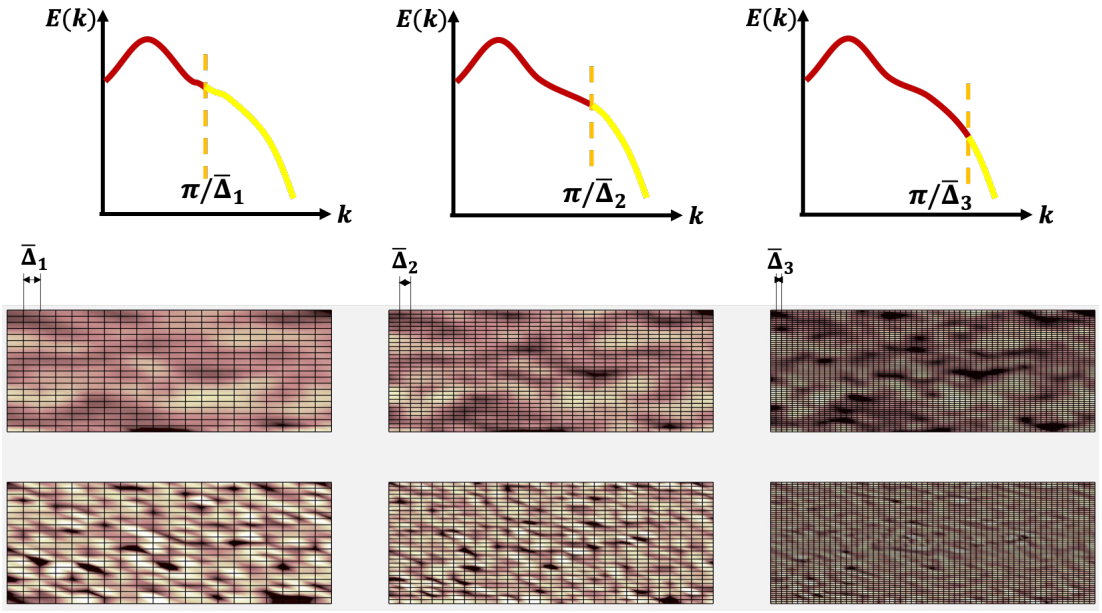

Figure 1.6: Difference between the effect of the grid in LES and other types of simulation. The cut-off length scale $\overline{\Delta}$ not only determines the accuracy of the resolved part of the spectrum (through its relation to the numerical error in the resolved eddies) but also the portion of the spectrum that is modeled and hence the modeling errors.

This motivates the error-estimation portion of this dissertation (discussed in Chapters 3, 5, and 8).

Error-indicators estimate the sources of error introduction into the solution, but they do not directly determine the appropriate grid resolution to minimize those errors. This is done by a model that connects the error-indicator to the grid resolution and a criterion that determines what distribution of the error-indicator would lead to the lowest overall error in the outputs from the solution. The models used to connect the error-indicator and the grid resolution are usually simple in their functional form, and they usually do not affect the final outcome (since the optimal state is when the error-indicator itself has a distribution described by the criteria, regardless of how it was achieved); as a result, we have not paid much

attention to those models here. On the other hand, the criteria that determines the optimal distribution of the error-indicator (i.e., the distribution that leads to the lowest overall errors in the solution) have a very significant effect on the grid selection process and motivate the other part of this thesis (Chapter 4).

The definition of convergence in LES is also different from its definition in laminar, RANS, and direct simulations. LES is by its definition under resolved, meaning that the solution necessarily develops smaller scales on finer grids (see the grids in Fig. 1.6). As a result, in a point-wise sense (in space and time) LES does not converge as the "filter-width" (length scales denoted by $\overline{\Delta}_1$, $\overline{\Delta}_2$, $\overline{\Delta}_3$ in Fig. 1.6) is refined, at least not until the DNS limit is reached. The National Research Council [10] suggests that the best-practice is to identify important simulation outputs ("quantities of interest", or QoIs), defined as functionals of the LES solution, and assess the convergence of these specific outputs only.

Apart from the need for a more elaborate definition of grid convergence in LES, the fact that some of the scales of the flow are fully unresolved poses additional problems to the robustness of any convergence test, even for carefully defined QoIs. This happens because of what is called the "projection error", meaning that any information about the scales below the grid resolution is completely lost, and thus, those scales cannot be approximated with absolute certainty from only the resolved scales (see Fig. 1.7). This means that the modeling error (that depend on both the filtered field and the original field) cannot be robustly estimated, nor can be its effect on the QoIs. Since the convergence is judged by the error in the QoIs, it directly affects our ability to make robust judgements of convergence.

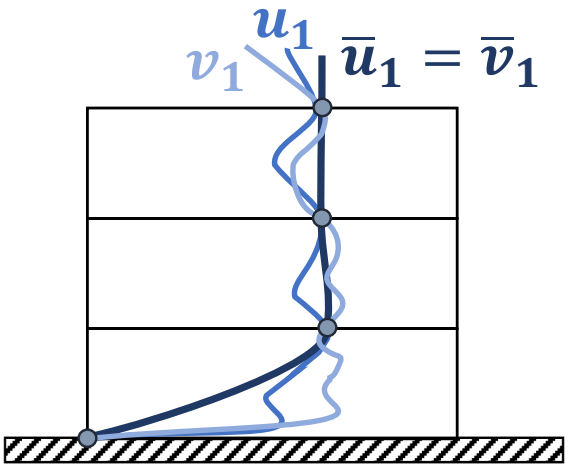

Figure 1.7: An illustration of the uncertainty due to the projection errors in LES: two velocity fields u_1 and v_1 may have very different shapes, while their resolved versions $\overline{u}_1$ and $\overline{v}_1$ are almost identical due to the effect of the projection error. Robust error-estimation would require us to estimate the original velocity fields from their filtered versions, which is obviously not possible in a deterministic sense. This introduces an uncertainty in our estimated errors that is followed by an uncertainty in the estimated error in the QoIs.

This motivates the other part of this thesis, focusing on outlining a more robust approach to test for grid convergence in LES (Chapter 7).

1.4 Contributions and novelties of the work

List of contributions:

(i) defined three different error-indicators that are all accurate and can be used for both error-estimation and grid generation/adaptation (Chapters 3, 5, and 8);

(ii) enabled anisotropic grid selection/adaptation in LES by making the error-indicators anisotropic (Chapters 3 and 5);

(iii) identifying the correct criteria to use in grid selection/adaptation (Chapter 4);

(iv) introducing a systematic and more robust approach for convergence-verification

(Chapter 7);

(v) integrating the convergence-verification and grid-adaptation as part of a systematic algorithm for LES (Chapter 9).

All of the error-indicators were completely novel in the field, one of them is already published [11], the other one is under review for publication [12], and the third one has been published as part of a conference paper [13] but is still undergoing some modifications before its final submission as a journal paper. The first two of these error-indicators are inherently anisotropic, with a clear distinction between different resolutions in different directions, while the last one is a scalar value on its own, but is combined with either of the two anisotropic error-indicators to enable directional error-estimation and grid selection/adaptation. This anisotropic error-estimation and grid generation in LES is completely new in the field and has not been done before.

The proposed convergence-verification methodology is not a separate paper on its own, but instead is a section of the conference paper (and its journal version), that also combines the convergence-verification and grid-adaptation as part of an integrated algorithm. The proposed algorithm is novel to the field; however, the novelty of the proposed convergence-verification method is somewhat arguable.

The modifications made in the equidistribution principle are also not novel *per se*, as its correct form has been known and used for a relatively long time in many of the works in the field of grid-adaptation [14–16]; although, its application in grid selection and adaptation in LES was less well-established.

Chapter 2: Background

The dynamics of the incompressible, Newtonian, and constant-viscosity fluids is described by the Navier-Stokes equations

$$\frac{\partial u_i}{\partial t} + \frac{\partial u_i u_j}{\partial x_j} = -\frac{1}{\rho}\frac{\partial p}{\partial x_i} + \nu \frac{\partial^2 u_i}{\partial x_j \partial x_j}\,, \tag{2.1}$$

where u_i and p are the instantaneous velocity and pressure fields, ρ and ν are density and kinematic viscosity of the fluid, and summation over the repeated index j is implied. This set of equations is then closed by the mass conservation equation

$$\frac{\partial u_i}{\partial x_i} = 0\,, \tag{2.2}$$

and/or the Poisson equation for pressure. These equations describe the full dynamics of the system. In the turbulent regime, solving these equations corresponds to performing a full DNS of the flow.

The governing equations for large eddy simulation (LES) can be formally derived by applying a low-pass filter with characteristic filter width $\overline{\Delta}$ to the above equations. If we denote this filtering process by $\bar{\cdot}$, we can write the filtered Navier-Stokes equations as

$$\frac{\partial \overline{u}_i}{\partial t} + \frac{\partial \overline{u_i u_j}}{\partial x_j} = -\frac{1}{\rho}\frac{\partial \overline{p}}{\partial x_i} + \nu \frac{\partial^2 \overline{u}_i}{\partial x_j \partial x_j}\,, \tag{2.3}$$

where $\overline{u}_i$ and $\overline{p}$ are the low-pass filtered part of the full velocity and pressure fields (usually referred to as the "resolved" fields), and we have assumed that the filtering and differentiation commute, i.e., that $\overline{\partial\phi/\partial x_i} \approx \partial\overline{\phi}/\partial x_i$. This assumption is not always satisfied (e.g., for spatially varying filter kernels), but is generally known to be sufficiently good for most cases.

The filtered mass conservation equation and filtered Poisson equation of pressure can be similarly derived by applying the same filtering operations (cf. the books by Pope [17] or Sagaut [3]).

The filtering process, or the "coarse-graining" process, is in fact just a formal way of removing (or highly attenuating) the length-scales below the filter-width $\overline{\Delta}$. In practice, it can be done either implicitly when generating the grid (since the scales below the Nyquist cut-off of the grid are removed) or explicitly by application of a low-pass filter to the equation and then using a grid that is fine enough to solve the coarse-grained equations (obviously the grid resolution cannot be coarser than the filter-width).

The nonlinearity of the convective term of the Navier-Stokes equation gives rise to the expression $\overline{u_i u_j}$ in Eqn. 2.3 that is not described in terms of the resolved fields. This means that the filtered equations are not in closed form. All the modeling effort in LES focuses on the closure of this term by describing it based on the resolved fields. In the most popular approach one expands this term as $\overline{u_i u_j} = \overline{u}_i\overline{u}_j + (\overline{u_i u_j} - \overline{u}_i\overline{u}_j)$ and moves the second term of the expansion to the right-hand side (rhs) of the

equation, i.e.,

$$\frac{\partial \overline{u}_i}{\partial t} + \frac{\partial \overline{u}_i \overline{u}_j}{\partial x_j} = -\frac{1}{\rho}\frac{\partial \overline{p}}{\partial x_i} + \nu \frac{\partial^2 \overline{u}_i}{\partial x_j \partial x_j} - \frac{\partial \tau_{ij}}{\partial x_j}\,, \tag{2.4}$$

where $\tau_{ij} \equiv \overline{u_i u_j} - \overline{u}_i \overline{u}_j$ is referred to as the "subgrid-scale" (SGS) stress term and is subject to modeling. This general approach is referred to as the "implicitly filtered LES", since one simply uses the grid-filtered velocity field (i.e. the implicitly filtered fields due to the Nyquist cut-off of the grid) in computation of the convective term.

Another approach is to decompose the convective term as $\overline{u_i u_j} = \overline{\overline{u}_i \overline{u}_j} + (\overline{u_i u_j} - \overline{\overline{u}_i \overline{u}_j})$ and define the "subfilter-scale" (SFS) stress as $\overline{\tau}_{ij} \equiv \overline{u_i u_j} - \overline{\overline{u}_i \overline{u}_j}$, where again $\overline{\tau}_{ij}$ is the subject of modeling. This is usually called "explicitly filtered LES", in reference to the explicit filtering of the convective term (and the resulting stress term).

Regardless of the approach, the SGS/SFS stress describes the interaction between the resolved and unresolved scales of motion. These are the same interactions mentioned in Chapter 1, where we argued that their accurate modeling is essential to the success of LES. Needless to say, there has been extensive work in the literature to develop better and more accurate models (see [3] for a survey on different LES models and approaches). For the purpose of this study, the key point is that all modeling approaches have an error that scales in some way with $\overline{\Delta}$ and should vanish in the limit $\overline{\Delta} \to 0$. This error is referred to as the "modeling error". For example, in the specific case of Eqn. 2.4 the modeling error can be quantified as $\overline{u_i u_j} - \overline{u}_i \overline{u}_j - \tau_{ij}^{\mathrm{mod}}(\overline{u}_k)$, where τ_{ij}^{mod} is the LES model used to describe τ_{ij} based on the resolved velocity field $\overline{u}_i$.

The other source of error in LES is numerical in nature, and happens due to the fact that the filtered equations are solved on a discrete grid with a finite characteristic resolution $\overline{h}$ (i.e., the equation that the code actually solves is similar to Eqn. 2.4, but the exact derivatives $\partial/\partial t$ and $\partial/\partial x_j$ are replaced by their numerical versions $\delta/\delta t$ and $\delta/\delta x_j$; more on this in Chapter 8). Similar to the modeling errors, the "numerical errors" scale with $\overline{h}$ and vanish in the limit of infinite resolution $\overline{h} \to 0$.

In the case of implicitly filtered LES with $\overline{\Delta} \approx \overline{h}$, the modeling and numerical errors can strongly interact with each other, especially since the resolved fields that enter the LES model are already contaminated by the numerical errors. This does not have to be the case, and the two errors can be separated by choosing a $\overline{\Delta}/\overline{h}$ ratio that is larger than unity. In such cases, the numerical errors are negligible ($\overline{\Delta}/\overline{h} \approx 2$ for a sixth-order numerical scheme and $\overline{\Delta}/\overline{h} \approx 4$ for second-order schemes [4]) and the modeling errors become the dominant source of errors; however, it is usually not desirable since the increase in the modeling error (by choosing $\overline{\Delta}$ that is larger than what it could be, and increasing the modeled portion of turbulence) is larger that the effect of the decrease in the numerical errors, leading to higher overall errors in the QoIs (see Fig. 2.1). As a result, in most practical cases we choose $\overline{\Delta} \approx \overline{h}$ and have to deal with an LES solution that is contaminated by both the modeling and numerical errors.

The other type of error in LES is the "projection error". These errors happen due to the finite resolution of the grid and the fact that we may only resolve turbulent scales that are larger than the grid resolution, while the original turbulent field may

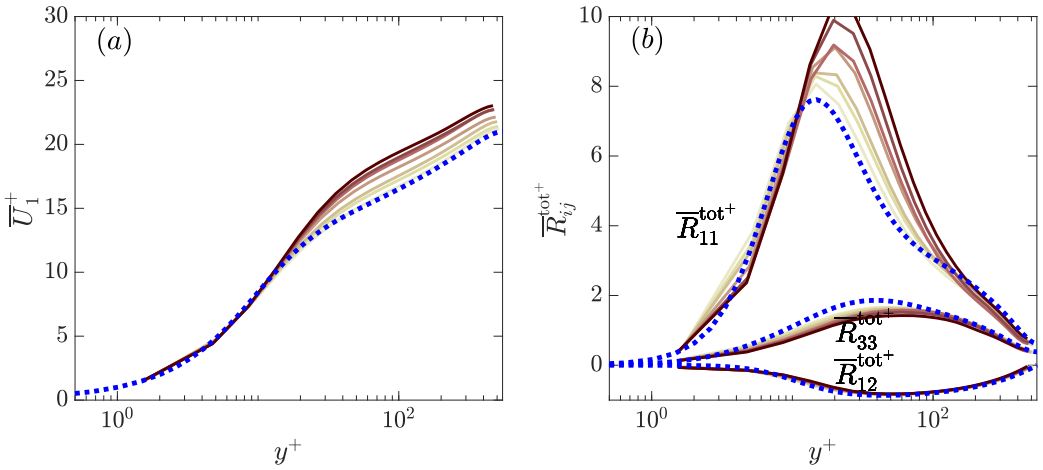

Figure 2.1: The overall effect of $\overline{\Delta}/\overline{h}$ ratio on the accuracy of LES of channel flow at $Re_\tau \approx 545$ on a fixed computational grid. The dotted blue lines correspond to the DNS solution of Del Alamo & Jimenez [18] for the same setup. The other colors from brightest to darkest correspond to $\overline{\Delta}/\overline{h}$ ratios of 1, 1.15, 1.3, 1.6, 1.8, 2.0, 2.25, respectively. The subgrid stress is modeled using the Vreman model [19] with a constant (static) coefficient of $c_v = 0.03$.

have much smaller scales $\eta \ll \overline{h}$. Similar to the numerical errors, the projection errors also scale with $\overline{h}$ and vanish as $\overline{h} \to 0$, although they describe a completely different type of error. The direct contribution of the projection error to the error in the QoIs is relatively small, given that the QoIs are consistent with the definition of LES and are only functions of the larger scales of the motion (for instance, their direct effect on the Reynolds stress, which is a large scale quantity, can be quantified as $u_i u_j - \overline{u_i u_j}$, which should be small given that the filter is not too wide). However, as discussed in Section 1.3, the projection error introduces an innate uncertainty in estimating the modeling errors based on the resolved fields (since we have to estimate $\overline{u_i u_j}$ solely based on the resolved velocity field $\overline{u}_i$, which is the only data we have available from LES). This breaks down the certainty (and somewhat the robustness) of error-estimation in LES, and consequently, the robustness of any convergence-

verification test based on the estimated sources of errors. This is discussed in more detail in Section 2.2.

2.1 Literature survey: error-estimation and grid selection in LES

In the following, we review some of the available error-indicators in the literature. In order to have a more meaningful discussion about their relative accuracy, we also assess them on a typical LES of channel flow at $Re_\tau \approx 545$ that exhibits some of the signature LES errors (e.g., a mean velocity profile that lands above the log law and an overprediction of the turbulent kinetic energy; see Fig. 2.2) to see how well they can localize the sources of errors. We should keep in mind that the primary target of most of these error-indicators is to estimate the errors due to modeling of the unresolved scales. Accordingly, we have chosen an LES with sixth-order accurate numerics and $\overline{\Delta}/\overline{h} \approx 1.6$ (and a Vreman model [19] with a model coefficient of 0.03) to have low numerical errors, and thus a fair comparison between them. An accurate error-indicator for LES (explained in Chapter 5) that identifies the important areas of error generation is plotted in Fig. 2.3 as a reference for comparison, along with the error in the dissipation rate that could also be somewhat indicative of the local sources of error generation in this flow.

Consistent with what we said in Chapter 1, some early attempts relied on the theoretical importance of dissipation for correct predictions of dynamics of the large-scale system (thus, accuracy of the LES solution) and defined their error-indicator based on the dissipation rate. More specifically, they used the fraction of energy

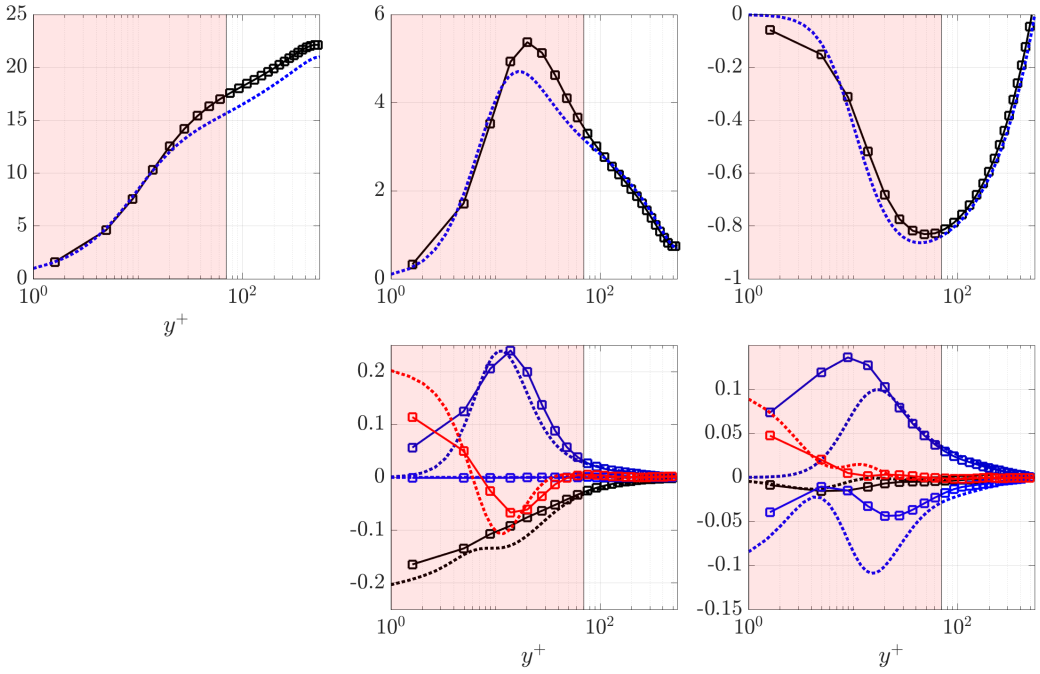

Figure 2.2: The error in some of the typical quantities computed from an LES solution of the channel flow at $Re_\tau \approx 545$. The grid has a near-wall resolution of $(\overline{h}_x^+, \overline{h}_{y_w}^+/2, \overline{h}_z^+) \approx (45, 1.7, 19)$ in friction units, and $\overline{\Delta}/\overline{h} = 1.6$. The top row shows the normalized mean velocity $\overline{U}_1^+$ (left), normalized turbulent kinetic energy $\overline{R}_{kk}^{\text{tot}^+}/2$ (middle), and normalized turbulent shear stress $\overline{R}_{12}^{\text{tot}^+}$ (right). The bottom row shows the normalized budgets of the turbulent kinetic energy (middle) and turbulent shear stress (right, multiplied by -1). In all plots the solid lines are the LES solution, while the dotted lines are from the DNS solution of Del Alamo & Jimenez [18] for the same setup. The LES profiles for turbulent kinetic energy, turbulent shear stress, and their budgets are for the total values, i.e. sum of the resolved and SGS model contributions. Budgets include: dissipation rate (black lines), production (dark blue), pressure-strain (blue), and all the transport terms (red) that includes the pressure, turbulent and viscous transport. The shaded region highlights the areas of error generation based on typical LES judgement for this flow.

dissipation caused by the SGS/SFS model to the total (cf. [20]) as a measure of error. This is closely related to using the ratio of the eddy viscosity to the molecular viscosity as a measure of accuracy (cf. [28]). This ratio is plotted in Fig. 2.3(a). Using this indicator, the "optimal" LES grid can presumably be constructed by requiring that the ratio remains constant and equal to a few percents throughout the domain.

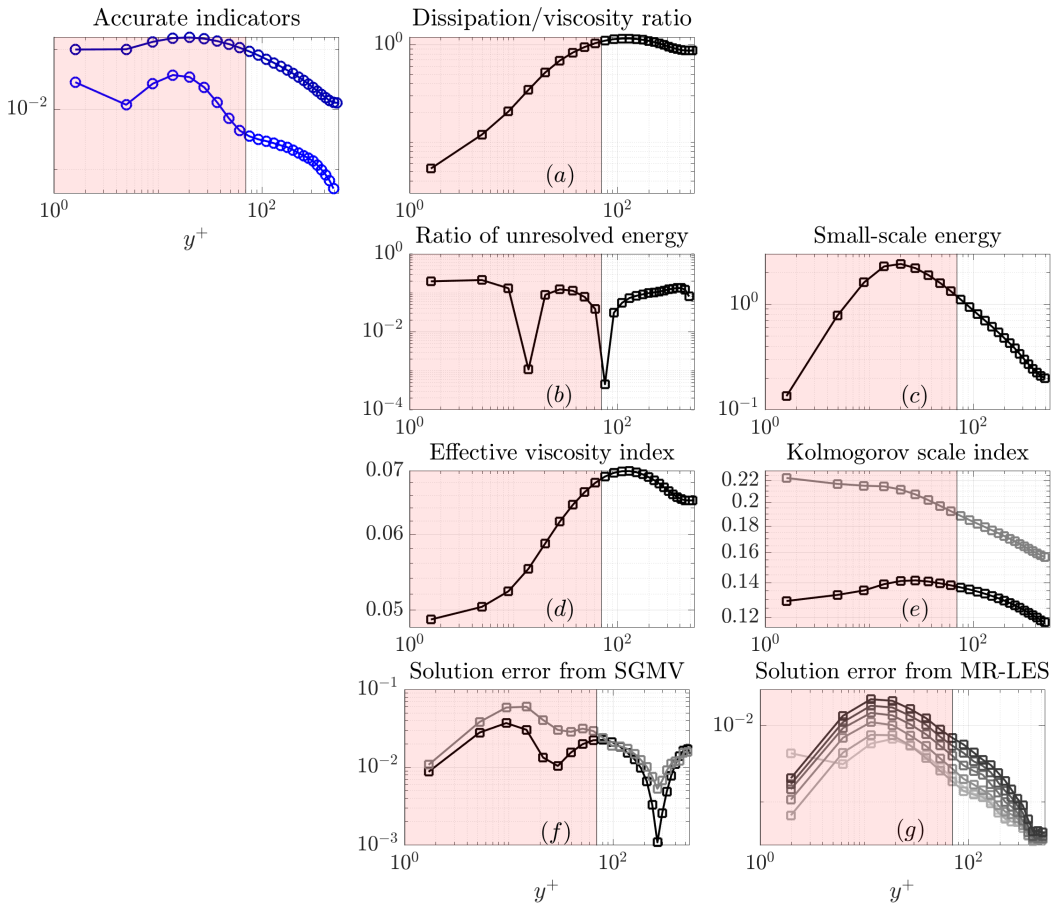

Figure 2.3: A comparative study of different LES error estimators for the channel flow of Fig. 2.2. The region of error generation (based on experience) is shaded in all plots. Panels $(a-g)$ are indicators from the literature vs the top left panel that plots a realistic error generation profile (dark blue, see Chapter 5) consistent with experience, as well as the error in the total dissipation rate (blue): (a) ratio of eddy viscosity to molecular viscosity proposed by Geurts and Fröhlich [20], (b) ratio of unresolved to total kinetic energy proposed by Pope [21] (1−modified value, proposed by Celik *et al.* [22]), (c) the small-scale energy without local scaling proposed by Bose [23], (d) the ratio of effective viscosity index proposed by Celik *et al.* [22,24] (1−value), (e) the ratio of Kolmogorov scale index proposed by Celik *et al.* [22,24] for cell volume (black) and diagonal length of the cell (grey) as cell length scales (1−value), (f) sum of the absolute values of the numerical and modeling errors in the mean velocity profile from the SGMV method proposed by Klein *et al.* [22,25,26] for $m = 2/3$ and $n = 6$ (black) and $m = n = 2$ (grey), (g) solution error from the MR-LES method proposed by Legrand *et al.* [27] (lightest to darkest colors correspond to different times after the last synchronization for $(t-t_s)U_b/H = 0$, 1, 2, 3, 4, 5, respectively). Some methods are modified such that the larger values correspond to higher error generation (modifications are mentioned in the parentheses). Only the general shape of the profiles should be compared, not their actual magnitudes.

Despite the undeniable importance of dissipation, the approach of using the ratio between the modeled and molecular/total dissipation rate is meaningful only at low Reynolds numbers, since the whole idea of LES is to avoid having to resolve the viscous dissipation (we are actually being a bit too optimistic here; our channel flow test case has a relatively low Reynolds number, but the dissipation-based error-indicator still fails to correctly identify where errors are generated).

A more accurate version of the dissipation-based error-indicators could perhaps be constructed if we could somehow estimate what the total dissipation rate (i.e., the sum of molecular and LES) should actually be and use the error in that quantity as a local error-indicator (see Fig. 2.3 where this error is computed from the available DNS data and plotted as a reference). This is generally not possible based on current LES methods (most LES models are defined to predict the most accurate level of dissipation; so, if we could have a more accurate estimate of the total dissipation rate we could have instead used it in our LES model) and thus requires some extra steps (e.g., LES solution on a slightly coarsened or refined version of the grid and employing Richardson extrapolation), where in that case one can also go all the way with the extra information that is now available and define more comprehensive error-indicators instead (see Chapter 8).

Driven by an appeal for simplicity and use of information from a single LES solution, a more successful class of methods was inspired by the alternative argument that the LES is accurate whenever the contribution of the modeled scales to the total kinetic energy is sufficiently small [29]. This general thinking is supported by the fact that the modeling errors should essentially go down as a lesser portion of the

turbulent scales are being modeled. This decreases the projection errors as well. And due to the decaying spectrum of turbulence, the numerical errors (that are somewhat proportional to how energetic the smallest resolved scales are) become less significant as one resolves a larger portion of the spectrum, and the Nyquist cut-off $\pi/\overline{h}$ shifts towards higher wavenumbers (this decay of energy for higher wavenumbers is clear from the energy spectrum of Fig. 1.1). Pope [21] used this intuitive argument to suggest that the proportion of resolved to total kinetic energy could be used as a local indicator function (plotted in Fig. 2.3(b)). Alternatively, Bose [23] used the kinetic energy in the smallest resolved scales directly (i.e., without scaling with the resolved or total energy) as an error-indicator (Fig. 2.3(c)). In both approaches, the next LES grid was found by requiring a constant and uniform indicator function everywhere in space (e.g., that no more than 10% of the total kinetic energy was in the unresolved scales).

While this general idea of connecting the accuracy of LES to the amount of unresolved or small-scale kinetic energy is quite intuitive and has been found to work well in some cases [11, 23], it is important to acknowledge that it is still only heuristic in nature: there is no equation showing that error scales with unresolved kinetic energy. For instance, the approach proposed by Pope does not seem to be able to identify the areas of error generation in the channel flow.

Several researchers tried to modify and improve the error-indicators discussed so far, or even used the LES solution on more than one grid (usually combined with Richardson extrapolation) to define more accurate indicators (cf. [22, 25, 26, 28, 30]), but still based on the same heuristic ideas about the importance of energy or dis-

sipation to LES accuracy. Some of these modified indicators are: the modified activity parameter such that it also accounts for the effect of numerical dissipation [22,28] which was a modification to the ratio of dissipations originally proposed by Geurts and Fröhlich [20] (not plotted here, since our test case uses a high-order and non-dissipative numerical scheme with $\overline{\Delta}/\overline{h} = 1.6$), the relative SGS viscosity index [22,24] (Fig. 2.3(d)), relative Kolmogorov scale index [22,24] (Fig. 2.3(e)), the modification made in the indicator proposed by Pope [21] for cases where the total energy is less that the resolved part [22], using the Richardson extrapolation and the LES solution on two or three grids to estimate the total kinetic energy in Pope's indicator [22,24] (not plotted, since we took the actual total kinetic energy from the DNS data), etc. Similarly, in the method of Systematic Grid and Model Variation (SGMV) the Richardson extrapolation was employed as a way of deconvolution of the mean velocity [22,25,26,31] and Reynolds stresses [31]. The primary focus of the SGMV method was on uncertainty quantification (UQ) of the LES solution due to modeling and numerical errors, and not exactly on local error-estimation; however, all the ingredients are already there, and one can use it for finding a better grid by enforcing some criteria on the distribution of these resolution-induced uncertainties. As an example, the total error in the mean velocity field computed from the SGMV method (as the sum of the absolute values of the estimated modeling and numerical errors) is plotted in Fig. 2.3(f).

We should also mention the class of multi-resolution LES (MR-LES) methods (cf. [3, 27]) where two parallel simulations are performed on two slightly different grids, with the difference between the two solutions used to infer the sources of error.

The chaotic nature of the equations then requires regular synchronization of the two solutions (through interpolation between the two grids). The time between two synchronizations should be sufficiently long to allow for the LES solution to develop to a new state where it is contaminated by both the modeling and numerical errors on the second grid (immediately after interpolation the solution is only affected by the interpolation errors), yet short enough to avoid the divergence of the two solutions. This introduces an additional parameter, i.e. the simulation time between any two synchronizations, that will most probably be set by the user (or found based on the solution itself) and is not a big problem in general (see Fig. 2.3(g) for an example of the effect of this time scale for times $(t-t_s)U_b/H = 0$, 1, 2, 3, 4, and 5, where H is the channel half-width, U_b is the bulk velocity, t is time, and t_s is the time at which the last synchronization has taken place). The more important question is whether the difference between the two LES solutions (i.e. $\overline{u}_i^{\overline{\Delta}\to\widetilde{\Delta}} - \widetilde{u}_i$, where $\overline{u}_i$ denotes the solution on grid $\overline{\Delta}$, $\widetilde{u}_i$ is the solution on the second grid $\widetilde{\Delta}$, and $\cdot^{\overline{\Delta}\to\widetilde{\Delta}}$ denotes interpolation from $\overline{\Delta}$ to $\widetilde{\Delta}$) is in itself indicative of the local sources of error (we discuss this in Chapters 5 and 8). Figure 2.3(g) shows this error-indicator computed for the channel flow based on the LES solution on a second grid that is 1.25 times coarser in all three directions, i.e. $\widetilde{\Delta} = 1.25\overline{\Delta}$. Note that for this case we took $\overline{\Delta}/\overline{h} = \widetilde{\Delta}/\widetilde{h} = 1.3$ in order to increase the numerical errors.

The most sophisticated approach to date was developed by Hoffman and Johnsson (cf. [32, 33]) and later Barth [34] who defined error-indicators within a finite-element framework that included both the numerical errors and the estimated modeling errors through a scale-similarity model. They also solved the adjoint equa-

tion to directly connect the estimated local errors to integrated quantities of interest (QoIs). Despite the comprehensive treatment in these papers and their successful results, this approach has not been adopted extensively in the community. Part of the reason is probably that the work was focused on the finite-element approach, another is that the adjoint equations diverge exponentially for long-time integration (cf. [35, 36]).

One major shortcoming of most existing error-indicators is that they are defined as scalar values and are unable to infer anything about the effect of insufficient directional resolution of the grid on the overall errors. This becomes a major problem when one wants to use them for grid selection/adaptation, since the optimal LES grids are often highly anisotropic: for example, the optimal LES grid near a solid wall is about 20 and 10 times coarser in the streamwise and spanwise directions than in the wall-normal one. Among the few studies that did address the anisotropy was that of Addad *et al.* [37], who instead of defining an error-indicator and a criterion on how it should be distributed, directly defined their optimal directional resolution based on an empirical criterion about the relative size of the LES filter $\overline{\Delta}$ compared to the Taylor microscale and the RANS dissipation length scale.

This leaves a clear gap in the field for anisotropic error-indicators, capable of producing meaningful information about the directional resolution of the grid.

The other issue is that, despite what many (though not all) researchers heuristically assumed, the uniform distribution of the error-indicator (even assuming that the error-indicator exactly measures the local source of errors) does not lead to the lowest global error generation. This is the other aspect of grid selection that needs

to be addressed.

2.2 Literature survey: convergence-verification in LES

Convergence can be generally defined as the state in which the error in the solution is below some acceptable threshold and no further refinement of the computational grid (independently of the exact way of refinement, e.g., local or global refinement, refinement in one direction or in all directions, with the same refinement factor everywhere or different factors in different locations or directions, etc.) can change the solution beyond an acceptable threshold.

There are two main differences between LES and other types of simulations that can affect the above definition of grid-convergence.

First, in LES there are two relevant length scales that are affecting the solution: the filter-width $\overline{\Delta}$ and the grid resolution $\overline{h}$. As a result, if we refine the grid but keep the filter-width unchanged, we can achieve a "grid-independent" solution [38], but this does not mean that the solution is converged: it is still a function of $\overline{\Delta}$.

The next difference between LES and any of the laminar, RANS, or direct simulations is that the LES solution will necessarily change and develop smaller scales as one refines the filter. This is in contrast with other methods of turbulence simulation, where a change in the solution is a sign that the convergence is not yet reached. In fact, the whole purpose of LES is to carry out underresolved simulations of turbulence: any real LES will necessarily develop smaller scales as the filter-width $\overline{\Delta}$ is refined (until it reaches the DNS limit and resolves all the scales). This means

that judging the convergence by the change in the solution itself $\overline{u}_i$ is not meaningful in the context of LES.

The National Research Council [10] suggests that the best-practice to examine the convergence of any simulation (including LES) is to identify important simulation outputs (QoIs). In LES, the quantities of interest must be defined as statistics of the solution that are strong functions of the larger scales of turbulence (essentially the resolved LES fields) but have little to no *explicit* dependence on the smaller scales (of course, they are still implicitly dependent on the smaller scales, through the effect of smaller scales on the dynamics of the larger ones), and assess the convergence of these specific outputs only. This makes sense: if the QoIs we are interested in did *not* converge well before the DNS limit, LES would be a pointless tool. In other words, LES makes sense for QoIs that depend on the larger scales (e.g., lift, drag, pressure rms, Reynolds stress, etc.) but not if the purpose is to predict QoIs that depend on the smallest scales (e.g., molecular dissipation or similar).

Figure 2.4 illustrates the importance of the QoIs used to judge the convergence of the solution from a large eddy simulation. Note that although the mean velocity is converged on all grids and the Reynolds stresses are converged on the finer two grids, both the energy spectrum and the dissipation spectrum are developing smaller scales (higher wavenumbers) on the finer grids. The resolved part of the energy spectrum seems to be converged on the finer grids (for wavenumbers not very close to the cut-off), but the molecular dissipation is far from converged on any of the three grids.

Based on the outlined definition of convergence, if the error in the large-scale

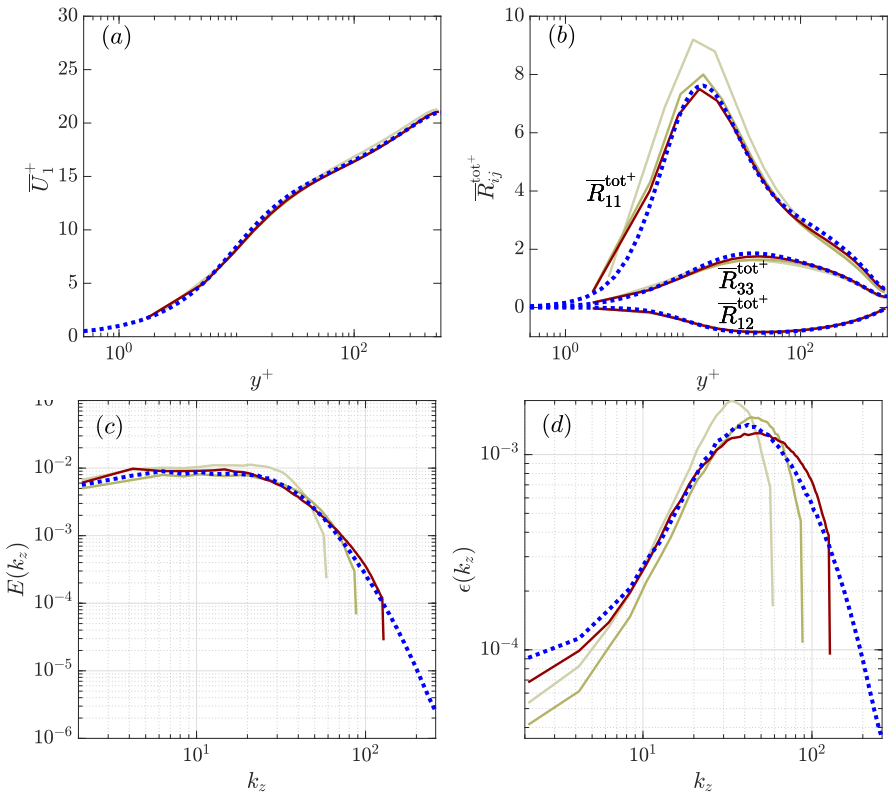

Figure 2.4: Importance of identifying the quantities of interest (QoIs) when judging the convergence of an LES solution: Panels (a) and (b) show the mean velocity and Reynolds stress profiles obtained from LES of channel flow. Panel (c) plots the convergence of the spanwise energy spectrum for a wall parallel plane located at $y^+ \approx 12$, while panel (d) shows the convergence of the spanwise molecular dissipation spectrum (a small-scale quantity) at $y^+ \approx 12$. The dotted blue lines correspond to the DNS solution. The other colors correspond to three grids with different resolutions (the coarsest to finest grids are shown by the lightest to darkest colors, in that same order).

QoIs is below some acceptable value, and remains to be in the acceptable region with any further refinement of $\overline{\Delta}$, we can declare our LES to be converged, even though the solution $\overline{u}_i$ is still changing with refinement of the filter. This also means that we do not explicitly require the LES solution (i.e., the instantaneous resolved fields) to be "grid-independent" [38, 39], or the filter-width to be within the inertial subrange, or there to be 10-20 grid points across a specific physical feature, etc.; as long as the error in the QoIs is and remains to be below the acceptable threshold

(for any possible refinements of the filter) we consider our LES converged.

This systematic definition of convergence in LES draws the attention away from the discussions of grid independence in LES (or other such discussions) and focus it more on how to assess the accuracy of QoIs. This is a real problem in LES, because of the inevitable presence of projection errors; and to see why, we need to study in more detail how the convergence of QoIs is robustly assessed.

The exact computation of error in the QoIs would essentially require access to the fully converged solution, which, obviously, cannot be the case in any realistic scenario. The alternative is to either use the change in the QoIs from one grid to the other as a representation of their actual error (method 1 in Fig. 2.5), or to somehow estimate their error in some other way. The former option is much easier in reality, but it may not be robust: the two grids used to compute the QoIs (and thus to compute the change in the QoIs) are often being generated by the same user or by the same error-estimation and grid-adaptation technique (for instance, when we compare the change in the QoIs on two grids from the same sequence of adapted grids). It is quite possible for a user, or even an error-indicator, to completely miss an important region of refinement and keep refining the grid in the same already overrefined regions, and then to conclude that the QoIs are converged while in reality they are not (cf. [40] for some examples in the context of Hessian-based grid-adaptation).

To avoid these issues, researchers have developed more rigorous techniques to estimate the error in the QoIs without having to solve the equations on extra fine grids (see methods 2 and 3 of Fig. 2.5). In the simpler and more basic approach, one

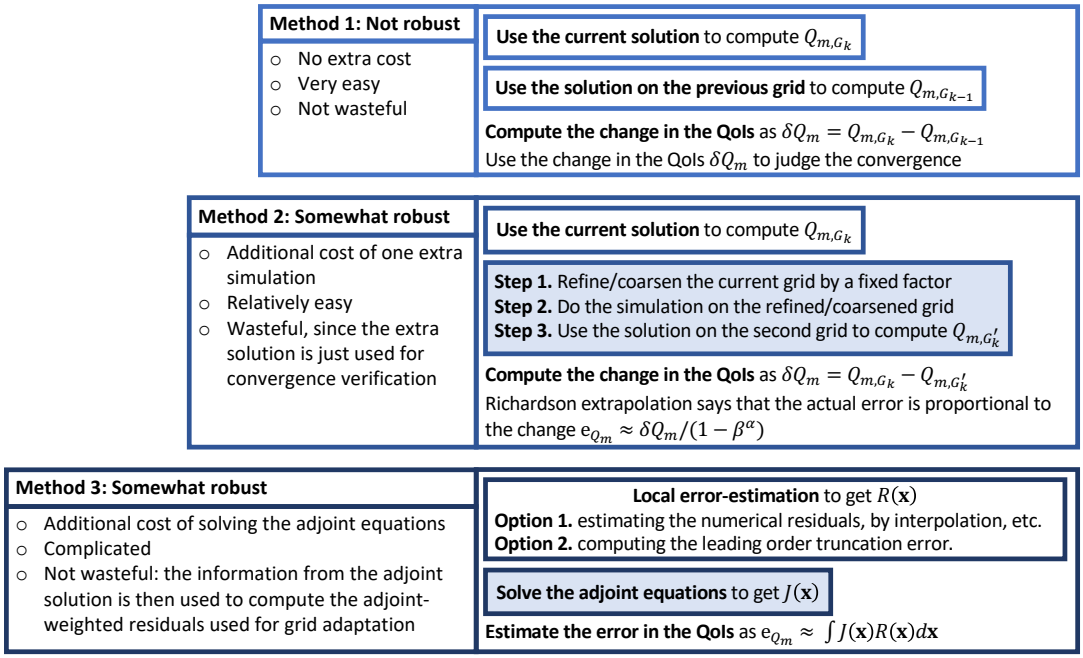

Figure 2.5: A review of different approaches to convergence-verification. The shaded boxes denote the processes with computational costs that are of the same order of magnitude as the original simulation. Robustness of the methods are judged for laminar and RANS simulations. Methods 1 and 2 can be readily applied to both LES and DNS, while for application of method 3 to DNS we should first find a way to avoid the chaotic divergence of the adjoint fields for long time integrations. Having found a way to compute the adjoint fields, method 3 can be used for convergence-verification in LES as well; however, it is no longer fully robust, since error-estimation in LES cannot be fully robust (because of the projection errors).

refines or coarsens the grid that is the subject of convergence assessment by a fixed and uniform factor throughout the domain (in the context of LES this is similar to the SGVM method [22,25,26,31] mentioned in Section 2.1). Assuming that the error in the QoIs is in the asymptotic range and scales with filter-width/grid-resolution in some known way, one can either back out an estimate of the converged value of the QoIs (from a Richardson extrapolation method), or equivalently, assume that the actual error in the QoIs is proportional to the change in the QoIs between the two grids: if the grid resolution changes by a factor β and the asymptotic scaling

exponent is α, the error in any QoI (computed as the difference from its extrapolated value) can be computed by multiplying the change in the QoI by a factor $1/(1-\beta^{\alpha})$.

The exact assumptions of the Richardson extrapolation (that the solution over the entire domain is in the asymptotic range, with the same grid dependence exponent α) may not be necessarily satisfied, especially on the coarser grids, and thus the estimated error in the QoIs may be somewhat different from the actual errors. However, it is still a much better test of convergence compared to the previous approach (method 1 of Fig. 2.5). Note that instead of comparing the QoIs on two grids that were generated based on the same assumptions (error-indicator, user knowledge and experience, etc.), one compares them between two grids where the second one is now generated without any assumption about the flowfield or its resolution requirements: no matter what the original grid or the flowfield looked like, we always change the resolution everywhere, and thus expose the QoIs to changes in the local error sources everywhere in the domain (and not just some specific region where we thought was more important). The real problem with this approach is the extra cost associated with the second simulation which is done only to test for grid convergence. In other words, if the solution is not converged, this extra solution is wasted and one moves on to generating the next grid.

The third method of Fig. 2.5 was specifically designed, in the context of non-broadband simulations, to overcome some of the issues mentioned so far. This approach is called the "adjoint-weighted residual" method, and is carried out in two steps: (i) estimation of the local sources of errors through interpolation of the solution onto a (uniformly) refined version of the grid and computing the numerical

residuals of the governing equations on the refined grid, and (ii) solving the so-called adjoint equations for each of the QoIs to connect the local sources of errors (numerical residuals) to the error in the QoIs. As a result, the error in each of the QoIs can be approximated as the inner product of the local adjoint fields and the local numerical residuals; convergence of the solution can then be judged by whether or not these estimated errors in the QoIs are below the acceptable threshold. Even though this is still just an estimate of the error in the QoIs, it is much more robust than method 1 and arguably more robust than method 2. Additionally, it is not wasteful: if the QoIs are not converged we can multiply the local values of the numerical residuals by the local value of the adjoint fields to compute the "adjoint-weighted residuals" that can be used to find a much more optimal grid for accurate predictions of our specific outputs.

Unfortunately, direct application of the adjoint-weighted residual method to chaotic problems is not really possible at this point. The first issue is the so-called "butterfly effect" [35,36] that causes the adjoint equations to diverge for long time integrations (required for statistically stationary problems with low-frequency motions). There are ways around this, like the method of "least-squares shadowing" (LSS) proposed by Wang [36]; however, computation of the adjoint fields using the LSS method is several orders of magnitude more expensive that the original LES (the "forward" problem).

There is another problem with applying the adjoint-weighted residual method to LES (assuming that the computation of the adjoint fields is not an issue). This is because of the inherent uncertainty that the projection errors introduce into the

error estimates in LES (the actual u_i, or more accurately $\overline{u_i u_j}$, cannot be exactly known based solely on $\overline{u}_i$; see Fig. 2.6). In fact, even in the case of laminar and RANS simulations the projection errors are known to cause problems in the robustness of the convergence-verification using the adjoint-weighted residual method, by under-predicting the error in the QoIs (see Fig. 2.6). The difference is that in a laminar/RANS simulation one can be conservative and keep refining the grid until the estimated QoI errors are below the acceptable threshold for a few consecutive grids and then assume that there is no longer an effect from the projection errors and the convergence test is robust; however, there is no way of avoiding the projection errors in LES, at least not until the DNS limit is reached. As a result, there is always an uncertainty associated with all of the LES error estimates and the estimated error in the QoIs using those error estimates.

The lack of systematic tests for robust convergence-verification in LES is the other gap in the field that we briefly discuss as part of this dissertation (Chapter 7).

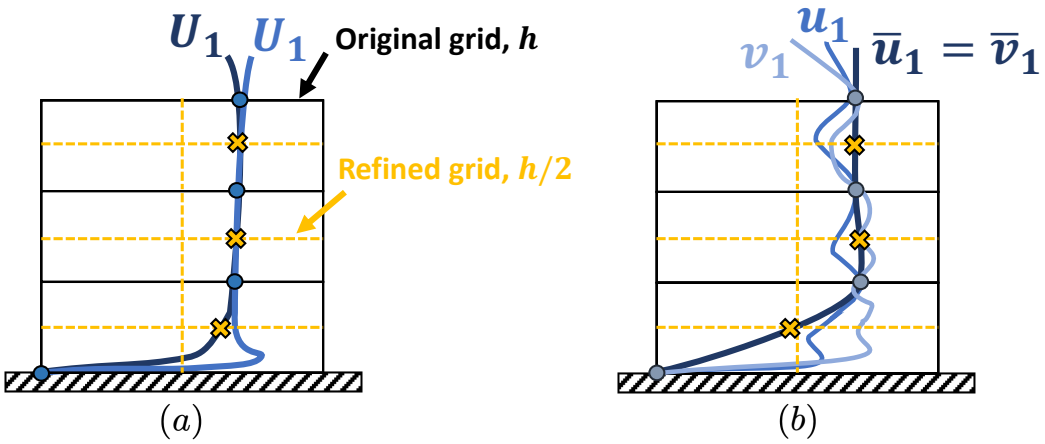

Figure 2.6: An illustration of the effect of projection errors in the context of broadband and non-broadband simulations: (a) a non-broadband simulation where the interpolation onto a finer grid (used in the adjoint-weighted residual method) cannot capture the correct shape of the exact profile and the computed residuals are highly affected by the projection errors; (b) two broadband velocity fields, and the inherent uncertainty in estimation of the original fileds using only the resolved field. Note that even interpolation onto a refined grid does not recover the original shape of the of unfiltered fields. The only way is presumably to actually run the simulation on the refined grid and let the velocity fields develop smaller scales.

Chapter 3: Our first attempt: a fully intuition-based approach to anisotropic error-estimation and grid selection in LES

Among all the areas mentioned in Section 1.4 as gaps in the field, the most important is arguably the lack of any method for anisotropic grid selection and adaptation in LES. Consider the case of wall-bounded turbulent flow computed using wall-resolved LES, for which a typical grid will have a grid-spacing of $(\overline{\Delta}_x^+, \overline{\Delta}_y^+, \overline{\Delta}_z^+) \approx (40, 2, 20)$ close to the wall. Any isotropic grid-adaptation process, no matter how accurate, is still incapable of modifying the aspect ratio of the cells of the initial grid. Therefore, if the initial grid has cubic cells, the final grid for wall-resolved LES would be $(\overline{\Delta}_x^+, \overline{\Delta}_y^+, \overline{\Delta}_z^+) \approx (2, 2, 2)$ near the wall. The potential saving in grid-points for an accurate anisotropic error-indicator is thus a factor of about 200 for this particular case. Naturally, our first attempt was targeted at addressing this major shortcoming.

In this Chapter we rely on the heuristic importance of the small-scale energy in determining the accuracy of LES, and define our error-indicator based on that small-scale energy. Our use of the small-scale energy is supported by a few heuristic arguments that connect it to all types of errors in LES:

Modeling errors: the modeling errors (i.e., $\overline{u_i u_j} - \overline{u}_i \overline{u}_j - \tau_{ij}^{\mathrm{mod}}(\overline{u}_k)$) should decrease

as a smaller portion of the turbulent scales are being modeled (a decrease in both $\overline{u_i u_j} - \overline{u}_i \overline{u}_j$ and $\tau_{ij}^{\text{mod}}(\overline{u}_k)$, and usually their difference); how much of the turbulence is being modeled is related to the energy of the smallest scales.

Numerical errors: the numerical errors affect the resolved turbulent scales that are of a similar size to the grid-resolution. For instance, we can roughly apply the findings of Ghosal [4] here and say that depending on the order of accuracy of the numerical scheme, only scales that are smaller than 4 times the cut-off resolution of the grid (for second order methods; or twice the resolution for sixth order methods) are directly affected by the numerical errors; and, the effect on the larger scales is only indirect, through the errors introduced into the smallest resolved scales and their interaction with the larger scales. Based on this argument, the important factor in determining the numerical error is how active the smallest resolved scales are.

Projection errors: generally speaking, the projection errors are proportional to how much of the turbulence is not directly resolved. The degree of importance of these unresolved scales is different in different problems (e.g. in DNS or in LES) and should be measured differently for each case according to the role of the projection errors in the final solution (e.g., while the difference between $u_i u_j$ and $\overline{u_i u_j}$, which is the relevant quantity in LES, is presumably small, the difference in $\partial u_i/\partial x_k \partial u_j/\partial x_k$ and $\partial \overline{u}_i/\partial x_k \partial \overline{u}_j/\partial x_k$, as the relevant quantity in DNS, may by quite large). For the specific case of LES the energy of those scales seems to be a particularly good measure (in a heuristic sense), descriptive of their importance.

These arguments suggest that the use of the small-scale energy can be a good

estimate of the sources of errors in LES. In fact, even in our preliminary tests of the channel flow in Fig. 2.3(c), the indicator proposed by Bose [23] was one of the most promising in the literature. The question then becomes how we can extend this idea to enable anisotropic grid selection and adaptation in LES.

We note that the idea of using the small-scale energy as a measure of errors in LES is not something new that we came up with, or something that Pope [21] or Bose [23], or Jimenez & Moser [29] invented. Instead, it is almost interwoven with the whole idea of large eddy simulation and has been used for a long time, either implicitly or explicitly, to judge the accuracy of LES solutions. In that sense, our use of the energy as an error-indicator for LES in not novel. Instead, the novelty of the work presented in this Chapter lies in the extension of the idea to enable anisotropic grid selection and generation; i.e., to find $\Delta_{\text{opt}}(\mathbf{x}, \mathbf{n})$, where Δ_{opt} is the optimal filter-width, $\mathbf{x}$ is the spatial coordinate, and $\mathbf{n}$ is the direction.

3.1 Grid selection methodology

In the following we consider $\overline{u}_i$ to be the resolved velocity field from an LES, where (in this Chapter) we do not distinguish between different LES formulations; i.e., $\overline{u}_i$ can be the velocity field that has been filtered either implicitly (by the numerical errors and the subgrid model) or explicitly (by the application of a filter at the end of each time step). Throughout this Chapter we assume that the $\overline{\Delta}/\overline{h}$ ratio (whatever value it has) is fixed. As a result, by a finer grid we imply reducing the filter width and vice versa.

3.1.1 The essence of the idea

Consider an anisotropic turbulent flow, e.g. the flow in the buffer layer of wall-bounded turbulence as shown in Fig. 3.1. For such a flow the turbulent structures are elongated in the streamwise (x) direction, while they have much shorter length scales in the spanwise (z) direction. The figure also shows two imagined computational grids, with the same spanwise resolution ($\overline{\Delta}_z$) but with different streamwise resolutions ($\overline{\Delta}_x$). Turbulence in large eddy simulation is under-resolved on purpose; as the grid is refined, the solution will develop smaller and smaller scales (assuming a constant $\overline{\Delta}/\overline{h}$ ratio). However, this is true only when the grid is refined in all directions. If the grid is refined in an anisotropic fashion (e.g., in one direction only, as is the case in Fig. 3.1), the effective turbulence resolution is determined by the limiting directional resolution. For example, it is visually clear that in Fig. 3.1 the spanwise resolution is the limiting one for both grids; in other words, further refinement of the grid in the streamwise direction does not increase the effective resolution, since the grid can only resolve turbulent scales that are of size $\lambda_z^+ \gtrsim 30$ in the spanwise direction. Since the turbulence is elongated in the streamwise direction, these scales have a larger length in x (say, $\lambda_x^+ \approx 80 - 90$), and thus any streamwise resolution finer than a certain threshold does not really add to the LES resolution. As a result, both grids in Fig. 3.1 would lead to essentially the same accuracy, and the additional streamwise resolution in the first grid is wasteful and unnecessary. This also implies that the "optimal" grid for an LES would be one for which the level of resolution is similar in all directions (and where the turbulence is

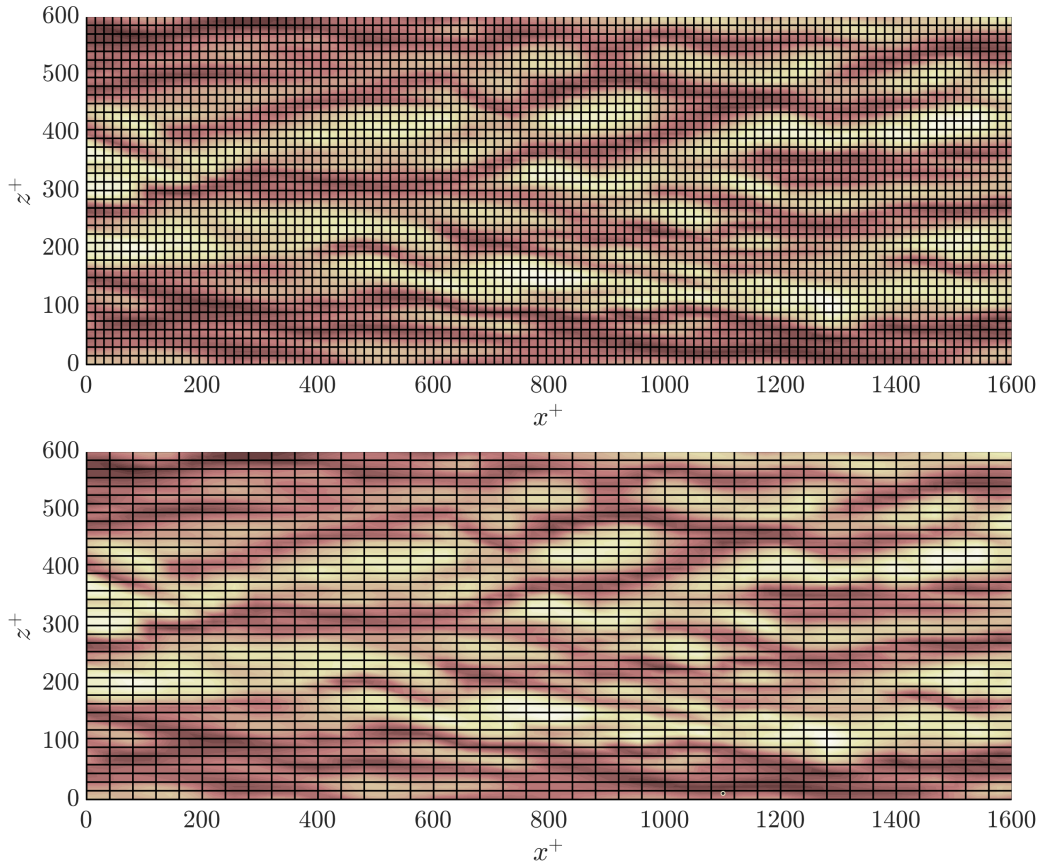

Figure 3.1: The essence of the proposed anisotropic error-indicator: instantaneous streamwise velocity u_1 (from a DNS) in a channel flow at $y^+ \approx 12$ with two imagined computational grids overlaid. The first grid has $(\overline{\Delta}_x^+, \overline{\Delta}_z^+) = (15, 15)$ while the second has $(\overline{\Delta}_x^+, \overline{\Delta}_z^+) = (40, 15)$; performing an LES on either of the two grids would lead to essentially the same accuracy.

resolved "sufficiently well" everywhere throughout the domain).

What exactly measures the resolution in LES is a difficult question. In the present study, we base our estimates on the energy in the barely resolved small-scale velocity field, following our discussion at the beginning of this Chapter. By looking at the energy in a directional sense, where direction refers to the filtering direction rather than the velocity component, we get a directional error-indicator that can later be used for anisotropic grid selection and adaptation. For example, by looking at the energy spectrum of Fig. 3.2, it is obvious that the imagined isotropic grid in

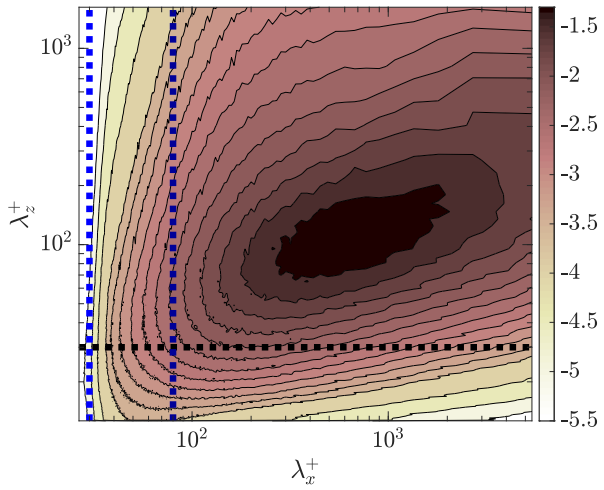

Figure 3.2: Pre-multiplied energy spectrum of the channel flow at $y^+ \approx 12$ (corresponding to the flow shown in Fig. 3.1). The colormap is logarithmic, i.e. -5 corresponds to 10^{-5}. The horizontal dotted black line corresponds to the spanwise cut-off of the grids in Fig. 3.1 (i.e., $\overline{\Delta}_z^+ = 15$), while the vertical dotted blue and dotted dark blue lines, respectively, correspond to the finer ($\overline{\Delta}_x^+ = 15$) and coarser ($\overline{\Delta}_x^+ = 40$) streamwise resolutions. The directional small-scale energy is roughly proportional to the area below the horizontal line for the spanwise direction, and the area to the left of the vertical lines for the streamwise direction. In a grid with $(\overline{\Delta}_x^+, \overline{\Delta}_z^+) = (40, 15)$ the directional small scale energies are very close to being equal, in constrast to a grid with $(\overline{\Delta}_x^+, \overline{\Delta}_z^+) = (15, 15)$. This justifies our choice of small-scale energy as a measure of resolution.

Fig. 3.1 has more small-scale energy in the spanwise direction (the energy in the area below the horizontal dotted black line) than in the streamwise direction (the area to the left of the vertical dotted blue line). The second grid in Fig. 3.1 has the same small-scale energy in the spanwise direction, but now more small-scale energy in the streamwise direction (area to the left of the vertical dotted dark blue line). It appears that the second grid of Fig. 3.1 would have something close to equi-distribution of energy in the streamwise and spanwise directions. This similarity between what we expected from heuristic arguments and physical intuition with what we concluded by comparing the directional small-scale energies further supports the suitability

of the directional small-scale energy as a good measure of directional resolution. We also take the idea of equi-distribution across different directions as a desirable property of the adapted grid in this work, i.e. equivalence of "similar resolution" in all directions.

3.1.2 The proposed error-indicator

In order to measure the small-scale energy we need to first extract the smallest resolved scales as $\overline{u}_i^* = \overline{u}_i - \widehat{\overline{u}}_i$ where $\widehat{\cdot}$ is a low-pass test filter (cf. [3,17,41]). Similarly, to measure the small-scale energy in a directional sense, we need a directional low-pass test filter $\widehat{\cdot}^{(\mathbf{n}_0)}$ that filters the solution only in the specified direction $\mathbf{n}_0$, where $\mathbf{n}_0$ is a unit vector. On structured grids such a uni-directional test-filter along the grid lines is trivial to implement. In order to make the error-indicator applicable to grids with arbitrary topologies (e.g., unstructured grids with any type of elements) in complex geometries, we define this directional low-pass test filter as a modified differential filter [3, 42]. For filtering in the $\mathbf{n}_0$ direction, it is defined implicitly as

$$\overline{u}_i = \left(I - \frac{\overline{\Delta}_{\mathbf{n}_0}^2}{4} \mathbf{n}_0^T \nabla \nabla^T \mathbf{n}_0 \right) \widehat{\overline{u}}_i^{(\mathbf{n}_0)} ,$$

where I is the identity operator and $\overline{\Delta}_{\mathbf{n}_0} = \overline{\Delta}(\mathbf{x}, \mathbf{n}_0)$ is the filter-width in the $\mathbf{n}_0$ direction ($\overline{\Delta}$ is the same filter-width that was used in the original LES to obtain $\overline{u}_i$). The doubly-projected Hessian operator $\mathbf{n}_0^T \nabla \nabla^T \mathbf{n}_0$ can equivalently be written in tensor notation as $n_{0,j} n_{0,k} \, \partial^2 / \partial x_j \partial x_k = \partial^2 / \partial x_{\mathbf{n}_0}^2$. Application of this filter requires the inversion of a linear system of equations (after discretization). While this is not a major problem, we instead follow the route of an approximate inversion since the

test filtered field will be used only to inform a grid-adaptation algorithm (e.g., it will not enter into a subgrid-scale model or similar). The van Cittert approximation [43] of the inverse, truncated after two terms, is

$$\widehat{\overline{u}}_i^{(\mathbf{n}_0)} \approx \left(I + \frac{\overline{\Delta}_{\mathbf{n}_0}^2}{4} \, \mathbf{n}_0^T \nabla \nabla^T \mathbf{n}_0 \right) \overline{u}_i \,, \tag{3.1}$$

which provides an explicit formulation of the low-pass test filter. The van Cittert approximation was introduced to the field of LES by Stolz and Adams [44] as a means to model the subgrid stress through an approximate deconvolution of $\overline{u}_i$. The van Cittert approximation technically requires that the operator norm $\| (\overline{\Delta}_{\mathbf{n}_0}^2/4) \, \mathbf{n}_0^T \nabla \nabla^T \mathbf{n}_0 \| < 1$ for convergence of the infinite series. In practice, the approximation is regularized both by the discretization and the truncation of the series; as a result, no issues of ill-posedness are expected due to this approximate inversion.

For a structured grid with uniform grid-spacing and using second-order central differencing, the filter of Eqn. 3.1 simplifies to a uni-directional box filter of width $2\overline{\Delta}(\mathbf{x}, \mathbf{n}_0)$ (applied using the trapezoidal rule).

We thus compute the directionally small-scale (i.e., the directionally high-pass test filtered) field $\overline{u}_i^{*,(\mathbf{n}_0)}$ as

$$\overline{u}_i^{*,(\mathbf{n}_0)} \equiv \overline{u}_i - \widehat{\overline{u}}_i^{(\mathbf{n}_0)} \approx - \frac{\overline{\Delta}_{\mathbf{n}_0}^2}{4} \, \mathbf{n}_0^T \left(\nabla \nabla^T \overline{u}_i \right) \mathbf{n}_0 \,, \tag{3.2}$$

and then define the anisotropic error-indicator in any arbitrary direction $\mathbf{n}$ as the square root of (twice) the small-scale energy in that direction,

$$\overline{\mathcal{A}}(\mathbf{x}, \mathbf{n}) = \sqrt{\left\langle \overline{u}_i^{*,(\mathbf{n})} \overline{u}_i^{*,(\mathbf{n})} \right\rangle} \,, \tag{3.3}$$

where $\langle\cdot\rangle$ denotes a suitable average (time-average, phase-average, etc; the key point is to average out the turbulent fluctuations) and summation over the tensor index i is implied. The overbar on $\overline{\mathcal{A}}$ only signifies the filter width $\overline{\Delta}$ used in calculation of the error-indicator, i.e. it does not mean a filtering of $\overline{\mathcal{A}}$.

This error-indicator is defined as an estimate of the energy of those components of the solution that have small-scale variation along direction $\mathbf{n}$, and should be interpreted as such in all scale-resolving simulations of turbulence. However, for the case of laminar flow where the averaging operation is redundant, the error-indicator reduces to the doubly-projected Hessian of the velocity field (or equivalently, the length of $\mathbf{r} = \mathbf{n}(\overline{\Delta}_{\mathbf{n}}/2)$ with respect to a Hessian-based metric); it is therefore related to the many prior usages of the Hessian matrix in grid-adaptation for non-chaotic flows (cf. [40, 45–48]). For flows with broadband turbulence, however, the meaning and interpretation of $\overline{\mathcal{A}}(\mathbf{x}, \mathbf{n})$ is quite different. Specifically, one should not interpret $\overline{\mathcal{A}}(\mathbf{x}, \mathbf{n})$ as a measure of the numerical error: note, for example, that $\overline{\mathcal{A}}(\mathbf{x}, \mathbf{n})$ is agnostic (in terms of its functional form) to the numerical method, the $\overline{\Delta}/\overline{h}$ ratio, and the grid-spacing $\overline{h}$ in general.

While only statistically stationary problems are considered in this Chapter (and throughout this dissertation), the proposed error-indicator should be applicable to problems with large-scale unsteadiness (e.g., vortex shedding in the turbulent regime) provided that the averaging operation $\langle\cdot\rangle$ is modified accordingly.

We note that the contribution from the "cross-term" $2\left\langle \widehat{\overline{u}}_i^{(\mathbf{n})} \overline{u}_i^{*,(\mathbf{n})} \right\rangle$ is not included in the error-indicator. While we have no solid proof for excluding it, the hypothesis is that the direct effect of insufficient resolution is measured by the small

scale energy and thus that we should only estimate the energy of those small scales. Finally, the proposed error-indicator in (3.3) is not scaled by the resolved turbulent kinetic energy (as suggested by Pope [21]) since this was found to produce clearly inferior results in preliminary tests on channel flows.

We end this section by noting that the directional test filter could have been derived in different ways, e.g. through a Taylor expansion of a convolution-based filter (cf. [3,17]). Other similar anisotropic error-indicators could also be constructed using different techniques or different assumptions, e.g. through the use of structure functions (analogously to the method used by Moser and Haering [49–51] to construct an anisotropic subgrid model). A brief discussion of the application and suitability of structure functions for anisotropic grid-adaptation in LES is included in Section 3.4.

3.1.3 Scaling and limiting behavior

It is instructive to study the scaling behavior of the proposed error indicator in some idealized situations, including the channel flow of Figs. 3.1 and 3.2. For a spatially homogeneous turbulent field (in at least one direction) an energy spectrum tensor Φ_{ij} can be defined as the Fourier transform of the two-point velocity correlation $R_{ij}(\mathbf{x},\mathbf{r}) = \langle u_i'(\mathbf{x}) u_j'(\mathbf{x}+\mathbf{r}) \rangle$ [17] (where $u_i' = u_i - \langle u_i \rangle$ is the fluctuating velocity). For such flows, the error-indicator $\overline{\mathcal{A}}$ can be expressed in terms of the energy spectrum tensor $\Phi_{ij}(\mathbf{x},\mathbf{k})$ as

$$\overline{\mathcal{A}}^2(\mathbf{x},\mathbf{n}) = \frac{\overline{\Delta}_{\mathbf{n}}^4}{16} \int_{-\infty}^{\infty} k_{\mathbf{n}}^4 \Phi_{ii}(\mathbf{x},\mathbf{k}) d\mathbf{k}\,, \tag{3.4}$$

where sum over i is implied, and $k_{\mathbf{n}} = \mathbf{k} \cdot \mathbf{n}$ is the wavenumber in direction $\mathbf{n}$.

Figure 3.3 shows the integrand of Eqn. 3.4, for the wall-bounded turbulence of Fig. 3.1 and for directional filtering in both the spanwise and streamwise directions. The energy spectrum itself, Φ_{ii}, is also shown for the ease of comparison (same as Fig. 3.2). The error-indicators computed for the imagined grids show how the directional filtering amplifies those modes with small wavelengths (high wavenumbers) along direction $\mathbf{n}$. It is visually clear that the directional small scale energy is relatively small for streamwise filtering with $\overline{\Delta}_x^+ = 15$ but much larger for spanwise filtering with $\overline{\Delta}_z^+ = 15$, and thus that $\overline{\mathcal{A}}(\mathbf{x}, \mathbf{n}_z)$ is much larger than $\overline{\mathcal{A}}(\mathbf{x}, \mathbf{n}_x)$ for this imagined isotropic grid. The assumed principle of directional equi-distribution then means that we should increase $\overline{\Delta}_x$ relative to $\overline{\Delta}_z$. For the grid with $\overline{\Delta}_x^+ = 40$, the two values are much closer to each other, meaning that this directional equi-distribution is almost satisfied.

On a finite grid, the integration bounds in Eqn. (3.4) become proportional to the inverse of the grid-spacing, and it is useful to study how $\overline{\mathcal{A}}(\mathbf{x}, \mathbf{n})$ varies with $\overline{\Delta}_{\mathbf{n}}$ in some special cases.

In the limit of well-resolved DNS, the grid resolution falls in the dissipative range where the spectrum is exponentially decaying. This means that the integral in Eqn. 3.4 becomes independent of the grid-spacing, and thus that $\overline{\mathcal{A}}(\mathbf{x}, \mathbf{n}) \sim \overline{\Delta}_{\mathbf{n}}^2$. This is approximately the case for $\overline{\mathcal{A}}(\mathbf{x}, \mathbf{n}_x)$ in Fig. 3.3 for grid with $\overline{\Delta}_x^+ = 15$.

For a laminar flow (or more precisely, for a flow without broadband energy), the integral is also independent of the grid-spacing and thus $\overline{\mathcal{A}}(\mathbf{x}, \mathbf{n}) \sim \overline{\Delta}_{\mathbf{n}}^2$.

In LES, the grid resolution should generally be such that most of the energy is

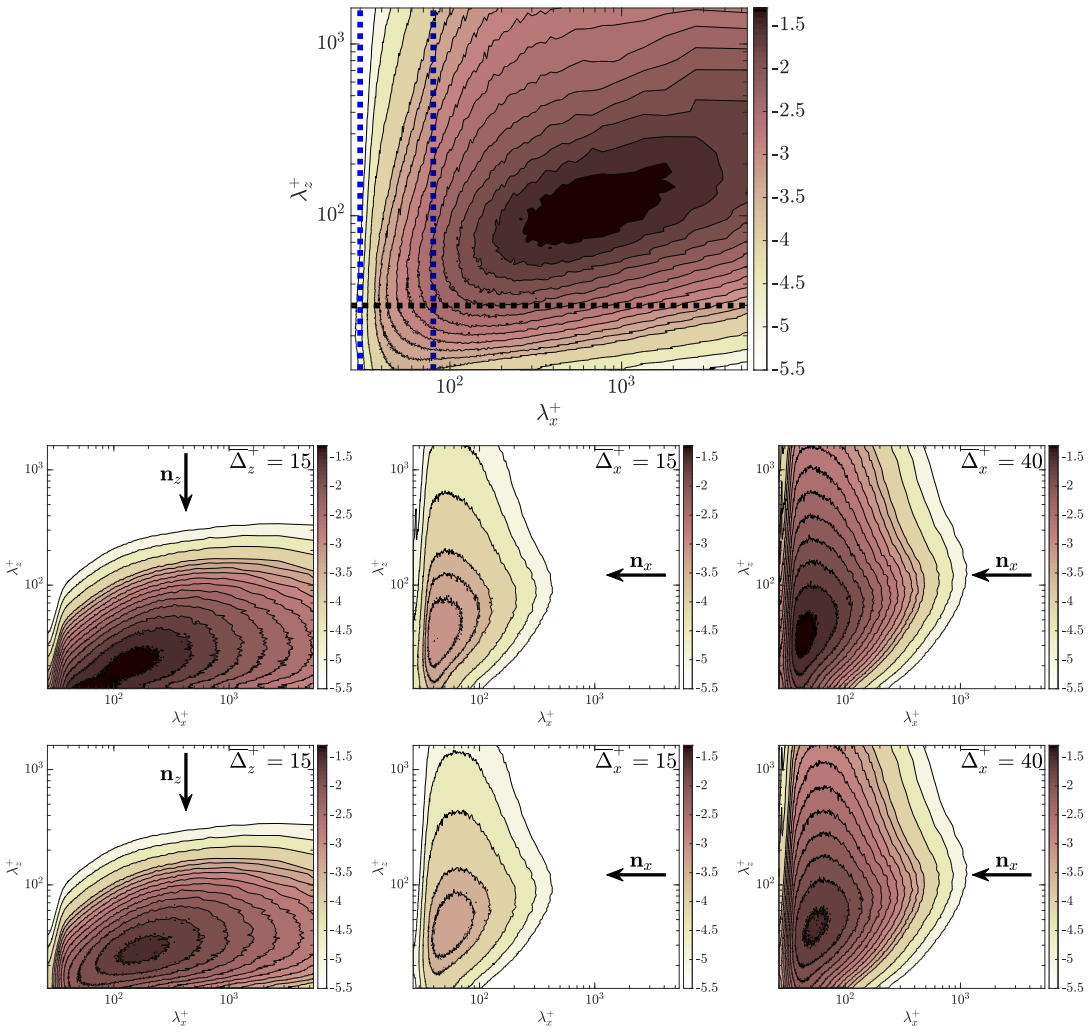

Figure 3.3: Pre-multiplied spectral density of the energy, $k_x k_z \Phi_{ii}$, in the turbulent channel flow at $y^+ \approx 12$ (top), and the premultiplied integrand of Eqn. 3.4, $k_x k_z \frac{\overline{\Delta}_{\mathbf{n}}^4}{16} k_{\mathbf{n}}^4 \Phi_{ii}$ ($\overline{\Delta}_{\mathbf{n}}$ is constant and is moved inside the integral) at the same location, corresponding to the error-indicator $\overline{\mathcal{A}}$, for: exact computation of the second order derivatives in the definition of the error-indicator (middle row), and the second-order central differencing used throughout this dissertation (bottom row). See text for more details. The colormap is logarithmic.

resolved without requiring that any of the dissipation is resolved. In those situations the scaling of $\overline{\mathcal{A}}(\mathbf{x}, \mathbf{n})$ depends on the slope of the energy spectrum near the cut-off. Assuming that the spectrum decays as $\sim k_{\mathbf{n}}^{-\beta_{\mathbf{n}}}$ in direction $\mathbf{n}$, we get

$$\overline{\mathcal{A}}(\mathbf{x}, \mathbf{n}) \sim \overline{\Delta}_{\mathbf{n}}^2 \sqrt{\int k_{\mathbf{n}}^4 k_{\mathbf{n}}^{-\beta_{\mathbf{n}}} dk_{\mathbf{n}}} \sim \overline{\Delta}_{\mathbf{n}}^{(\beta_{\mathbf{n}}-1)/2} . \tag{3.5}$$

In ideal homogeneous isotropic turbulence, for example, the one-dimensional density of the energy scales as $\sim k_{\mathbf{n}}^{-5/3}$ (cf. [17]) which results in $\overline{\mathcal{A}}(\mathbf{x},\mathbf{n}) \sim \overline{\Delta}_{\mathbf{n}}^{1/3}$ for any $\mathbf{n}$. In a more general flow with anisotropic turbulent structures it is plausible that the spectrum decays differently in different directions and thus that $\overline{\mathcal{A}}(\mathbf{x},\mathbf{n})$ scales differently for different $\mathbf{n}$. This is true more broadly, in the sense that the spectrum in LES will depend on the flow, the grid spacing in all directions (not just direction $\mathbf{n}$), the subgrid model, and the numerics; the scalings derived here are thus merely estimates.

We should emphasize that all the results presented in this Section were obtained by assuming an exact differentiation operator in the filter definition of Eqn. 3.2. For numerical differentiation, the wavenumber inside the integral of Eqn. 3.4 should be replaced by the modified wavenumber of the numerical scheme $k'_{\mathbf{n}}$. For instance, for a second order central differencing on uniform grids (which is equivalent to a unidirectional box filter of size $2\overline{\Delta}_{\mathbf{n}}$ applied using the trapezoidal rule) the modified wavenumbers $k'_{\mathbf{n}}$ have lower values compared to the exact $k_{\mathbf{n}}$, especially close to the cut-off of the grid [52], and the filtered spectrums are slightly modified (see Fig. 3.3). The important point here is that even though the computed values of the small scale energies are being slightly affected, both the streamwise and spanwise error-indicators are affected in the same way (i.e. both have lower values compared to the exact differentiation); therefore, these changes do not significantly affect the final aspect ratio of the grid. As for the scaling exponent of the error-indicator, we can expect to see more significant variations with the choice of the numerical scheme. However, this scaling exponent does not affect our prediction of the opti-

mal grid; in other words, the optimal grid is achieved when the error-indicator itself has a spatial distribution that is described by the optimality criteria. Throughout this Chapter we have used the approximate scaling $\overline{\mathcal{A}}(\mathbf{x}, \mathbf{n}) \sim \overline{\Delta}_{\mathbf{n}}^2$ in generating the adapted grids, with good results in all tests.

3.1.4 Use when adapting a grid

Our primary focus so far has been on using the directional error-indicator $\overline{\mathcal{A}}$ for finding the correct anisotropy (aspect ratio) of the filter or computational cells. The next question to answer is what distribution of the error-indicator leads to the most optimal distribution of filter width in space $\mathbf{x}$. In other words, how the level of resolution of different turbulent scales should vary in space to achieve the highest possible accuracy. This is a much more complicated question to answer, one that also depends on the quantity of interest. For instance, in an LES of a wing with flow separation where the main purpose of the simulation is finding the drag coefficient, it is not optimal to resolve the turbulent scales far downstream of the wing with the same level of resolution as the turbulent scales near the solid wall. In the relatively simple test cases of this Chapter, where we do not really have a strong preference towards a specific QoI and the goal is to have a good "all-around" solution, we assume that the most optimal filter should provide similar resolution in different locations as well. Intuitively speaking, this amounts for the equidistribution of the error-indicator in both space and direction, i.e.,

$$\check{\mathcal{A}}_{\text{opt}}(\mathbf{x}, \mathbf{n}) = \text{const.} = \mathcal{A}_{\text{thresh}} \,, \tag{3.6}$$

where $\check{\mathcal{A}}_{\text{opt}}$ denotes the "optimal" distribution of the error-indicator, and $\mathcal{A}_{\text{thresh}}$ is a scalar value. This can be used in grid selection and adaptation.

The first step is to choose a threshold value $\mathcal{A}_{\text{thresh}}$. Since there is no known connection between $\overline{\mathcal{A}}(\mathbf{x}, \mathbf{n})$ and the error in the solution (or in specific outputs of the solution), there is no way to derive or specify a suitable threshold *a priori*. The threshold $\mathcal{A}_{\text{thresh}}$ must therefore be either chosen heuristically, similar to what Pope [21] and Bose [23] did, or based on a desired increase of the size of the grid. The former approach is completely heuristic and does not necessarily lead to convergence (there is really no reason why all the QoIs should converge if 80% or 90% or 95% of the energy is resolved), while the latter approach then requires a direct monitoring of the convergence of the solution and its QoIs. The important argument in the second approach is that if we assume that the grid is close to its optimal state at each iteration (since all grids are generated by enforcing Eqn. 3.6 that describes an "optimal" distribution for the filter $\check{\Delta}$), the first grid for which the convergence criterion is satisfied will be our optimal grid. This will be our approach throughout this Chapter (and in fact the whole dissertation).

Once a threshold $\mathcal{A}_{\text{thresh}}$ is chosen, the simplest way is to refine cells in those directions $\mathbf{n}$ for which $\overline{\mathcal{A}}(\mathbf{x}, \mathbf{n}) > \mathcal{A}_{\text{thresh}}$. This is basically a binary decision, where cells would be refined at most once in each iteration. While simple, it is not the most efficient. An alternative (and more efficient) approach is to assume a scaling $\overline{\mathcal{A}}(\mathbf{x}, \mathbf{n}) \sim \overline{\Delta}_{\mathbf{n}}^{\alpha_{\mathbf{n}}}$ and then find the "target" filter-width as,

$$\check{\Delta}_{\text{opt}}(\mathbf{x}, \mathbf{n}) = \left[\frac{\mathcal{A}_{\text{thresh}}}{\overline{\mathcal{A}}(\mathbf{x}, \mathbf{n})}\right]^{1/\alpha_{\mathbf{n}}} \overline{\Delta}(\mathbf{x}, \mathbf{n}) \,, \tag{3.7}$$

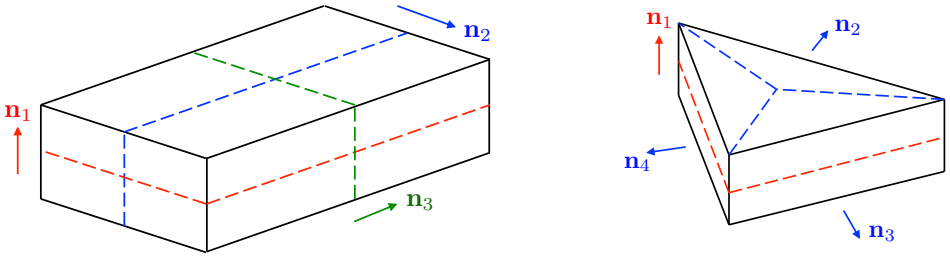

Figure 3.4: Two types of cells, their possible ways of refinement (in dashed lines), and the assoctiated directions $\mathbf{n}_1$-$\mathbf{n}_3$ or $\mathbf{n}_1$-$\mathbf{n}_4$ in which to compute the error-indicator $\overline{\mathcal{A}}(\mathbf{x}, \mathbf{n})$.

where $\check{\Delta}_{\text{opt}}$ is our best estimate of the optimal distribution at that specific level of accuracy (or resolution), and $\overline{\mathcal{A}}(\mathbf{x}, \mathbf{n})$ is the value of the error-indicator computed on the original LES grid with filter-width $\overline{\Delta}(\mathbf{x}, \mathbf{n})$. Since the exponent $\alpha_{\mathbf{n}}$ is flow-dependent and potentially also direction-dependent, it is necessary to choose this value in an approximate way. The flow problems tested in the present work are dominated by wall-bounded turbulence for which we perform wall-resolved LES. Since wall-resolved LES is known to behave properly for wall-bounded turbulence only when the grid approaches "quasi-DNS" resolution, we use $\alpha_{\mathbf{n}} = 2$ in this work (in all directions) without any attempts at finding the "best" value. In Section 4.4 we further justify our choice of $\alpha_{\mathbf{n}} = 2$ from another perspective.

Which directions $\mathbf{n}$ to evaluate the error-indicator for will depend on the nature of the grid (what types of cells it has) and the solver (what types of cells it can handle).

A hexahedral cell (which is the cell topology used in all test cases of this Chapter) is most naturally refined in one, two or all three of the natural directions, as sketched in Fig. 3.4. One would therefore compute the error-indicator $\overline{\mathcal{A}}(\mathbf{x}, \mathbf{n})$ for those three directions only ($\mathbf{n}_1$, $\mathbf{n}_2$ and $\mathbf{n}_3$ in the figure) and refine accordingly.

Figure 3.4 also shows a prism cell, which could for example be refined by either: (a) slicing it in half in the plane of the triangular faces, i.e., normal to the $\mathbf{n}_1$ direction; or (b) inserting grid points in the center of the triangular faces, thus creating three new prisms. Option (a) would reduce the characteristic size of the cell only in the $\mathbf{n}_1$ direction; therefore, this refinement should be done only if $\overline{\mathcal{A}}(\mathbf{x}, \mathbf{n}_1)$ is larger than some threshold. Option (b) would reduce the characteristic size of the cell in the directions of the face normals, and thus one should compute and check all of $\overline{\mathcal{A}}(\mathbf{x}, \mathbf{n}_2)$, $\overline{\mathcal{A}}(\mathbf{x}, \mathbf{n}_3)$ and $\overline{\mathcal{A}}(\mathbf{x}, \mathbf{n}_4)$ in order to make this refinement decision.

For other refinement strategies, and possibly for other types of solvers (e.g., cell- or vertex-based), one may possibly need to compute the error-indicator for other directions as well. In any case, the general idea would be to refine the cell in any given manner only if the maximum of all $\overline{\mathcal{A}}(\mathbf{x}, \mathbf{n})$ values is above some threshold, where one should include all those directions $\mathbf{n}$ for which the refinement would reduce the characteristic filter-width.

We note that the computation of the error-indicator is entirely a post-processing operation. One needs to compute the Hessian of the instantaneous velocity field $\nabla\nabla^T\overline{u}_i$ for a number of solution snapshots, project this onto all (locally) possible refinement directions $\mathbf{n}$, and average. The computation of the Hessian is straightforward on grids with structure (e.g., Cartesian AMR), but will require a more elaborate technique on unstructured grids, e.g., a Taylor expansion of the solution followed by a least-squares method [46] or a quadratic reconstruction of the solution [47].

In situations where the grid is completely re-generated rather than adapted,

one could assess the directional structure of $\overline{\mathcal{A}}(\mathbf{x}, \mathbf{n})$ in more detail in order to locally align the new grid to the local resolution requirements. An approach similar to that of Frey and Alauzet [46] or Park [48] could be used for this, where one assembles a modified metric tensor for use in anisotropic grid generation. These considerations are beyond the scope of this dissertation, which is focused on assessing the proposed error-indicator itself.

3.1.5 Stopping criterion

Grid-adaptation is iterative and it is thus important to devise a criterion for when to stop, i.e., for when to declare the grid sufficiently fine. A stopping criterion must necessarily measure the error in the quantities of interest from the solution. In contrast, the error-indicator $\overline{\mathcal{A}}(\mathbf{x}, \mathbf{n})$ attempts to measure the local sources of error into the problem. In grid-adaptation for non-chaotic problems, the adjoint provides a link between the error sources and the quantities of interest (cf. [9]). In the present approach we have no such link, and thus the stopping criterion cannot be defined in terms of the error-indicator at all. Instead, the only reasonable approach is to monitor the convergence of the QoIs during the grid-adaptation process.

Assuming that we have M quantities of interest $\overline{Q}_m$ in the simulation ($\bar{\cdot}$ means that $\overline{Q}_m$ was computed on grid $\overline{\Delta}$) allows for the total error in these QoIs to be defined as

$$\overline{e}^{\text{ref}}_{\text{QoI}} = \sum_{m=1}^{M} w_m \delta \overline{Q}^{\text{ref}}_m \,, \tag{3.8}$$

where $\delta \overline{Q}^{\text{ref}}_m$ is the difference in $\overline{Q}_m$ compared to a reference solution and w_m is an

appropriate weight.

Two different reference solutions are used to compute the total error in this paper: (i) the LES solution on the previous grid that was used to compute the error-indicator and generate the current grid (labeled $\overline{e}_{\text{QoI}}^{\text{prev}}$); and (ii) a converged DNS solution (labeled $\overline{e}_{\text{QoI}}^{\text{DNS}}$). The DNS-based error $\overline{e}_{\text{QoI}}^{\text{DNS}}$ is obviously a better measure of convergence, but is not available in practice. As a result, both $\overline{e}_{\text{QoI}}^{\text{DNS}}$ and $\overline{e}_{\text{QoI}}^{\text{prev}}$ are reported for all cases. Since our primary purpose in this Chapter is to assess the error-indicator and the grid-adaptation process (and not to discuss how we can judge the convergence in a real grid-adaptation scenario) $\overline{e}_{\text{QoI}}^{\text{DNS}}$ will be our primary measure in deciding whether or not the results are converged.

The first grid that satisfies the criterion on $\overline{e}_{\text{QoI}}^{\text{DNS}}$ is taken as the "optimal" grid in this Chapter. A more conservative criterion would be to require multiple sequential grids to satisfy the convergence criterion. Chapter 7 of this dissertation focuses on convergence-verification in LES, and any further discussions of the subject are delayed until then.

3.2 Assessment on turbulent channel flow

The filter-width selection and adaptation problem is inherently an optimization problem: we should therefore check whether the predicted grids/filter-widths are "optimal" in the sense of leading to the best accuracy at the lowest cost. While true optimality is probably impossible to assess in the context of LES, the turbulent channel flow is arguably as close as we can get given the many decades of

experience with this flow in the LES community. For the turbulent channel cases, we therefore ask whether the adaptation algorithm can produce grids close to the $(\Delta_x^+, \Delta_{y_w}^+/2, \Delta_z^+) \approx (40, 1, 20)$ or so that is widely considered a "good" grid for wall-resolved LES.

All simulations are started from exceedingly coarse grids that are essentially ignorant of the flow physics; this is done to test the robustness with severely under-resolved solutions. The idea here is that, no matter how coarse the grid might be, a robust method should always drive the grid towards a distribution that leads to lower errors in the solution.

To further test the robustness of the method, we consider three different approaches: (i) implicitly filtered LES with an explicit LES model (dynamic Smagorinsky model) and a mixture of modeling and numerical errors; (ii) Implicit LES (ILES) with a dissipative WENO scheme (as a completely different approach to LES modeling); and (iii) DNS, which is purely affected by numerical errors.

3.2.1 Code and problem specification

The code used for this problem is the *Hybrid* code that solves the compressible Navier-Stokes equations for a calorically perfect gas on structured Cartesian grids using sixth-order accurate central differencing schemes with a split form of the convective terms [53] (skew-symmetric in the limit of zero Mach number) for increased numerical stability. Numerical noise is removed by a numerical sixth-order hyperviscosity term in conservative form; the effect of this (very low level of) numerical

high wave-number dissipation has been assessed and found negligible for the cases in this study. Time-integration is handled by classic fourth-order Runge-Kutta.

The channel flows are driven by a spatially uniform body force that is adjusted at each time step to maintain a constant bulk velocity U_b. The walls are isothermal. The bulk Mach number, defined as the ratio of U_b and the speed-of-sound at the walls, is 0.8, which is a compromise between having minimal effects of compressibility while avoiding an excessively small time step. The computational domain is of size $(L_x, L_y, L_z) = (10H, 2H, 3H)$ where H is the channel half-width. The grids are stretched in the wall-normal direction using a tanh-function. The simulations are initialized either from a laminar profile with random, approximately solendoidal, noise added to the velocity (with 10% amplitude), or by interpolating an existing fully developed solution from a different grid. They are integrated for a time of $400H/U_b$ before collecting statistics over a period of $400H/U_b$. The convergence of the statistics is verified by computing averages using only parts of the complete record in time, and then estimating the associated standard deviation of the averages. The convergence error is found to be sufficiently small as to not affect any conclusions in this study. This long integration time is primarily required for convergence of the solution, while the grid-adaptation can actually be performed with averages collected over a much shorter time. A careful study of the required statistical convergence of the error indicator is deferred until Chapter 6.

To measure convergence, the QoIs are defined based on the mean velocity and

the Reynolds stresses. Specifically, the errors in the QoIs are defined as

$$\begin{aligned}\delta\overline{Q}_1^{\text{ref}} &= \frac{\int_a^b \left|\overline{U}_1^+ - \widetilde{U}_{1,\text{ref}}^+\right| d\left(\ln y^+\right)}{\int_a^b \widetilde{U}_{1,\text{ref}}^+ \, d\left(\ln y^+\right)} \\ \delta\overline{Q}_{2\text{-}5}^{\text{ref}} &= \frac{\int_a^b \left|\overline{R}_{ij}^+ - \widetilde{R}_{ij,\text{ref}}^+\right| d\left(\ln y^+\right)}{\int_a^b \widetilde{R}_{kk,\text{ref}}^+/2 \, d\left(\ln y^+\right)} \;, \quad (i,j) = (1,1),\,(2,2),\,(3,3),\,(1,2)\,.\end{aligned} \tag{3.9}$$

where $\overline{U}_1 = \langle \overline{u}_1 \rangle$ and $\overline{R}_{ij} = \langle \overline{u}_i' \overline{u}_j' \rangle$ are the resolved mean velocity and resolved Reynolds stress on the LES grid (with characteristic filter-width $\overline{\Delta}$). The reference quantities $\widetilde{U}_{1,\text{ref}}$ and $\widetilde{R}_{ij,\text{ref}}$ are taken either from the previous LES grid in the sequence of adapted grids (for $\overline{e}_{\text{QoI}}^{\text{prev}}$) or from our own DNS for the same setup (for $\overline{e}_{\text{QoI}}^{\text{DNS}}$). The integration limits (a and b) are taken as $y^+ = 2$ to $y^+ = Re_\tau/2$ (i.e. $y = H/2$), where the core of the channel is excluded since it is the most affected by the domain size. Note that the error in all of the Reynolds stresses is normalized by the (integral of the) kinetic energy $\widetilde{R}_{kk}/2$. These five $\delta\overline{Q}_m^{\text{ref}}$ are then equally weighted to form the final error metric

$$e_{\text{QoI}}^{\text{ref}} = \frac{1}{5}\sum_{m=1}^{5} \delta\overline{Q}_m^{\text{ref}} \,. \tag{3.10}$$

Admittedly, we should use the total Reynolds stress $\overline{R}_{ij}^{\text{tot}} = \langle \overline{u}_i' \overline{u}_j' \rangle + \langle \tau_{ij}^{\text{mod}} \rangle$ (where τ_{ij}^{mod} is the modeled SGS stress) for judging the convergence of any LES. Unfortunately, for the channel flow cases of this Chapter (and only this Chapter) we had not stored the eddy viscosity in the original simulations and we did not want to repeat all of them. That is why we are instead using the resolved Reynolds stress $\overline{R}_{ij} = \langle \overline{u}_i' \overline{u}_j' \rangle$. Besides, a good wall-resolved LES (i.e., on a converged grid, or not far from it) must have a resolution that is close to the DNS, meaning that the LES model is not really that active on the finer grids anyway. In other words, in the

wall-resolved LES of the channel flow the effect of $\langle \tau_{ij}^{\text{mod}} \rangle$ is significant only on the coarser grids, where $e_{\text{QoI}}^{\text{ref}}$ is high anyways, and it is negligible on finer grids that have a lower $e_{\text{QoI}}^{\text{ref}}$; therefore, none of the conclusions of this Section should be affected by using the resolved Reynolds stress.

3.2.2 LES with a dynamic Smagorinsky model at $Re_\tau \approx 830$

The main test case is to run an implicitly filtered LES with an explicit subgrid model. Specifically, the dynamic Smagorinsky model [54, 55] is used, with filtering and averaging in the wall-parallel directions. Combined with the use of numerics with low numerical dissipation, this produces solutions that are contaminated by both modeling and numerical errors of about similar magnitudes (cf. [4, 56]).

The bulk Reynolds number $Re_b = \rho_b U_b H/\mu_w$ (where ρ_b is the bulk density and μ_w is the viscosity at the wall) is 15,000, which leads to a friction Reynolds number of about $Re_\tau \approx 830$ (for a fine grid on which the solution is converged).

To really test the proposed error-indicator, the initial grid is chosen to be both isotropic and exceedingly coarse. This approximates a realistic engineering scenario where the user has little idea about how to generate the initial grid. Specifically, the initial grid (labeled LES-1) has cells of size $\overline{\Delta}_x = \overline{\Delta}_y = \overline{\Delta}_z = 0.25H$, which corresponds to $\overline{\Delta}_x^+ = \overline{\Delta}_y^+ = \overline{\Delta}_z^+ \approx 210$ at the converged Re_τ. The mean velocity and streamwise Reynolds stress are shown in Fig. 3.5 with some details given in Table 3.1. Both profiles are, of course, completely inaccurate on this exceedingly coarse grid. The threshold $\mathcal{A}_{\text{thresh}}$ is chosen such that it leads to an increase in the

Grid	N_{tot}	N_y	$(\overline{\Delta}_x^+, \overline{\Delta}_{y_w}^+/2, \overline{\Delta}_z^+)$	$(\overline{\Delta}_x, \overline{\Delta}_{y_c}, \overline{\Delta}_z)/H$	Re_τ	$\overline{e}_{\text{QoI}}^{\text{prev}}$ (%)	$\overline{e}_{\text{QoI}}^{\text{DNS}}$ (%)
LES-1	3.84k	8	$(89, 45, 89)$	$(0.25, 0.25, 0.25)$	356	–	110
LES-2	16.8k	32	$(170, 2.2, 120)$	$(0.29, 0.14, 0.20)$	611	200	53
LES-3	144k	50	$(130, 1.7, 57)$	$(0.17, 0.090, 0.075)$	758	17	22
LES-4	553k	60	$(85, 1.6, 26)$	$(0.10, 0.075, 0.031)$	820	13	8.3
LES-5	1.97M	72	$(54, 1.3, 14)$	$(0.066, 0.063, 0.017)$	822	5.8	3.1
LES-6	4.75M	80	$(38, 1.5, 9.2)$	$(0.046, 0.052, 0.011)$	827	2.1	2.0

Table 3.1: LES of channel flow at $Re_\tau \approx 830$ starting from a very coarse isotropic grid. Note that $\overline{\Delta}_{y_c}$ is the value at the channel centerline, while $\overline{\Delta}_{y_w}^+$ is the value at the wall. N_{tot} is the total number of grid points in the computational domain. N_y is the number of points across the channel in the wall normal direction. The convergence is monitored by the difference compared to the DNS ($\overline{e}_{\text{QoI}}^{\text{DNS}}$); for completeness we have also measured the difference compared to a previous grid ($\overline{e}_{\text{QoI}}^{\text{prev}}$). Results shown in Fig. 3.5.

cell count by approximately a factor of 4; adaptation based on this threshold then leads to a new grid (labeled LES-2) with $\overline{\Delta}_x = 0.29H$, $\overline{\Delta}_y = 0.007H \rightarrow 0.14H$ and $\overline{\Delta}_z = 0.20H$. Note that we use the minimum values of $\breve{\Delta}_{\text{opt}}(\mathbf{x}, \mathbf{n})$ in the x and z directions, respectively, in order to ensure a structured grid (for the channel cases).

The process continues in the same manner, generating the 6 grids listed in Table 3.1 for which the key results are shown in Fig. 3.5. The threshold value $\mathcal{A}_{\text{thresh}}$ is chosen, at each stage, based on the approximate increase in the number of grid points; this is taken as a factor of 4 or above on the first few grids and then as factors of 3 and 2 on the final grids. These choices are necessarily based on user judgment, but the exact choices do not qualitatively change the grid-adaptation process.

The solution clearly converges as the grid is refined. More importantly, as the grid progresses through the adaptation process, note how the directional error-indicator becomes progressively closer to equal in the different directions. The fact

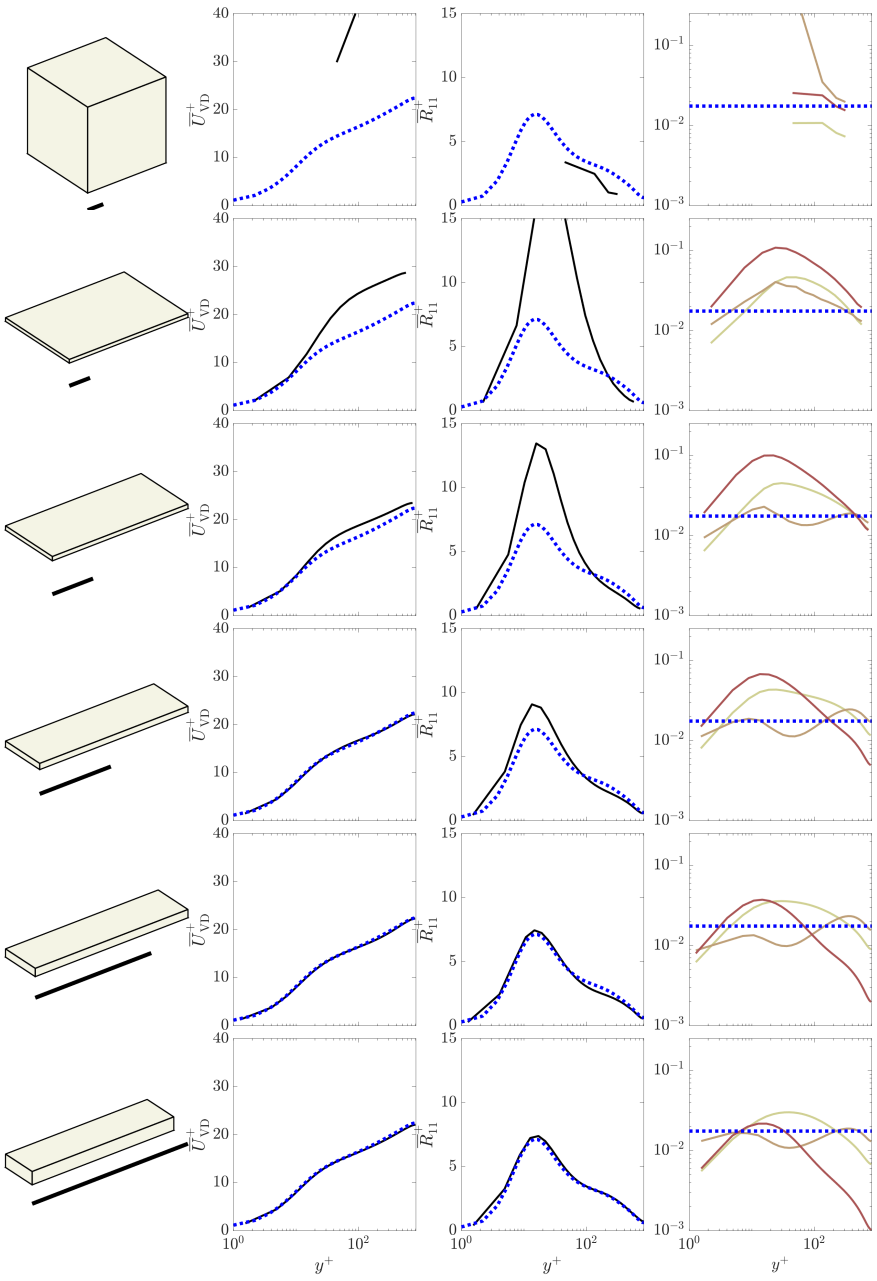

Figure 3.5: LES of channel flow at $Re_\tau \approx 830$ starting from a very coarse isotropic grid. The rows show the progression of grids from the initial (LES-1; top row) to the final (LES-6; bottom row). The columns show, from left: (i) the shape of a wall-adjacent cell; (ii) the mean (van Driest transformed) velocity $\overline{U}^+_{\mathrm{VD}}$; (iii) the resolved streamwise Reynolds stress $\overline{R}^+_{11}$; and (iv) the error-indicators $\overline{\mathcal{A}}(y^+, \mathbf{n}_x)$ (brightest color), $\overline{\mathcal{A}}(y^+, \mathbf{n}_y)$ (mid-bright), and $\overline{\mathcal{A}}(y^+, \mathbf{n}_z)$ (darkest color). The dotted line in columns (ii) and (iii) shows the converged DNS result. The dotted line in column (iv) shows the threshold $\mathcal{A}_{\mathrm{thresh}}$ used at each stage. The thick line in column (i) is of length $0.05H$. Key quantities are listed in Table 3.1.

that it takes a few iterations is partly due to the fact that the resolved turbulence changes as the grid is refined (particularly from the exceedingly coarse initial grid used here) and partly due to the fact that the true scaling exponents $\alpha_{\mathbf{n}}$ are different from the assumed value of 2.

It is interesting to note how the first adaptation step (from LES-1 to LES-2) essentially only targets $\overline{\Delta}_y$, especially near the wall. In fact, $\overline{\Delta}_x$ even increases slightly in this adaptation step. After this step, the $\overline{\Delta}_y$ is sufficient to allow for a more meaningful resolved turbulence, which then requires refinement in all directions but primarily in $\overline{\Delta}_z$.

Looking at the plots in Fig. 3.5, based on typical "LES judgment", one might argue that the solution is sufficiently accurate on grids LES-5 and LES-6. The solution error metric (based on the DNS solution) $\bar{e}^{\text{DNS}}_{\text{QoI}}$ is 3% and 2% on these grids, that are arguably small enough for an LES. The grid-adaptation process is therefore terminated after LES-6.

The LES-5 and LES-6 grids have grid-spacings $(\overline{\Delta}^+_x, \overline{\Delta}^+_{y_w}/2, \overline{\Delta}^+_z)$ of $(54, 1.3, 14)$ and $(38, 1.5, 9)$. These grid-spacings are commensurate with the literature and experience on LES, albeit with arguably slightly finer spanwise grid-spacing than is considered "best practice" or "optimal". In the next Chapter (Section 4.5) we show that the fine spanwise resolution happens primarily because of the assumption of uniform distribution of the error-indicator in space, and show that with a modified criteria this is no longer an issue.

Grid	N_{tot}	N_y	$(\overline{\Delta}_x^+, \overline{\Delta}_{y_w}^+/2, \overline{\Delta}_z^+)$	$(\overline{\Delta}_x, \overline{\Delta}_{y_c}, \overline{\Delta}_z)/H$	Re_τ	$\overline{e}_{\text{QoI}}^{\text{prev}}$ (%)	$\overline{e}_{\text{QoI}}^{\text{DNS}}$ (%)
DNS-1	1.62k	6	$(86, 43, 86)$	$(0.33, 0.33, 0.33)$	257	–	72
DNS-2	12.5k	28	$(170, 6, 120)$	$(0.31, 0.12, 0.21)$	547	140	47
DNS-3	28.7k	38	$(130, 4.4, 89)$	$(0.24, 0.087, 0.17)$	535	8.7	33
DNS-4	821k	85	$(41, 1.0, 26)$	$(0.071, 0.049, 0.044)$	581	22	5.9
DNS-5	6.38M	110	$(20, 0.9, 8.6)$	$(0.035, 0.036, 0.015)$	572	5.2	1.4
DNS-6	14.8M	110	$(14, 0.9, 5.3)$	$(0.024, 0.036, 0.009)$	571	1.0	1.1
DNS-7	16.9M	110	$(12, 0.9, 5.3)$	$(0.021, 0.036, 0.009)$	571	0.8	0.3

Table 3.2: DNS of channel flow at $Re_\tau \approx 570$ starting from a very coarse isotropic grid. Note that $\overline{\Delta}_{y_c}$ is the value at the channel centerline, while $\overline{\Delta}_{y_w}^+$ is the value at the wall. Results shown in Fig. 3.6.

3.2.3 DNS at $Re_\tau \approx 570$

To assess the robustness of the grid-adaptation process, we next consider DNS of the same channel flow. This problem has no explicit subgrid model, and thus all errors are numerical in nature. The Reynolds number is reduced to $Re_b = 10,000$ in order to limit the computational cost; this leads to a friction Reynolds number of $Re_\tau \approx 570$. We again start from a very coarse grid with cubic cells, taken here as $\overline{\Delta}_x = \overline{\Delta}_y = \overline{\Delta}_z = 0.33H$ in order to have similar dimensions in viscous units as in the LES case. The results are shown in Fig. 3.6 and listed in Table 3.2.

The process is terminated when the solution error metric $\overline{e}_{\text{QoI}}^{\text{DNS}}$ is less than 1%, since one would require greater accuracy from a DNS than an LES. At the point of termination, the grid-spacing is $(\overline{\Delta}_x^+, \overline{\Delta}_{y_w}^+/2, \overline{\Delta}_z^+) \approx (12, 0.9, 5)$ which agrees quite well with the standard practice in DNS [17] (albeit slightly too coarse in y).

We should note that the success of the proposed error-indicator in DNS of the channel flow was to some degree due to the nature of the wall-bounded turbulence and the similarity between the grids used in DNS and wall-resolved LES. In other

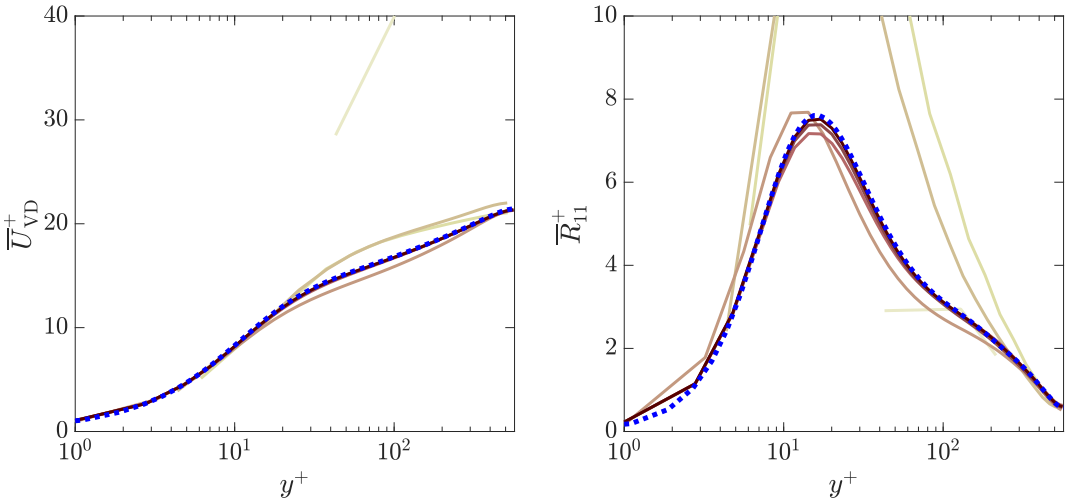

Figure 3.6: DNS of channel flow at $Re_\tau \approx 570$ starting from a very coarse isotropic grid. Mean velocity (left) and resolved streamwise Reynolds stress (right). The dotted blue line shows the converged DNS result. Sequence of grids DNS-1 to DNS-7 shown by the brightest to the darkest colors, respectively. Key quantities are listed in Table 3.2.

words, the final decision on the suitability of $\overline{\mathcal{A}}(\mathbf{x}, \mathbf{n})$ in grid selection for DNS requires a much more comprehensive assessment and cannot be simply concluded based on the favorable results of this Section.

3.2.4 Implicit LES (ILES) with the 5th-order WENO scheme at $Re_\tau \approx 310$

The final channel test case is to consider ILES, i.e., an LES with a numerically dissipative scheme and no explicit subgrid model. A 5th-order WENO scheme with Roe flux-splitting is used for this test, at $Re_b = 5,000$ (or $Re_\tau \approx 310$). The initial grid is $\overline{\Delta}_x = \overline{\Delta}_y = \overline{\Delta}_z = 0.125H$, which was the coarsest isotropic grid for which we could achieve sustained turbulence for this WENO scheme at this low Reynolds number.

Grid	N_{tot}	N_y	$(\overline{\Delta}_x^+, \overline{\Delta}_{y_w}^+/2, \overline{\Delta}_z^+)$	$(\overline{\Delta}_x, \overline{\Delta}_{y_c}, \overline{\Delta}_z)/H$	Re_τ	$\overline{e}_{\text{QoI}}^{\text{prev}}$ (%)	$\overline{e}_{\text{QoI}}^{\text{DNS}}$ (%)
WENO-1	30.7k	16	$(23, 12, 23)$	$(0.13, 0.13, 0.13)$	185	–	35
WENO-2	220k	70	$(29, 1.0, 16)$	$(0.13, 0.047, 0.071)$	219	48	47
WENO-3	1.10M	100	$(27, 0.4, 7.2)$	$(0.10, 0.042, 0.027)$	265	17	22
WENO-4	4.03M	120	$(18, 0.4, 4.1)$	$(0.063, 0.034, 0.014)$	291	9.8	9.7
WENO-5	9.43M	130	$(12, 0.5, 3.1)$	$(0.040, 0.029, 0.010)$	301	4.2	5.1
WENO-6	16.7M	140	$(8.7, 0.4, 2.7)$	$(0.029, 0.027, 0.009)$	305	2.4	2.4

Table 3.3: Implicit LES using a 5th-order WENO scheme of channel flow at $Re_\tau \approx 310$ starting from a very coarse isotropic grid. Note that $\overline{\Delta}_{y_c}$ is the value at the channel centerline, while $\overline{\Delta}_{y_w}^+$ is the value at the wall. Results shown in Fig. 3.7.

The results from the sequence of grids produced by the grid-adaptation are shown in Fig. 3.7 and Table 3.3. At comparable solution error levels, these grids are clearly finer than those for the prior LES. Nevertheless, the final grids have cell aspect ratios (or anisotropies) that seem quite reasonable.

Note that the difference in Reynolds numbers between the different channel flow test cases does not change the conclusions at all, since the anisotropy of near-wall turbulence is not very sensitive to Reynolds number. This was also confirmed by performing the LES test at all three Reynolds numbers and the DNS test at the two lower Reynolds numbers, with no significant difference in the results.

3.3 Assessment on the flow over a backward facing step at $Re_H = 5100$

The grid-adaptation process is next assessed on the flow over a backward-facing step. The purpose of this test case is to expose the adaptation algorithm to a more complex flow, with multiple different canonical flow elements: an attached

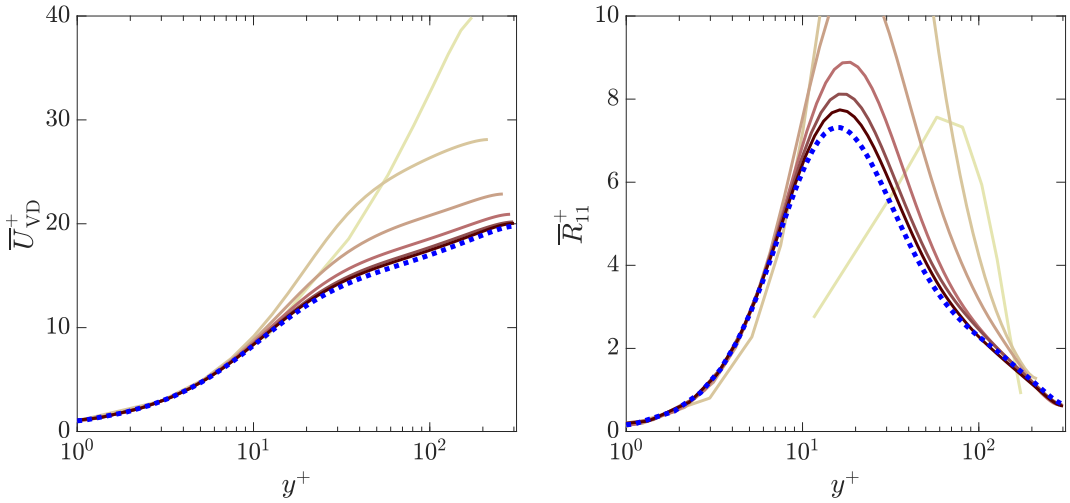

Figure 3.7: Implicit LES using a 5th-order WENO scheme of channel flow at $Re_\tau \approx 310$ starting from a very coarse isotropic grid. Mean velocity (left) and resolved streamwise Reynolds stress (right). The dotted line shows the converged DNS result. Sequence of grids WENO-1 to WENO-6 shown by the brightest to the darkest colors, respectively. Key quantities are listed in Table 3.3.

boundary layer upstream of the step, a free shear layer after the separation, an impingement/reattachment region, and a large recirculation zone.

The flow geometry and conditions are chosen based on the experiment of Jovic and Driver [57,58] and the DNS of Le *et al.* [59]. The computational domain is shown in Fig. 3.8. The Reynolds number based on the step height H and inflow velocity U_∞ is $Re_H = U_\infty H/\nu = 5100$. This corresponds to a momentum Reynolds number of $Re_\theta \approx 780$ for the incoming boundary layer (at $x/H = -3$) and a friction Reynolds number of $Re_\tau \approx 208$ based on the δ_{95} boundary layer thickness (or $Re_\tau \approx 448$ based on δ_{99}) at that same location. Note that the flow conditions are close to those of the experiment and the DNS, but not exactly the same: the present setup has a thicker boundary layer compared to that of the experiment (which had $Re_\theta \approx 610$).

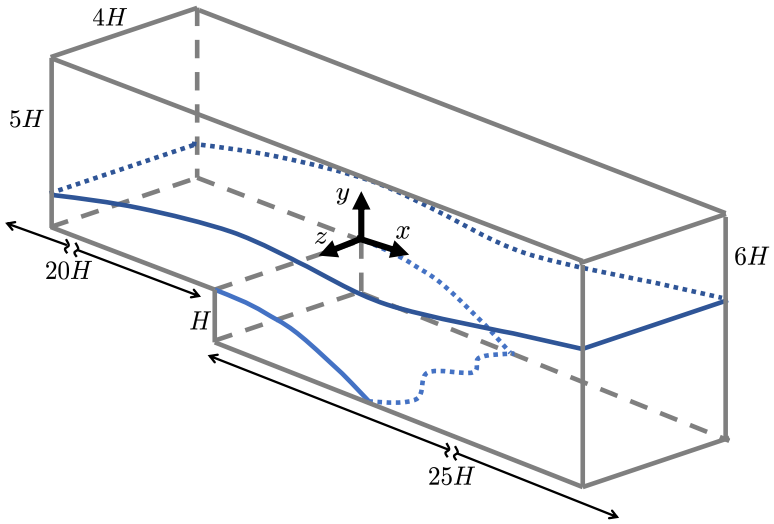

Figure 3.8: Schematic of the computational domain for the flow over a backward-facing step. The top boundary is a slip wall (modeling the centerline in the experiment) while periodic boundary conditions are used in the spanwise direction. The origin of the coordinate systems is placed at the upper corner of the step.

3.3.1 Code and computational details

The OpenFOAM code version 2.3.1 [60] is used for this test case to allow for fully unstructured adapted grids. Spatial discretization is done using the linear Gauss scheme (second-order accurate), with second-order backward method for time integration. The pressure-velocity coupling is performed using the PISO algorithm with three iterations of nonorthogonality correction. We use the dynamic k_{sgs}-equation model [61–64] with the cube-root of the cell volume as the filter-width.

The quantities of interest for this flow are taken to be the two non-zero mean velocity components, the four non-zero Reynolds stress components, and the friction and pressure coefficient profiles on the horizontal walls. The errors in the QoIs are

defined as

$$\begin{aligned}
\delta\overline{Q}^{\text{ref}}_{\text{1-2}} &= \frac{\iint_\Omega \left|\overline{U}_i - \widetilde{U}_{i,\text{ref}}\right| dxdy}{0.2U_\infty\, A_\Omega}; \quad i = 1,\, 2 \\
\delta\overline{Q}^{\text{ref}}_{\text{3-6}} &= \frac{\iint_\Omega \left|\overline{R}^{\text{tot}}_{ij} - \widetilde{R}^{\text{tot}}_{ij,\text{ref}}\right| dxdy}{0.015U^2_\infty\, A_\Omega}; \quad (i,j) = (1,1),\, (2,2),\, (3,3),\, (1,2) \\
\delta\overline{Q}^{\text{ref}}_{7} &= \frac{\int_\Psi \left|\overline{c}_f - \widetilde{c}_{f,\text{ref}}\right| dx}{0.002\, L_\Psi}; \\
\delta\overline{Q}^{\text{ref}}_{8} &= \frac{\int_\Psi \left|\overline{c}_p - \widetilde{c}_{p,\text{ref}}\right| dx}{0.1\, L_\Psi}.
\end{aligned} \tag{3.11}$$

where the first two integrals are taken over the region $\Omega : (x, y) \in [-10H, 20H] \times [-H, 2H]$, with $A_\Omega = 10H \times 2H + 20H \times 3H$ denoting the area of this region. The remaining two integrals are taken over the horizontal walls in the region $\Psi : x \in [-10H, 20H]$ with $L_\Psi = 30H$ denoting the normalizing length. Note that here we use the correct QoI, i.e. the total Reynolds stress $\overline{R}^{\text{tot}}_{ij} = \left\langle \overline{u}'_i \overline{u}'_j \right\rangle + \left\langle \tau^{\text{mod}}_{ij} \right\rangle$, when judging the convergence of our LES. The quantities are scaled by representative values to make the $\delta\overline{Q}_m$ comparable, and then weighted and added together to define the convergence metric as

$$\overline{e}^{\text{ref}}_{\text{QoI}} = \frac{1}{3}\sum_{m=1}^{2} \frac{\delta\overline{Q}^{\text{ref}}_m}{2} + \frac{1}{3}\sum_{m=3}^{6} \frac{\delta\overline{Q}^{\text{ref}}_m}{4} + \frac{1}{3}\sum_{m=7}^{8} \frac{\delta\overline{Q}^{\text{ref}}_m}{2}. \tag{3.12}$$

As in the previous section, we compute both $\overline{e}^{\text{prev}}_{\text{QoI}}$ defined with respect to the previous grid in the sequence and $\overline{e}^{\text{DNS}}_{\text{QoI}}$ defined with respect to a converged DNS. The reference DNS is computed on a very fine unstructured grid with about 54M cells.

Each case was run for $500H/U_\infty$ time units to remove the initial transients, after which 400 snapshots were collected over a period of $1000H/U_\infty$. The convergence of the averaging was judged by dividing the full record into four separate batches with 200 snapshots in each, computing the QoIs for each batch, and then computing

the sample standard deviation between the batch averages. We then constructed 95% confidence intervals for each quantity using the Student's t-distribution with 3 degrees of freedom (cf. [65]). The confidence intervals for the integrated errors in the QoIs are very small (and thus omitted below), but they are significant for some of the profiles especially downstream of the step. This is consistent with the expectation of low frequency unsteadiness in the separated flow. The long averaging times are required only for the QoI profiles to converge; the error-indicator converges about an order of magnitude more quickly due to its dependence on small scales. The statistical convergence of the error-indicator and the resulting predicted grids are investigated in detail in Chapter 6.

We emphasize that the differences in the numerics and models between the channel and backward-facing steps are viewed as a strength in the assessment of the grid-adaptation method, by exposing the adaptation process to numerical and modeling errors that are qualitatively and quantitatively different (high vs low order, less vs more numerical dissipation, compressible vs incompressible, etc).

3.3.2 Results

The initial grid (labeled LES-1) has a resolution of $\overline{\Delta}(\mathbf{x}, \mathbf{n})/H = 0.2$ everywhere in the domain except for close to the walls where the wall-normal direction is refined by a factor of two (this is done to enable a direct comparison between the sequences of grids generated by all three of the error-indicators proposed in this dissertation; since the indicator of Chapter 8 is based on assumptions that are only

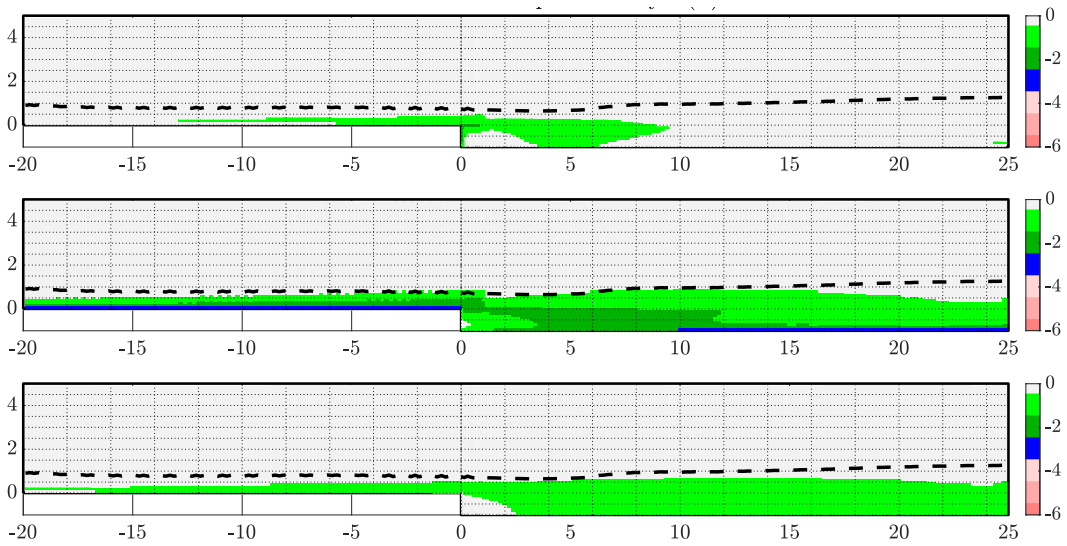

Figure 3.9: The grid LES-2 from Table 3.4 illustrated by its refinement levels in x (top), y (middle), and z (bottom). Refinement levels are computed based on a skeletal grid with $\Delta_0(\mathbf{x}, \mathbf{n}) = 0.2H$ for all $\mathbf{x}$ and $\mathbf{n}$. The light green, dark green and blue colors illustrate regions with one ($\overline{\Delta}_{\mathbf{n}}/H = 0.1$), two ($\overline{\Delta}_{\mathbf{n}}/H = 0.05$), and three ($\overline{\Delta}_{\mathbf{n}}/H = 0.025$) refinement levels, respectively. The white areas are associated with regions that are left untouched (i.e. $\overline{\Delta}_{\mathbf{n}}/H = 0.2$). The dashed black lines highlight the δ_{95} boundary layer thickness.

true when there is a sufficient level of turbulent activity in the flow). After running the LES on this initial grid, the error-indicator $\overline{\mathcal{A}}(\mathbf{x}, \mathbf{n})$ is computed for the three directions of possible refinement and the target grid-spacing distributions $\check{\Delta}_{\text{opt}}(\mathbf{x}, \mathbf{n})$ for $\mathbf{n}_x$, $\mathbf{n}_y$ and $\mathbf{n}_z$ are computed based on Eqn. 3.7 for a threshold value $\mathcal{A}_{\text{thresh}}$ that leads to the doubling of the number of cells.

Figure 3.9 illustrates how the adaptation methodology targets different regions of the domain for refinement. The algorithm predicts a single level of refinement in the y direction ($\overline{\Delta}_y = \overline{\Delta}(\mathbf{x}, \mathbf{n}_y) = 0.1H$) in most of the domain inside the boundary layer, with a second level of refinement ($\overline{\Delta}_y/H = 0.05$) closer to the horizontal walls and in the shear layer, and a third level of refinement ($\overline{\Delta}_y/H = 0.025$) immediately above the horizontal walls in both incoming and recovering boundary layers. The

spanwise resolution $\overline{\Delta}_z$ is targeted for a single level of refinement ($\overline{\Delta}_z/H = 0.1$) for the most part of the domain inside the turbulent boundary layers, while the relaminarized region inside the recirculation bubble is left untouched. The resolution of the skeletal grid in the x direction ($\overline{\Delta}_x/H = 0.2$) is deemed adequate (at this resolution level, compared to resolution in y and z) for the most part of the domain downstream of the reattachment point. Half of the incoming boundary layer, the shear layer formed by separation at the step, the reattachment point and some area around it are marked for one level of refinement in the x direction. The vertical wall of the step (where the recirculation bubble causes shear) is also predicted to need some refinement (the wall-normal resolution for this wall is $\overline{\Delta}_x/H = 0.05$). We also note that the aspect ratio of the cells in the boundary layers, the shear layer, and the recirculation bubble are quite close to what we expect from experience for those flows. The fact that the resulting LES-2 grid seems this reasonable from an "LES experience" point-of-view is actually quite remarkable, since it was created entirely by an algorithm, using a heuristic-based error-indicator applied by an even more heuristic criterion on how the error-indicator should be spatially distributed, and from a solution on a highly underresolved mesh.

The adapted grid is then generated using OpenFOAM's refineMesh utility, by using the target grid-spacings to produce an input file to refineMesh. Since refineMesh can only refine hexahedral cells by factors of $2^{\mathcal{R}}$ in any direction ($\mathcal{R}$ being the refinement level), a cell is cut in half until the grid-spacing is less than or equal to the target grid-spacing in that location and direction. For instance, a target resolution of $\breve{\Delta} = 0.17H$ is projected down to the first available value of

Grid	N_{tot}	$(\overline{\Delta}_x^+, \overline{\Delta}_{y_w}^+/2, \overline{\Delta}_z^+)$	$(\overline{\Delta}_x, \overline{\Delta}_y, \overline{\Delta}_z)/\delta_{\text{shear}}$	$\overline{e}_{\text{QoI}}^{\text{prev}}$ (%)	$\overline{e}_{\text{QoI}}^{\text{DNS}}$ (%)
LES-1	149k	$(42, 10, 42)$	$(0.21, 0.17, 0.33)$	–	11.2
LES-2	293k	$(21, 2.6, 21)$	$(0.17, 0.087, 0.17)$	6.9	11.0
LES-3	596k	$(22, 2.7, 11)$	$(0.076, 0.038, 0.076)$	4.8	7.7
LES-4	1.28M	$(23, 2.9, 5.7)$	$(0.076, 0.038, 0.038)$	4.2	5.8
LES-5	2.22M	$(23, 1.5, 5.9)$	$(0.048, 0.019, 0.038)$	2.4	4.3
LES-6	3.59M	$(25, 1.5, 6.2)$	$(0.034, 0.017, 0.034)$	2.8	3.9
DNS	54M	$(6.0, 0.38.3.0)$	$(0.017, 0.0086, 0.017)$	–	0

Table 3.4: LES of the flow over a backward-facing step. N_{tot} is the actual number of cells in the computational domain. The filter width in inner units is taken from $x/H = -3$ (upstream of the step). The filter width in outer units is taken from the middle of the shear layer and is scaled by the approximate thickness of that shear layer δ_{shear}. See Fig. 3.14 for more details. $\overline{e}_{\text{QoI}}^{\text{DNS}}$ and $\overline{e}_{\text{QoI}}^{\text{prev}}$ are defined in Eqn. 3.12.

$0.10H$. Consequently, the adapted grid has cells that may be up to a factor of almost 2 finer than the target grid-spacing.

The threshold level $\mathcal{A}_{\text{thresh}}$ was chosen to produce an approximate doubling of the number of cells. This approximation was done before the actual construction of the adapted grid, by estimating the number of cells from the target grid-spacings: therefore, the actual adapted grid has slightly higher or lower cell counts than the target values. The process is then repeated, with the sequence of resulting grids listed in Table 3.4.

As can be seen in Table 3.4, the error in quantities of interest $\overline{e}_{\text{QoI}}^{\text{DNS}}$ is below 5% on the last two grids and thus we can declare LES-6 to be sufficiently converged. The convergence of some key profiles are shown in a few figures. Figure 3.10 shows the friction and pressure coefficients on the bottom wall of the geometry. The results are reasonable on LES-5 and almost converged on LES-6. The LES results converge to the present DNS, which in turn shows slight differences with the experimental

results. Most notably, the experimental friction coefficient $\overline{c}_f$ has a deeper negative peak around $x/H \approx 3$ and a slightly higher level around $x/H \approx 15-20$. These slight differences are commensurate with the known differences in the incoming boundary layer between the present computations and the experiments. The slow convergence of $\overline{c}_f$ upstream of the step (compared to the downstream) is also notable. We note the presence of some sudden jumps in the friction coefficient $\overline{c}_f$; these are mostly post-processing artifacts that happen due to the interpolation of the unstructured grid data onto a structured grid for computation of the friction coefficient.

The mean velocity and the Reynolds stresses at $x/H = 6$ are shown in Fig. 3.12. This is near the reattachment point. All quantities are basically converged on LES-6. Similar results at the incoming boundary layer at $x/H = -3$ and the recovering boundary layer at $x/H = 15$ are shown in Figs. 3.11 and 3.13.

The converged LES-6 grid is shown in Fig. 3.14. The regions where the grid has been refined basically agree with one's expectation for this flow, with the most refinement in the incoming boundary layer and the initial part of the shear layer. The anisotropic nature of the final grid is clearly visible, particularly when comparing $\overline{\Delta}_y$ to $\overline{\Delta}_x$ or $\overline{\Delta}_z$ for those resolutions that are reported in Table 3.4. It is interesting to note the very coarse grid in the lower part of the recirculation bubble, where the flow is slow and less turbulent.

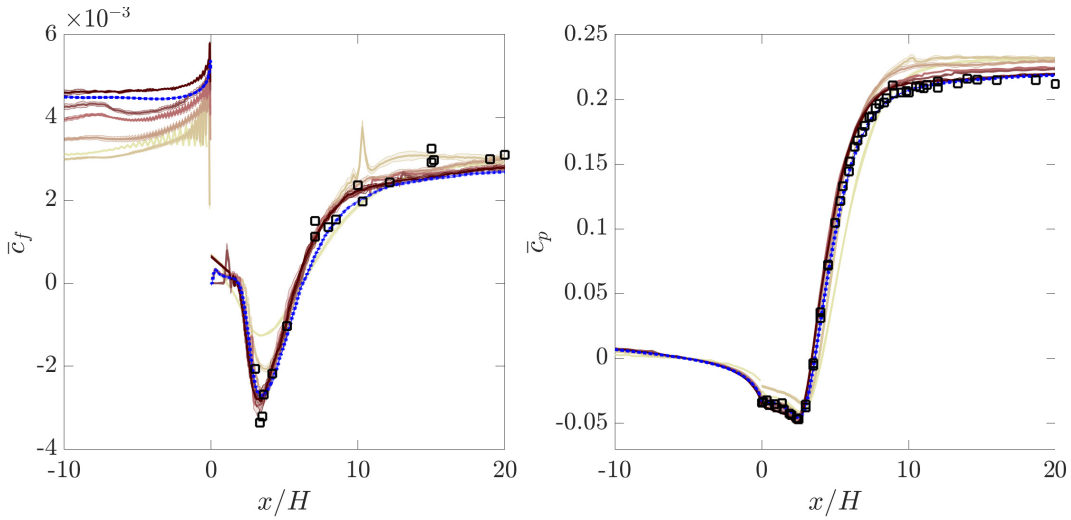

Figure 3.10: Convergence of (a) friction coefficient $\overline{c}_f$ and (b) pressure coefficient $\overline{c}_p$ for LES of flow over a backward-facing step. Grids in Table 3.4 are shown by the lightest color for LES-1 to the darkest for LES-6. Solid lines denote the sample means, while the shaded regions correspond to the approximate confidence intervals (computed locally). The dotted blue lines and their shaded regions denote our DNS results and their confidence intervals. Symbols correspond to the experimental data of Jovic & Driver [57,58] with slightly different setup (error bars on the experimental data are not shown). Experimental measurements of $\overline{c}_f$ and $\overline{c}_p$ are not available upstream of the step.

3.4 Alternative definition of the error-indicator using structure functions

The directional filter used in obtaining the high-pass filtered velocity $\overline{u}_i^{*,(\mathbf{n})}$ in Eqn. 3.2 is, in fact, only one of many choices that are potentially available. Generally speaking, any filter that can be applied in a single direction can also be used to compute the error-indicator; e.g., the box filter, the Gaussian filter, the spectral filter, differential filters other than the one used in Eqn. 3.2, etc. One of the most popular of these directional filters in the turbulence literature has been the structure function, that has been in use since the early days in the development

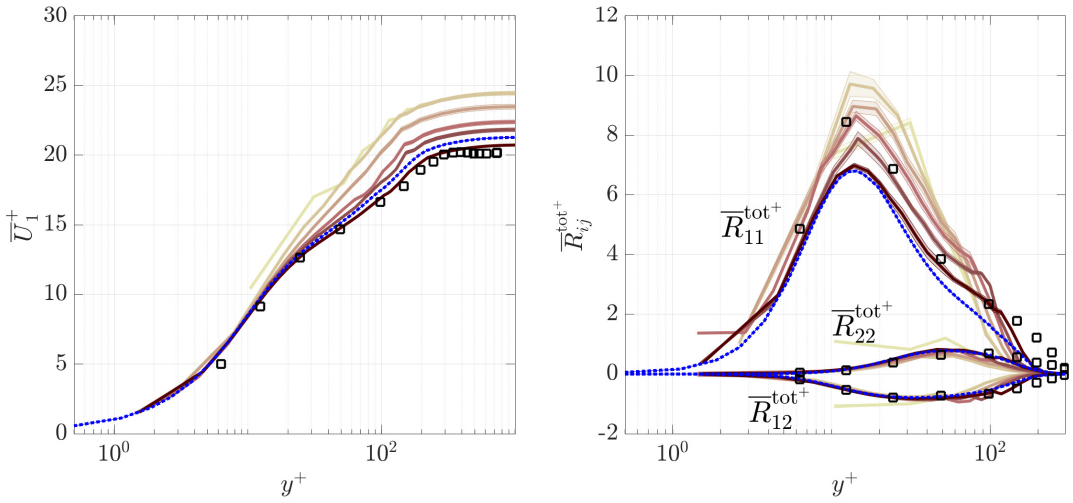

Figure 3.11: Convergence of the mean velocity and Reynolds stress profiles for the sequence of grids in Table 3.4 at the incoming boundary layer at $x/H = -3$. Grids in the sequence are shown by the lightest color for LES-1 to the darkest for LES-6. Solid lines denote the sample means, while the shaded regions correspond to the approximate confidence intervals (computed locally). The dotted blue lines and their shaded regions denote our DNS results and their confidence intervals. Symbols correspond to the experimental data of Jovic & Driver [57, 58] (error bars on the experimental data are not shown).

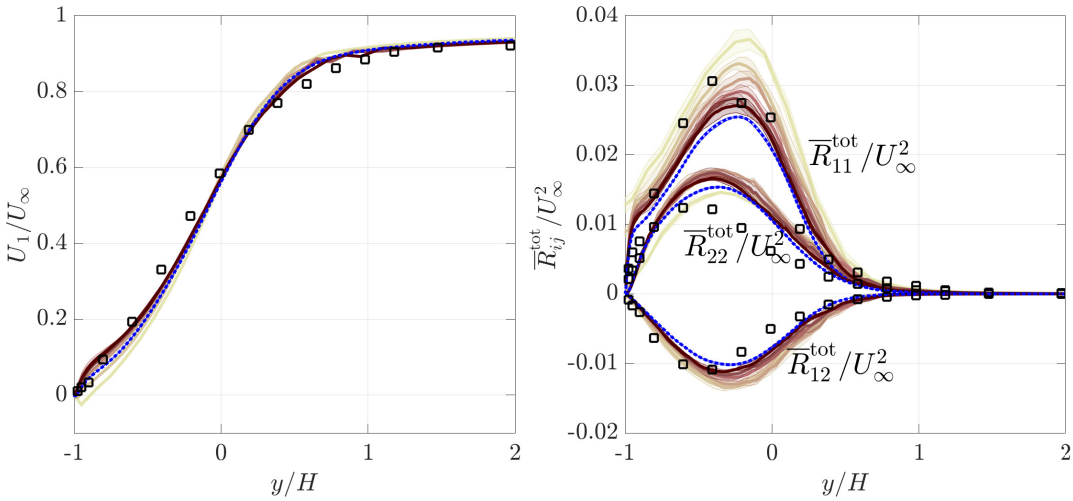

Figure 3.12: Convergence of the mean velocity and Reynolds stress profles for grids in Table 3.4 at $x/H = 6$ near the reattachment point. See Fig. 3.11 for more details.

of the turbulence theory (cf. [17]). In this Section, we briefly discuss an alternative definition of the error-indicator based on the second-order structure function and comment on its performance and suitability.

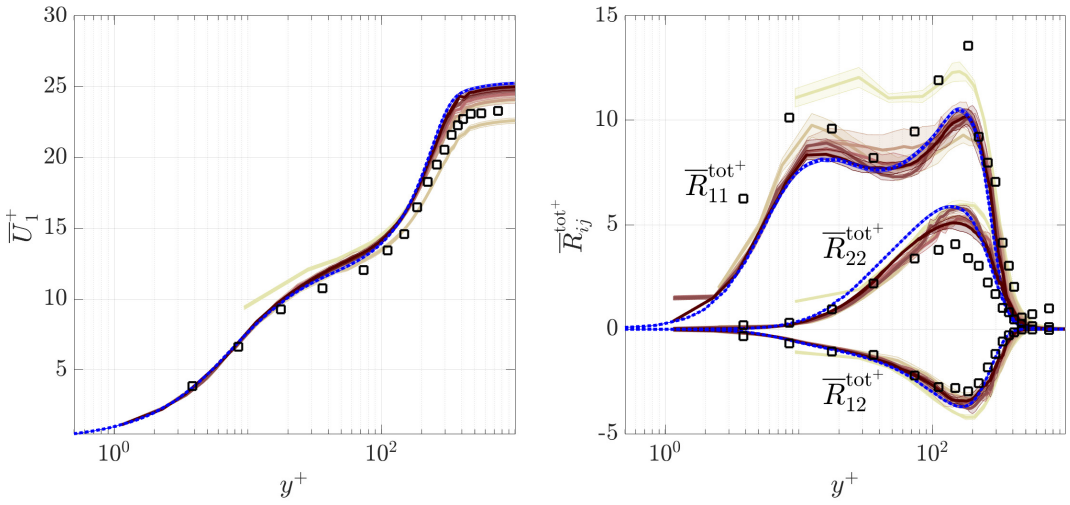

Figure 3.13: Convergence of the mean velocity and Reynolds stress profiles for the recovering boundary layer at $x/H = 15$ for the sequence of grids in Table 3.4. See Fig. 3.11 for more details.

The advantage of this alternative formulation is that it is readily implementable in almost any unstructured code without any complications; the disadvantage is that it leads to less "optimal" predictions of the filter width.

The second-order velocity structure function at position $\mathbf{x}$ for the resolved velocity field $\overline{u}_i$ is defined as [17]

$$D_{ij}(\mathbf{x}, \mathbf{r}) = \langle [\overline{u}_i(\mathbf{x} + \mathbf{r}) - \overline{u}_i(\mathbf{x})] \, [\overline{u}_j(\mathbf{x} + \mathbf{r}) - \overline{u}_j(\mathbf{x})] \rangle \ ,$$

which is the covariance of the difference in velocities between two points separated by $\mathbf{r}$. Taking $\mathbf{r} = \mathbf{n}\overline{\Delta}_{\mathbf{n}}$ allows us to define an alternative anisotropic error-indicator as

$$\overline{\mathcal{A}}'(\mathbf{x}, \mathbf{n}) = \sqrt{D_{ii}(\mathbf{x}, \mathbf{n}\Delta_{\mathbf{n}})} \, . \tag{3.13}$$

One could take $\mathbf{n}\overline{\Delta}_{\mathbf{n}}$ to be the vector connecting two cell centers on two adjacent cells (for example two prisms in Fig. 3.4) which makes the method applicable to all types of grids. This error-indicator can also be approximated using a Taylor series

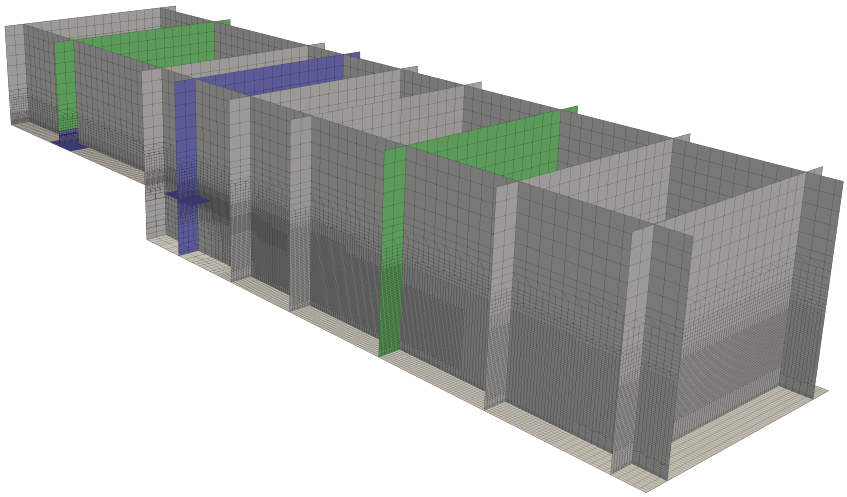

Figure 3.14: The generated grid LES-6 of Table 3.4 with 3.59M cells. Intersections of the blue planes denote locations whose resolutions are reported in Table 3.4, while the green planes correspond to $x/H = -3$ and $x/H = 6$ whose velocity and Reynolds stress profiles are plotted in Figs. 3.11 and 3.12. The grid is resulted from computation of the proposed error-indicator (Eqns. 3.2 and 3.3) and enforcing Eqn. 3.7, with no user experience involved.

as

$$\overline{\mathcal{A}}'(\mathbf{x},\mathbf{n}) \approx \overline{\Delta}_{\mathbf{n}} \sqrt{\langle (\mathbf{n}^T \nabla \overline{u}_i)\,(\mathbf{n}^T \nabla \overline{u}_i) \rangle}\,. \tag{3.14}$$

which gives us a more clear idea of its scaling with directional resolution $\overline{\Delta}_{\mathbf{n}}$. For LES of isotropic turbulence, this leads to a scaling $\overline{\mathcal{A}}'(\mathbf{x},\mathbf{n}) \sim \overline{\Delta}_{\mathbf{n}}^{1/3}$ exactly as for the standard definition of the error-indicator $\overline{\mathcal{A}}(\mathbf{x},\mathbf{n})$ (for both the original formulation and its differential approximation; assuming exact differentiation in the latter). For DNS and laminar flows, however, it produces a different scaling of $\overline{\mathcal{A}}'(\mathbf{x},\mathbf{n}) \sim \overline{\Delta}_{\mathbf{n}}$ (from the differential approximation). For steady laminar flows, this alternative error-indicator then effectively becomes a gradient-based adaptation.

This alternative error-indicator $\overline{\mathcal{A}}'(\mathbf{x},\mathbf{n})$ was assessed on the same cases. For the channel flows, it was found to favor refinement in the wall normal direction when

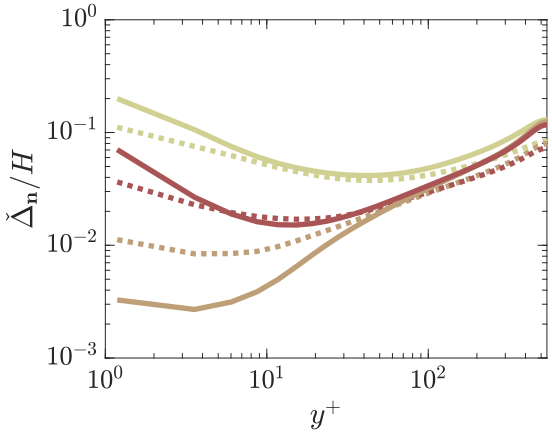

Figure 3.15: The target resolutions predicted by $\overline{\mathcal{A}}'(\mathbf{x},\mathbf{n})$ (solid lines) and $\overline{\mathcal{A}}(\mathbf{x},\mathbf{n})$ (dotted lines) for turbulent channel flow at $Re_\tau \approx 545$. The streamwise, wall-normal, and spanwise resolutions are shown by the brightest to the darkest colors, in that same order. Resolutions correspond to target grids with around 1.10M cells. Both target resolutions are obtained by Eqn. 3.7 assuming $\check{\mathcal{A}}'(\mathbf{x},\mathbf{n}) \sim \check{\Delta}_{\mathbf{n}}$ and $\check{\mathcal{A}}(\mathbf{x},\mathbf{n}) \sim \check{\Delta}^2_{\mathbf{n}}$. Note that compared to $\overline{\mathcal{A}}(\mathbf{x},\mathbf{n})$, the alternative error-indicator $\overline{\mathcal{A}}'(\mathbf{x},\mathbf{n})$ leads to coarser resolutions in the streamwise and spanwise directions, while the wall-normal resolution is much finer in the region, $y^+ \lesssim$ 10-20.

compared to the main definition $\overline{\mathcal{A}}(\mathbf{x},\mathbf{n})$. In other words, if the threshold is chosen such that the cell count of the target grids from both error-indicators are almost equal, $\overline{\mathcal{A}}'(\mathbf{x},\mathbf{n})$ will produce a finer grid in y than $\overline{\mathcal{A}}(\mathbf{x},\mathbf{n})$ will (see Fig 3.15).

A sample target grid-spacing for the backward-facing step is shown in Fig. 3.16. These target values were computed using the differential approximation and the assumed scaling $\overline{\mathcal{A}}'(\mathbf{x},\mathbf{n}) \sim \overline{\Delta}_{\mathbf{n}}$, i.e. the scaling in the DNS limit exactly as done for $\overline{\mathcal{A}}(\mathbf{x},\mathbf{n})$. Comparing Figs. 3.16 and 3.9 reveals that the grid produced by $\overline{\mathcal{A}}'(\mathbf{x},\mathbf{n})$ has much finer resolution in the wall-normal direction of the boundary layers. In the original paper [11], we have generated a full sequence of grids for the backward-facing step using $\overline{\mathcal{A}}'(\mathbf{x},\mathbf{n})$ and compared it with the sequence generated by $\overline{\mathcal{A}}(\mathbf{x},\mathbf{n})$. The conclusion was that the alternative definition $\overline{\mathcal{A}}'$ leads to less optimal grids (higher $\overline{e}^{\text{DNS}}_{\text{QoI}}$ on grids with same number of cells). We expect the same conclusion

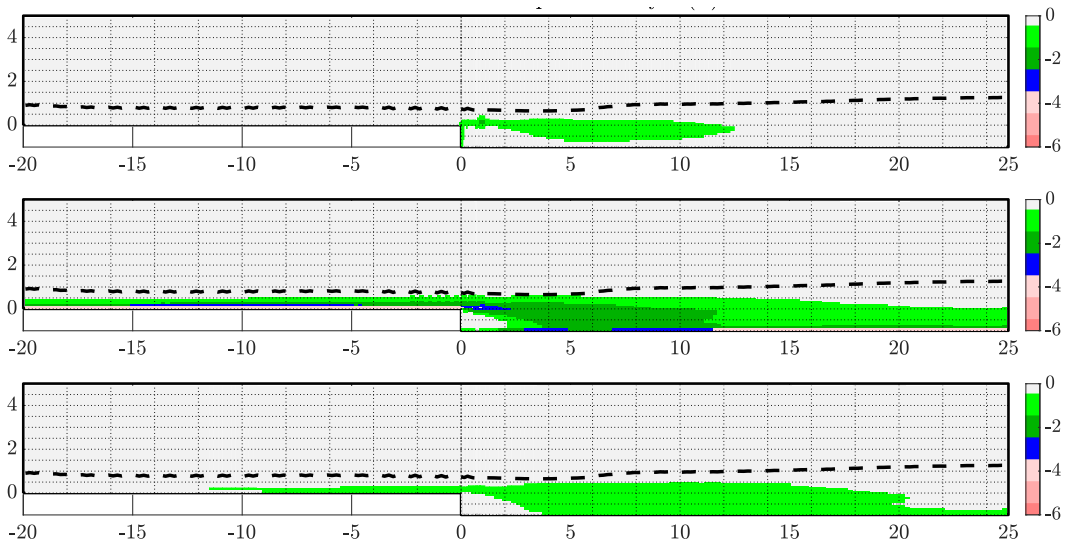

Figure 3.16: The alternative grid LES′-2 predicted by $\overline{\mathcal{A}}'(\mathbf{x}, \mathbf{n})$ illustrated by its refinement levels in x (top), y (middle), and z (bottom). See Fig. 3.9 for interpretation of the colored regions.

here; even though, the flow setup in the paper is slightly different than the results presented here, and thus that sequence is not added to this dissertation.

3.5 Cost

One potential criticism of this type of adaptation algorithm is the additional cost of performing LES on a full sequence of grids. We make four counter-arguments and observations.

First, assuming that the cell count is doubled at each iteration and that the time step scales as $N_{\text{tot}}^{1/3}$, the total cost of computing all grids in the sequence (including the final one) is $\lesssim 1.66 N_{\text{final}}$. If the cell count is quadrupled at each iteration, the total cost is $\lesssim 1.19 N_{\text{final}}$ instead.

Second, one could in practice start from a "best guess" grid (based on prior experience with the flow in question), thus reducing the number of steps of the

algorithm. We only started from exceedingly coarse and "ignorant" initial grids here in order to test the robustness of the method.

Third, as mentioned in the text (and will be shown in Chapter 6), the error indicator converges faster (in terms of the integration time) than the QoI profiles from LES, due to its dependence on the smallest resolved scales. Therefore, one could run the simulations on the first several grids for shorter times.

Finally, the minor added computational cost must of course be balanced against the larger cost saving of having a more "optimal" final grid. This saving will presumably become larger for more complex flow problems.

3.6 Concluding remarks

The objective of this Chapter was to introduce the first anisotropic, or directional, error-indicator that could be used for grid selection and adaptation in LES. The proposed error-indicator $\overline{\mathcal{A}}$ provides an estimate of the energy of components of the solution that have small-scale variation in any arbitrary direction $\mathbf{n}$. It is then argued that, due to the intuitive connection between the small-scales energy and all types of errors in LES, this measure of directional small-scale energy can be used as an anisotropic error-indicator in LES and thus to adapt the grids. The link between $\mathcal{A}(\mathbf{x}, \mathbf{n})$ and the grid-adaptation process is the assumption that the "optimal" grid should satisfy an equi-distribution principle, with equal value of the error-indicator in different directions and at different locations in space (Eqn. 3.7). This is what we call the "grid selection criteria".

As far as a first attempt goes, the success of the proposed method was quite remarkable. Our tests on the canonical problem of turbulent channel flow led to a final grid with resolutions of $(\overline{\Delta}_x^+, \overline{\Delta}_{y_w}^+/2, \overline{\Delta}_z^+) \approx (38, 1.5, 9)$ for the case of the implicitly filtered LES with the dynamic Smagorinsky model. While the "optimal" grid for a backward-facing step is not known, the final grid LES-6 (see Table 3.4 and Fig. 3.14) is consistent with our understanding of the flow field and the resolution needs in LES.

One of the weaknesses in the methodology and the results presented in this Chapter is the grid selection criterion of Eqn. 3.7: while the assumption of equi-distribution of the small-scale energy in different directions appears to be reasonable (at least at this stage), the equi-distribution in space is really way too simplistic. Of course, the adjoint fields can provide a better measure of how important the resolution in each location $\mathbf{x}$ is, and thus, how the resolution (the error-indicator) can be more optimally distributed. However, even without using the adjoint fields (i.e., assuming a uniform importance for different locations) the solution to the constrained optimization problem of minimizing the errors at a given grid size, N_{tot}, is not the uniform distribution of the error-indicator itself. This is discussed in more detail in the next Chapter (Chapter 4).

It should be emphasized that the proposed error-indicator of this Chapter is agnostic to the LES code and models: regardless of the approach, the high-pass filtered velocity is always computed using Eqn. 3.2 and the error-indicator is computed from Eqn. 3.3. Here, the method was tested with: (i) a compressible, high-order, minimally-dissipative code (the channel LES case); (ii) a compressible implicit

LES code (the channel WENO case), also mimicking a situation where $\overline{\Delta}/\overline{h} \gg 1$; and (iii) an incompressible, low-order, unstructured code with $\overline{\Delta}/\overline{h} = 1$ (the backward-facing step case). The physical models were also different: the dynamic Smagorinsky model in the channel vs the dynamic k_{sgs}-equation eddy viscosity model in the backward-facing step. The fact that the grid-adaptation method produced reasonable results in all cases suggests that it is robust to the numerical method and physical model.

The agnostic nature of the error-indicator $\overline{\mathcal{A}}(\mathbf{x}, \mathbf{n})$ has its own advantages and disadvantages. The most notable benefit of such generic formulations is perhaps the fact that it offers a "one solution fits all" sort of approach, meaning that a single post-processing script can be written and used for all LES cases, over all numerical codes and using all LES models; and it would probably work, at least to some degree, in all of them. The main disadvantage is that such generic methods are incapable of optimizing the outcome for different codes and models. In other words, in none of the cases can we reach the most "optimal" distribution of the filter: the predicted grids may always be close to the "optimal", but still with some distance from it. As a results, a more efficient approach would be to have an error-indicator that is customizable to the specific code and the LES model, but is still robust to the changes. Such an error-indicator would lead to target grids that are (at least theoretically) as optimal as possible for the customized case, while still somewhat close the optimal in all other cases.

And finally, while the general idea of connecting the accuracy of LES to the amount of unresolved or small-scale kinetic energy is quite intuitive and has been

found to work well in several cases in this Chapter and in the literature [23], it is important to acknowledge that it is heuristic in nature: there is no equation showing that error scales with unresolved kinetic energy. For example, a perfect SGS/SFS model would introduce no modeling error regardless of the unresolved kinetic energy. If one then uses a $\overline{\Delta}/\overline{h}$ that eliminates the numerical errors, our predictions of the QoIs are always accurate (for QoIs that are consistent with LES), independent of the small-scale or unresolved kinetic energy. Another example of failure of the energy-based indicators (although primarily for those based on the unresolved energy) is in the channel flow, where the LES-predicted kinetic energy is known to be (typically) larger than DNS (for instance, see all the grids in Figs. 3.1, 3.7, and 3.11) and the unresolved energy becomes a negative value; therefore, judging the modeling errors by the amount of "unresolved" energy becomes almost meaningless (similarly, for the ratio of resolved to total kinetic energy that is now larger than unity).

In Chapter 5 we revisit the problem of error-estimation in LES, this time from an equation-based point of view, and define a new error-indicator that is customizable to the LES model and the code, and is not affected (or at least less affected) by such flaws in the heuristic argument.

Chapter 4: The optimality criteria for grid selection and adaptation

Grid selection is a multi-objective optimization problem with the goal of producing a grid that simultaneously minimizes the error in the "quantities of interest" (QoIs) and the computational cost. In practice, the problem is often framed as the constrained minimization problem of minimizing the error (in the QoIs) for a fixed number of computational cells N_{tot}; or equivalently, minimizing the number of cells N_{tot} for a fixed threshold on the error in the QoIs.

The purpose of this Chapter is to highlight that the correct solution to the optimization problem is the equidistribution of the cell-integrated error, not the pointwise error as has been assumed in multiple grid-adaptation studies in the literature. While this is clearly well known in parts of the grid-adaptation community, it appears to not be broadly known. We therefore include a derivation of the correct equidistribution principle here and also show how this impacts the adapted grids.

4.1 The grid selection problem in an arbitrary number of dimensions

The global error in a quantity of interest is assumed to be (cf. [9,35,48,66–69])

$$\overline{e}^{\text{ref}}_{\text{QoI}} = \int_{\Omega} \overline{e}^{\text{ref}}_{\text{local}}(\mathbf{x}) J(\mathbf{x})\, d\mathbf{x}\,, \tag{4.1}$$

where $\overline{e}^{\text{ref}}_{\text{local}}(\mathbf{x})$ is the local source error on grid $\overline{\Delta}$ compared to a reference solution, $J(\mathbf{x})$ is the adjoint field [9,35,48,66–69] that connects the global error in the quantities of interest to the local error source $\overline{e}^{\text{ref}}_{\text{local}}(\mathbf{x})$, and Ω is the computational domain.

For grid selection we usually assume that the local error at an arbitrary grid-resolution or filter-width $\check{\Delta}$ can be found as

$$\check{e}^{\text{ref}}_{\text{local}}(\mathbf{x}) \approx \overline{c}(\mathbf{x}) \check{\Delta}^{\alpha}(\mathbf{x})\,, \tag{4.2}$$

where $c(\mathbf{x})$ is only a function of space (not the grid/filter size $\check{\Delta}$) and can be computed from the evaluation of the error-indicator on grid $\overline{\Delta}$ as

$$\overline{c}(\mathbf{x}) = \frac{\overline{e}^{\text{ref}}_{\text{local}}(\mathbf{x})}{\overline{\Delta}^{\alpha}(\mathbf{x})}\,. \tag{4.3}$$

Using Eqns. 4.2, 4.3, and 4.1 we can estimate the value of $\check{e}^{\text{ref}}_{\text{QoI}}(\mathbf{x})$ on any given grid $\check{\Delta}$ as

$$\check{e}^{\text{ref}}_{\text{QoI}} = \int_{\Omega} \overline{c}(\mathbf{x}) \check{\Delta}^{\alpha}(\mathbf{x}) J(\mathbf{x})\, d\mathbf{x}\,, \tag{4.4}$$

and try to find the one that leads to the minimum value.

The constraint of a fixed number of cells N_{tot} cannot be directly enforced in the continuous setting (at least not in physical space), but can be approximately

enforced by requiring that

$$N_{\text{tot}} = \int_{\Omega} \frac{d\mathbf{x}}{\check{V}_c}\,, \tag{4.5}$$

where $\check{V}_c$ is a continuous measure of the volume (or area in 2D, or length in 1D) of each cell.

The characteristic resolution of the filter/grid $\check{\Delta}$ that enters the definition of $\check{e}^{\text{ref}}_{\text{local}}$ can be expressed as

$$\check{\Delta}(\mathbf{x}) = r(\mathbf{x})\check{V}_c^{1/d}(\mathbf{x})\,, \tag{4.6}$$

where d is the number of spatial dimensions, such that the second factor in the right-hand side of the equation is the cube-root of the cell volume in 3D or the square-root of the cell area in 2D. In the definition above, $r(\mathbf{x}) \equiv 1$ describes a case with the cube root of the cell volume as the relevant length-scale and $\overline{\Delta}/\overline{h} = 1$, while other values of $r(\mathbf{x})$ describe $\check{\Delta}/\check{h}$ ratios other than unity, or alternative definitions of $\check{\Delta}(\mathbf{x})$ in the error-indicator (e.g., the maximum cell size, the diagonal length of the cells, etc.) that are all proportional to $\check{V}_c^{1/d}$, provided that the aspect ratio of the cell remains unchanged during the optimization process (which is usually true).

The goal of the optimization process is to find the $\check{\Delta}(\mathbf{x})$ that minimizes Eqn. 4.4 given that Eqn. 4.5 (the constraint on the number of cells on that grid) is satisfied. This constrained optimization problem can be solved by finding the minimum of the Lagrangian

$$\mathcal{L} = \check{e}^{\text{ref}}_{\text{QoI}} - \lambda\left(N_{\text{tot}} - \int_{\Omega}\frac{d\mathbf{x}}{\check{V}_c}\right) = \int_{\Omega}\left(\overline{c}(\mathbf{x})\check{\Delta}^{\alpha}(\mathbf{x})J(\mathbf{x}) + \lambda\frac{r^d(\mathbf{x})}{\check{\Delta}^d(\mathbf{x})}\right)d\mathbf{x} - \lambda N_{\text{tot}}\,,$$

which can be done by setting the functional derivative $\delta\mathcal{L}/\delta\check{\Delta}$ to zero. This yields

$$\alpha\,\overline{c}(\mathbf{x})\check{\Delta}^{\alpha-1}_{\text{opt}}(\mathbf{x})J(\mathbf{x}) - \lambda\,d\,r^d(\mathbf{x})\check{\Delta}^{-d-1}_{\text{opt}}(\mathbf{x}) = 0$$

or equivalently

$$J(\mathbf{x})\ \underbrace{\overline{c}(\mathbf{x})\check{\Delta}^{\alpha}_{\text{opt}}(\mathbf{x})}_{\check{e}^{\text{ref}}_{\text{local,opt}}(\mathbf{x})}\underbrace{\check{\Delta}^{d}_{\text{opt}}(\mathbf{x})r^{-d}(\mathbf{x})}_{\check{V}_{c,\text{opt}}} = \frac{\lambda\, d}{\alpha} = \text{const.} \tag{4.7}$$

This means that the optimal grid is achieved when each computational cell contributes equally to the error in the QoIs (equidistribution of the cell-wise contribution to the error in the QoI), and not when the error-indicator $\check{e}^{\text{ref}}_{\text{local}}(\mathbf{x})$ is uniformly distributed. This means that our intuitive assumption in the previous Chapter that (for $J(\mathbf{x}) \equiv 1$) the most "optimal grid" is achieved when the error-indicator is uniformly distributed in space was sub-optimal.

We are not considering the adjoint fields in this dissertation. Besides, we want to have "generally good" solutions with no emphasis on a specific QoI or a specific part of the domain. As a result, and for the lack of any better option, from now on we take a constant $J(\mathbf{x})$ in space,

$$J(\mathbf{x}) \equiv 1\,. \tag{4.8}$$

If we also assume that $r(\mathbf{x})$ is some fixed value for all $\mathbf{x}$, i.e. $r(\mathbf{x}) = r = \text{const.}$, Eqn. 4.7 simplifies to

$$c(\mathbf{x})\check{\Delta}^{\alpha+d}_{\text{opt}}(\mathbf{x}) = \text{const.} \tag{4.9}$$

This shows that the optimal grid-spacing distribution for the continuous problem with no adjoint field is the one for which $c(\mathbf{x})\check{\Delta}^{\alpha+d}_{\text{opt}}(\mathbf{x})$ (the cell-integrated error-indicator) is equidistributed, and not $c(\mathbf{x})\check{\Delta}^{\alpha}_{\text{opt}}(\mathbf{x})$ (the error-indicator itself).

We should mention that this equidistribution principle is exact only for the continuous problem, and is only an approximation for the actual discrete problem

of grid selection. Nevertheless, it is an $\mathcal{O}(\check{\Delta})$ accurate approximation of the discrete problem [14, 15] (under certain assumptions), which suggests that it is a good approximation provided that $\check{\Delta}$ is not too coarse.

4.2 Verification on a toy problem

To verify the equidistribution principle and to assess the effect on the global error, the following numerical experiment is performed. We define the three-dimensional field

$$\overline{c}(\mathbf{x}) = c(x, y, z) = [1.01 + \cos(2\pi x)] \exp\left(-4y^2\right) [1 + \tanh(3z)] ,$$

for $\mathbf{x} = (x, y, z) \in [-1, 1]^3$ and assume that the pointwise error-indicator scales with $\check{\Delta}^2(\mathbf{x})$ (i.e., that $\alpha = 2$). We then find the grid-spacing distribution $\check{\Delta}(\mathbf{x})$ that satisfies equidistribution of $c(\mathbf{x})\check{\Delta}^\zeta(\mathbf{x})$ for values of the exponent ζ between 1 and 10. For every value of ζ, the Lagrange multiplier λ (or, equivalently, the level at which we are equidistributing) is adjusted until the estimated number of cells $\int_\Omega d\mathbf{x}/\check{V}_c$ is equal to 40^d. After finding the $\check{\Delta}(\mathbf{x})$ distribution, the global error $\check{e}^{\text{ref}}_{\text{QoI}}$ is computed from Eqn. 4.4 with $J(\mathbf{x}) \equiv 1$ and plotted in Fig. 4.1 vs the exponent ζ. This is then repeated in 2D (with $z = 0$) and 1D (with $y = z = 0$).

The figure illustrates quite clearly that the minimum error occurs very near $\zeta = \alpha + d$ in each case, which supports the continuous formulation of the optimization problem and the implied equidistribution principle. It also shows that the global error is about 2.5 times higher if one equidistributes $\overline{c}(\mathbf{x})\check{\Delta}^\alpha(\mathbf{x})$ (i.e., the error-indicator itself) rather than the correct quantity $\overline{c}(\mathbf{x})\check{\Delta}^{\alpha+3}(\mathbf{x})$ in 3D; the specific

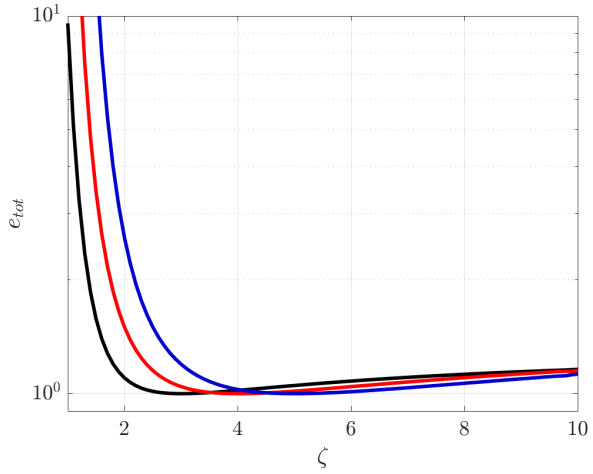

Figure 4.1: The global error $\check{e}^{\text{ref}}_{\text{QoI}}$ (Eqn. 4.4 with $J(\mathbf{x}) \equiv 1$) for grids that equidistribute $\overline{c}(\mathbf{x})\check{\Delta}^{\zeta}(\mathbf{x})$ for the numerical experiment described in the text. Tested in 1D (black), 2D (red), and 3D (blue). All curves are normalized by their corresponding minimum value to make them comparable. Note how the minimum occurs at $\zeta = 3$ (1D), $\zeta = 4$ (2D), and $\zeta = 5$ (3D), as predicted by the continuous formulation.

factor is of course unique to this particular setup (i.e., $\overline{c}(\mathbf{x})$ field, etc.), but illustrates that this does have an impact on the global error.

4.3 Effect on the resulting grids

It is also interesting to see how the equidistribution principle affects the resulting grids. Figure 4.2 shows the target grid-spacing $\check{\Delta}_{\text{opt}}$ that one gets from an instantaneous snapshot of laminar (two-dimensional) vortex shedding behind a square cylinder at a free stream Reynolds number of $Re_H = U_\infty H/\nu = 100$ (where H is the square height) . The $\overline{c}(\mathbf{x})$ field is computed from a Hessian-based grid-adaptation method [40, 46, 70–72] here, and the figure compares the target grid-spacings $\check{\Delta}_{\text{opt}}$ that one would get by imposing equidistribution of $\overline{c}(\mathbf{x})\Delta^2(\mathbf{x})$ (the error-indicator itself) and that by equidistribution of $\overline{c}(\mathbf{x})\Delta^4(\mathbf{x})$ (from the continuous formulation, for 2D). Note how the latter suppresses extreme variations in the grid-spacing, leading

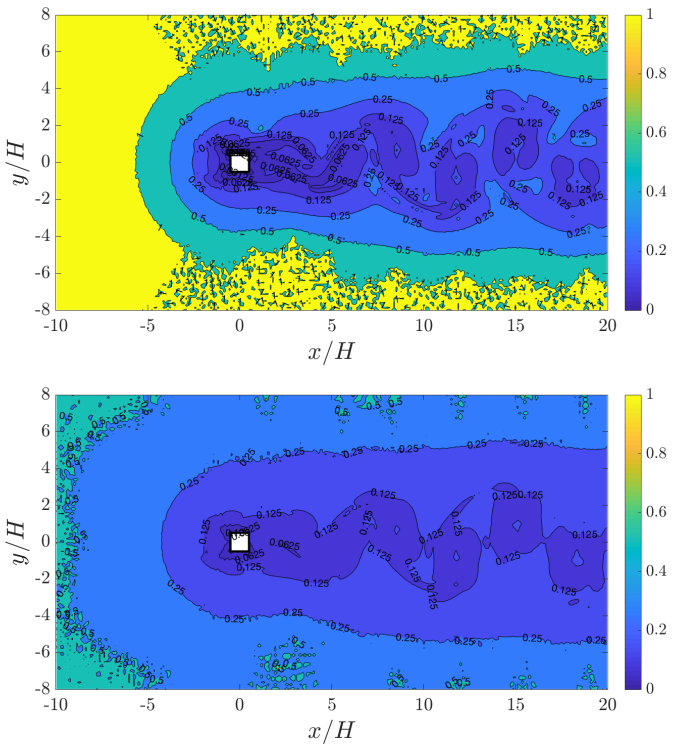

Figure 4.2: The predicted characteristic cell size $\check{\Delta}(\mathbf{x})$ (normalized by the square height H) for laminar vortex shedding from a square cylinder in 2D, based on a Hessian-based grid-adaptation method. Comparing equidistribution of the local error-indicator $\overline{c}(\mathbf{x})\check{\Delta}^2(\mathbf{x})$ (top) with equidistribution of the local cell-area-weighted error-indicator $\overline{c}(\mathbf{x})\check{\Delta}^4(\mathbf{x})$ (bottom). Both grids have the same number of cells (15k).

to less coarse cells in the free stream and less refined cells near the cylinder.

This is even more true in 3D, which can be seen in Fig. 4.3 which shows a similar example from LES of the flow over a backward-facing step. Again, the corrected equidistribution principle produces much smaller variations in $\check{\Delta}_{\text{opt}}(\mathbf{x})$. This latter example is from the error-indicator $\overline{\mathcal{A}}(\mathbf{x}, \mathbf{n})$ of the previous Chapter, where the "equidistribution of error-indicator" (Eqn. 3.7) was imposed. The most significant change in the results is in the freestream in Fig. 4.3, where the old principle leads to extremely coarse grids. We actually failed to fully appreciate this at the time of submission or even publication of the original paper [11], since

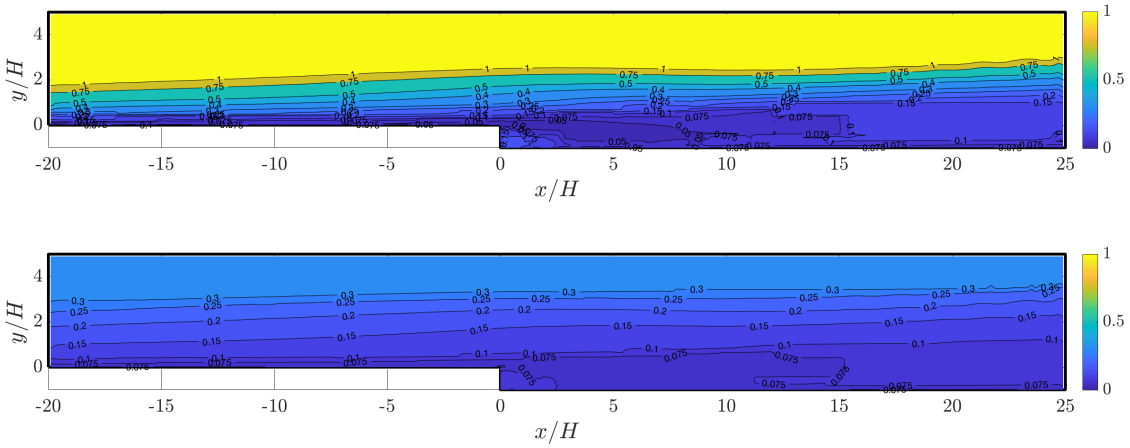

Figure 4.3: The predicted characteristic cell size $\check{\Delta}(\mathbf{x})$ (normalized by the step height H) for the flow over a backward-facing step using equidistribution of the error-indicator (top) and the cell-volume-weighted error-indicator (bottom). The $\overline{c}(\mathbf{x})$ field is computed from the anisotropic error-indicator of Chapter 3. Both grids have about 1 million cells.

the grids were adaptively refined from the "skeletal" mesh with $\Delta_0(\mathbf{x}, \mathbf{n})/H = 0.2$ with no ability to coarsen beyond that size; hence the extremely coarse cells in the freestream were never realized. With the equidistribution principle derived from the continuous formulation, this is much less of an issue.

4.4 Optimal criteria for anisotropic grid selection in LES

Everything discussed so far in this Chapter was for the case of a local error-indicator that is only a function of $\mathbf{x}$. In this Section we focus on extending the grid selection criterion to anisotropic error-indicators, like $\overline{\mathcal{A}}(\mathbf{x}, \mathbf{n})$ of Chapter 3, to enable optimal anisotropic grid selection.

Assuming that the local error source at any $\mathbf{x}$ is proportional to the total small-scale energy at that location, which can be approximated for a hexahedral

cell as

$$\check{\mathcal{A}}^2_{\text{tot}}(\mathbf{x}) = \check{\mathcal{A}}^2(\mathbf{x}, \mathbf{n}_1) + \check{\mathcal{A}}^2(\mathbf{x}, \mathbf{n}_2) + \check{\mathcal{A}}^2(\mathbf{x}, \mathbf{n}_3)$$

(where the $\mathbf{n}_1$, $\mathbf{n}_2$ and $\mathbf{n}_3$ directions are the three directions of the hexahedral cells; see Fig. 3.4), provides a link between our anisotropic error-indicator $\check{\mathcal{A}}(\mathbf{x}, \mathbf{n})$ and the local error-indicator $\check{e}^{\text{ref}}_{\text{local}}(\mathbf{x})$ as

$$\check{e}^{\text{ref}}_{\text{local}}(\mathbf{x}) \propto \check{\mathcal{A}}_{\text{tot}}(\mathbf{x}) = \sqrt{\check{\mathcal{A}}^2(\mathbf{x}, \mathbf{n}_1) + \check{\mathcal{A}}^2(\mathbf{x}, \mathbf{n}_2) + \check{\mathcal{A}}^2(\mathbf{x}, \mathbf{n}_3)}\,. \tag{4.10}$$

This definition of the local error-indicator can be substituted into Eqn. 4.1 and the resulting optimization problem can be solved by setting the functional derivatives of the Lagrangian to zero, i.e., $\delta\mathcal{L}/\delta\check{\Delta}_1 = 0$, $\delta\mathcal{L}/\delta\check{\Delta}_2 = 0$, and $\delta\mathcal{L}/\delta\check{\Delta}_3 = 0$. After a bit of simple algebraic manipulation, it can be shown that for this specific definition of $\check{\mathcal{A}}_{\text{tot}}(\mathbf{x})$ the solution to the directional optimization problem is

$$\alpha_1\, \check{\mathcal{A}}(\mathbf{x}, \mathbf{n}_1) = \alpha_2\, \check{\mathcal{A}}(\mathbf{x}, \mathbf{n}_2) = \alpha_3\, \check{\mathcal{A}}(\mathbf{x}, \mathbf{n}_3)\,, \tag{4.11}$$

where α_i is the scaling exponent in direction $\mathbf{n}_i$, i.e., from the model $\check{\mathcal{A}}(\mathbf{x}, \mathbf{n}_i) \sim \check{\Delta}^{\alpha_i}_{\mathbf{n}_i}$ in Section 3.1.3. In the previous Chapter we assumed that the scaling exponent is the same in all directions, $\alpha_1 \approx \alpha_2 \approx \alpha_3 \approx \alpha \approx 2$, meaning that the optimal directional distribution of the error-indicator is in fact the intuitively assumed uniform distribution in different directions

$$\check{\mathcal{A}}(\mathbf{x}, \mathbf{n}_1) = \check{\mathcal{A}}(\mathbf{x}, \mathbf{n}_2) = \check{\mathcal{A}}(\mathbf{x}, \mathbf{n}_3)\,. \tag{4.12}$$

Note that for different scaling exponents in different directions the selection criteria is again different from what we assumed heuristically.

This criterion can be expressed in an equivalent form as

$$\check{\mathcal{A}}(\mathbf{x},\mathbf{n}_i) = \overline{a}(\mathbf{x},\mathbf{n}_i)\check{\Delta}^{\alpha}(\mathbf{x},\mathbf{n}_i) = \overline{a}_{\mathrm{vol}}(\mathbf{x})\check{\Delta}^{\alpha}_{\mathrm{vol}}(\mathbf{x}) \;, \quad i = 1,2,3\,, \tag{4.13}$$

where

$$\overline{a}(\mathbf{x},\mathbf{n}_i) = \frac{\overline{\mathcal{A}}(\mathbf{x},\mathbf{n}_i)}{\overline{\Delta}^{\alpha}(\mathbf{x},\mathbf{n}_i)}$$

is computed from evaluation of the error-indicator on the original LES grid, and

$$\overline{a}_{\mathrm{vol}} = \left(\overline{a}(\mathbf{x},\mathbf{n}_1)\overline{a}(\mathbf{x},\mathbf{n}_2)\overline{a}(\mathbf{x},\mathbf{n}_3)\right)^{1/3} \;, \quad \check{\Delta}_{\mathrm{vol}} = \left(\check{\Delta}(\mathbf{x},\mathbf{n}_1)\check{\Delta}(\mathbf{x},\mathbf{n}_2)\check{\Delta}(\mathbf{x},\mathbf{n}_3)\right)^{1/3} .$$

This implies that the predicted optimal cell aspect ratio is, for example,

$$\frac{\check{\Delta}(\mathbf{x},\mathbf{n}_j)}{\check{\Delta}(\mathbf{x},\mathbf{n}_1)} = \left(\frac{\overline{a}(\mathbf{x},\mathbf{n}_1)}{\overline{a}(\mathbf{x},\mathbf{n}_j)}\right)^{1/\alpha} \;, \; j = 2,3\,. \tag{4.14}$$

Examples of the predicted optimal cell aspect ratios are given in Fig. 4.4 for a turbulent channel flow and in the recirculation region of the flow over a backward-facing step. We note that the target aspect ratio can be a function of the scaling exponent α. This is only true in the intermediate grids in the sequence where the resolutions are still adjusting to satisfy the directional equidistribution of the error-indicator, while the final "optimal" grid that should have an equal error-indicator in all directions $\mathbf{n}$ is not really affected by the choice of α. Since a lower scaling exponent α generally leads to more extreme aspect ratios of the filter (see Fig. 4.4) and since the turbulence on the coarser grids is underresolved and potentially inaccurate, selecting a lower α that may be closer to its theoretical value for that flow might instead lead to less optimal intermediate grids and delay the convergence of the sequence. As a result, the choice of $\alpha = 2$ may actually help improving the performance of

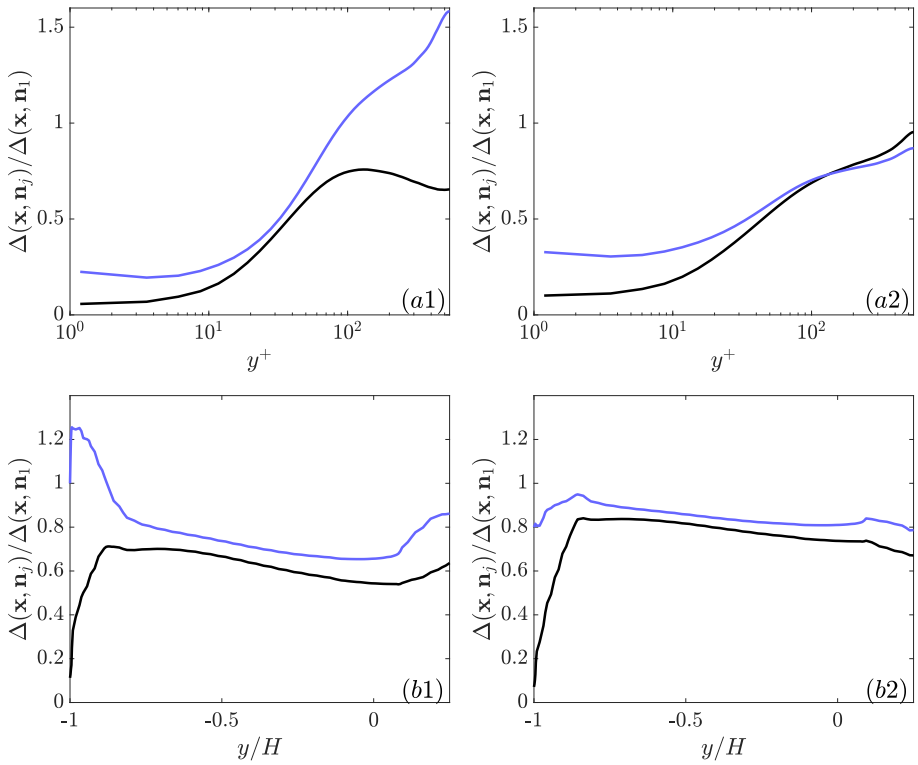

Figure 4.4: Examples of the predicted optimal cell aspect ratios $\check{\Delta}(\mathbf{x},\mathbf{n}_2)/\check{\Delta}(\mathbf{x},\mathbf{n}_1)$ (black lines) and $\check{\Delta}(\mathbf{x},\mathbf{n}_3)/\check{\Delta}(\mathbf{x},\mathbf{n}_1)$ (blue lines) for: $(a1)$ turbulent channel flow at $Re_\tau \approx 545$, for $\alpha = 1$ $(a2)$ same flow as $(a1)$, $\alpha = 2$, $(b1)$ in the recirculation region of the flow over a backward-facing step at $x/H = 4$, for $\alpha = 1$, and $(b2)$ same flow and region as $(b1)$, $\alpha = 2$. Note that $\alpha = 1$ leads to more extreme aspect ratios of the cells, leading to possibly low-quality computational cells, and is thus less robust. The aspect ratio on the final "optimal" grid does not depend on the scaling exponent (as long as $\alpha_{\mathbf{n}}$ is the same in all directions).

the adaptation algorithm by making it more robust to such unwanted errors. This further justifies our choice of $\alpha = 2$ in the previous Chapter, and in the rest of this dissertation.

We should also note that the target cell aspect ratios are the same for both the modified criterion and the one used in the previous Chapter; although, the aspect ratio of the generated grids may still be different because of the limitations like the structured nature of the grids, or the ability to refine by factors of two only.

Equations 4.13 and 4.9 can be combined to find the optimal value of $\check{\Delta}_{\text{vol}}$ as

$$\overline{a}_{\text{vol}}(\mathbf{x})\check{\Delta}^{\alpha+3}_{\text{vol,opt}}(\mathbf{x}) = \Lambda = \text{const.}\,, \tag{4.15}$$

where $\check{\Delta}_{\text{vol,opt}}$ is then used to find the optimal directional filter as

$$\check{\Delta}_{\text{opt}}(\mathbf{x}, \mathbf{n}_i) = \left(\frac{\overline{a}_{\text{vol}}(\mathbf{x})}{\overline{a}(\mathbf{x}, \mathbf{n}_i)}\right)^{1/\alpha} \check{\Delta}_{\text{vol,opt}}(\mathbf{x})\,. \tag{4.16}$$

Equations 4.15 and 4.16 define our optimal filter-width $\check{\Delta}_{\text{opt}}(\mathbf{x}, \mathbf{n})$ on any given grid with a specified N_{tot} number of cells.

Figure 4.5 shows a comparison between the optimal grids for the channel flow where one is predicted by the grid selection criterion of this Chapter (Eqns. 4.15 and 4.16) and the other from the equidistribution of the error-indicator itself, used in the previous Chapter (Eqn. 3.7). Note that the grids generated by the new criteria: (i) have the same directional resolution at the wall; (ii) have much smoother variations of the grid; (iii) are about a factor of two finer at the center of the channel; and (iv) are a little coarser in the region $y^+ \lesssim 100$.

In the rest of this Chapter we repeat our assessments of the error-indicator $\overline{\mathcal{A}}(\mathbf{x}, \mathbf{n})$ on both the channel flow and the flow over a backward-facing step, and compare the sequence of grids generated by the modified criteria of this Chapter (Eqns. 4.15 and 4.16) with the one generated by the heuristic criterion of equidistribution of the error-indicator itself (Eqn. 3.7).

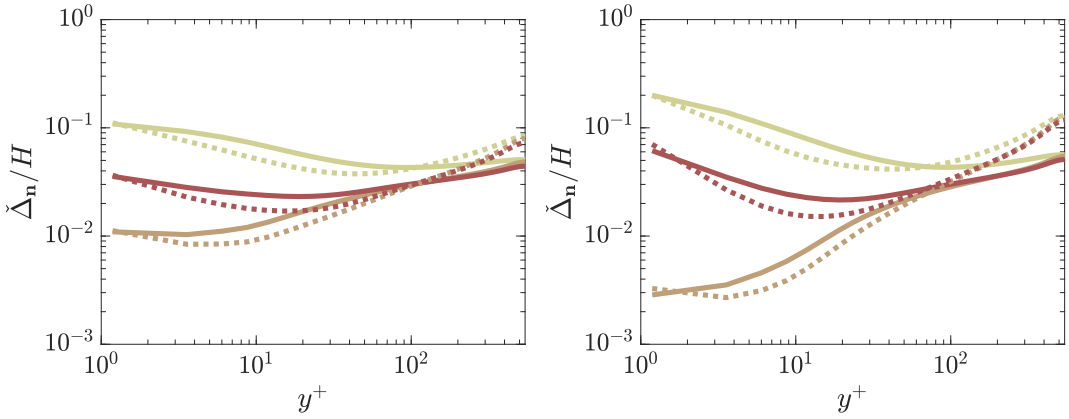

Figure 4.5: A comparison of the optimal directional filter-width $\check{\Delta}_{\text{opt}}(\mathbf{x}, \mathbf{n})$ using the modified criteria of this Chapter (solid lines) vs the heuristic criterion of Chapter 3 (dotted lines), for grids generated using: (a) the standard definition of the error-indicator $\overline{\mathcal{A}}(\mathbf{x}, \mathbf{n})$, and (b) the alternative definition based on the structure-functions $\overline{\mathcal{A}}'(\mathbf{x}, \mathbf{n})$. The streamwise, wall-normal, and spanwise directions are shown by the brightest to the darkest colors, in that order.

4.5 Assessment on the turbulent channel flow at $Re_\tau \approx 545$

4.5.1 Setup

The code used for this problem is the *Hybrid* code that is described in some detail in Section 3.2.1. The code solves the compressible Navier-Stokes equations for a calorically perfect gas on structured Cartesian grids using sixth-order accurate central differencing schemes.

The bulk Mach number, defined as the ratio of the bulk velocity U_b and the speed-of-sound at the walls, is 0.2 for this case, which is a compromise between having minimal effects of compressibility while avoiding an excessively small time step. The bulk Reynolds number $Re_b = \rho_b U_b H/\mu_w$ is 10,000, which leads to a friction Reynolds number of about $Re_\tau \approx 545$. This is the same Reynolds number used in the benchmark incompressible DNS of del Alamo & Jimenez [18] which is used here

as the reference solution in computing $\overline{e}^{\mathrm{DNS}}_{\mathrm{QoI}}$ and in plots of the mean velocity and Reynolds stress profiles. The error in the QoIs is computed from Eqn. 3.10, where $\delta\overline{Q}^{\mathrm{ref}}_m$ are defined by Eqn. 3.9, except that the resolved Reynolds stress $\overline{R}_{ij} = \langle \overline{u}'_i \overline{u}'_j \rangle$ is now replaced by the correct quantity $\overline{R}^{\mathrm{tot}}_{ij} = \langle \overline{u}'_i \overline{u}'_j \rangle + \langle \tau^{\mathrm{mod}}_{ij} \rangle$ where τ^{mod}_{ij} is the SGS stress from the LES model.

All simulations are started from a fully developed snapshot on a sufficiently fine grid. They are integrated for a time of $200H/U_b$ before collecting statistics over a period of $600H/U_b$, using 400 snapshots at a distance of $1.5H/U_b$ from each other. The convergence error is found to be sufficiently small as to not affect any conclusions in this study.

Only the implicitly filtered LES with explicit modeling using the dynamic Smagorinsky model is considered in this Section. The results for the other cases (including DNS with only the numerical errors, and ILES) will be very similar to this case.

One important difference between the problem setup in this Section and that of Section 3.2.1 is that here we can freely input the target $\overline{\Delta}_y$ to the code and thus have a wall-normal resolution that matches the target values as closely as possible (in Section 3.2.1 we could only use *tanh* functions). This allows us to make interesting observations that are discussed below.

4.5.2 Process

Two new sequences of grids are generated for the new setup of this Section, one with the old and heuristic-based criterion of Eqn. 3.7 and the second sequence using the correct and modified criteria of this Chapter. Both sequences are started from the same initial grid with $(\overline{\Delta}_x, \overline{\Delta}_y, \overline{\Delta}_z)/H = (0.20, 0.10, 0.20)$. The finer wall-normal resolution is to allow for a later comparison of the results with those of Chapter 8 whose error-indicator is based on certain assumptions that require sufficient turbulent activity to be valid. The next grid in the sequence is selected such that the cell count increases by a factor of 4 in the first iteration, a factor of 3 in the second iteration, and factors of 2 afterwards. The number of cells N_{tot} is closely matched between the grids generated by the old and new criteria to allow for a direct comparison of their optimality, i.e. lowest $\overline{e}^{\text{DNS}}_{\text{QoI}}$ for a given N_{tot}.

4.5.3 Results

Figures 4.6 and 4.7 illustrate this step-by-step adaptation process, in terms of the shape of the predicted cells, convergence of the mean velocity $\overline{U}_1^+ = \langle \overline{u}_1 \rangle / u_\tau$ and total streamwise Reynolds stress $\overline{R}_{11}^{\text{tot}} = \langle \overline{u}_1' \overline{u}_1' \rangle + \langle \tau_{11}^{\text{mod}} \rangle$, as well as the error-indicator in each of the three directions of refinement ($\overline{\mathcal{A}}(y^+, \mathbf{n}_x)$, $\overline{\mathcal{A}}(y^+, \mathbf{n}_y)$ and $\overline{\mathcal{A}}(y^+, \mathbf{n}_z)$) as well as $\overline{\mathcal{A}}_{\text{tot}}(y^+) = \sqrt{\overline{\mathcal{A}}^2(y^+, \mathbf{n}_x) + \overline{\mathcal{A}}^2(y^+, \mathbf{n}_y) + \overline{\mathcal{A}}^2(y^+, \mathbf{n}_z)}$. Table 4.1 summarizes the generated grids and some of their key quantities. Figure 4.8 plots the overall error in the QoIs $\overline{e}^{\text{DNS}}_{\text{QoI}}$ vs the number of cells N_{tot}. Note that the modified criterion was derived based on the assumptions that $J(\mathbf{x}) \approx 1$ and $\check{e}^{\text{ref}}_{\text{local}}(\mathbf{x}) \propto \check{\mathcal{A}}_{\text{tot}}(\mathbf{x})$. Therefore,

Grid	N_{tot}	N_y	$(\overline{\Delta}_x^+, \overline{\Delta}_{y_w}^+, \overline{\Delta}_z^+)$	$(\overline{\Delta}_x, \overline{\Delta}_{y_c}, \overline{\Delta}_z)/H$	Re_τ	$\overline{e}_{\text{QoI}}^{\text{DNS}}$ (%)
OLD-2	76k	34	$(77, 5.5, 54)$	$(0.14, 0.10, 0.097)$	554	12
NEW-2	76k	36	$(80, 6.9, 56)$	$(0.14, 0.075, 0.10)$	562	12
OLD-3	246k	38	$(51, 3.0, 28)$	$(0.093, 0.12, 0.050)$	551	7.1
NEW-3	245k	48	$(57, 3.6, 32)$	$(0.10, 0.061, 0.058)$	560	8.3
OLD-4	525k	42	$(45, 2.7, 17)$	$(0.080, 0.12, 0.030)$	558	4.0
NEW-4	526k	56	$(46, 2.9, 22)$	$(0.082, 0.052, 0.039)$	559	5.5
OLD-5	1.18M	48	$(36, 2.6, 11)$	$(0.064, 0.11, 0.019)$	563	3.4
NEW-5	1.17M	66	$(35, 2.6, 15)$	$(0.063, 0.044, 0.027)$	559	4.2
OLD-6	2.56M	58	$(26, 2.2, 7.9)$	$(0.048, 0.095, 0.014)$	553	1.9
NEW-6	2.52M	80	$(26, 2.2, 11)$	$(0.048, 0.035, 0.020)$	552	2.4
OLD-7	5.81M	74	$(19, 1.9, 6.2)$	$(0.034, 0.072, 0.011)$	548	1.2
NEW-7	5.90M	100	$(18, 1.8, 8.2)$	$(0.034, 0.028, 0.015)$	543	0.8

Table 4.1: Sequence of grids generated for LES of channel flow at $Re_\tau \approx 545$ using the dynamic Smagorinsky model. All the "OLD" grids are generated using the heuristic grid selection criterion of Eqn. 3.7, while the "NEW" grids are generated by enforcing the modified criteria of Eqns. 4.15 and 4.16. Note that $\overline{\Delta}_{y_c}$ is the value at the channel centerline, while $\overline{\Delta}_{y_w}^+$ is the value at the wall. N_{tot} is the total number of grid points in the computational domain. N_y is the number of points across the channel in the wall normal direction. The sequences are also illustrated in Fig. 4.6 for the OLD sequence and in Fig. 4.7 for the set of NEW grids. Convergence of $\overline{e}_{\text{QoI}}^{\text{DNS}}$ vs N_{tot} is plotted in Fig. 4.8 for both the OLD and NEW grids.

the convergence of

$$\overline{e}_{\text{surr}} = \frac{1}{V_\Omega} \int_\Omega \overline{\mathcal{A}}_{\text{tot}}(\mathbf{x}) d\mathbf{x}\,, \tag{4.17}$$

where V_Ω is the volume of the computational domain, is also plotted in Fig. 4.8 to compare with the convergence of $\overline{e}_{\text{QoI}}^{\text{DNS}}$.

4.5.4 Discussion

If we follow the succession of the grids labeled "NEW" (for the modified criteria of this Chapter) and "OLD" (for the heuristic grid selection criterion of Chapter 3), we can clearly see that both the sequences have a qualitatively similar behavior.

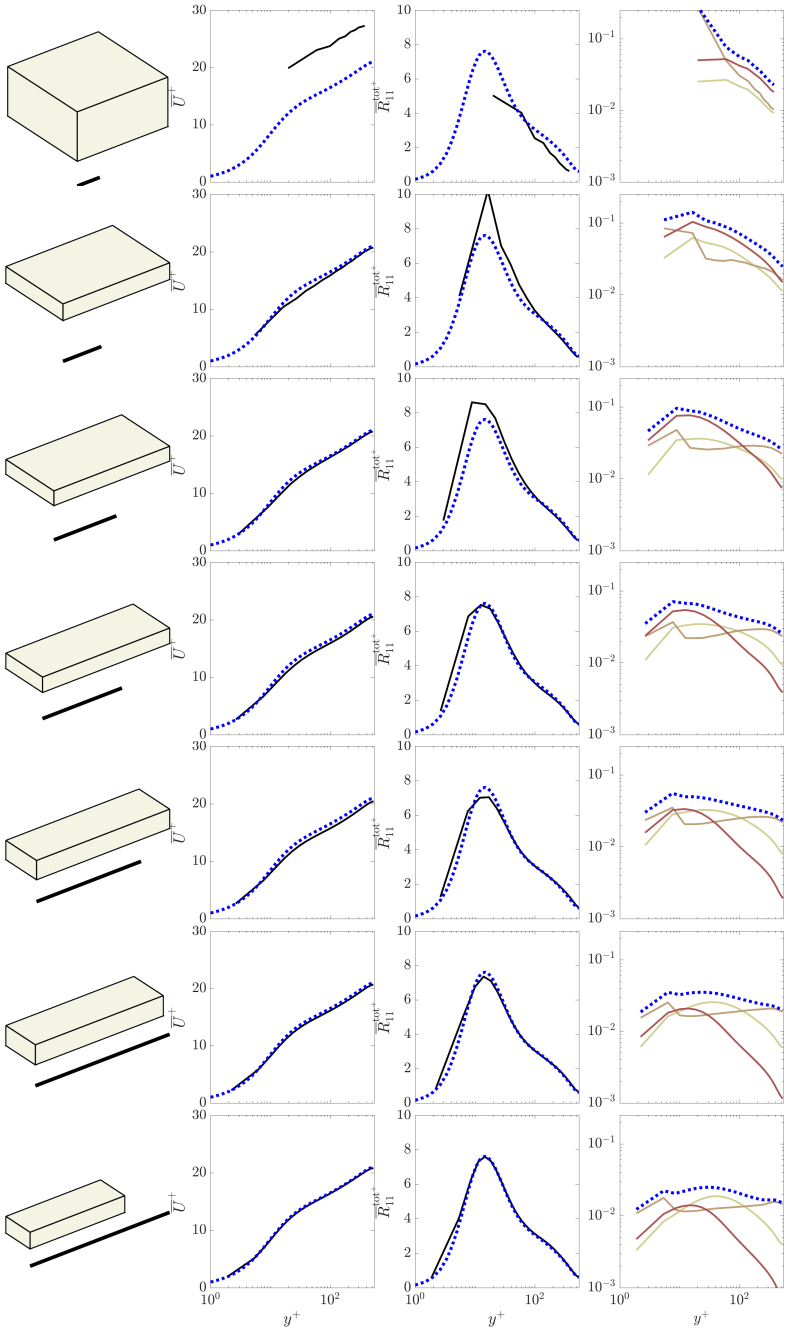

Figure 4.6: Sequence of grids generated by the heuristic grid selection criterion of Eqn. 3.7 for LES of the channel flow at $Re_\tau \approx 545$. The rows show the progression of grids from OLD-1 (top row) to OLD-7 (bottom row). Key quantities are listed in Table 4.1. The left column shows the shape of a wall-adjacent cell, while the right column shows the streamwise, wall-normal, and spanwise error-indicators by the brightest to the darkest colors. The dotted lines shows $\overline{\mathcal{A}}_{\text{tot}}(y^+)$ in the right column and the reference DNS solution of del Alamo and Jimenez [18] in the middle columns.

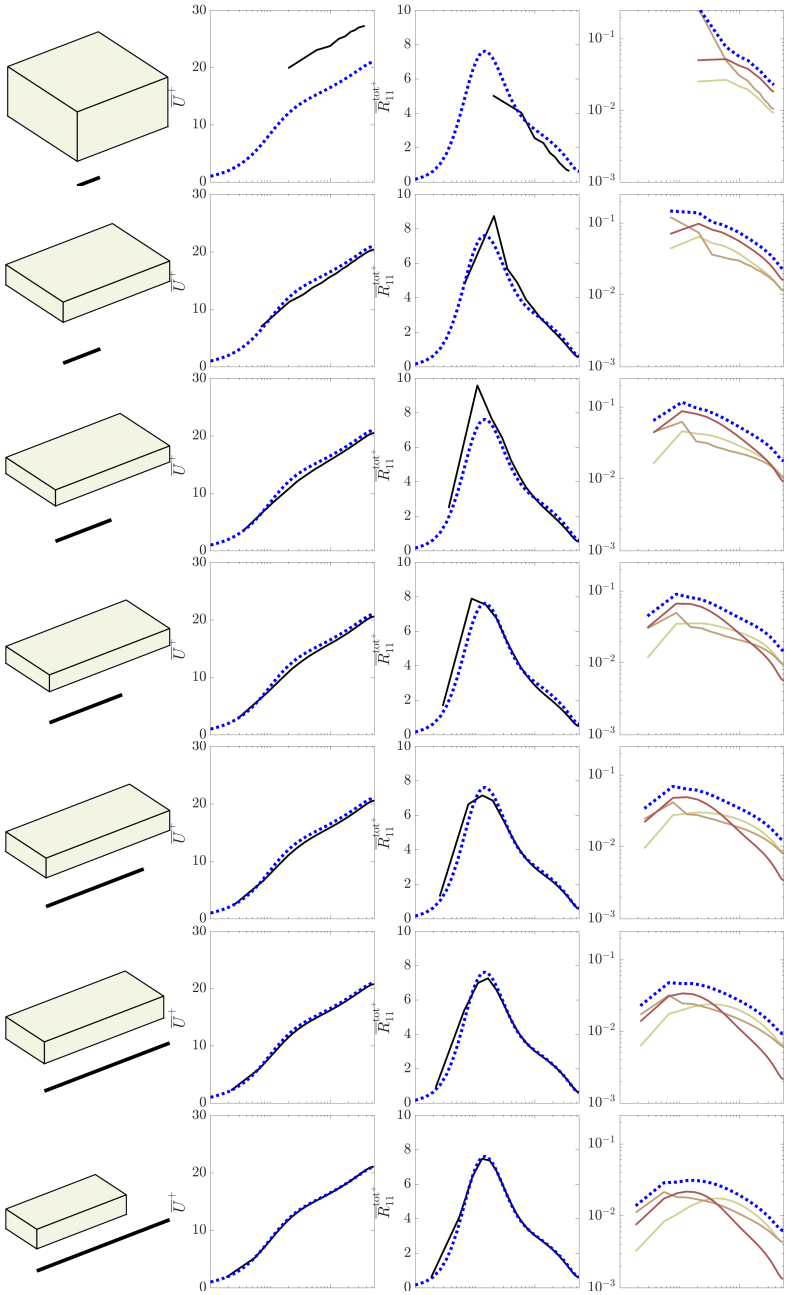

Figure 4.7: Sequence of grids generated by the modified grid selection criteria of Eqns. 4.15 and 4.16 for LES of the channel flow at $Re_\tau \approx 545$. The rows show the progression of grids from NEW-1 (top row) to NEW-7 (bottom row). See the caption of Fig. 4.6. Key quantities are listed in Table 4.1.

For example, both primarily target $\overline{\Delta}_{y_w}$ for refinement in the first iteration (to generate OLD-2 and NEW-2), followed by a refinement of both $\overline{\Delta}_y$ and $\overline{\Delta}_z$ in the next iteration (generating OLD-3 and NEW-3), and then a focus on the spanwise

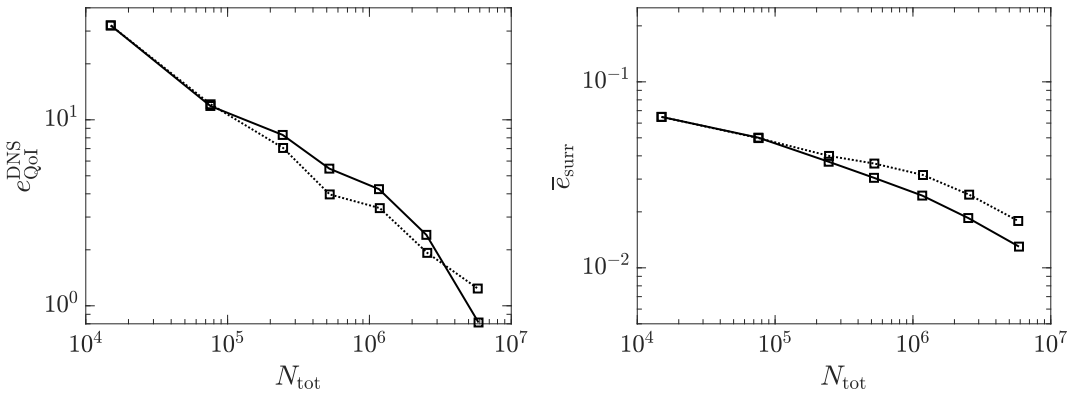

Figure 4.8: Convergence of $\overline{e}^{\mathrm{DNS}}_{\mathrm{QoI}}$ (left) and $\overline{e}_{\mathrm{surr}}$ (right) defined in Eqn. 4.17, both vs the number of cells N_{tot} for the LES of channel flow at $Re_\tau \approx 545$ reported in Table 4.1. The solid lines correspond to the NEW grids, while the dotted lines denote the OLD grids. The y-axes are scaled such that the slopes can be directly compared between the two panels. Note that $\overline{e}^{\mathrm{DNS}}_{\mathrm{QoI}}$ has a faster convergence than $\overline{e}^{\mathrm{surr}}_{\mathrm{local}}$. See text for explanation.

refinement in both NEW-4 and OLD-4 grids.

Note that the aspect ratio of the grids labeled "NEW" are somewhat different from those labeled "OLD", even though the criterion for selecting the optimal aspect ratio has not changed. This is because of the structured nature of the predicted grids and the fact that the maximum value of the error-indicator in the spanwise direction occurs around $y^+ \approx 10-20$ which is different from where $\overline{\mathcal{A}}(y^+, \mathbf{n}_x)$ reaches its maximum ($y^+ \approx 40-50$); therefore, the final aspect ratio that is determined by $\min_y \overline{\Delta}_x$ and $\min_y \overline{\Delta}_z$, changes between the two methods.

Despite the qualitative similarity between the two sequences, there are a few key differences between them as well. Most notably, the grids labeled "NEW" have finer wall-normal resolutions almost everywhere (except at the walls where $\overline{\Delta}_{y_w}$ is surprisingly similar between the two sequences) and thus a higher N_y. These are consistent with our observations from Fig. 4.5. On the other hand, the spanwise

resolutions of these grids are coarser. In fact, both of these changes are favorable as the grids in the "NEW" sequence now have resolutions and aspect ratios that are closer to what we expect from experience.

An interesting observation from Fig. 4.6 is that for grids "OLD-3" or "OLD-4" and after the wall normal error-indicator $\overline{\mathcal{A}}(y^+, \mathbf{n}_y)$ is almost constant across the channel. For grids "OLD-5" and after the maximum value of $\overline{\mathcal{A}}(y^+, \mathbf{n}_x)$ and $\overline{\mathcal{A}}(y^+, \mathbf{n}_z)$ are also equal to each other and equal to the nearly constant value of $\overline{\mathcal{A}}(y^+, \mathbf{n}_y)$. It means that for "OLD-5" and all the grids after it the optimality criterion of Eqn. 3.6 is reached: the first grid after "OLD-5" that satisfies the threshold on $\overline{e}^{\text{DNS}}_{\text{QoI}}$ is the "optimal" grid based on the proposed methodology of Chapter 3. This also means that our choice of $\alpha = 2$ does not negatively impact the performance of the algorithm: the first few grids on which the optimality criterion was not accurately satisfied were too coarse to produce a converged solution anyway, and for grids "OLD-5" and after which may produce converged results the criterion is satisfied, despite the value of α being higher than its theoretical value for this flow. Note that our use of Fig. 4.6 and the "OLD" grids in our arguments were for the sake of clarity (since they require a constant error-indicator across the channel which is visually more clear).

It is quite clear from Figs. 4.6 and 4.7 that the locations corresponding to the maximum value of the streamwise and spanwise error-indicators move from one grid to the other. Note that $\overline{\Delta}_x$ and $\overline{\Delta}_z$ are fixed across the channel, and any qualitative difference in the profiles of $\overline{\mathcal{A}}(y^+, \mathbf{n}_x)$ and $\overline{\mathcal{A}}(y^+, \mathbf{n}_z)$ is due to the change in the underlying flowfield used in their computation; e.g., because of the change in

the LES solution (i.e., it is becoming more accurate), or some indirect effect from a change in the resolution in other directions. This further justifies our choice of $\alpha = 2$ for increased robustness.

Figure 4.8 summarizes the convergence of the NEW and OLD grids vs the number of cells N_{tot}. Two quantities are plotted in this figure: (i) the error in the QoIs, $\overline{e}^{\text{DNS}}_{\text{QoI}}$, which is the subject of minimization in any grid selection/adaptation process, and (ii) the surrogate error $\overline{e}_{\text{surr}}$ defined in Eqn. 4.17 which was used as an approximation to $\overline{e}^{\text{DNS}}_{\text{QoI}}$ when deriving the modified grid selection criteria. Note that the modified criteria leads to lower values of $\overline{e}_{\text{surr}}$ on almost all the NEW grids (as expected, since it was formulated to minimize that specific quantity); however, $\overline{e}^{\text{DNS}}_{\text{QoI}}$ does not follow the same behavior and is actually slightly lower on the OLD grids (except for the last grid). This can happen due to a number of reasons, including the assumption of $J(\mathbf{x}) \approx 1$, or the fact that $\check{\mathcal{A}}_{\text{tot}}(\mathbf{x})$ may not be a great estimate of $\check{e}^{\text{ref}}_{\text{local}}(\mathbf{x})$.

Another interesting point is that $\overline{e}^{\text{DNS}}_{\text{QoI}}$ seems to have a faster convergence than $\overline{e}_{\text{surr}}$. This is most probably due to the large-scale nature of the QoIs and the small-scale nature of what $\overline{e}_{\text{surr}}$ measures; in other words, $\overline{\mathcal{A}}_{\text{tot}}$ measures the total small scale energy, and since the resolved LES fields always develop smaller scales with refinement of the filter, $\overline{\mathcal{A}}_{\text{tot}}$ does not decay with filter refinement at the same rate as the large scale quantities (see Fig. 2.4 for an example of different convergence behaviors of LES for difference variables, and Section 3.1.3 for a more detailed discussion of the scaling of $\overline{\mathcal{A}}(\mathbf{x}, \mathbf{n})$ with $\overline{\Delta}(\mathbf{x}, \mathbf{n})$).

4.6 Assessment on the flow over a backward-facing step at $Re_H = 5100$

4.6.1 Setup

The flow setup and computational detail are identical to those of the previous Chapter, described is Section 3.3.1.

The OpenFOAM code version 2.3.1 is used for this flow, which is a second-order finite-volume solver capable of handling unstructured grids. All adapted grids in this Section have Cartesian topology, since they were all generated by refinement of an initially structured Cartesian "skeletal" grid with $\Delta_0(\mathbf{x}, \mathbf{n})/H = 0.2$. Coarsening beyond this "skeletal" grid is not possible, although the adaptation process may both coarsen or refine the cells (a refined cell in one iteration may be selected for coarsening in a future iteration, as long as $\check{\Delta}(\mathbf{x}, \mathbf{n})/H \leq 0.2$). Refinement is performed using the *refineMesh* utility of OpenFOAM, which refines the hexahedral cells with factors of two in any of the three refinement directions. Similar to the previous Chapter, the target resolutions are rounded down to the nearest available resolution; e.g., a target resolution of $0.09H$ is rounded down to $0.05H$ which is the coarsest finer resolution available.

4.6.2 Process

A new sequence (labeled "NEW") is generated using the modified criterion of this Chapter, starting from LES-1 in Table 3.4 as the initial grid. The setup is

exactly the same as the one used for grids in Table 3.4; these grids are relabeled "OLD" and repeated in Table 4.2. At each iteration we have tried to match the total number of cells N_{tot} between the corresponding grids in the two sequences as closely as possible, to allow for a direct comparison of optimality between any two grids; i.e., to see which grid has a lower $\overline{e}_{\text{QoI}}^{\text{DNS}}$ at the same N_{tot}.

4.6.3 Results

Figure 4.9 compares the target refinement regions of grids OLD-2 and NEW-2 with around $300k$ computational cells, while Fig. 4.10 compares the generated grids OLD-6 and NEW-6 with around $3.7M$ cells and converged solutions. Table 4.2 summarizes the two sequences of grids generated using the heuristic-based criterion ("OLD") and the modified criterion ("NEW") along with their resolutions in some of the key locations. The convergence of $\overline{e}_{\text{QoI}}^{\text{DNS}}$ and $\overline{e}_{\text{surr}}$ with N_{tot} are plotted in Fig. 4.11. Figure 4.12 compares the convergence of the friction and pressure coefficient profiles along the horizontal wall, while Figs 4.13. 4.14, and 4.15 compare the convergence of the mean velocity and Reynolds stress profiles at some of the more interesting locations.

4.6.4 Discussion

Figure 4.9 shows that the grids OLD-2 and NEW-2 have qualitatively similar regions of predicted refinement, although there are some differences between them as well. Most importantly, note that NEW-2 has only two refinement levels in the y

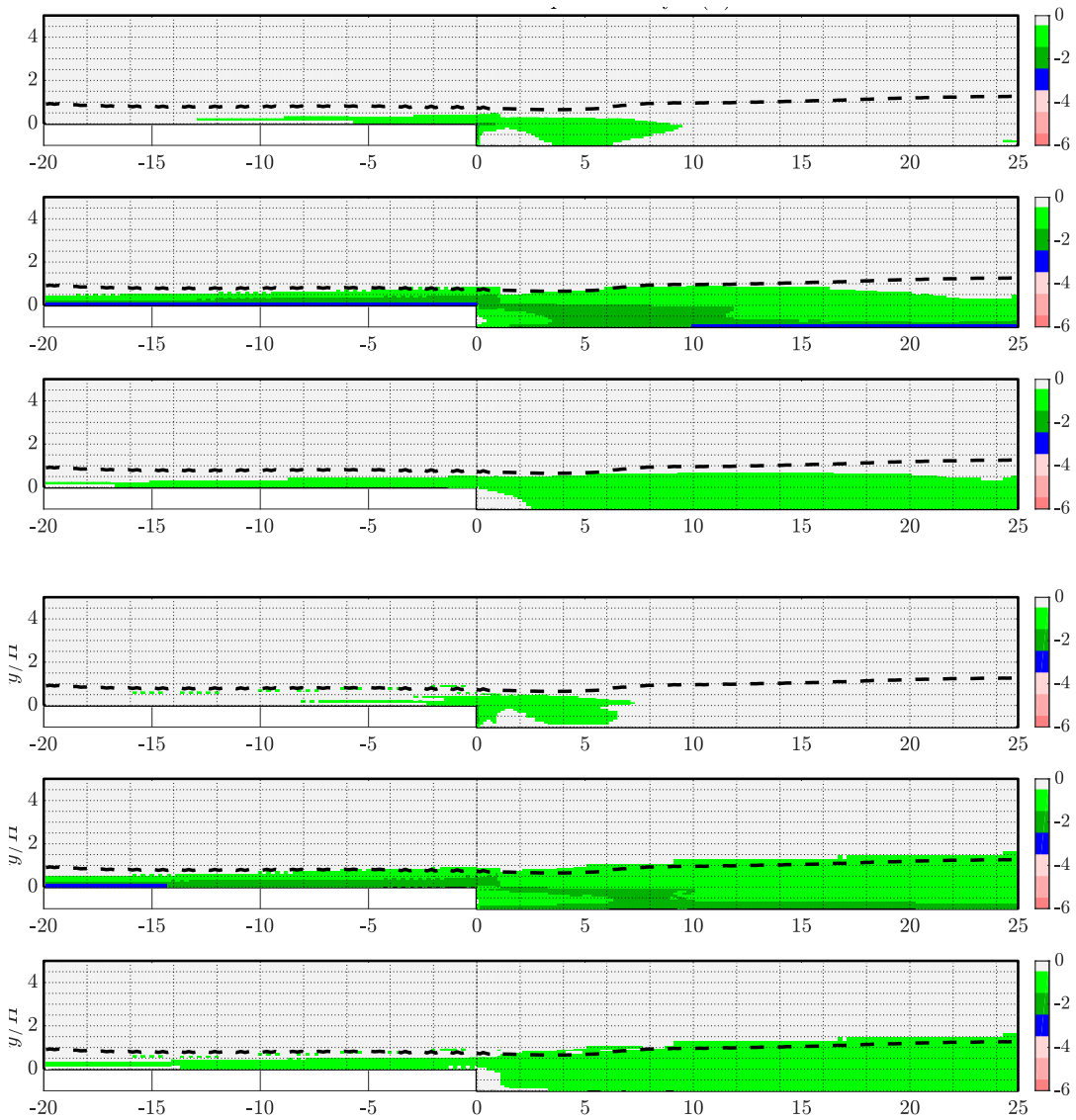

Figure 4.9: The grids OLD-2 (the top three) and NEW-2 (the bottom three) from Table 4.2 illustrated by their refinement levels in x (top plot, in each set), y (middle, in each set), and z (bottom, in each set). Refinement levels are computed based on a skeletal grid with $\Delta_0(\mathbf{x}, \mathbf{n}) = 0.2H$ for all $\mathbf{x}$ and $\mathbf{n}$. The light green, dark green and blue colors illustrate regions with one ($\overline{\Delta}_\mathbf{n}/H = 0.1$), two ($\overline{\Delta}_\mathbf{n}/H = 0.05$), and three ($\overline{\Delta}_\mathbf{n}/H = 0.025$) refinement levels, respectively. The white areas are associated with regions that are left untouched (i.e. $\overline{\Delta}_\mathbf{n}/H = 0.2$). The dashed black lines highlight the δ_{95} boundary layer thickness.

direction, even at the vicinity of the wall at the incoming and recovering boundary layers, while instead a larger portion of the domain is selected for refinement. The same general trend holds when comparing grids NEW-6 and OLD-6, where in the

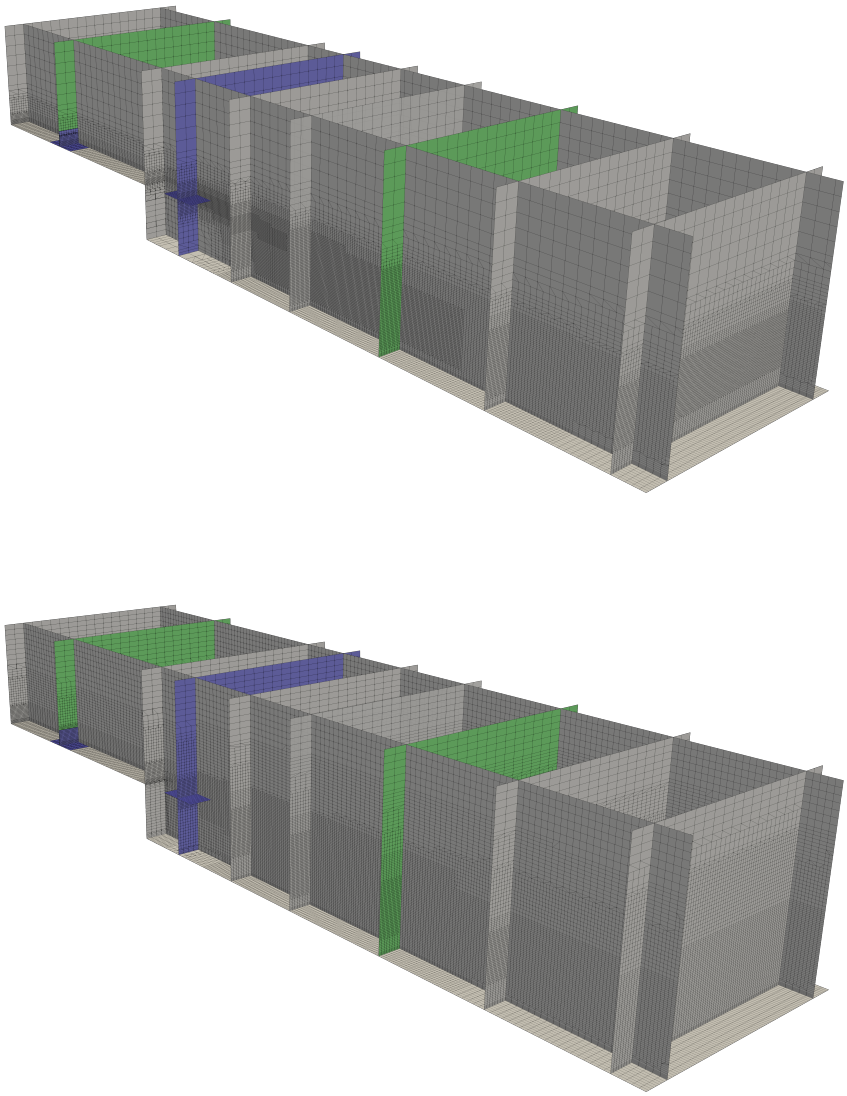

Figure 4.10: The generated grids OLD-6 (top) and NEW-6 (bottom). Intersections of the blue planes denote locations whose resolutions are reported in Table 4.2, while the green planes correspond to $x/H = -3$ and $x/H = 6$ whose velocity and Reynolds stress profiles are plotted and compared in Figs. 4.13 and 4.14. The grid is resulted from computation of the proposed error-indicator of Chapter 3 (Eqns. 3.2 and 3.3) and applying the heuristic grid selection criterion of Eqn. 3.7 (OLD-6, top) and the modified criteria of Eqns. 4.16 and 4.15 (NEW-6, bottom) with no user experience involved.

latter $\overline{\Delta}_y$ is only refined inside the δ_{95} boundary layer thickness, while in NEW-6 those refinement regions are extended far beyond the edge of the boundary layer.

Grid	N_{tot}	$(\overline{\Delta}_x^+, \overline{\Delta}_{y_w}^+/2, \overline{\Delta}_z^+)$	$(\overline{\Delta}_x, \overline{\Delta}_y, \overline{\Delta}_z)/\delta_{\text{shear}}$	$\overline{e}_{\text{QoI}}^{\text{DNS}}$ (%)
OLD-2	293k	$(21, 2.6, 21)$	$(0.17, 0.087, 0.17)$	11.0
NEW-2	297k	$(45, 5.7, 23)$	$(0.15, 0.093, 0.15)$	10.5
OLD-3	596k	$(22, 2.7, 11)$	$(0.076, 0.038, 0.076)$	7.7
NEW-3	599k	$(47, 2.9, 12)$	$(0.15, 0.074, 0.074)$	6.1
OLD-4	1.28M	$(23, 2.9, 5.7)$	$(0.076, 0.038, 0.038)$	5.8
NEW-4	1.35M	$(22, 2.8, 11)$	$(0.15, 0.036, 0.073)$	6.6
OLD-5	2.22M	$(23, 1.5, 5.9)$	$(0.048, 0.019, 0.038)$	4.3
NEW-5	2.17M	$(24, 1.5, 6.1)$	$(0.068, 0.034, 0.034)$	4.2
OLD-6	3.59M	$(25, 1.5, 6.2)$	$(0.034, 0.017, 0.034)$	3.9
NEW-6	3.70M	$(25, 1.6, 6.2)$	$(0.065, 0.033, 0.033)$	4.4

Table 4.2: LES of the flow over a backward-facing step. "OLD" grids are generated by the heuristic criterion of Eqn. 3.7, while the modified criteria (Eqns. 4.16 and 4.15) are used for generation of the "NEW" grids. N_{tot} is the actual number of cells in the computational domain. The grid-spacing in inner units is taken from $x/H = -3$ (upstream of the step). The grid-spacing in outer units is taken from the middle of the shear layer and is scaled by the approximate thickness of that shear layer δ_{shear}. See Fig. 4.10 for more details on the locations of resolution sampling. $\overline{e}_{\text{QoI}}^{\text{DNS}}$ and $\overline{e}_{\text{QoI}}^{\text{prev}}$ are defined in equation 3.12.

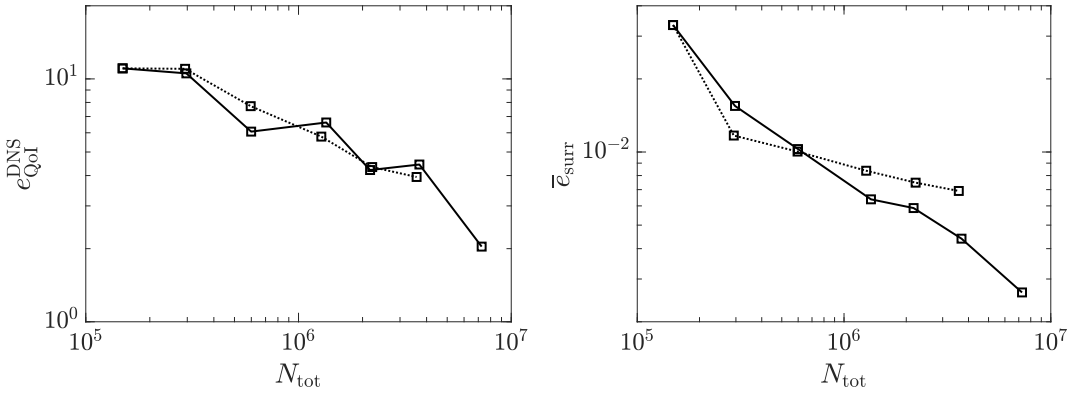

Figure 4.11: Convergence of $\overline{e}_{\text{QoI}}^{\text{DNS}}$ (left) and $\overline{e}_{\text{surr}}$ (right) with N_{tot} in the sequence of grids generated by $\overline{\mathcal{A}}(\mathbf{x}, \mathbf{n})$ for LES of the flow over a backward-facing step using the heuristic (dotted lines with square symbols) and modified (solid lines with square symbols) grid selection criteria. See Table 4.2 for more details on the grids. See Figs. 4.12, 4.13, 4.14, and 4.15 for convergence of the QoI profiles.

Same goes true for refinements inside the shear layer where NEW-6 has coarser cells

in general compared to OLD-6.

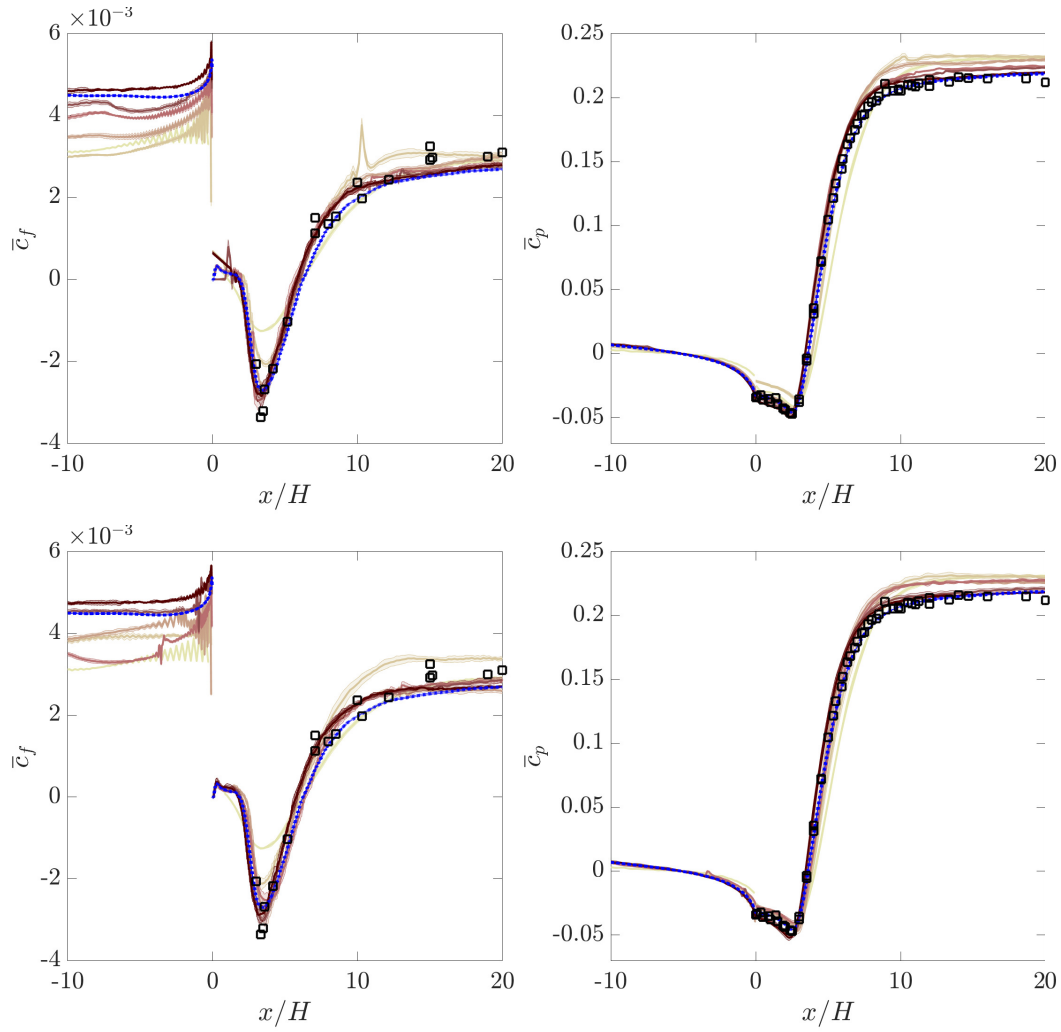

Figure 4.12: Convergence of friction coefficient $\overline{c}_f$ (left column) and pressure coefficient $\overline{c}_p$ (right column) for LES of flow over a backward-facing step, for the OLD (top row) and NEW (bottom row) grids in Table 4.2. Different grids are shown by the lightest color for OLD/NEW-1 to the darkest for OLD/NEW-6. Solid lines denote the sample means, while the shaded regions correspond to the approximate confidence intervals (computed locally). The dotted blue lines and their shaded regions denote our DNS results and their confidence intervals. Symbols correspond to the experimental data of Jovic & Driver [57, 58] with slightly different setup (error bars on the experimental data are not shown). Experimental measurements of $\overline{c}_f$ and $\overline{c}_p$ are not available upstream of the step.

The convergence of $\overline{e}_{\text{surr}}$ (defined in Eqn. 4.17) is faster for the sequence of grids generated by the modified grid selection criterion (Fig. 4.11), confirming the superiority of this criterion over the heuristic one; however, just like the channel

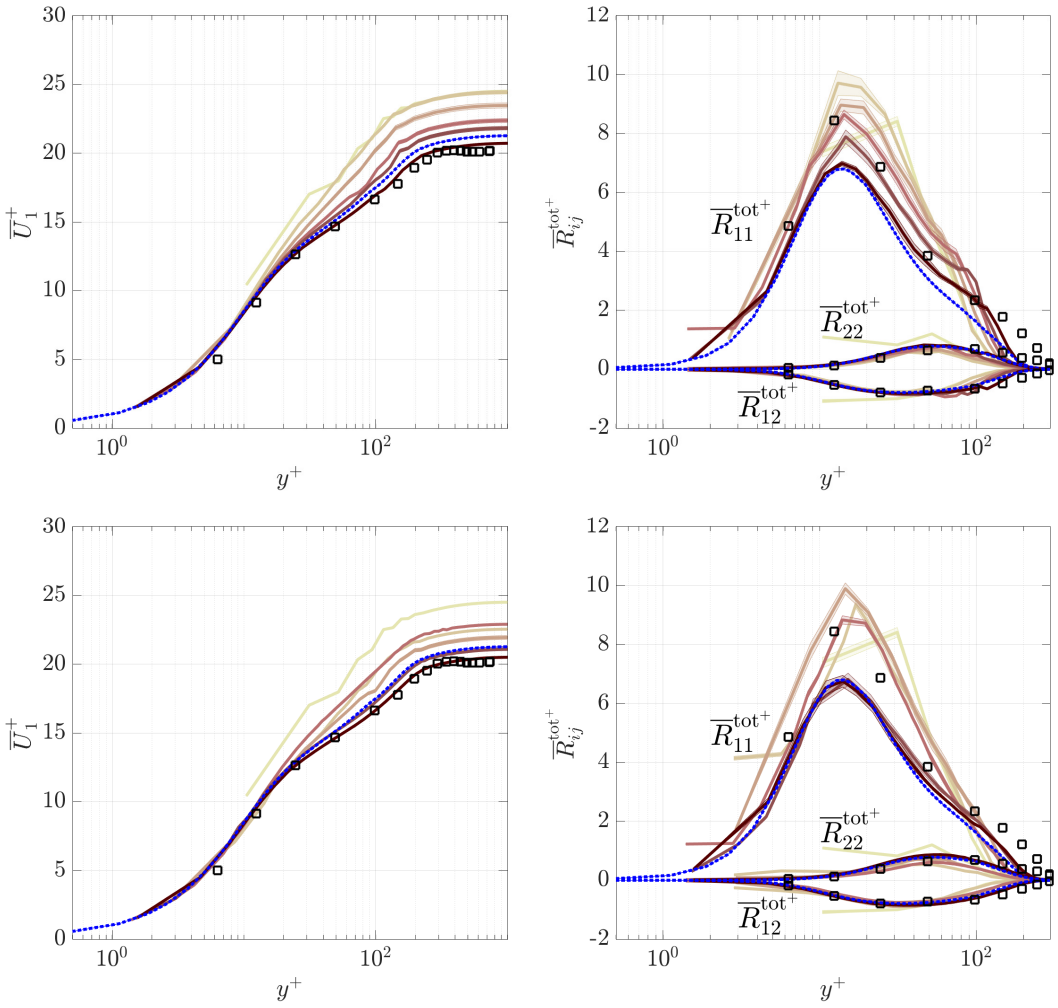

Figure 4.13: Convergence of the mean velocity and Reynolds stress profiles for the sequence of the OLD (top) and NEW (bottom) grids in Table 4.2 at the incoming boundary layer at $x/H = -3$. Grids in the sequence are shown by the lightest color for NEW/OLD-1 to the darkest for NEW/OLD-6. Solid lines denote the sample means, while the shaded regions correspond to the approximate confidence intervals (computed locally). The dotted blue lines and their shaded regions denote our DNS results and their confidence intervals. Symbols correspond to the experimental data of Jovic & Driver [57, 58] (error bars on the experimental data are not shown).

flow, the convergence of $\bar{e}_{\mathrm{QoI}}^{\mathrm{DNS}}$ does not seem to follow the same trend of improvement. The same can be observed in the convergence of the QoI profiles, where the modified criterion leads to improved results in some of the grids, while the heuristic criterion still produces more "optimal" grids in the others. We should note that this

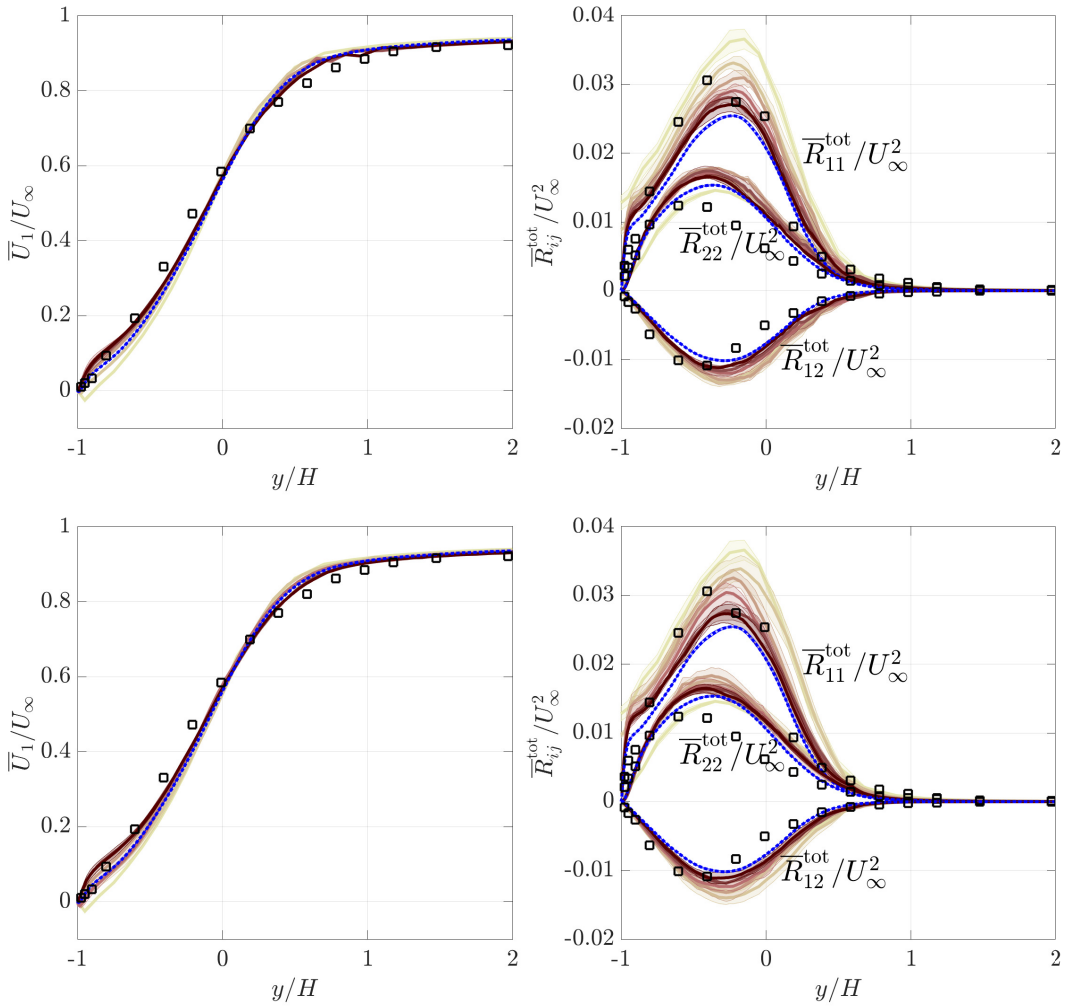

Figure 4.14: Convergence of the mean velocity and Reynolds stress profiles for the OLD (top) and NEW (bottom) grids of Table 4.2 at $x/H = 6$ near the reattachment point. See Fig. 4.13 for more details.

conclusion is based on a skeletal grid with $\Delta_0(\mathbf{x}, \mathbf{n}) = 0.2H$, with no coarsening of the grid beyond this skeletal resolution. This means that the very coarse cells in the free stream outside the boundary layer (see Fig. 4.3) are automatically prevented by this skeletal grid. As a result, the conclusion may have been completely different if the skeletal grid had a coarser Δ_0: it is quite unlikely that a grid with cells as coarse as what is depicted in Fig. 4.3 could lead to $\overline{e}_{\text{QoI}}^{\text{DNS}}$ less than 7%.

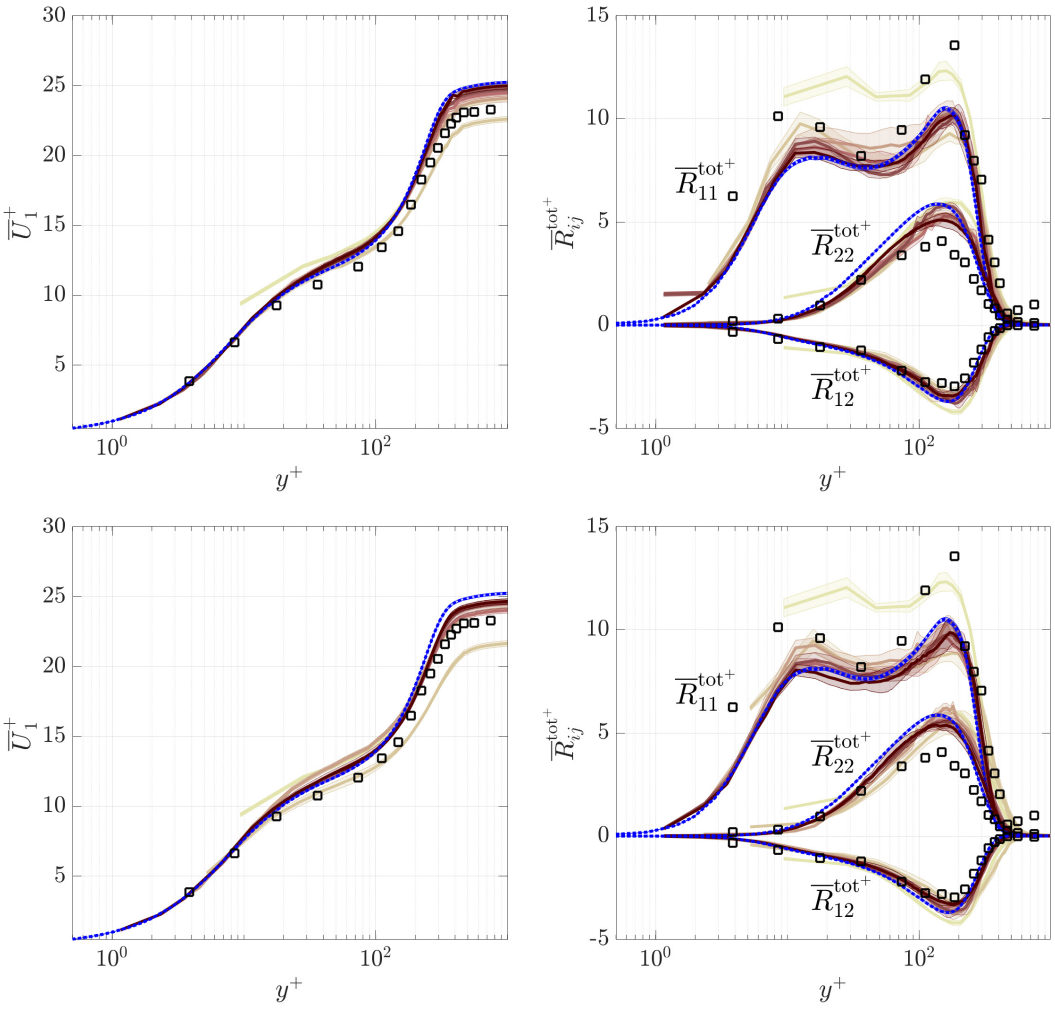

Figure 4.15: Convergence of the mean velocity and Reynolds stress profles for the OLD (top) and NEW (bottom) grids of Table 4.2 at $x/H = 15$ at the recovering boundary layer. See Fig. 4.13 for more details.

4.7 Concluding remarks

The purpose of this Chapter was to investigate the grid-selection criterion and its effect on the target grids. We showed that the correct criterion is to enforce an equidistribution of the cell-integrated error-indicator, and not the error-indicator itself. The modified approach leads to lower error in the QoIs (Fig. 4.1), and perhaps more importantly also leads to a less extreme spatial distribution of the grid-spacing

(Figs. 4.2 and 4.3). Specifically, it may alleviate the problems of excessively coarse cells in the far-field reported in some studies for feature-based grid-adaptation appraches (cf. [40, 73, 74]). The less extreme spatial variation of the target $\check{\Delta}_{\text{opt}}$ also naturally produces grids with less stretching and thus higher quality in terms of grid metrics.

Application of the same formulation to anisotropic grid selection required an estimation of the total local source of error $\check{e}^{\text{ref}}_{\text{local}}$ based on the directional structure of the anisotropic error-indicator $\check{\mathcal{A}}(\mathbf{x}, \mathbf{n})$. For the simple case of hexahedral cells, we assumed that $\check{e}^{\text{ref}}_{\text{local}}$ is proportional to the magnitude of the error-indicator $\check{\mathcal{A}}_{\text{tot}}$ (Eqn. 4.10), which then led to a criterion for the optimal aspect ratio of the grids (Eqn. 4.14) and one for their optimal spatial distribution (Eqn. 4.15).

The modified criteria were then tested on grid selection and adaptation of the turbulent channel flow and the flow over a backward-facing step. Contrary to our *a priori* conclusions, the final grids generated by the new criteria did not improve upon the QoI errors $\overline{e}^{\text{DNS}}_{\text{QoI}}$ in neither of the cases. The exact reason for this is not obvious at this point, but two of the more likely explanations are (i) the lack of adjoint fields in our formulation, and (ii) the lack of direct connection between the small-scale energy and the LES errors. In the next Chapter we introduce a new error-indicator that is more directly connected to the LES equations, and we show that this new error-indicator leads to lower $\overline{e}^{\text{DNS}}_{\text{QoI}}$ compared to the energy-based indicator $\overline{\mathcal{A}}(\mathbf{x}, \mathbf{n})$.

There are still several possibilities to improve the optimality criteria used to generate the grids. For compressible solvers with explicit time-stepping, it may

be important to include the number of time steps in the estimated computational cost. This would then effectively "penalize" very thin cells near boundaries. More generally, since it is well known that numerical errors are highly sensitive to the smoothness of the mesh, one should certainly include a penalization of too rapid filter-width transitions when solving the optimization problem. None of these issues seemed to be a problem for the LES grids of this Chapter, since $\overline{\mathcal{A}}(\mathbf{x}, \mathbf{n})$ automatically produced grids with smooth variations of the resolution and prevented very fine cells (for the modified criterion); however, this may not be necessarily the case for other error-indicators.

A major improvement would be to include the adjoint of the QoIs and thus make the adaptation "output-based". This has been the major advancement in steady-state grid-adaptation over the last few decades (cf. [9]). Inclusion of the adjoint would first require the problem of exponential divergence of the adjoint for chaotic problems to be solved (cf. [75]). The adjoint fields are not considered in this dissertation.

Chapter 5: An equation-based error-indicator based on the sensitivity of LES equation to the coarse-graining length scale

The framework discussed in Chapter 3 was a first attempt at anisotropic error-estimation and grid selection in LES, where both the error-indicator $\overline{\mathcal{A}}(\mathbf{x}, \mathbf{n})$ and the criterion used for grid selection based on it were entirely based on heuristic arguments. In Chapter 4 we tried to modify our grid-selection criterion based on mathematical reasoning; in this Chapter we define a new error-indicator that addresses some of the shortcomings of the old indicator $\overline{\mathcal{A}}(\mathbf{x}, \mathbf{n})$. These shortcomings were discussed in some detail in Section 3.6 and can be summarized here as:

- First and foremost, $\overline{\mathcal{A}}(\mathbf{x}, \mathbf{n})$ is a fully heuristic error-indicator that is based on an assumed connection between the small scale energies and all types of errors in LES. It is not necessarily true and there are many examples where the small-scale energy is completely irrelevant.
- $\overline{\mathcal{A}}(\mathbf{x}, \mathbf{n})$ has a generic functional form, independent of the LES formulation (implicitly filtered LES, explicitly filtered LES, ILES), the $\overline{\Delta}/\overline{h}$ ratio, and the LES model. This means that it (most probably) cannot find the most "optimal" distribution of the filter-width for that specific setup, formulation,

and model; even though the target grids may always be "close to the optimal".

- The wall-normal resolutions of the grids (especially in the channel flow, see Table 4.1) were slightly coarser than what is known as the "best-practice" in LES of wall-bounded flows. Note that the spanwise resolution was also slightly finer than the "optimal" when the heuristic selection criterion was used, but it was fixed for the modified criterion (see Table 4.1).

In this Chapter we define a new error-indicator that is derived more directly from the governing equation and thus requires less heuristics. The key assumption in the definition of this error-indicator becomes that the LES equations should be minimally sensitive to a change in the filter-width. This is a much weaker requirement than the arguments of Chapter 3 on the connection between the LES errors and the small-scale energy. Besides, the equation-based nature of the error-indicator allows for an explicit account of the the specific LES formulation, the $\overline{\Delta}/\overline{h}$ ratio, and the specific LES model in the error-indicator, and consequently, in the "target" grids.

This Chapter only focuses on statistically stationary problems for which we seek a stationary grid/filter-width (as is the general theme in this entire dissertation). In other words, the grid/filter-width is adjusted only between LES runs, and the adaptation step becomes solely a post-processing operation with no changes needed in the LES solver at all. We should also emphasize that the focus of this dissertation is entirely on the problem of *finding* $\Delta_{\text{opt}}(\mathbf{x}, \mathbf{n})$ and not at all the exact way of *creating* this new grid; we simply use currently available tools to generate these

grids without worrying about parallel performance, data structures, etc. Other factors like the grid quality, stretching factor, etc. have not been considered either. Consequently, the results presented in this Chapter could presumably be improved by imposing some constraints on the grid quality metrics or stretching factors, or by the use of more sophisticated and flexible grid-generation toolboxes capable of generating a closer grid to the target $\Delta_{\text{opt}}(\mathbf{x}, \mathbf{n})$.

The final definition of the error-indicator (and in part the reasoning leading to it) becomes closely related to the dynamic procedure [54,55], and in fact leads to an alternative explanation for why the dynamic procedure works; this is discussed briefly in Section 5.1.2.

5.1 Methodology

The developments in this Section are based on the implicitly filtered LES equation which is arguably the most popular formulation. For incompressible flows of the Newtonian fluids the governing equation is

$$\frac{\partial \overline{u}_i}{\partial t} + \frac{\partial \overline{u}_i \overline{u}_j}{\partial x_j} = -\frac{1}{\rho}\frac{\partial \overline{p}}{\partial x_i} + \nu \frac{\partial^2 \overline{u}_i}{\partial x_j \partial x_j} - \frac{\partial \tau_{ij}^{\text{mod}}(\overline{u}_k)}{\partial x_j}\,, \tag{5.1}$$

where $\overline{u}_i$ and $\overline{p}$ are the resolved velocity and pressure fields, ρ and ν are density and kinematic viscosity of the fluid (both assumed constant), and $\tau_{ij}^{\text{mod}}(\overline{u}_k)$ is the SGS stress tensor computed from the LES model.

Derivations of the error-indicator for some alternative forms of this equation are given in Section 5.6, including: (i) when the convective flux is written as $\overline{\overline{u}_i \overline{u}_j}$ (used when applying an explicit filter in the solver, known as the explicitly filtered

LES); (ii) when solving LES without an explicit subgrid model (implicit LES, or ILES); and (iii) for implicitly filtered LES of compressible flows.

5.1.1 The proposed error-indicator

The idea of this Section is to estimate how sensitive the LES equation (Eqn. 5.1) is to a change in the filter-width in any given direction and at any given location, and to use that to define our error-indicator. The estimate will be derived and computed using a low-pass test filter, which must be able to filter only in a single direction (i.e., filter modes with high wavenumber in that single direction) in order to infer anything about the directional structure of the errors (or sensitivity), and thus the anisotropy of the "optimal" filter-width. To make this work applicable to general geometries and grid topologies, we will use the same directional differential filter of Section 3.1.2, defined as

$$\widehat{\overline{\phi}}^{(\mathbf{n}_0)} \approx \left(I + \frac{\overline{\Delta}_{\mathbf{n}_0}^2}{4} \mathbf{n}_0^T \nabla \nabla^T \mathbf{n}_0 \right) \overline{\phi}\,, \tag{5.2}$$

where $\overline{\phi} = \overline{\phi}(\mathbf{x})$ is the original resolved LES field, $\widehat{\overline{\phi}}^{(\mathbf{n}_0)} = \widehat{\overline{\phi}}^{(\mathbf{n}_0)}(\mathbf{x})$ is the directionally low-pass test-filtered (in direction $\mathbf{n}_0$) field, $\overline{\Delta}_{\mathbf{n}_0} = \overline{\Delta}(\mathbf{x}, \mathbf{n}_0)$ is the filter-width in direction $\mathbf{n}_0$ (where $\mathbf{n}_0$ is the unit direction vector), and I is the identity tensor. For a structured grid with uniform grid-spacing and using second-order central differencing this filter simplifies to a unidirectional box filter of size $2\overline{\Delta}(\mathbf{x}, \mathbf{n}_0)$ applied using a trapezoidal rule. More details about this differential filter is given in Section 3.1.2 (also see [42, 76] for the definition of the filter kernel).

Applying the directional test-filter to Eqn. 5.1 yields (assuming that filtering

and differentiation commute) an evolution equation for the filtered instantaneous fields at the test-filter level as

$$\frac{\partial \widehat{\overline{u}}_i^{(\mathbf{n}_0)}}{\partial t} + \frac{\partial \widehat{\overline{u}_i \overline{u}_j}^{(\mathbf{n}_0)}}{\partial x_j} = -\frac{1}{\rho}\frac{\partial \widehat{\overline{p}}^{(\mathbf{n}_0)}}{\partial x_i} + \nu \frac{\partial^2 \widehat{\overline{u}}_i^{(\mathbf{n}_0)}}{\partial x_j \partial x_j} - \frac{\partial \widehat{\tau_{ij}^{\mathrm{mod}}(\overline{u}_k)}^{(\mathbf{n}_0)}}{\partial x_j}\,. \tag{5.3}$$

An alternative way to get an evolution equation for the solution at the test-filter level is to write the filtered Navier-Stokes equations (Eqn. 5.1) directly at the test-filter level instead

$$\frac{\partial \widehat{\overline{v}}_i^{(\mathbf{n}_0)}}{\partial t} + \frac{\partial \widehat{\overline{v}}_i^{(\mathbf{n}_0)} \widehat{\overline{v}}_j^{(\mathbf{n}_0)}}{\partial x_j} = -\frac{1}{\rho}\frac{\partial \widehat{\overline{q}}^{(\mathbf{n}_0)}}{\partial x_i} + \nu \frac{\partial^2 \widehat{\overline{v}}_i^{(\mathbf{n}_0)}}{\partial x_j \partial x_j} - \frac{\partial \tau_{ij}^{\mathrm{mod}}\left(\widehat{\overline{v}}_k^{(\mathbf{n}_0)}\right)}{\partial x_j}\,, \tag{5.4}$$

where $\widehat{\overline{v}}_i^{(\mathbf{n}_0)}$ and $\widehat{\overline{q}}^{(\mathbf{n}_0)}$ are the resolved velocity and pressure fields at the test-filter level $\widehat{\Delta}^{(\mathbf{n}_0)} = \widehat{\Delta}(\mathbf{x}, \mathbf{n})$.

Defining the difference between the two solutions as

$$\widehat{\overline{e}}_i^{(\mathbf{n}_0)} = \widehat{\overline{v}}_i^{(\mathbf{n}_0)} - \widehat{\overline{u}}_i^{(\mathbf{n}_0)} \quad , \quad \widehat{\overline{\Pi}}^{(\mathbf{n}_0)} = \widehat{\overline{q}}^{(\mathbf{n}_0)} - \widehat{\overline{p}}^{(\mathbf{n}_0)}\,,$$

and subtracting Eqn. 5.3 from Eqn. 5.4 then yields an evolution equation for the difference as

$$\underbrace{\frac{\partial \widehat{\overline{e}}_i^{(\mathbf{n}_0)}}{\partial t} + \widehat{\overline{u}}_j^{(\mathbf{n}_0)} \frac{\partial \widehat{\overline{e}}_i^{(\mathbf{n}_0)}}{\partial x_j}}_{T_1} \underbrace{- \nu \frac{\partial^2 \widehat{\overline{e}}_i^{(\mathbf{n}_0)}}{\partial x_j \partial x_j}}_{T_2} + \underbrace{\frac{\partial \widehat{\overline{e}}_i^{(\mathbf{n}_0)} \widehat{\overline{e}}_j^{(\mathbf{n}_0)}}{\partial x_j}}_{T_3} + \underbrace{\widehat{\overline{e}}_j^{(\mathbf{n}_0)} \frac{\partial \widehat{\overline{u}}_i^{(\mathbf{n}_0)}}{\partial x_j}}_{T_4} + \underbrace{\frac{1}{\rho}\frac{\partial \widehat{\overline{\Pi}}^{(\mathbf{n}_0)}}{\partial x_i}}_{T_5} = \widehat{\overline{\mathcal{F}}}_i^{(\mathbf{n}_0)}\,, \tag{5.5}$$

where

$$\widehat{\overline{\mathcal{F}}}_i^{(\mathbf{n}_0)}(\mathbf{x}) = \frac{\partial}{\partial x_j}\left(\widehat{\overline{u}_i \overline{u}_j}^{(\mathbf{n}_0)} - \widehat{\overline{u}}_i^{(\mathbf{n}_0)} \widehat{\overline{u}}_j^{(\mathbf{n}_0)}\right) + \frac{\partial}{\partial x_j}\left(\widehat{\tau_{ij}^{\mathrm{mod}}(\overline{u}_k)}^{(\mathbf{n}_0)} - \tau_{ij}^{\mathrm{mod}}\left(\widehat{\overline{v}}_k^{(\mathbf{n}_0)}\right)\right)\,. \tag{5.6}$$

The difference $\widehat{\overline{e}}_i^{(\mathbf{n}_0)}$ can be interpreted as a measure of sensitivity of the solution to the filter level used in its computation.

The procedure so far was very similar to the multi-resolution LES (MR-LES) method [3, 27], where the interpolation is here replaced by test-filtering. The MR-LES method takes the error $\widehat{\overline{e}}_i$ (where $\widehat{\cdot}$ is a regular test filter, not directional, corresponding to a grid that is finer/coarser in all directions) directly as a measure of the local source of error, and define its error-indicator based on the magnitude of $\widehat{\overline{e}}_i$ (this is the same error-indicator plotted in Fig. 2.3(g)). The primary goal of the MR-LES method is also to minimize the solution sensitivity $\widehat{\overline{e}}_i$, although, the assumption that $\widehat{\overline{e}}_i$ itself is a local measure of error (which is implied when $\widehat{\overline{e}}_i$ is used to define a local error-indicator) is probably not true in a general configuration. Here, we instead use the governing equation of this error (Eqn. 5.5) to infer the local source of its generation.

Terms T_1 and T_2 in the error evolution equation, Eqn. 5.5, describe convective and viscous transport, term T_3 is a nonlinear transport term, term T_4 becomes a production term in the governing equation of $\widehat{\overline{e}}_i^{(\mathbf{n}_0)}\widehat{\overline{e}}_j^{(\mathbf{n}_0)}$, and term T_5 is a pressure-like term that keeps $\widehat{\overline{e}}_i^{(\mathbf{n}_0)}$ divergence-free. The terms in Eqn. 5.5 are grouped such that all terms involving $\widehat{\overline{e}}_i^{(\mathbf{n}_0)}$ are on the left, while the terms not involving the error are grouped in $\widehat{\overline{\mathcal{F}}}_i^{(\mathbf{n}_0)}(\mathbf{x})$.

In a chaotic system (like LES), the difference $\widehat{\overline{e}}_i^{(\mathbf{n}_0)}$ will of course grow exponentially and thus rapidly becomes meaningless. Having said that, over short time scales, when starting from identical solutions ($\widehat{\overline{e}}_i^{(\mathbf{n}_0)} = 0$), Eqn. 5.5 shows that $\widehat{\overline{\mathcal{F}}}_i^{(\mathbf{n}_0)}(\mathbf{x})$ is the source of initial divergence between the two solutions (since, with $\widehat{\overline{e}}_i^{(\mathbf{n}_0)} = 0$, all terms of the left side of Eqn. 5.5 are zero). We can then hypothesize that the magnitude of $\widehat{\overline{\mathcal{F}}}_i^{(\mathbf{n}_0)}(\mathbf{x})$ remains a meaningful estimate of the error generation in an

LES, even beyond the short time horizon.

The proposed error-indicator is then defined as

$$\overline{\mathcal{G}}(\mathbf{x},\mathbf{n}) = \sqrt{\left\langle \widehat{\overline{\mathcal{F}}}_i^{(\mathbf{n})}(\mathbf{x})\, \widehat{\overline{\mathcal{F}}}_i^{(\mathbf{n})}(\mathbf{x}) \right\rangle}, \tag{5.7}$$

where $\langle\cdot\rangle$ denotes a suitable averaging operator, and $\bar{\cdot}$ signifies the filter-level on which the test-filtering is applied (i.e. $\overline{\Delta}$). In this Chapter (and more generally this dissertation) we are interested in finding the optimal static grids for statistically stationary problems, and hence averaging is performed over time and any homogeneous spatial directions. For more general settings the averaging operator could be adjusted accordingly. For example, in flows with strong unsteady effects at a slow time-scale (e.g., vortex shedding) one could use a low-pass time filter, and for temporally periodic flows (e.g., pulsating flows) one could use a phase average.

The first term (the Leonard-like stress) in $\widehat{\overline{\mathcal{F}}}_i^{(\mathbf{n})}(\mathbf{x})$ can be directly computed from the LES solution $\overline{u}_i$, and $\tau_{ij}^{\mathrm{mod}}(\overline{u}_k)$ is also known from the LES. On the other hand, the subgrid tensor in the imagined evolution equation at the test filter level is defined based on the imagined velocity field $\widehat{\overline{v}}_i^{(\mathbf{n})}$. One option would be to actually run an additional LES solving Eqn. 5.4 but in a synchronized way (similar to the MR-LES methods of Legrand *et al.* [27]). The alternative, which is applied here, is to use the test-filtered velocity field from the original LES solution to expand the SGS tensor as well, i.e.,

$$\tau_{ij}^{\mathrm{mod}}\left(\widehat{\overline{v}}_k^{(\mathbf{n})}\right) = \tau_{ij}^{\mathrm{mod}}\left(\widehat{\overline{u}}_k^{(\mathbf{n})}\right) + \mathcal{T}_{ij}\left(\widehat{\overline{u}}_k^{(\mathbf{n})}, \widehat{\overline{e}}_l^{(\mathbf{n})}\right),$$

where $\mathcal{T}_{ij}$ must vanish when $\widehat{\overline{e}}_l^{(\mathbf{n})} = 0$ for consistent SGS models. As a result, $T_6 = \partial\mathcal{T}_{ij}/\partial x_j$ can be moved to the left-hand side of Eqn. 5.5 where it becomes

excluded from the imagined error source (based on the same reasoning used before). Note that expanding $\tau_{ij}^{\text{mod}}(\widehat{\overline{v}}_k^{(\mathbf{n})})$ using the test-filtered field $\widehat{\overline{u}}_k^{(\mathbf{n})}$ is not only simpler (and cheaper), but also more consistent with our current formulation.

5.1.2 Connection to the dynamic procedure

The dynamic procedure [54,55] is a way to compute model constant(s) through test-filtering, which has received a lot of attention in the LES community. It finds the model coefficient that minimizes

$$e_{\text{dyn}} = \left\langle (\widehat{\mathcal{L}}_{ij} + \widehat{\mathcal{M}}_{ij})(\widehat{\mathcal{L}}_{ij} + \widehat{\mathcal{M}}_{ij}) \right\rangle ,$$

where $\widehat{\cdot}$ is a regular test-filter (i.e. not directional), and

$$\widehat{\mathcal{L}}_{ij} = \widehat{\overline{u}_i \overline{u}_j} - \widehat{\overline{u}}_i \widehat{\overline{u}}_j \quad , \quad \widehat{\mathcal{M}}_{ij} = \widehat{\tau_{ij}^{\text{mod}}(\overline{u}_k)} - \tau_{ij}^{\text{mod}}\left(\widehat{\overline{u}}_k\right) .$$

There have been multiple explanations for how/why the dynamic procedure works. The original explanation appealed to scale similarity in the inertial range (cf. [77]), but as pointed out by others (cf. [21,29]) this fails to explain why the dynamic procedure works during transition to turbulence or in the near-wall region of turbulent boundary layers (arguably its greatest success). The lack of any scale similarity at the test-filter level in those scenarios (the filter is close to the dissipative range in wall-resolved LES) therefore makes the original explanation unlikely. Jimenez & Moser [29] suggested that the explanation has to do (among other things) with dissipation, that the dynamic procedure makes the dissipation by the LES model equal to the production of the Leonard stresses. An alternative explanation was

put forth by Pope [21], who showed that the dynamic procedure can be derived by requiring that the total Reynolds stress (i.e., resolved plus modeled) should be minimally sensitive to the filtering level, i.e., that the model coefficient should be chosen to minimize (in magnitude)

$$\left(\widehat{\overline{u}_i\overline{u}_j} + \tau_{ij}^{\widehat{\text{mod}}(\overline{u}_k)}\right) - \left(\widehat{\overline{u}}_i\widehat{\overline{u}}_j + \tau_{ij}^{\text{mod}}(\widehat{\overline{u}}_k)\right) ,$$

which is equal to minimizing $\widehat{\overline{\mathcal{L}}}_{ij} + \widehat{\overline{\mathcal{M}}}_{ij}$. Although not directly stated in [21], the choice of the total Reynolds stress as the critical quantity presumably comes from the importance of stresses in momentum transport.

The present derivation of the error-indicator $\overline{\mathcal{G}}(\mathbf{x}, \mathbf{n})$ implies a somewhat similar but slightly different explanation for why the dynamic procedure works, without any specific assumption about turbulent properties like scale-similarity or about the importance of Reynolds stresses, energy or dissipation in the accuracy of the LES solution.

The residual force $\widehat{\overline{\mathcal{F}}}_i$ of Eqn. 5.6 is simply the divergence of the total tensor subject to minimization in the dynamic procedure, i.e.,

$$\widehat{\overline{\mathcal{F}}}_i = \frac{\partial}{\partial x_j}\left(\widehat{\overline{\mathcal{L}}}_{ij} + \widehat{\overline{\mathcal{M}}}_{ij}\right) .$$

Pope arrived at the minimization of this tensor by requiring that the predicted total stress from an LES should be insensitive to the filter level; here, we instead arrive at the same thing by requiring that the assumed source term in the evolution equation for the difference between the two solutions at the same filter levels be as small as possible (leading to filter-insensitivity of the solution itself).

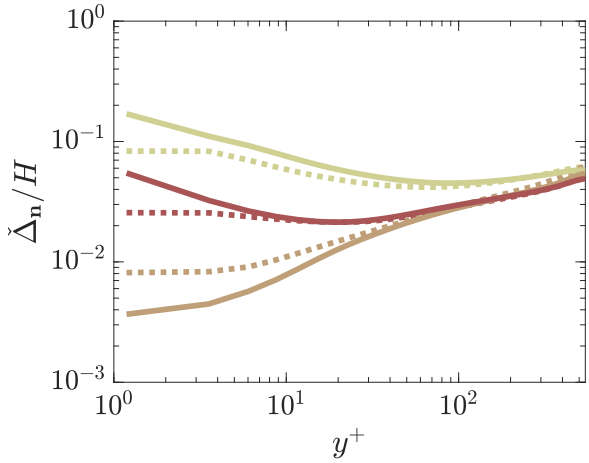

Figure 5.1: A comparison of the target grids between the tensorial (solid lines) and vectorial (dotted lines) definitions of $\overline{\mathcal{G}}(\mathbf{x}, \mathbf{n})$. The streamwise, wall-normal, and spanwise resolutions are shown by the brightest to darkest colors. Note that the tensorial definition leads to excessively fine cells at the wall and is discouraged. Both grids have the same number of cells ($1.10M$).

We should also note that the present work clearly suggests that the force $\widehat{\overline{\mathcal{F}}}_i$ rather than the tensor $\widehat{\overline{\mathcal{L}}}_{ij} + \widehat{\overline{\mathcal{M}}}_{ij}$ should be minimized in the dynamic procedure. This has actually been tested before in the literature, in the work of Morinishi & Vasyliev [78]. The downside is that this leads to a nonlinear second-order PDE for the model coefficient, which is presumably why this version of the dynamic procedure has not received the attention and popularity it arguably deserved.

Interestingly, our tests on the channel flow suggest that using the full tensor to drive filter-width adaptation leads to excessively fine cells in the wall-normal direction in the vicinity of the walls (Fig 5.1) and is therefore strongly discouraged.

5.1.3 Finding the optimal filter-width

The error-indicator estimates the introduction of error into the evolution equation due to insufficient resolution, but does not automatically determine how much

the resolution needs to be changed for the error to go down to a certain level. This link is provided by means of a model that estimates how much the error-indicator would change by a certain change in the filter-width. In this Chapter, we adopt the same simplistic model of Section 3.1.4, as

$$\check{\mathcal{G}}(\mathbf{x},\mathbf{n}) \approx \overline{\mathcal{G}}(\mathbf{x},\mathbf{n})\check{\Delta}^{\alpha}(\mathbf{x},\mathbf{n})\,, \tag{5.8}$$

where $\check{\mathcal{G}}(\mathbf{x},\mathbf{n})$ is the predicted value of the error-indicator on the filter-level $\check{\Delta}(\mathbf{x},\mathbf{n})$ and the "error source density" $\overline{\mathcal{G}}(\mathbf{x},\mathbf{n})$ is computed from the existing LES solution as

$$\overline{\mathcal{G}}(\mathbf{x},\mathbf{n}) = \frac{\overline{\mathcal{G}}(\mathbf{x},\mathbf{n})}{\overline{\Delta}^{\alpha}(\mathbf{x},\mathbf{n})}\,.$$

The exponent $\alpha = \alpha(\mathbf{x},\mathbf{n})$ should be different in different flow regimes (free-shear turbulence, near-wall turbulence, etc.), in different directions, and for different LES models (e.g. for an exact LES model $\alpha \equiv 0$), but is simply taken as $\alpha = 2$ in the present study without any attempt at finding the best (case-specific) value. This is justified by our discussion in Section 4.4 that (i) the choice of α does not affect the "optimal" grid, but only the way the final grid is approached, and (ii) due to the error in the LES solution on intermediate grids it is usually more appealing to use higher values of α to increase robustness.

If we assume that the local error source $\check{e}^{\mathrm{ref}}_{\mathrm{local}}(\mathbf{x})$ is proportional to the magnitude of $\check{\mathcal{G}}(\mathbf{x})$ the error to be minimized (for the special case of a grid with only hexahedral cells) is

$$\check{e}^{\mathrm{ref}}_{\mathrm{local}}(\mathbf{x}) \propto \check{\mathcal{G}}_{\mathrm{tot}}(\mathbf{x}) = \sqrt{\check{\mathcal{G}}^2(\mathbf{x},\mathbf{n}_1) + \check{\mathcal{G}}^2(\mathbf{x},\mathbf{n}_2) + \check{\mathcal{G}}^2(\mathbf{x},\mathbf{n}_3)}\,. \tag{5.9}$$

This approximation of $\check{e}^{\text{ref}}_{\text{local}}(\mathbf{x})$ is identical to Eqn. 4.10 with $\check{\mathcal{A}}(\mathbf{x}, \mathbf{n}_i)$ being replaced by $\check{\mathcal{G}}(\mathbf{x}, \mathbf{n}_i)$, which results in the equidistribution of the error-indicator in different directions (assuming the same $\alpha_{\mathbf{n}}$ in all directions),

$$\check{\mathcal{G}}_{\text{opt}}(\mathbf{x}, \mathbf{n}_i) = \overline{g}(\mathbf{x}, \mathbf{n}_i)\check{\Delta}^{\alpha}_{\text{opt}}(\mathbf{x}, \mathbf{n}_i) = \overline{g}_{\text{vol}}(\mathbf{x})\check{\Delta}^{\alpha}_{\text{vol,opt}}(\mathbf{x}) \ , \quad i = 1, 2, 3 \, , \tag{5.10}$$

where

$$\overline{g}_{\text{vol}} = \left(\overline{g}(\mathbf{x}, \mathbf{n}_1)\overline{g}(\mathbf{x}, \mathbf{n}_2)\overline{g}(\mathbf{x}, \mathbf{n}_3)\right)^{1/3}$$

$$\check{\Delta}_{\text{vol,opt}} = \left(\check{\Delta}_{\text{opt}}(\mathbf{x}, \mathbf{n}_1)\check{\Delta}_{\text{opt}}(\mathbf{x}, \mathbf{n}_2)\check{\Delta}_{\text{opt}}(\mathbf{x}, \mathbf{n}_3)\right)^{1/3} \, .$$

This implies that the predicted optimal cell aspect ratio is

$$\frac{\check{\Delta}_{\text{opt}}(\mathbf{x}, \mathbf{n}_j)}{\check{\Delta}_{\text{opt}}(\mathbf{x}, \mathbf{n}_1)} = \left(\frac{\overline{g}(\mathbf{x}, \mathbf{n}_1)}{\overline{g}(\mathbf{x}, \mathbf{n}_j)}\right)^{1/\alpha} \ , \ j = 2, 3 \, .$$

Examples of the predicted optimal cell aspect ratios for $\alpha = 1$ and $\alpha = 2$ are given in Fig. 5.2 for a turbulent channel flow and in the recirculation region of the flow over a backward-facing step.

The optimal filter-width $\check{\Delta}_{\text{vol,opt}}(\mathbf{x})$ can be found as,

$$\overline{g}_{\text{vol}}(\mathbf{x})\check{\Delta}^{\alpha+3}_{\text{vol,opt}}(\mathbf{x}) = \Lambda = \text{const.} \, , \tag{5.11}$$

which is then used to find the optimal direction filter-width $\check{\Delta}_{\text{opt}}(\mathbf{x}, \mathbf{n}_i)$ as

$$\check{\Delta}_{\text{opt}}(\mathbf{x}, \mathbf{n}_i) = \left(\frac{\overline{g}_{\text{vol}}(\mathbf{x})}{\overline{g}(\mathbf{x}, \mathbf{n}_i)}\right)^{1/\alpha} \check{\Delta}_{\text{vol,opt}}(\mathbf{x}) \, . \tag{5.12}$$

Equations 5.11 and 5.12 define our optimal filter-width $\check{\Delta}_{\text{opt}}(\mathbf{x}, \mathbf{n})$ on any given grid with a specified N_{tot} number of cells.

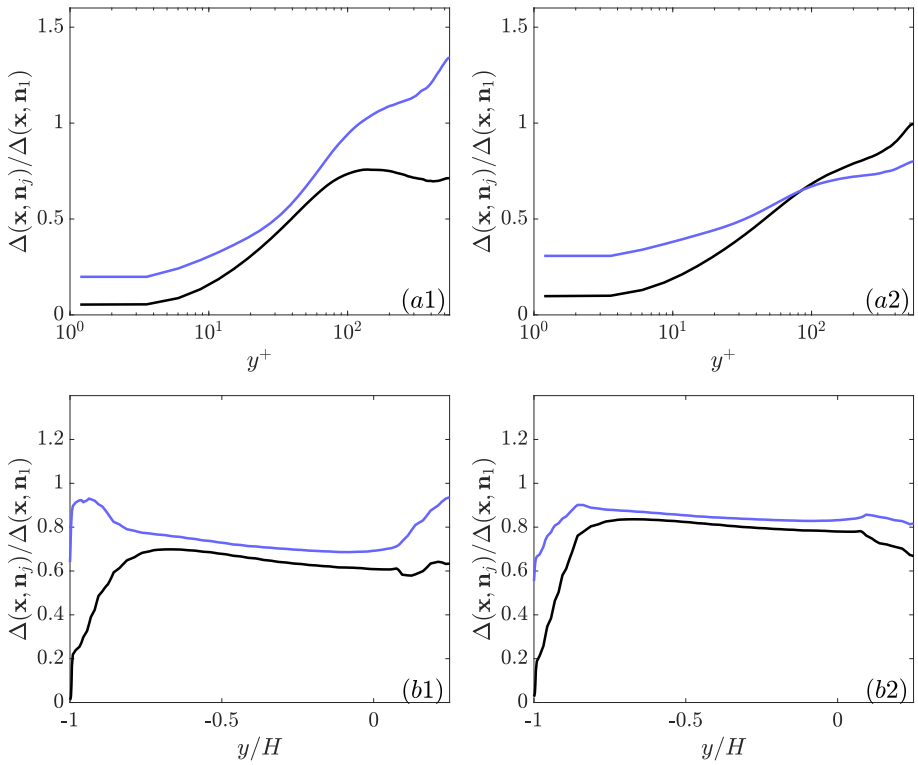

Figure 5.2: Examples of the predicted optimal cell aspect ratios $\check{\Delta}(\mathbf{x},\mathbf{n}_2)/\check{\Delta}(\mathbf{x},\mathbf{n}_1)$ (black lines) and $\check{\Delta}(\mathbf{x},\mathbf{n}_3)/\check{\Delta}(\mathbf{x},\mathbf{n}_1)$ (blue lines) for: $(a1)$ turbulent channel flow at $Re_\tau \approx 545$, for $\alpha = 1$, $(a2)$ same flow, $\alpha = 2$, $(b1)$ in the recirculation region of the flow over a backward-facing step at $x/H = 4$, for $\alpha = 1$, and $(b2)$ same flow and region, $\alpha = 2$. Note that $\alpha = 1$ leads to more extreme aspect ratios of the cells, leading to possibly low-quality computational cells, and is thus less robust.

5.1.4 The stopping criterion

Assuming that we have M quantities of interest Q_m in the simulation allows for the total error in these QoIs to be defined as

$$\overline{e}^{\text{ref}}_{\text{QoI}} = \sum_{m=1}^{M} w_m \delta\overline{Q}^{\text{ref}}_m \,, \tag{5.13}$$

where $\delta\overline{Q}^{\text{ref}}_m$ is the change in $\overline{Q}_m$ (computed on grid $\overline{\Delta}$) compared to a reference solution and w_m is an appropriate weight with $\sum w_m = 1$. In this Section we report the error in the QoIs by comparison to a DNS solution, labeled $\overline{e}^{\text{DNS}}_{\text{QoI}}$, and to the

previous grid that was used to generate the grid $\overline{\Delta}$, labeled $\overline{e}^{\text{prev}}_{\text{QoI}}$. The first grid that satisfies the criterion on $\overline{e}^{\text{DNS}}_{\text{QoI}}$ is taken as the "optimal" grid.

5.2 Assessment on turbulent channel flow at $Re_\tau \approx 545$

We start our assessments by the turbulent channel flow, which is *the* specific flowfield with which the LES community has the most experience, and the response of the LES solution to the insufficient resolution in different directions and the optimal resolutions are rather well-known.

In order to test the robustness with severely underresolved solutions, all simulations are started from exceedingly coarse grids that are essentially ignorant of the flow physics. In the same spirit, we push the resolution of the final grids to the DNS limit, to make sure that the method is still robust when the LES model becomes effectively inactive. The idea is that, no matter how coarse or fine the grid might be, a robust method should always drive the grid towards a distribution that leads to lower errors in the solution.

To further test the robustness of the method, we consider three different approaches: (i) LES with a mixture of modeling and numerical errors; (ii) LES where the modeling errors are dominant; and (iii) DNS, which is purely affected by numerical errors.

5.2.1 Code and problem specification

The code used for this problem is the *Hybrid* code (used is Sections 3.2 and 4.5), which solves the compressible Navier-Stokes equations for a calorically perfect gas on structured Cartesian grids using sixth-order accurate central differencing schemes with a split form of the convective term. Time-integration is handled by classic fourth-order Runge-Kutta. The code solves the implicitly-filtered LES equations with an explicit eddy viscosity model.

The bulk Reynolds number $Re_b = \rho_b U_b H/\mu_w$ is 10,000, which is identical to the setup in Section 4.5 and leads to a friction Reynolds number of about $Re_\tau \approx 545$. The bulk Mach number is 0.2. The simulations are integrated for a time of $200H/U_b$ (around $11H/u_\tau$) before collecting statistics over a period of $600H/U_b$ (slightly more than $32H/u_\tau$), by post-processing 400 snapshots that are $1.5H/U_b$ (close to $0.08H/u_\tau$) apart from each other. The convergence error is found to be sufficiently small Similar to the error-indicator of Chapter 3, this long integration time is primarily required for convergence of the mean profiles. A careful study of the statistical convergence of the error-indicator and its predicted grids is given in Chapter 6.

Since the code uses structured grids, the grid-spacing in the wall-parallel directions is taken as the smallest predicted value along y. The wall-normal resolution, on the other hand, is directly matched to the target values, by giving the code a list of y coordinates for the grid points across the channel.

Quantities of interest are taken to be the streamwise mean velocity and the four

non-zero Reynolds stresses. The error in the QoIs $\delta\overline{Q}_m$ are defined by Eqn. 3.9, where the resolved Reynolds stress $\overline{R}_{ij}$ is replaced by the total $\overline{R}_{ij}^{\text{tot}} = \langle \overline{u}_i' \overline{u}_j' \rangle + \langle \tau_{ij}^{\text{mod}}(\overline{u}_k) \rangle$. The convergence criterion is computed from Eqn. 3.10, repeated here, as

$$\overline{e}_{\text{QoI}}^{\text{ref}} = \frac{1}{5} \sum_{m=1}^{5} \delta \overline{Q}_m^{\text{ref}} \, .$$

5.2.2 LES with a mixture of modeling and numerical errors

We first use the dynamic Smagorinsky model [54, 55] with filtering and averaging in the wall-parallel directions to compute τ_{ij}^{mod}. The use of implicitly filtered LES equations, combined with the use of numerics with low numerical dissipation, produces solutions that are contaminated by both modeling and numerical errors of about similar magnitudes (cf. [4, 56]).

This first grid has a uniform resolution of $(\overline{\Delta}_x, \overline{\Delta}_y, \overline{\Delta}_z)/H = (0.20, 0.10, 0.20)$, corresponding to $(\overline{\Delta}_x^+, \overline{\Delta}_{y_w}^+/2, \overline{\Delta}_z^+) \approx (110, 28, 110)$ if one uses the fully converged friction velocity. Note that $\overline{\Delta}_{y_w}^+$ is the wall-normal filter width at the wall.

After performing an LES on this grid, we need to compute the error indicator which requires the computation of the eddy viscosity at the test-filter level. Assuming that the model coefficient is the same at the grid- and test-filter levels, this can be computed approximately as

$$\widehat{\overline{\nu}}_{\text{sgs}}^{(\mathbf{n}_0)} \approx \left[\frac{\widehat{\overline{\Delta}}^{(\mathbf{n}_0)}}{\overline{\Delta}} \right]^2 \frac{\left| \widehat{\overline{S}}^{(\mathbf{n}_0)} \right|}{|\overline{S}|} \nu_{\text{sgs}} \, , \tag{5.14}$$

where ν_{sgs} is the eddy viscosity in the underlying LES. The effect of this approximation is minor, with a full assessment shown in Section 5.5. We assume $\widehat{\overline{\Delta}}^{(\mathbf{n}_0)}/\overline{\Delta} \approx \sqrt[3]{2}$

for all 3 directions, since the test-filter of Eqn. 5.2 is wider by a factor of two in only one direction. This assumes that the characteristic filter-width is taken as the cube-root of the cell volume, which is actually not explicitly enforced in the dynamic model since the filter-width definition can be absorbed into the model constant in the dynamic procedure.

An step-by-step illustration of the adaptation process is given in Fig. 5.3, including the shape of the first computational cell next to the wall, the mean streamwise velocity, the total streamwise Reynolds stress, and the three components of the error-indicator $\overline{\mathcal{G}}(\mathbf{x}, \mathbf{n}_i)$ along with $\overline{\mathcal{G}}_{\text{tot}}(\mathbf{x})$.

In the first grid, the largest error-indicator is for the wall-normal direction in the vicinity of the wall (as expected for this coarse uniform grid). The next grid (DSM-2) is then generated by enforcing the optimality criteria of Eqns. 5.11 and 5.12. Note that due to the structured nature of the computational grid we have to take the minimum of the target streamwise and spanwise resolutions across the channel in order to generate each of the grids. The constant Λ in Eqn. 5.11 is adjusted (in an iterative process) such that the number of grid points in the next grid DSM-2 increases by a factor of 5.

The key metrics for all grids are reported in Table 5.1.

The grid DSM-2 has a grid-spacing of $(\overline{\Delta}_x^+, \overline{\Delta}_{y_w}^+/2, \overline{\Delta}_z^+) = (77, 5.6, 55)$. The solution on this grid is actually not bad, but of course not converged. The error-indicator computed from the DSM-2 solution again shows the largest error coming from the wall-normal resolution near the wall, followed by the spanwise resolution throughout much of the buffer layer. The resulting grid DSM-3 produces a solution

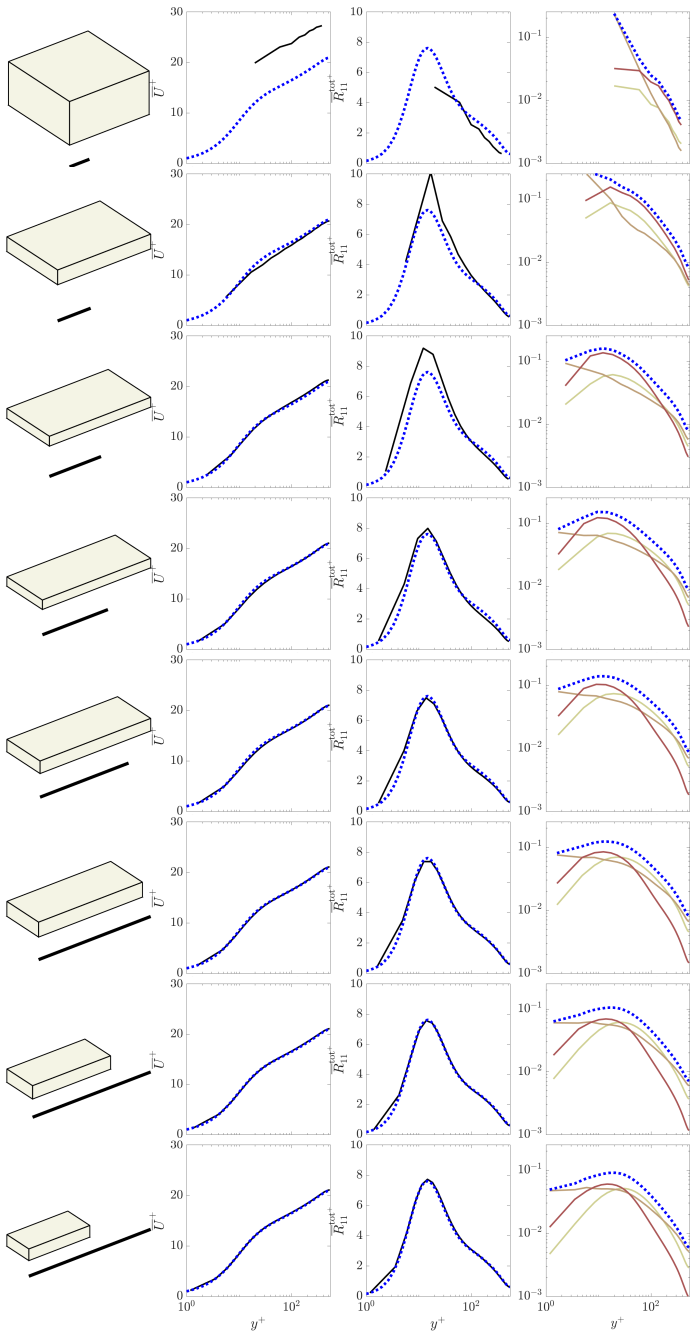

Figure 5.3: Sequence of grids generated by $\overline{\mathcal{G}}(\mathbf{x}, \mathbf{n})$ (Eqns. 5.6 and 5.7) for LES of the channel flow at $Re_\tau \approx 545$. The rows show the progression of grids from DSM-1 (top row) to DSM-8 (bottom row). Key quantities are listed in Table 5.1. The left column shows the shape of a wall-adjacent cell, while the right column shows the streamwise, wall-normal, and spanwise error-indicators by the brightest to the darkest colors. The dotted lines show $\overline{\mathcal{G}}_{\text{tot}}(y^+)$ in the right column and the reference DNS solution of del Alamo and Jimenez [18] in the middle columns.

Grid	N_{tot}	N_y	$(\overline{\Delta}_x^+, \overline{\Delta}_{y_w}^+/2, \overline{\Delta}_z^+)$	$(\overline{\Delta}_x, \overline{\Delta}_{y_c}, \overline{\Delta}_z)/H$	Re_τ	$\overline{e}_{\text{QoI}}^{\text{prev}}$ (%)	$\overline{e}_{\text{QoI}}^{\text{DNS}}$ (%)
DSM-1	$15k$	20	$(80, 20, 80)$	$(0.20, 0.10, 0.20)$	398	–	32
DSM-2	$74k$	34	$(77, 5.6, 55)$	$(0.14, 0.099, 0.10)$	553	27	11
DSM-3	$251k$	44	$(53, 2.3, 29)$	$(0.098, 0.091, 0.054)$	536	8.0	7.3
DSM-4	$514k$	50	$(45, 1.7, 19)$	$(0.082, 0.080, 0.035)$	544	4.2	3.3
DSM-5	$1.18M$	60	$(34, 1.4, 13)$	$(0.063, 0.065, 0.024)$	544	2.1	1.8
DSM-6	$2.53M$	72	$(25, 1.6, 10)$	$(0.046, 0.052, 0.018)$	542	1.0	1.1
DSM-7	$5.80M$	90	$(18, 1.4, 7.6)$	$(0.033, 0.041, 0.014)$	540	0.6	1.1
DSM-8	$11.1M$	108	$(14, 1.2, 6.3)$	$(0.025, 0.033, 0.012)$	541	0.6	0.9

Table 5.1: Sequence of grids generated for LES of channel flow at $Re_\tau \approx 545$ using the dynamic Smagorinsky model. N_{tot} is the total number of grid points, while N_y denotes the number of points across the channel. $\overline{\Delta}_{\mathbf{n}} = \overline{\Delta}(\mathbf{x}, \mathbf{n})$ is both the filter-width and the grid-resolution. Friction resolutions $\overline{\Delta}_{\mathbf{n}}^+$ are computed based on grid-specific values. $\overline{\Delta}_{y_c}$ is the wall-normal filter-width at the center of the channel, while $\overline{\Delta}_{y_w}$ is its value at the wall. $\overline{e}_{\text{QoI}}^{\text{DNS}}$ and $\overline{e}_{\text{QoI}}^{\text{prev}}$ are defined by Eqns. 3.9 (using the total Reynolds stress $\overline{R}_{ij}^{\text{tot}}$ instead) and 3.10.

where the streamwise Reynolds stress is close to the DNS and where the error-indicator values in the different directions are closer to being balanced, suggesting that the algorithm has started to find a nearly "optimal" state.

The adaptation process is continued until DSM-8. After the first two adaptations, the target number of cells is doubled each time. The solution is effectively converged on grid DSM-4 or DSM-5 depending on the desired accuracy. The grid-spacings on grids DSM-4 and up are quite close to what is considered "best practice" in LES and DNS for channel flows, with $(\overline{\Delta}_x^+, \overline{\Delta}_{y_w}^+/2, \overline{\Delta}_z^+)$ of $(45, 1.7, 19)$ on DSM-4 and $(14, 1.2, 6.3)$ on DSM-8.

Grid	N_{tot}	N_y	$(\overline{\Delta}_x^+, \overline{\Delta}_{y_w}^+/2, \overline{\Delta}_z^+)$	$(\overline{\Delta}_x, \overline{\Delta}_{y_c}, \overline{\Delta}_z)/H$	Re_τ	$\overline{e}_{\text{QoI}}^{\text{prev}}$ (%)	$\overline{e}_{\text{QoI}}^{\text{DNS}}$ (%)
Vr-1	$15k$	20	$(153, 38, 153)$	$(0.40, 0.20, 0.40)$	382	–	34
Vr-2	$73k$	34	$(135, 9.5, 97)$	$(0.28, 0.22, 0.20)$	487	25	21
Vr-3	$256k$	44	$(103, 4.7, 47)$	$(0.21, 0.18, 0.097$	484	7.7	18
Vr-4	$517k$	50	$(91, 4.1, 32)$	$(0.18, 0.16, 0.064)$	500	6.0	11
Vr-5	$1.16M$	62	$(68, 3.3, 24)$	$(0.13, 0.12, 0.048)$	510	2.3	9.7
Vr-6	$2.51M$	76	$(49, 2.8, 20)$	$(0.096, 0.096, 0.038)$	518	2.8	7.1
Vr-7	$5.83M$	96	$(35, 2.3, 15)$	$(0.068, 0.075, 0.029)$	524	2.1	5.1
Vr-8	$11.0M$	114	$(27, 1.9, 13)$	$(0.052, 0.061, 0.024)$	530	1.1	4.4

Table 5.2: Sequence of grids generated for LES of turbulent channel flow using the Vreman model with a model constant of $c_v = 0.03$ and $\overline{\Delta}/\overline{h} = 2$. Additional details on the notation are given in the caption of Table 5.1. All resolutions are based on the filter-width, not the grid-spacing.

5.2.3 LES with dominant modeling errors and small numerical errors

The next test case tries to assess the performance of the error-indicator in a flow where the numerical errors are relatively small and the solution is mostly dominated by the effect of modeling errors. This is achieved here by taking $\overline{\Delta}/\overline{h} = 2$ and using the eddy viscosity model by Vreman [19] with a constant coefficient of $c_v = 0.03$. The use of a filter-width larger than the grid-spacing causes the eddy viscosity to increase by a factor of 4, which dissipates most of the energy before reaching the Nyquist limit of the grid.

The sequence of grids and solutions are summarized in Table 5.2 and Fig. 5.4. The initial grid has the same number of grid points as for the dynamic Smagorinsky case, but twice the filter-width. The subsequent grids in the sequence have approximately the same number of grid points as the corresponding dynamic Smagorinsky cases.

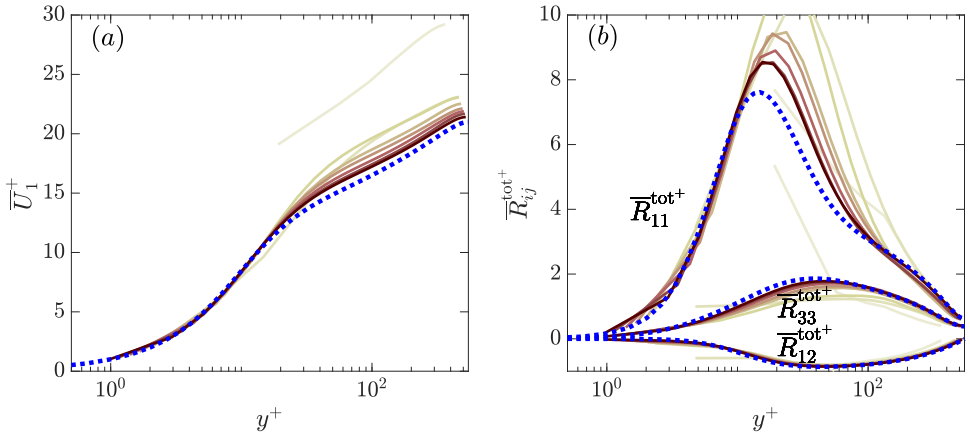

Figure 5.4: Convergence of the mean velocity and Reynolds stress profiles for grids in Table 5.2 generated for LES with the constant coefficient Vreman model [19] and $\overline{\Delta}/\overline{h} = 2$. Colors vary from the brightest for the first grid to the darkest for the last one. The dotted blue lines are the DNS of del Alamo & Jimenez [18].

The solutions converge much more slowly for this case, which is consistent with the broadly agreed upon notion that, for a given grid-spacing $\overline{h}$, the choice of $\overline{\Delta} \approx \overline{h}$ leads to the best LES accuracy in most cases (see Fig. 2.1). In other words, that the increase in modeling error for larger filter-widths is greater than the decrease in numerical error.

More interestingly (in the present context) is that the last few grids again agree quite closely with the "best practice" in LES, and in fact agree rather well with the grids for the dynamic Smagorinsky model. For example, grid Vr-5 in Table 5.2 has a grid-spacing (half the filter-width) of $(34, 1.6, 12)$ in viscous units, which is almost identical to the resolution of $(34, 1.4, 13)$ for grid DSM-5 in Table 5.1.

5.2.4 DNS affected solely by numerical errors

The final channel case is to turn off the LES subgrid model and thus have only numerical errors. The adaptation algorithm remains the same except that $\tau_{ij}^{\mathrm{mod}} = 0$

Grid	N_{tot}	N_y	$(\overline{\Delta}_x^+, \overline{\Delta}_{y_w}^+/2, \overline{\Delta}_z^+)$	$(\overline{\Delta}_x, \overline{\Delta}_{y_c}, \overline{\Delta}_z)/H$	Re_τ	$\overline{e}_{\text{QoI}}^{\text{prev}}$ (%)	$\overline{e}_{\text{QoI}}^{\text{DNS}}$ (%)
DNS-1	$15k$	20	$(81, 20, 81)$	$(0.20, 0.10, 0.20)$	405	–	30
DNS-2	$76k$	34	$(80, 6.2, 56)$	$(0.14, 0.094, 0.097)$	578	24	16
DNS-3	$252k$	44	$(51, 2.4, 31)$	$(0.093, 0.092, 0.057)$	547	13	6.7
DNS-4	$515k$	50	$(43, 1.6, 22)$	$(0.076, 0.086, 0.039)$	563	5.3	5.0
DNS-5	$1.14M$	60	$(34, 1.6, 15)$	$(0.060, 0.067, 0.026)$	566	2.2	4.4
DNS-6	$2.53M$	72	$(25, 1.5, 10)$	$(0.046, 0.054, 0.019)$	553	2.1	2.9
DNS-7	$5.87M$	90	$(18, 1.3, 7.7)$	$(0.033, 0.042, 0.014)$	545	2.4	1.8
DNS-8	$11.0M$	106	$(13, 1.2, 6.4)$	$(0.025, 0.034, 0.012)$	543	0.9	0.9

Table 5.3: Sequence of grids generated for DNS of turbulent channel flow at $Re_\tau \approx 545$. Additional details on the notation are given in the caption of Table 5.1.

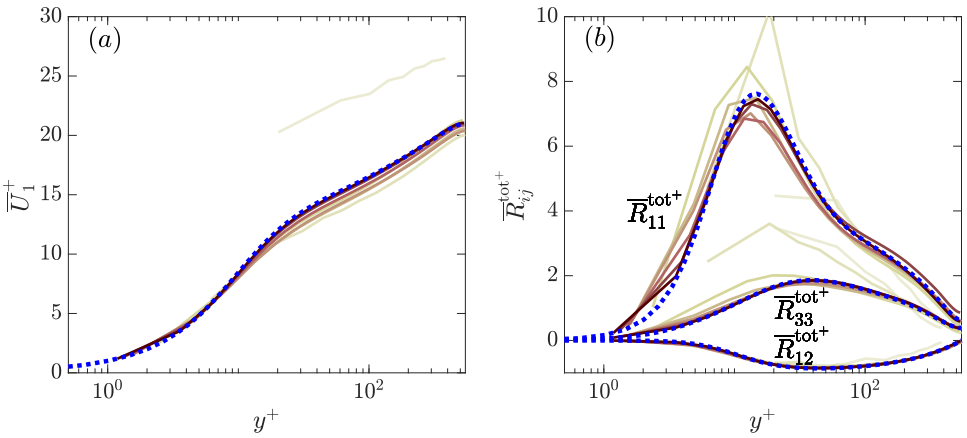

Figure 5.5: Convergence of the mean velocity and Reynolds stress profiles for grids in Table 5.3. Colors vary from the brightest for DNS-1 to the darkest for DNS-8. The dotted blue lines show the DNS of del Alamo & Jimenez [18].

in both the solver and when computing the error-indicator.

When creating the sequence of grids we target the same number of grid points as in the previous cases. Key metrics are summarized in Table 5.3 with the convergence of the mean velocity and Reynolds stress profiles shown in Fig. 5.5.

The sequence of grids is very similar to those produced for the dynamic Smagorinsky and constant Vreman models in the previous sections. Again, we should emphasize that this is mainly because the wall-resolved LES grids have "optimal" resolutions that are very close to DNS. The error in the QoIs is larger for

the DNS (no-model) cases than the dynamic Smagorinsky ones, showing that the model has a positive effect for this particular flow and code.

5.3 Assessment on the flow over a backward facing step at $Re_H = 5100$

The purpose of this test case is to expose the adaptation algorithm to a more complex flow, with multiple different canonical flow elements. This combination of different types of building-block flows is meant to challenge the adaptation algorithm, while it gives us s chance to analyze the predicted resolutions based on what we expect for LES of each of those flows.

The flowfield and setup are identical to what we used in Sections 3.3 and 4.6, and their details are not repeated here.

5.3.1 Code and computational details

The OpenFOAM code version 2.3.1 [60] (a second-order finite volume solver) is used for this test case to allow for fully unstructured adapted grids. The filter-width is taken as the cube-root of the cell volume. We use the dynamic k_{sgs}-equation LES model (cf. [61–64]) that defines the eddy viscosity as

$$\nu_{\text{sgs}} = c_k \overline{\Delta} \sqrt{\overline{k}_{\text{sgs}}}$$

and solves a transport equation for $\overline{k}_{\text{sgs}}$. This raises the question of how to compute $\widehat{\overline{k}}_{\text{sgs}}^{(\mathbf{n}_0)}$ and thus $\widehat{\overline{\mathcal{V}}}^{(\mathbf{n}_0)}$ at the test-filter level. In the present work, we use simple approach of assuming that the eddy viscosity scales as $\nu_{\text{sgs}} \sim \overline{\Delta}^2 |\overline{S}|$ (a consistency

requirement for eddy viscosity models), which then allows us to use the approximate relation (5.14) to compute the eddy viscosity at the test-filter level. Similar to for the channel case, the effect of this approximation is assumed to be small (the assessment is in Section 5.5). We again take $\widehat{\overline{\Delta}}^{(\mathbf{n}_0)}/\overline{\Delta} \approx \sqrt[3]{2}$, which comes from our definition of the characteristic filter-width as the cube root of the cell volume.

The quantities of interest for this flow are taken to be the two non-zero mean velocity components, the four non-zero Reynolds stress components, and the friction and pressure coefficient profiles on the horizontal walls. The error in each of the QoIs is defined by Eqn. 3.11, and the convergence criterion is computed using Eqn. 3.12, repeated here as

$$\overline{e}^{\text{ref}}_{\text{QoI}} = \frac{1}{3}\sum_{m=1}^{2}\frac{\delta\overline{Q}^{\text{ref}}_m}{2} + \frac{1}{3}\sum_{m=3}^{6}\frac{\delta\overline{Q}^{\text{ref}}_m}{4} + \frac{1}{3}\sum_{m=7}^{8}\frac{\delta\overline{Q}^{\text{ref}}_m}{2}\,.$$

The reference DNS is computed on a very fine unstructured grid with about 54M cells, which is generated by refinement of grid G-7 in Table 5.4 by a factor of 2, everywhere and in all directions.

Each case was run for $500H/U_\infty$ time units, after which 800 snapshots were collected over a period of $2000H/U_\infty$. The convergence of the averaging was judged by dividing the full record into four separate batches with 200 snapshots in each, computing the QoIs for each batch, and then computing the sample standard deviation between the batch averages. We then constructed 95% confidence intervals for each quantity using the Student's t-distribution with 3 degrees of freedom (cf. [65]). The confidence intervals for the integrated errors in the QoIs are very small (and thus omitted below), but they are significant for some of the profiles especially down-

stream of the step. These confidence intervals are shown in all convergence plots of this Section.

Once again, the long averaging times are required only for the solution to converge; the error-indicator converges about an order of magnitude more quickly due to its dependence on the small scales (Chapter 6).

5.3.2 Results

The initial grid (labeled G-1) has a resolution of $\overline{\Delta}(\mathbf{x}, \mathbf{n})/H = 0.2$ everywhere in the domain except close to the walls where the wall-normal direction is refined by a factor of two (same initial grid used in Sections 3.3 and 4.6). After computing the LES on this grid, the error-indicator is computed in the three possible directions of refinement/coarsening, and the target filter-width fields for the second grid (G-2) are computed. We then create the actual grid G-2 using the *refineMesh* utility in OpenFOAM. Since *refineMesh* can only refine hexahedral cells by factors of 2 in any direction, the resulting grid is different from the predicted target. The resulting grid G-2 (actually, the target filter-width field before creating the *refineMesh* input) is visualized in Fig. 5.6. Note that the constant Λ in Eqn. 5.11 was adjusted such that the resulting number of cells was approximately doubled.

Figure 5.6 illustrates how the adaptation methodology targets different regions of the domain for refinement. The algorithm predicts a single level of refinement in the y direction ($\overline{\Delta}(\mathbf{x}, \mathbf{n}_y) = \overline{\Delta}_y = 0.1H$) in most of the domain inside the boundary layer, while the y resolution is predicted to need a second level of refinement

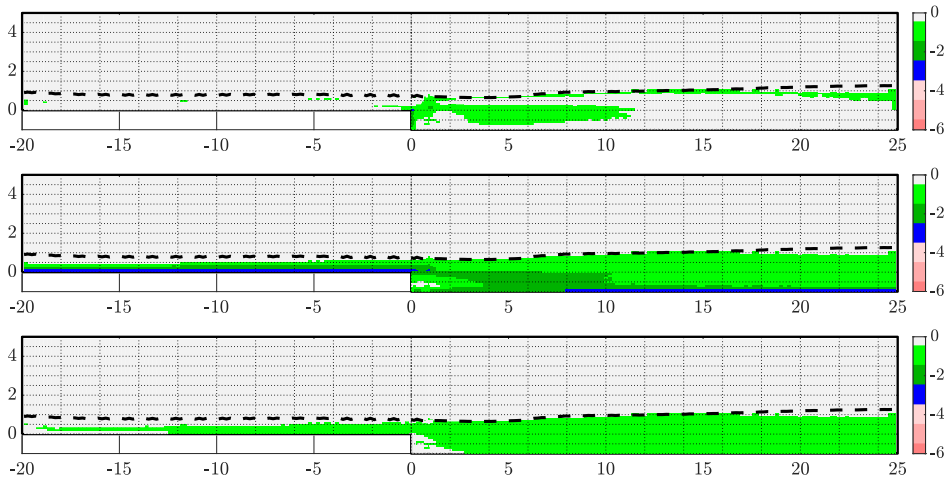

Figure 5.6: The grid G-2 from Table 5.4 illustrated by its refinement levels in x (top), y (middle), and z (bottom). Refinement levels are computed based on a skeletal grid with $\Delta_0(\mathbf{x}, \mathbf{n}) = 0.2H$ for all $\mathbf{x}$ and $\mathbf{n}$. The light green, dark green and blue colors illustrate regions with one ($\overline{\Delta}_\mathbf{n}/H = 0.1$), two ($\overline{\Delta}_\mathbf{n}/H = 0.05$), and three ($\overline{\Delta}_\mathbf{n}/H = 0.025$) refinement levels, respectively. The white regions are associated with regions that are left untouched (i.e. $\overline{\Delta}_\mathbf{n}/H = 0.2$). The dashed line highlights the δ_{95} boundary layer thickness.

($\overline{\Delta}_y/H = 0.05$) closer to the horizontal walls and in the shear layer, and a third level of refinement ($\overline{\Delta}_y/H = 0.025$) in close vicinity of the horizontal walls in both incoming and recovering boundary layers. The spanwise resolution $\overline{\Delta}_z$ is targeted for a single level of refinement ($\overline{\Delta}_z/H = 0.1$) for the most part of the domain inside the turbulent boundary layers, while the relaminarized region inside the recirculation bubble is left untouched. The resolution of the skeletal grid in the x direction ($\overline{\Delta}_x/H = 0.2$) is deemed adequate for the most part of the domain, except near the vertical wall of the step (where the recirculation bubble causes shear) and in the shear layer (where the turbulent fluctuations are significant in all three directions). We also note that the aspect ratio of the cells in the boundary layers and the shear layer are quite close to what we expect from experience for those flows. The fact

Grid	N_{tot}	$(\overline{\Delta}_x^+, \overline{\Delta}_{y_w}^+/2, \overline{\Delta}_z^+)$	$(\overline{\Delta}_x, \overline{\Delta}_y, \overline{\Delta}_z)/\delta_{\text{shear}}$	$\overline{e}_{\text{QoI}}^{\text{prev}}$ (%)	$\overline{e}_{\text{QoI}}^{\text{DNS}}$ (%)
G-1	149k	$(42, 10, 42)$	$(0.21, 0.17, 0.33)$	–	11.1
G-2	297k	$(42, 2.6, 21)$	$(0.16, 0.078, 0.16)$	5.3	10.5
G-3	611k	$(45, 1.4, 11)$	$(0.16, 0.049, 0.078)$	6.4	5.6
G-4	1.32M	$(47, 1.5, 12)$	$(0.076, 0.038, 0.076)$	3.8	4.9
G-5	2.13M	$(25, 0.77, 6.2)$	$(0.070, 0.035, 0.035)$	2.8	5.4
G-6	3.41M	$(25, 0.77, 6.1)$	$(0.068, 0.034, 0.034)$	3.4	3.5
G-7	6.72M	$(12, 0.76.6.0)$	$(0.034, 0.017, 0.034)$	2.2	2.5
DNS	54M	$(6.0, 0.38.3.0)$	$(0.017, 0.0086, 0.017)$	–	0

Table 5.4: Sequence of grids generated for LES of flow over a backward-facing step. $(\overline{\Delta}_x^+, \overline{\Delta}_{y_w}^+/2, \overline{\Delta}_z^+)$ correspond to the boundary layer resolutions at $x/H = -3$ upstream of the step, δ_{shear} is the approximate shear layer thickness at $(x, y)/H = (1, 0)$, and $(\overline{\Delta}_x, \overline{\Delta}_y, \overline{\Delta}_z)$ is the resolution at that location. See Fig. 5.11 for more details. $\overline{e}_{\text{QoI}}^{\text{DNS}}$ and $\overline{e}_{\text{QoI}}^{\text{prev}}$ are defined in Eqn. 3.12.

that the resulting G-2 grid seems this reasonable from an "LES experience" point-of-view is actually quite remarkable, since it was created entirely by an algorithm from a solution on a highly underresolved mesh.

The adaptation process is continued until grid G-7 where the QoIs are deemed converged. Each target grid is generated by aiming for approximately doubling the number of cells, without trying to match this ratio exactly. The sequence of generated grids is reported in Table 5.4 by their total number of cells N_{tot} and QoI errors (both $\overline{e}_{\text{QoI}}^{\text{DNS}}$ and $\overline{e}_{\text{QoI}}^{\text{prev}}$). The table also reports the grid-spacings in the approaching boundary layer at $x/H = -3$ and shortly after the step at $x/H = 1$ (for $y/H = 0$) in the shear layer formed by separation at the step. The convergence of the QoIs is shown in Fig. 5.7 for the pressure and friction coefficients and Figs. 5.8, 5.9 and 5.10 for the mean velocity and Reynolds stress profiles at some of the more interesting locations.

The computed error $\overline{e}_{\text{QoI}}^{\text{DNS}}$ decreases after every adaptation except for grid G-5.

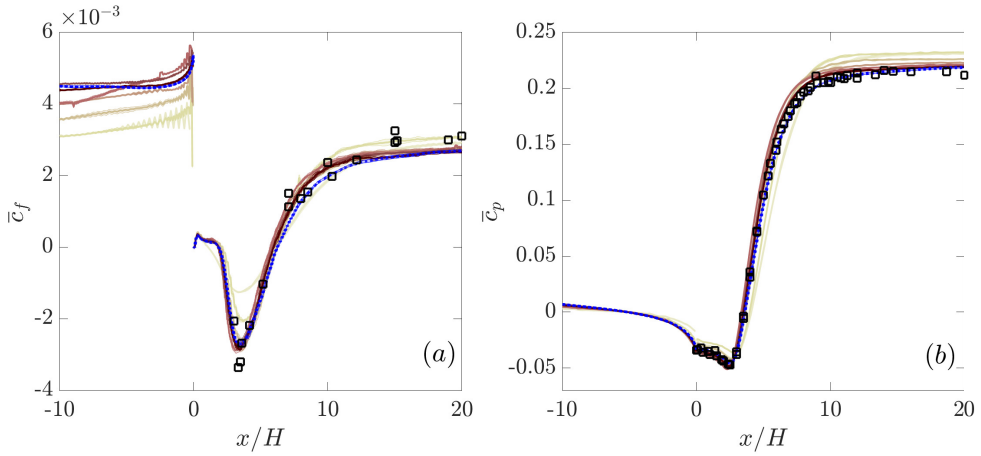

Figure 5.7: Convergence of (a) friction coefficient $\overline{c}_f$ and (b) pressure coefficient $\overline{c}_p$ for LES of flow over a backward-facing step. Grids in Table 5.4 are shown by the lightest color for G-1 to the darkest for G-7. Solid lines denote the sample means, while the shaded regions correspond to the approximate confidence intervals (computed locally). The dotted blue lines and their shaded regions denote our DNS results and their confidence intervals. Symbols correspond to the experimental data of Jovic & Driver [57,58] with slightly different setup (error bars on the experimental data are not shown). Experimental measurements of $\overline{c}_f$ and $\overline{c}_p$ are not available upstream of the step.

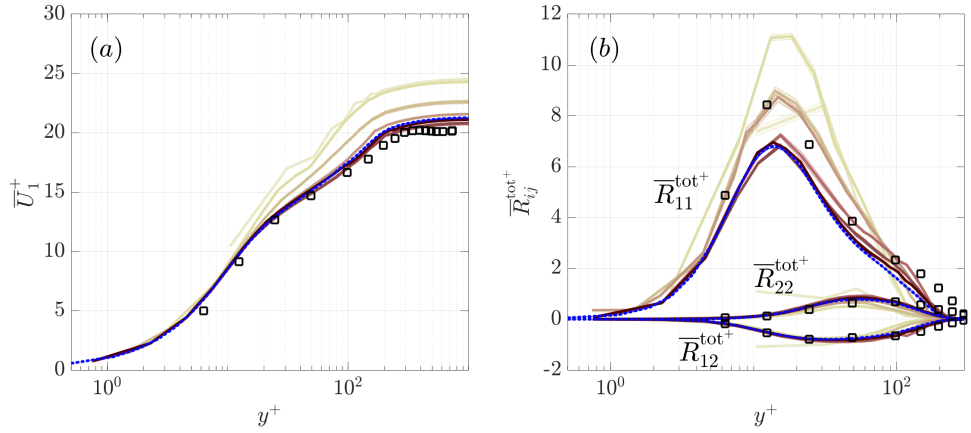

Figure 5.8: Convergence of the mean velocity and Reynolds stress profiles for the sequence of grids in Table 5.4 at the incoming boundary layer at $x/H = -3$. Grids in the sequence are shown by the lightest color for G-1 to the darkest for G-7. Solid lines denote the sample means, while the shaded regions correspond to the approximate confidence intervals (computed locally). The dotted blue lines and their shaded regions denote our DNS results and their confidence intervals. Symbols correspond to the experimental data of Jovic & Driver [57, 58] (error bars on the experimental data are not shown).

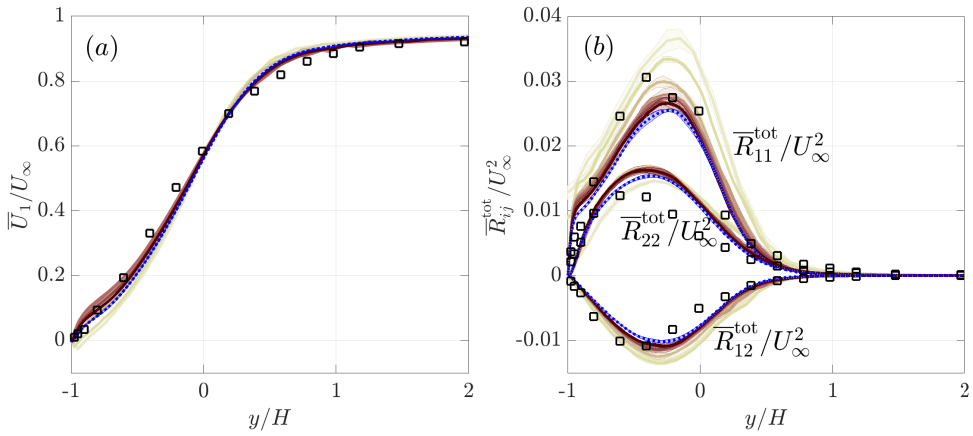

Figure 5.9: Convergence of the mean velocity and Reynolds stress profles for grids in Table 5.4 at $x/H = 6$ near the reattachment point. See Fig. 5.8 for more details.

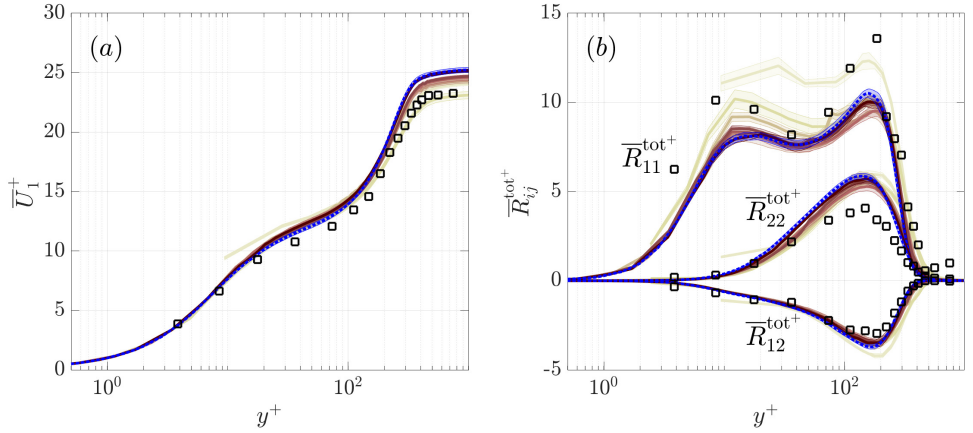

Figure 5.10: Convergence of the mean velocity and Reynolds stress profiles for the recovering boundary layer at $x/H = 15$ for the sequence of grids in Table 5.4. See Fig. 5.8 for more details.

The relatively large value of the error for this grid is primarily due to the error in the friction coefficient of the incoming boundary layer (see Fig. 5.7), that happens despite the apparently sufficient resolution of the grid, and affects the entire flowfield downstream of the step.

Figure 5.11 shows the constructed grid G-6 of Table 5.4 as an example of a converged LES grid for this specific setup. Note how complicated this grid has become, with many transitions between different grid-resolutions and cells that have

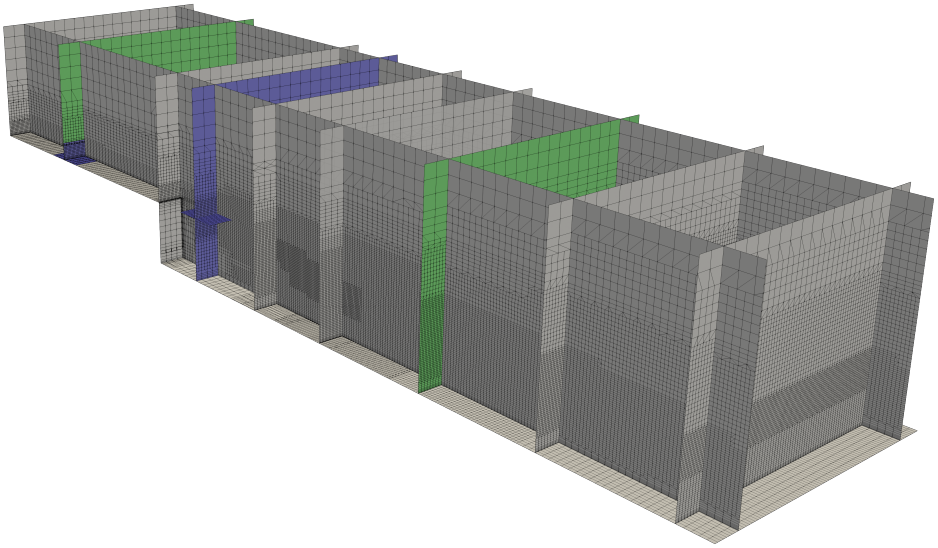

Figure 5.11: The generated grid G-6 of Table 5.4 with 3.41M cells. Intersections of the blue planes denote locations whose resolutions are reported in Table 5.4, while the green planes correspond to $x/H = -3$ and $x/H = 6$ whose velocity and Reynolds stress profiles are plotted in Figs. 5.8 and 5.9. The grid is resulted from computation of the proposed error-indicator (Eqns. 5.7 and 5.6) and applying the grid selection criteria of Eqns. 5.11 and 5.12 with no user experience involved.

completely different aspect ratios from one region of the domain to another (e.g., compare the aspect ratios at the locations reported in Table 5.4). It is interesting to note how coarse the grid is in the recirculation bubble, expect for the wall-normal directions that are refined to predict the right level of shear at the wall. The most important observation is that these predicted resolutions are very similar to what an experienced user would use when generating a grid for LES of the flow over a backward-facing step.

5.4 Comparison with the heuristic-based error-indicator $\overline{\mathcal{A}}(\mathbf{x}, \mathbf{n})$

We defined our heuristic-based error-indicator (Section 3.1.2) as

$$\overline{\mathcal{A}}(\mathbf{x}, \mathbf{n}) = \sqrt{\left\langle \overline{u}_i^{*,(\mathbf{n})} \overline{u}_i^{*,(\mathbf{n})} \right\rangle} \tag{5.15}$$

where $\overline{u}_i^{*,(\mathbf{n})} = \overline{u}_i - \widehat{\overline{u}}_i^{(\mathbf{n})}$ is the directionally high-pass test-filtered LES velocity field (using the same filter of Eqn. 5.2).

It is useful to compare the grids generated by the proposed error-indicator of this Chapter $\overline{\mathcal{G}}(\mathbf{x}, \mathbf{n})$ (Eqn. 5.7) with those of $\overline{\mathcal{A}}(\mathbf{x}, \mathbf{n})$. In that sense, the results of this Section complement our assessments of $\overline{\mathcal{G}}(\mathbf{x}, \mathbf{n})$ in Sections 5.2.2 (channel flow with the dynamic Smagorinsky model) and 5.3 (flow over a backward-facing step). For both of our error-indicators we only consider the grids that are generated by the modified grid selection criteria.

Figure 5.12 compares the target aspect ratios from the two error-indicators. Note how similar the profiles are, meaning that our intuitive arguments in Section 3.1.1 (about the optimal selection of the size of the LES filter in any direction compared to the filter width in the limiting direction) were quite close to what can be inferred directly from the governing equation.

The results for LES of the channel flow using the dynamic Smagorinsky model are shown in Table 5.5. An interesting observation is the qualitative difference between the two sets of grids: although the grids generated using $\overline{\mathcal{G}}(\mathbf{x}, \mathbf{n})$ have a similar streamwise resolution to those generated by $\overline{\mathcal{A}}(\mathbf{x}, \mathbf{n})$, their wall-normal resolution is finer near the wall and coarser at the center of the channel. Note that

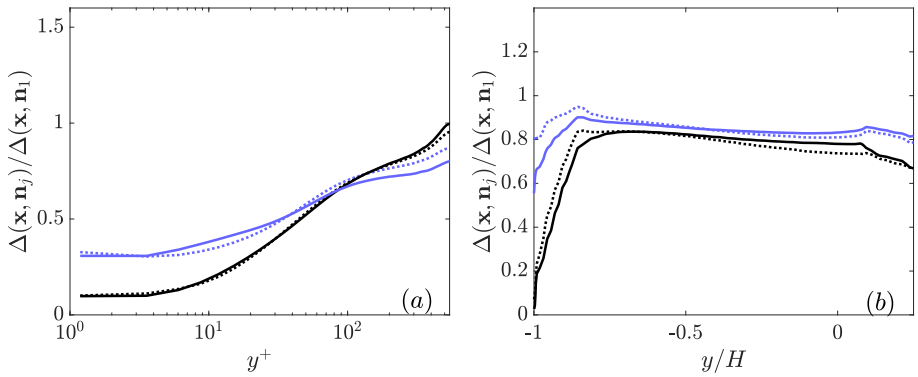

Figure 5.12: Examples of the predicted optimal cell aspect ratios $\check{\Delta}(\mathbf{x},\mathbf{n}_2)/\check{\Delta}(\mathbf{x},\mathbf{n}_1)$ (black lines) and $\check{\Delta}(\mathbf{x},\mathbf{n}_3)/\check{\Delta}(\mathbf{x},\mathbf{n}_1)$ (blue lines) for (a) turbulent channel flow at $Re_\tau \approx 545$ and $\alpha = 2$, $(b1)$ in the recirculation region of the flow over a backward-facing step at $x/H = 4$, for $\alpha = 2$. Note how similar the target aspect ratio are between $\overline{\mathcal{G}}(\mathbf{x},\mathbf{n})$ (solid lines) and $\overline{\mathcal{A}}(\mathbf{x},\mathbf{n})$ (dotted lines).

this basically fixes the coarse wall-normal resolution of the target grids by $\overline{\mathcal{A}}(\mathbf{x},\mathbf{n})$ at the wall (for example, compare the grids DSM-4 and A-4 from Table 5.5), which was mentioned in the beginning of this Chapter as one of the shortcomings we wished to address.

Figure 5.13 summarizes the convergence of $\overline{e}^{\text{DNS}}_{\text{QoI}}$ for all grids in Table 5.5 with the increase in the number of cells N_{tot}. Note that almost all grids generated using the new error-indicator $\overline{\mathcal{G}}(\mathbf{x},\mathbf{n})$ have lower values of the error metric $\overline{e}^{\text{DNS}}_{\text{QoI}}$. If we accept the lower values of $\overline{e}^{\text{DNS}}_{\text{QoI}}$ as a measure of optimality (this is not exactly true) we can conclude that the grids generated by $\overline{\mathcal{G}}(\mathbf{x},\mathbf{n})$ have a more optimal distribution. This conclusion is consistent with our experience; in fact, grids generated by $\overline{\mathcal{A}}(\mathbf{x},\mathbf{n})$ seem to have a slightly coarser resolution near the wall (especially in the last grids) compared to what we expect for such high-resolution grids.

Figure 5.13 also plots the convergence of the indicator values themselves, defined as the volume averages (denoted by $\overline{e}_{\text{surr}}$, defined in Eqn. 4.17) of $\overline{\mathcal{A}}_{\text{tot}}$ (defined

Grid	N_{tot}	N_y	$(\overline{\Delta}_x^+, \overline{\Delta}_{y_w}^+/2, \overline{\Delta}_z^+)$	$(\overline{\Delta}_x, \overline{\Delta}_{y_c}, \overline{\Delta}_z)/H$	Re_τ	$\overline{e}_{\text{QoI}}^{\text{DNS}}$ (%)
DSM-2	$74k$	34	$(77, 5.6, 55)$	$(0.14, 0.099, 0.10)$	553	11
A-2	$76k$	36	$(80, 6.9, 56)$	$(0.14, 0.075, 0.10)$	562	12
DSM-3	$251k$	44	$(53, 2.3, 29)$	$(0.098, 0.091, 0.054)$	536	7.3
A-3	$245k$	48	$(57, 3.6, 32)$	$(0.10, 0.061, 0.058)$	560	8.3
DSM-4	$514k$	50	$(45, 1.7, 19)$	$(0.082, 0.080, 0.035)$	544	3.3
A-4	$526k$	56	$(46, 2.9, 22)$	$(0.082, 0.052, 0.039)$	559	5.5
DSM-5	$1.18M$	60	$(34, 1.4, 13)$	$(0.063, 0.065, 0.024)$	544	1.8
A-5	$1.17M$	66	$(35, 2.6, 15)$	$(0.063, 0.044, 0.027)$	559	4.2
DSM-6	$2.53M$	72	$(25, 1.6, 10)$	$(0.046, 0.052, 0.018)$	542	1.1
A-6	$2.52M$	80	$(26, 2.2, 11)$	$(0.048, 0.035, 0.020)$	552	2.4
DSM-7	$5.80M$	90	$(18, 1.4, 7.6)$	$(0.033, 0.041, 0.014)$	540	1.1
A-7	$5.90M$	100	$(18, 1.8, 8.2)$	$(0.034, 0.028, 0.015)$	543	0.8
DSM-8	$11.1M$	108	$(14, 1.2, 6.3)$	$(0.025, 0.033, 0.012)$	541	0.9
A-8	$11.3M$	118	$(14, 1.6, 6.8)$	$(0.025, 0.024, 0.013)$	542	1.4

Table 5.5: Sequence of grids generated for LES of channel flow at $Re_\tau \approx 545$ using the dynamic Smagorinsky model. The "DSM" grids are copied from Table 5.1, while the "A" grids are the "NEW" grids in Table 4.1 and are copied from there. See caption of Table 5.1 for more details.

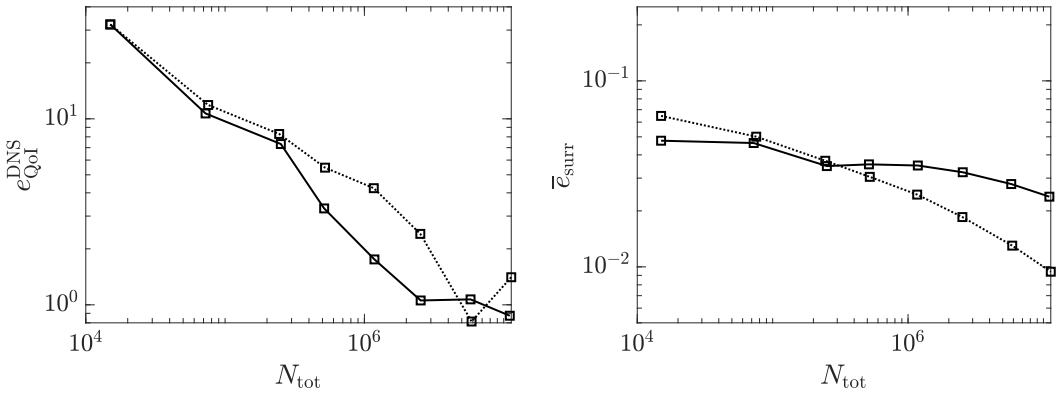

Figure 5.13: Comparison between the convergence of $\overline{e}_{\text{QoI}}^{\text{DNS}}$ and $\overline{e}_{\text{surr}}$ with N_{tot} for the sequences of grids generated by $\overline{\mathcal{G}}(\mathbf{x}, \mathbf{n})$ (solid lines) and $\overline{\mathcal{A}}(\mathbf{x}, \mathbf{n})$ (dotted lines) for the turbulent channel flow at $Re_\tau \approx 545$.

in Eqn. 4.10) and $\overline{\mathcal{G}}_{\text{tot}}$ (defined in Eqn. 5.9), respectively. It is quite interesting to see that neither of the error-indicators exhibit a similar convergence behavior to that of $\overline{e}_{\text{QoI}}^{\text{DNS}}$. Even more interestingly, $\int_\Omega \overline{\mathcal{G}}_{\text{tot}}(\mathbf{x}) d\mathbf{x}$ remains nearly constant between grids

Grid	N_{tot}	$(\overline{\Delta}_x^+, \overline{\Delta}_{y_w}^+/2, \overline{\Delta}_z^+)$	$(\overline{\Delta}_x, \overline{\Delta}_y, \overline{\Delta}_z)/\delta_{\text{shear}}$	$\overline{e}_{\text{QoI}}^{\text{DNS}}$ (%)
G-2	297k	$(42, 2.6, 21)$	$(0.16, 0.078, 0.16)$	10.5
A-2	297k	$(45, 5.7, 23)$	$(0.15, 0.093, 0.15)$	10.5
G-3	611k	$(45, 1.4, 11)$	$(0.16, 0.049, 0.078)$	5.6
A-3	599k	$(47, 2.9, 12)$	$(0.15, 0.074, 0.074)$	6.1
G-4	1.32M	$(47, 1.5, 12)$	$(0.076, 0.038, 0.076)$	4.9
A-4	1.35M	$(22, 2.8, 11)$	$(0.15, 0.036, 0.073)$	6.6
G-5	2.13M	$(25, 0.77, 6.2)$	$(0.070, 0.035, 0.035)$	5.4
A-5	2.17M	$(24, 1.5, 6.1)$	$(0.068, 0.034, 0.034)$	4.2
G-6	3.41M	$(25, 0.77, 6.1)$	$(0.068, 0.034, 0.034)$	3.5
A-6	3.70M	$(25, 1.6, 6.2)$	$(0.065, 0.033, 0.033)$	4.4
G-7	6.72M	$(12, 0.76.6.0)$	$(0.034, 0.017, 0.034)$	2.5
A-7	7.26M	$(12, 1.5, 6.0)$	$(0.068, 0.034, 0.034)$	2.0

Table 5.6: A comparison between the sequence of grids generated for LES of flow over a backward-facing step using $\overline{\mathcal{A}}(\mathbf{x}, \mathbf{n})$ (grids labeled "A", copied from Table 4.2) and $\overline{\mathcal{G}}(\mathbf{x}, \mathbf{n})$ (grids labeled "G", copied from Table 5.4) Refer to Table 5.4 for more details including interpretation of each quantity.

DSM-3, DSM-4, DSM-5 and DSM-6, and only starts decreasing again on DSM-7 where the LES model has become effectively inactive. Note that at the same time $\int_\Omega \overline{\mathcal{A}}_{\text{tot}}(\mathbf{x}) d\mathbf{x}$ decays at a somewhat constant rate (its convergence rate is different from $\overline{e}_{\text{QoI}}^{\text{DNS}}$). This nearly constant value of $\int_\Omega \overline{\mathcal{G}}_{\text{tot}}(\mathbf{x}) d\mathbf{x}$ in the intermediate grids may be at first interpreted as a sign that the choice of $\check{\mathcal{G}}_{\text{tot}}(\mathbf{x})$ as an estimate of $\check{e}_{\text{local}}^{\text{ref}}(\mathbf{x})$ was not accurate; while probably true, it stands in some contrast to the consistent improvement in $\overline{e}_{\text{QoI}}^{\text{DNS}}$ on almost all the grids that were generated by $\overline{\mathcal{G}}(\mathbf{x}, \mathbf{n})$. A more plausible explanation is that while the magnitude of $\check{\mathcal{G}}_{\text{tot}}(\mathbf{x})$ is probably not a great measure of magnitude of $\check{e}_{\text{local}}^{\text{ref}}(\mathbf{x})$ (which makes sense, since $\overline{\mathcal{G}}(\mathbf{x}, \mathbf{n})$ is based on small-scale quantities, while the QoIs are functions of the larger scale), the spatial distribution of $\check{\mathcal{G}}_{\text{tot}}(\mathbf{x})$ must qualitatively match that of $\check{e}_{\text{local}}^{\text{ref}}(\mathbf{x})$.

As a second comparison we consider the flow over a backward-facing step, with

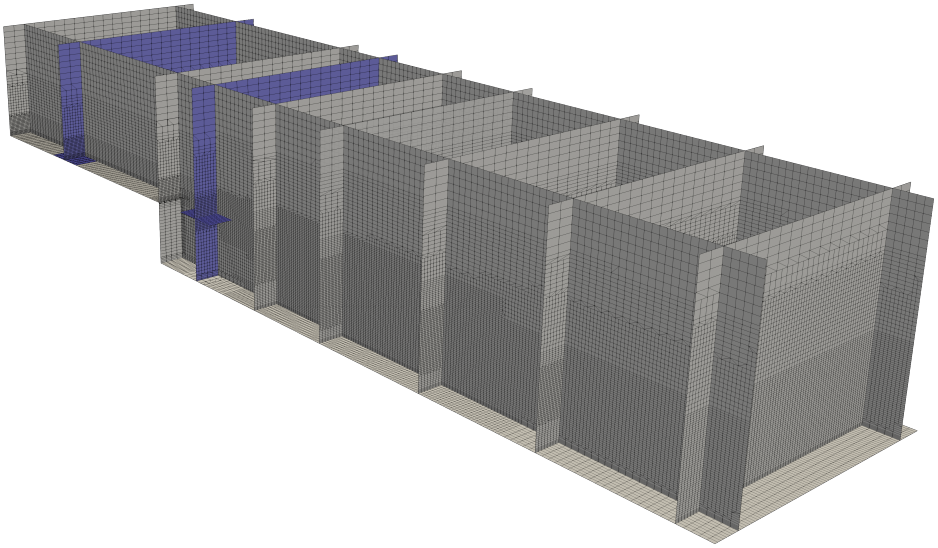

Figure 5.14: Grid A-6 in Table 5.6 with 3.70M cells. Intersections of the blue planes highlight locations whose resolutions are reported in Table 5.6. Note that this grid is qualitatively different from G-6 shown in Fig. 5.11. See text for more details.

results summarized in Table 5.6.

Figure 5.15 shows the convergence of the error in the QoIs, $\overline{e}^{\text{DNS}}_{\text{QoI}}$, and its surrogate quantity, $\overline{e}_{\text{surr}}$ (used when formulating the grid selection criteria), for grids in Table 5.6. The error in (our specific) quantities of interest is generally lower for grids generated by $\overline{\mathcal{G}}(\mathbf{x}, \mathbf{n})$. Again, (assuming $\overline{e}^{\text{DNS}}_{\text{QoI}}$ as a measure of optimality) we can conclude that the grids generated by $\overline{\mathcal{G}}(\mathbf{x}, \mathbf{n})$ have a more optimal distribution. Once more, our experience with LES confirms this conclusion, as the reported resolutions in the boundary layer and shear layer of the "G" grids are closer to what we expect, especially in the last few grids with relatively high resolutions. The convergence of $\int_\Omega \overline{\mathcal{G}}_{\text{tot}}(\mathbf{x}) d\mathbf{x}$ is also slower than that of $\int_\Omega \overline{\mathcal{A}}_{\text{tot}}(\mathbf{x}) d\mathbf{x}$, which is consistent with what we saw earlier in Fig. 5.13.

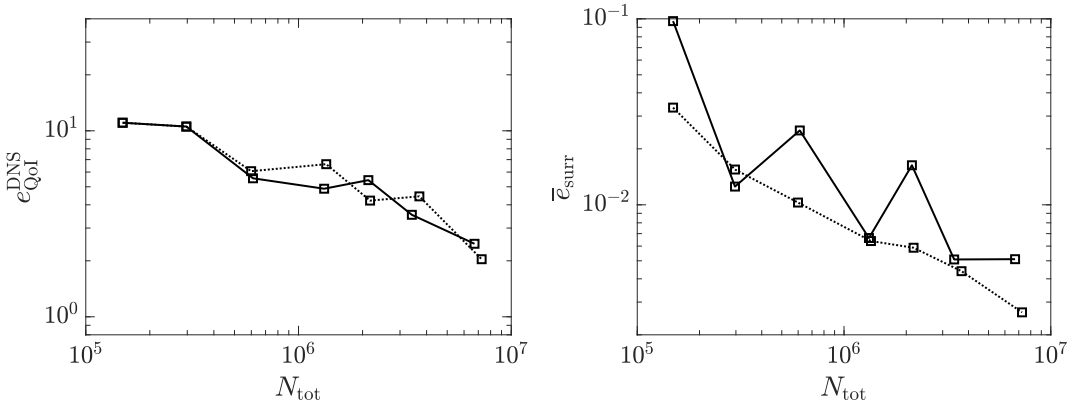

Figure 5.15: Comparison between the convergence of $\overline{e}^{\mathrm{DNS}}_{\mathrm{QoI}}$ and $\overline{e}_{\mathrm{surr}}$ with N_{tot} for the sequences of grids generated by $\overline{\mathcal{G}}(\mathbf{x},\mathbf{n})$ (solid lines) and $\overline{\mathcal{A}}(\mathbf{x},\mathbf{n})$ (dotted lines) for the flow over a backward-facing step.

5.5 Sensitivity of the target grids and robustness of the method

In this Section, we assess how sensitive the target grids are (in terms of the error in the QoIs and predicted distribution of the filter-width) to approximations made when computing $\check{\mathcal{G}}(\mathbf{x},\mathbf{n})$, or the use of a non-customized version of the error-indicator. This is of special interest to us because of two main reasons:

(i) it is extremely desirable that the error indicator is robust to changes in the LES code and the LES model

(ii) approximations are almost unavoidable in practice, the most common of which happens when computing $\tau^{\mathrm{mod}}_{ij}(\widehat{\overline{u}}^{(\mathbf{n})}_k)$ in Eqn. 5.6.

The former point follows from our discussions in Section 3.6 that the best error-indicator is one that is customizable to the LES formulation and model, while still robust to a change in them. Examples of the latter point include: our assumption that the model coefficients remain unchanged between filter levels $\overline{\Delta}$ and $\widehat{\overline{\Delta}}^{(\mathbf{n})}$ to avoid performing the full dynamic procedure (used in Sections 5.2.2 and 5.3), es-

timating the change in $\overline{k}_{\text{sgs}}$ by an approximate formula to avoid solving an extra transport equation (Section 5.3), different numerics used in computing $\overline{\mathcal{G}}(\mathbf{x}, \mathbf{n})$ to avoid reimplementation of the exhaustively elaborate numerical schemes used in the LES solver, and so on.

For the test cases of this Section, we use different LES models in the code and in computation of the error-indicator. To this end, we generate five new sequences of grids, all starting from an initial grid with resolution of $(\overline{\Delta}_x, \overline{\Delta}_y, \overline{\Delta}_z)/H = (0.20, 0.10, 0.20)$. In three of these sequences the constant Vreman model [19] is used in the LES solver with $c_v = 0.07$ and $\overline{\Delta}/\overline{h} = 1$ (slightly different from what was used in Section 5.2.3), while $\tau_{ij}^{\text{mod}}(\widehat{\overline{u}}_k^{(\mathbf{n})})$ in the error-indicator is computed once by the Vreman model (as it should be), once by using the (dynamic) Smagorinsky model (Eqn. 5.14), and once by setting the SGS terms to zero ($\tau_{ij}^{\text{mod}} \equiv 0$, corresponding to the DNS case). These three sets of grids are labeled "Vr/Vr" (same as the "Vr" grids in Table 5.2), "Vr/DSM" and "Vr/DNS", respectively. Similarly, the other three sequences are generated by using the dynamic Smagorinsky model in the LES solver and using the Smagorinsky model in $\overline{\mathcal{G}}(\mathbf{x}, \mathbf{n})$ (labeled "DSM/DSM", same as the "DSM" grids in Table 5.1), DSM in the solver and the Vreman model in the error-indicator (labeled "DSM/Vr") or setting the SGS terms to zero in the error-indicator. The last sequence (corresponding to "DSM/DNS" grids) is discontinued after the fourth grid, since the target grids had identical resolutions (within two significant digits) to "DSM/Vr" grids.

The generated grids are summarized in Tables 5.7 (for sequences with the Vreman model in the LES solver) and 5.8 (for DSM). Convergence of $\overline{e}_{\text{QoI}}^{\text{DNS}}$ with

Grid	N_{tot}	N_y	$(\overline{\Delta}_x^+, \overline{\Delta}_{y_w}^+/2, \overline{\Delta}_z^+)$	$(\overline{\Delta}_x, \overline{\Delta}_{y_c}, \overline{\Delta}_z)/H$	Re_τ	$\overline{e}_{\text{QoI}}^{\text{DNS}}$ (%)
Vr/Vr-2	$74k$	34	$(70, 4.0, 47)$	$(0.14, 0.10, 0.097)$	488	19
Vr/DSM-2	$76k$	32	$(64, 7.0, 55)$	$(0.12, 0.11, 0.10)$	528	13
Vr/DNS-2	$76k$	36	$(70, 3.3, 46)$	$(0.15, 0.096, 0.097)$	476	20
Vr/Vr-3	$253k$	48	$(58, 1.9, 25)$	$(0.11, 0.081, 0.050)$	507	11
Vr/DSM-3	$246k$	40	$(41, 3.8, 33)$	$(0.078, 0.10, 0.063)$	526	11
Vr/DNS-3	$245k$	48	$(59, 1.5, 25)$	$(0.12, 0.085, 0.050)$	504	11
Vr/Vr-4	$513k$	52	$(46, 2.0, 18)$	$(0.089, 0.076, 0.034)$	516	8.1
Vr/DSM-4	$517k$	48	$(34, 2.5, 22)$	$(0.065, 0.083, 0.043)$	522	8.2
Vr/DNS-4	$512k$	54	$(46, 1.1, 18)$	$(0.091, 0.075, 0.035)$	511	8.4
Vr/Vr-5	$1.18M$	64	$(34, 1.6, 13)$	$(0.065, 0.059, 0.025)$	521	5.7
Vr/DSM-5	$1.17M$	60	$(29, 2.0, 15)$	$(0.054, 0.065, 0.028)$	525	5.8
Vr/DNS-5	$1.15M$	64	$(34, 0.80, 13)$	$(0.067, 0.063, 0.025)$	517	6.7
Vr/Vr-6	$2.54M$	76	$(25, 1.4, 10)$	$(0.047, 0.049, 0.019)$	527	4.2
Vr/DSM-6	$2.52M$	74	$(23, 1.7, 11)$	$(0.044, 0.051, 0.020)$	530	4.1
Vr/DNS-6	$2.50M$	78	$(25, 0.61, 10)$	$(0.048, 0.050, 0.020$	521	5.0
Vr/Vr-7	$5.85M$	96	$(18, 1.1, 7.8)$	$(0.033, 0.037, 0.019)$	531	3.6
Vr/DSM-7	$5.83M$	94	$(17, 1.4, 8.0)$	$(0.032, 0.039, 0.015)$	534	3.7
Vr/DNS-7	$5.80M$	98	$(18, 0.47, 7.9)$	$(0.034, 0.038, 0.015)$	527	3.7
Vr/Vr-8	$10.7M$	112	$(14, 0.97, 6.5)$	$(0.026, 0.031, 0.012)$	533	2.7
Vr/DSM-8	$10.8M$	110	$(14, 1.2, 6.5)$	$(0.025, 0.032, 0.012)$	535	2.8
Vr/DNS-8	$10.9M$	114	$(14, 0.38, 6.5)$	$(0.026, 0.032, 0.012)$	530	2.9

Table 5.7: Sensitivity of the target grids to inaccuracies in the computation of $\tau_{ij}^{\text{mod}}(\widehat{\overline{u}}_k^{(\mathbf{n})})$ in Eqn. 5.6, or to the use of a non-customized version of the error-indicator. All simulations use the constant Vreman model [19] in the solver with $c_v = 0.07$ and $\overline{\Delta}/\overline{h} = 1$. Refer to caption of Table 5.1 for more details and interpretation of what each quantity means. See text for how grids "Vr/Vr", "Vr/DSM" and "Vr/DNS" are generated.

total number of cells N_{tot} is further illustrated in Fig. 5.16.

Note that the error in the QoIs is not significantly affected by these inconsistencies in our implementation of the error-indicator. The change in the target resolution is slightly more noticeable (Tables 5.7 and 5.8). For instance, the grid Vr/DSM-4 has a friction resolution of $(34, 2.5, 22)$ which is somewhat different from grid Vr-4 with resolution of $(46, 2.0, 18)$. Interestingly, this change in the target resolutions has a general trend that is present for almost all grids in the sequence

Grid	N_{tot}	N_y	$(\overline{\Delta}_x^+, \overline{\Delta}_{y_w}^+/2, \overline{\Delta}_z^+)$	$(\overline{\Delta}_x, \overline{\Delta}_{y_c}, \overline{\Delta}_z)/H$	Re_τ	$\overline{e}_{\text{QoI}}^{\text{DNS}}$ (%)
DSM/DSM-2	$74k$	34	$(77, 5.6, 55)$	$(0.14, 0.099, 0.10)$	553	11
DSM/Vr-2	$72k$	34	$(78, 4.1, 51)$	$(0.15, 0.10, 0.097)$	529	13
DSM/DSM-3	$251k$	44	$(53, 2.3, 29)$	$(0.098, 0.091, 0.054)$	536	7.3
DSM/Vr-3	$252k$	46	$(55, 1.4, 28)$	$(0.10, 0.091, 0.053)$	527	7.2
DSM/DSM-4	$514k$	50	$(45, 1.7, 19)$	$(0.082, 0.080, 0.035)$	544	3.3
DSM/Vr-4	$519k$	52	$(46, 1.0, 19)$	$(0.086, 0.079, 0.035)$	538	3.9
DSM/DSM-5	$1.18M$	60	$(34, 1.4, 13)$	$(0.063, 0.065, 0.024)$	544	1.8
DSM/Vr-5	$1.19M$	62	$(34, 0.79, 13)$	$(0.064, 0.065, 0.024)$	537	1.8
DSM/DSM-6	$2.53M$	72	$(25, 1.6, 10)$	$(0.046, 0.052, 0.018)$	542	1.1
DSM/Vr-6	$2.54M$	76	$(25, 0.62, 10)$	$(0.048, 0.051, 0.019)$	535	1.3
DSM/DSM-7	$5.80M$	90	$(18, 1.4, 7.6)$	$(0.033, 0.041, 0.014)$	540	1.1
DSM/Vr-7	$5.83M$	94	$(18, 0.51, 7.7)$	$(0.034, 0.040, 0.014)$	535	1.2
DSM/DSM-8	$11.1M$	108	$(14, 1.2, 6.3)$	$(0.025, 0.033, 0.012)$	541	0.9
DSM/Vr-8	$11.1M$	112	$(14, 0.43, 6.4)$	$(0.025, 0.032, 0.012)$	537	1.2

Table 5.8: Sensitivity of the target grids to inaccuracies in the computation of $\tau_{ij}^{\text{mod}}(\widehat{\overline{u}}_k^{(\mathbf{n})})$ in Eqn. 5.6, or to the use of a non-customized version of the error-indicator. Refer to caption of Table 5.1 for more details. All results are for LES using the dynamic Smagorinsky model. Grids labeled "DSM/DSM" are the same as those reported in Table 5.1 and are simply copied from there. See text for grids "DSM/Vr".

(e.g. "DSM/Vr" grids have similar streamwise and spanwise resolutions compared to "DSM/DSM" grids, while their wall-normal resolution is finer adjacent to the wall). However, we should emphasize that despite the relative change in the resolution of the target grids these are still suitable grids for LES of wall bounded turbulence. In other words, the aspect ratio of the cells may be slightly affected and suboptimal, but the spanwise resolutions of the cells are still significantly finer than their streamwise resolution, and their wall-normal resolution is such that it resolves all the scales (or at least most of them) in the y direction. The small change in $\overline{e}_{\text{QoI}}^{\text{DNS}}$ is in fact another proof of suitability of generated grids for channel flow: although this little effect on error in the QoIs is more related to the ability of the solver and

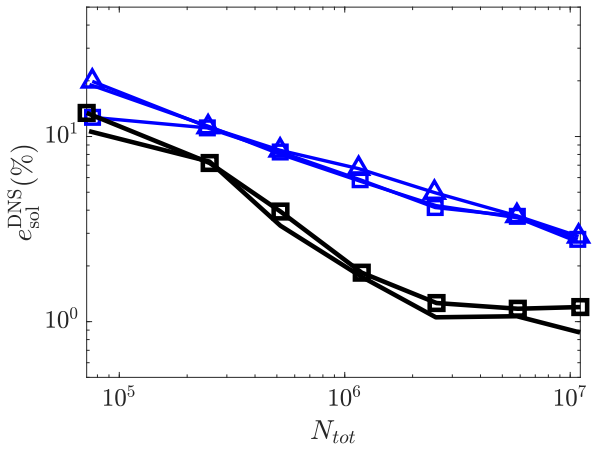

Figure 5.16: Sensitivity of the error in the QoIs to inaccuracies in the computation of $\overline{\mathcal{G}}(\mathbf{x}, \mathbf{n})$, and to the use of a non-customized version of the error-indicator. Figure summarizes results of Tables 5.7 and 5.8 for convergence of grids labeled as "DSM/DSM" (plain black line), "DSM/Vr" (black with squares), "Vr/Vr" (plain blue), "Vr/DSM" (blue with squares) and "Vr/DNS" (blue with triangles). See text and Tables 5.7 and 5.8 for more details.

its LES model in handling different grids, we can still conclude that the change in the target resolution is within some acceptable value to not deteriorate LES results significantly.

The presented results are specific to the LES code (numerics and models) and implementation of the error-indicator, while the conclusion that the target grids are still close to what we would get by customized and accurate implementation of the LES model is probably more general.

5.6 Definition of the error-indicator for other LES formulations

In this Section we define the error-indicator for the cases of explicitly filtered LES and implicit LES (ILES) of incompressible flows, as well as the implicitly filtered LES of compressible flows. Our formulation of the error-indicator suggests a small

modification to the standard compressible version of the dynamic procedure.

In explicitly filtered LES, the convective term of the momentum equation is filtered at each time step to take the form $\overline{\overline{u}_i\overline{u}_j}$, and the definition of the "subfilter" stress is modified accordingly as $\tau_{ij} = \overline{u_i u_j} - \overline{\overline{u}_i\overline{u}_j}$ (cf. [38]). The definition of $\widehat{\overline{\mathcal{F}}}_i^{(\mathbf{n})}(\mathbf{x})$ used in Eqn. 5.7 should also be modified as

$$\widehat{\overline{\mathcal{F}}}_i^{(\mathbf{n})}(\mathbf{x}) \equiv \frac{\partial}{\partial x_j}\left[\widehat{\overline{\overline{u}_i\overline{u}_j}}^{(\mathbf{n})} - \widehat{\overline{\widehat{\overline{u}}_i^{(\mathbf{n})}\widehat{\overline{u}}_j^{(\mathbf{n})}}}^{(\mathbf{n})}\right] + \frac{\partial}{\partial x_j}\left[\widehat{\tau_{ij}^{\mathrm{mod}}(\overline{u}_k)}^{(\mathbf{n})} - \tau_{ij}^{\mathrm{mod}}(\widehat{\overline{u}}_k^{(\mathbf{n})})\right] . \qquad (5.16)$$

This again becomes the divergence of the tensor that is used in formulation of the dynamic procedure in explicitly filtered LES.

In ILES there is no explicit SGS model in the code, i.e. $\tau_{ij}^{\mathrm{mod}} \equiv 0$ and the effect of the subgrid scales is accounted for by numerics designed to mimic an LES model. In this case, the definition of $\widehat{\overline{\mathcal{F}}}_i^{(\mathbf{n})}$ could be modified as

$$\widehat{\overline{\mathcal{F}}}_i^{(\mathbf{n})}(\mathbf{x}) = \frac{\delta}{\delta x_j}\left(\widehat{\overline{u}_i\overline{u}_j}^{(\mathbf{n})} - \widehat{\overline{u}}_i^{(\mathbf{n})}\widehat{\overline{u}}_j^{(\mathbf{n})}\right) , \qquad (5.17)$$

where $\delta/\delta x_j$ denotes the specific numerics used in the code and it has replaced $\partial/\partial x_j$ to emphasize the need to implement numerics that are consistent with the goal of mimicking a SGS model. We have not tested whether or not an inconsistent implementation of numerics (e.g. a central scheme) could produce acceptable results, but we should probably expect a similar behavior to what reported in Section 5.5 for "Vr/DNS" or "DSM/DNS" grids.

The definition of the error-indicator for LES of compressible flows becomes more involved due to the extra governing equations and the Favre-filtering of the primitive variables. The governing equations for implicitly filtered LES of compress-

ible flows (in their conservative form) read (cf. [79])

$$\frac{\partial \overline{\rho}}{\partial t} + \frac{\partial}{\partial x_j}\overline{\rho}\widetilde{u}_j = 0$$
$$\frac{\partial}{\partial t}\overline{\rho}\widetilde{u}_i + \frac{\partial}{\partial x_j}\overline{\rho}\widetilde{u}_i\widetilde{u}_j + \frac{\partial \overline{p}}{\partial x_i} - \frac{\partial \widetilde{\sigma}_{ij}}{\partial x_j} = \frac{\partial \mathcal{T}_{ij}}{\partial x_j}$$
$$\frac{\partial}{\partial t}\overline{\rho}\widetilde{E} + \frac{\partial}{\partial x_j}(\overline{\rho}\widetilde{E} + \overline{p})\widetilde{u}_j - \frac{\partial}{\partial x_j}\widetilde{\sigma}_{ij}\widetilde{u}_i + \frac{\partial \widetilde{\mathcal{Q}}_j}{\partial x_j} = \frac{\partial \mathcal{S}_j}{\partial x_j}$$

where $\bar{\cdot}$ is the filtering operation that is implicitly applied, $\overline{\rho}$ and $\overline{p}$ are the resolved density and pressure, respectively, and $\widetilde{u}_i$ and $\widetilde{E}$ are the Favre-filtered velocity and total internal energy, with Favre filtering defined as $\tilde{\phi} = \overline{\rho\phi}/\overline{\rho}$. The terms $\widetilde{\sigma}_{ij}$ and $\widetilde{\mathcal{Q}}_j$ describe the viscous stress and conductive heat flux, defined as

$$\widetilde{\sigma}_{ij} = \sigma_{ij}(\widetilde{T}, \widetilde{u}_i) = \mu(\widetilde{T})\left(2\widetilde{S}_{ij} - \frac{2}{3}\widetilde{S}_{kk}\delta_{ij}\right)$$
$$\widetilde{\mathcal{Q}}_j = \mathcal{Q}_j(\widetilde{T}) = -\kappa(\widetilde{T})\frac{\partial \widetilde{T}}{\partial x_j},$$

where $\widetilde{T} = \overline{p}/R\overline{\rho}$ is the Favre-filtered temperature and $\mu(\widetilde{T})$ and $\kappa(\widetilde{T})$ are the molecular viscosity and thermal conductivity that are functions of $\widetilde{T}$. The Favre-filtered strain rate is defined as $\widetilde{S}_{ij} = (\partial\widetilde{u}_i/\partial x_j + \partial\widetilde{u}_j/\partial x_i)/2$. The terms $\mathcal{T}_{ij}$ and $\mathcal{S}_j$ contain the entire effect of the subgrid scales in the momentum and energy equations and are closed by the LES model ($\mathcal{T}_{ij}$ could be slightly different from $\tau_{ij} = \overline{\rho}(\widetilde{u_i u_j} - \widetilde{u}_i\widetilde{u}_j)$ since there might be extra subgrid processes involved).

If we follow the approach of Section 5.1.1 and apply a directional test-filter $\widehat{\cdot}^{(\mathbf{n})}$ to the momentum equation at filter level $\overline{\Delta}$ and subtract it from the momentum equation at the test-filter level $\widehat{\bar{\cdot}}^{(\mathbf{n})}$, we can identify the following as the residual

forcing term,

$$\widehat{\overline{\mathcal{F}}}_i^{(\mathbf{n})}(\mathbf{x}) = \frac{\partial}{\partial x_j}\left[\frac{1}{\widehat{\overline{\rho}}^{(\mathbf{n})}}\widehat{\overline{\rho u_i}}^{(\mathbf{n})}\widehat{\overline{\rho u_j}}^{(\mathbf{n})} - \widehat{\overline{\rho}\widetilde{u}_i\widetilde{u}_j}^{(\mathbf{n})}\right] + \frac{\partial}{\partial x_j}\left[\mathcal{T}(\widehat{\overline{\rho}}^{(\mathbf{n})}, \breve{u}_i^{(\mathbf{n})}) - \widehat{\mathcal{T}(\overline{\rho}, \widetilde{u}_i)}^{(\mathbf{n})}\right] + \frac{\partial}{\partial x_j}\left[\sigma(\breve{T}^{(\mathbf{n})}, \breve{u}_i^{(\mathbf{n})}) - \widehat{\sigma(\widetilde{T}, \widetilde{u}_i)}^{(\mathbf{n})}\right], \tag{5.18}$$

where $\breve{\cdot}^{(\mathbf{n})}$ denotes Favre-filtering at the test-filter level $\widehat{\overline{\Delta}}^{(\mathbf{n})}$ defined as $\breve{\phi}^{(\mathbf{n})} = \widehat{\overline{\rho\phi}}^{(\mathbf{n})}/\widehat{\overline{\rho}}^{(\mathbf{n})}$. If we neglect the last term (the nonlinearity of the viscous term), the residual forcing term becomes the divergence of the tensor used in the standard compressible version of the dynamic procedure (cf. [79]). However, based on our discussions in Section 5.1.2, one should in principle include this term when calculating the model coefficient dynamically. The most important application of this modification is probably in flows with strong heating/cooling, where $\mu(\widetilde{T})$ has large variations, especially in complex flows where one cannot specify the preferred filtering direction.

If we repeat our approach for the mass conservation equation we end up with $\partial\widehat{\overline{\Gamma}}^{(\mathbf{n})}/\partial t + \partial\widehat{\overline{e}}_j^{(\mathbf{n})}/\partial x_j = 0$, where $\widehat{\overline{\Gamma}}^{(\mathbf{n})}$ and $\widehat{\overline{e}}_j^{(\mathbf{n})}$ are the errors in the density and mass flux, respectively. This suggests that we can exclude the mass conservation equation from our analysis of the source of error, since the momentum equation essentially leads to an evolution equation for error in the mass flux $\widehat{\overline{e}}_j^{(\mathbf{n})}$; thus, by minimizing the source of error in the momentum equation (Eqn. 5.18) we automatically minimize the error in the mass equation as well.

We can define a separate error-indicator for the energy equation as

$$\overline{\mathcal{G}}'(\mathbf{x}, \mathbf{n}) = \sqrt{\left\langle \widehat{\overline{\mathcal{J}}}^{(\mathbf{n})}(\mathbf{x})\widehat{\overline{\mathcal{J}}}^{(\mathbf{n})}(\mathbf{x}) \right\rangle} \tag{5.19}$$

where $\widehat{\overline{\mathcal{J}}}^{(\mathbf{n})}(\mathbf{x})$ is defined as

$$\begin{aligned}
\widehat{\overline{\mathcal{J}}}^{(\mathbf{n})}(\mathbf{x}) = &- \frac{\partial}{\partial x_j}\left[\widehat{\overline{\rho}}^{(\mathbf{n})}\breve{E}^{(\mathbf{n})}\breve{u}_j^{(\mathbf{n})} - \widehat{\overline{\rho}\widetilde{E}\widetilde{u}_j}^{(\mathbf{n})}\right] - \frac{\partial}{\partial x_j}\left[\widehat{\overline{p}}^{(\mathbf{n})}\breve{u}_j^{(\mathbf{n})} - \widehat{\overline{p}\widetilde{u}_j}^{(\mathbf{n})}\right] \\
&- \frac{\partial}{\partial x_j}\left\{\frac{1-\gamma}{2}\breve{u}_j^{(\mathbf{n})}\left[\widehat{\overline{\rho}}^{(\mathbf{n})}\breve{u}_k^{(\mathbf{n})}\breve{u}_k^{(\mathbf{n})} - \widehat{\overline{\rho}\widetilde{u}_k\widetilde{u}_k}^{(\mathbf{n})} + \tau_{kk}^{\mathrm{mod}}(\widehat{\overline{u}}_i^{(\mathbf{n})}) - \widehat{\tau_{kk}^{\mathrm{mod}}(\overline{u}_i)}^{(\mathbf{n})}\right]\right\} \\
&+ \frac{\partial}{\partial x_j}\left[\breve{u}_i^{(\mathbf{n})}\sigma_{ij}(\breve{T}^{(\mathbf{n})}, \breve{u}_k^{(\mathbf{n})}) - \widetilde{u}_i\widehat{\sigma_{ij}(\widetilde{T}, \widetilde{u}_k)}^{(\mathbf{n})}\right] - \frac{\partial}{\partial x_j}\left[\mathcal{Q}_j(\breve{T}^{(\mathbf{n})}) - \widehat{\mathcal{Q}_j(\widetilde{T})}^{(\mathbf{n})}\right] \\
&+ \frac{\partial}{\partial x_j}\left[\mathcal{S}_j^{\mathrm{mod}}(\widehat{\overline{\rho}}^{(\mathbf{n})}, \widehat{\overline{\rho u_i}}^{(\mathbf{n})}, \widehat{\overline{\rho E}}^{(\mathbf{n})}) - \widehat{\mathcal{S}_j^{\mathrm{mod}}(\overline{\rho}, \overline{\rho u_i}, \overline{\rho E})}^{(\mathbf{n})}\right].
\end{aligned} \tag{5.20}$$

Here γ is the ratio of the specific heats, and τ_{ij}^{mod} is the LES model used for $\tau_{ij} = \overline{\rho}(\widetilde{u_i u_j} - \widetilde{u}_i\widetilde{u}_j)$. Note how different this error-indicator is from an intuition-based error-indicator for the energy equation, that could be defined for instance as $\sqrt{\left\langle \widetilde{T}^{*,(\mathbf{n})}\widetilde{T}^{*,(\mathbf{n})}\right\rangle}$, where $\widetilde{T}^{*,(\mathbf{n})} = \widetilde{T} - \widehat{\widetilde{T}}^{(\mathbf{n})}$ (same as [80] but applied in a directional sense).

One important point to keep in mind is that we arrived at Eqns. 5.18 and 5.20 by excluding the error in the energy equation from the residual term in the momentum equation and vice versa. This is a relatively *ad hoc* assumption, driven by the desire to make the equations simpler, and could be suboptimal.

5.7 Concluding remarks

The goal of this Chapter has been to introduce a new error-indicator that is more directly connected to the governing equations of LES, and is less based on heuristic arguments about the importance of physical quantities (e.g., the small-scale energy or the dissipation rate).

The proposed error-indicator $\overline{\mathcal{G}}(\mathbf{x}, \mathbf{n})$, defined in Eqn. 5.7, estimates the error

introduced into the LES evolution equation at location $\mathbf{x}$ caused by an insufficient filter-width in direction $\mathbf{n}$. More specifically, the error-indicator measures the initial divergence between the test-filtered LES solution and an imagined solution to the test-filtered LES equation. In other words, it measures how sensitive the LES equation is to small (directional) changes in the filter-width. While the error-indicator is based on manipulations of the governing equation, it is also based on the assumption that the source of initial divergence between these different solutions is a meaningful measure of the error in the fully nonlinear long-time evolution of the LES. This is really the key physical assumption in this work.

For the channel, the algorithm consistently produces grids/filter-widths that are very close to what is considered "best practice" in LES and DNS: grids with $(\overline{\Delta}_x^+, \overline{\Delta}_{y_w}^+/2, \overline{\Delta}_z^+) \approx (45, 1.7, 19)$ and $(13, 1.2, 6.4)$, respectively. Note that the wall-normal resolutions of these grids are much finer than those generated by the previous error-indicator $\overline{\mathcal{A}}(\mathbf{x}, \mathbf{n})$ with resolutions of $(46, 2.9, 22)$ and $(14, 1.6, 6.8)$ on grids with the same N_{tot} (Table 5.5).

For the backward-facing step, the predicted grids are close to what an experienced user might produce. It is essentially impossible to say how "optimal" (in the mathematical sense) the grids are for this problem, but we note that the error (compared to DNS) reaches about 5% with only 600K to 2M cells; it is hard to imagine an experienced user creating a better grid than that, at least without significant trial-and-error. Once again, the wall normal resolution of the incoming boundary layer (Table 5.6) is much closer to what we expect, suggesting that the relatively coarse wall-normal resolution of the grids generated by $\overline{\mathcal{A}}(\mathbf{x}, \mathbf{n})$ that we

mentioned as one of its shortcomings that we wished to address is now fixed by the new indicator $\overline{\mathcal{G}}(\mathbf{x}, \mathbf{n})$.

The subgrid/subfilter model used in the LES solution enters directly into the definition of the residual forcing term and thus the error-indicator. Besides, the definition of the residual forcing term is different for different LES formulations (e.g., Eqn. 5.6 for implicitly filtered LES of incompressible flows, Eqn. 5.16 for explicitly filtered LES of incompressible flows, Eqn. 5.17 for ILES of incompressible flows, Eqn. 5.18 for errors in the momentum equation of the implicitly filtered LES of compressible flows, and 5.20 for errors in the energy equation of compressible implicitly filtered LES). In other words, the proposed error-indicator is fully customizable to the LES formulation and the LES model, meaning that at least theoretically it should be able to generate the most "optimal" grid for each case. This is further confirmed by the results in Tables 5.7 and 5.8 where different LES models led to slightly different target grids. Also clear from the Tables (and from Fig. 5.16) is the robustness of the error-indicator and its target grids to changes in the LES model (and probably LES formulation, although it has not been explicitly tested): despite the change in the target grids, all of them are still "good" grids for LES of wall-bounded flows, and errors in the QoIs are not significantly higher for non-customized formulations.

Another advantage of the proposed error-indicator is its straightforward extensibility to other flow regimes and to include other physics. A derivation for compressible flow is shown in Section 5.6, which creates a separate error-indicator for the energy equation. Following the same process, one could extend it to chemically

reacting flows, etc.

The proposed error-indicator has similarities with the dynamic procedure but was derived without any appeals to scale-similarity in the inertial subrange of turbulence. Its use is not restricted to filter-widths in the inertial subrange, and the derivation in fact offers an alternative explanation for the success of the dynamic procedure.

A potential criticism of this type of sequential refinement of an initial grid to find Δ_{opt} could be the apparent additional cost of performing LES on a full sequence of grids. We discussed this in some detail in Section 3.5, and made four counter arguments. Here we only repeat two of them: (i) for flows where we have a "good guess" of what the grid may be, we can start from our "best guess" and eliminate the first few grids in the sequence; this sequential refinement from coarse and ignorant grids is intended for cases where we do not have that knowledge. And (ii) the cost of doing LES on all grids before $\check{\Delta}_{\text{opt}}$ (i.e. the cost of finding the "optimal" grid) is less than 70% of the solving the LES on $\check{\Delta}_{\text{opt}}$ (assuming that the cell count is doubled in each iteration); this is not significant at all, especially when compared to the potential saving by having a more optimal $\check{\Delta}_{\text{opt}}(\mathbf{x}, \mathbf{n})$.

There are still a few possible directions in which the proposed error-indicator $\overline{\mathcal{G}}(\mathbf{x}, \mathbf{n})$ can be improved.

The present error-indicator was derived for the continuous governing equation and as such does not directly estimate any numerical errors. The adaptation algorithm was still found to perform well for the DNS of the channel flow (which has only numerical errors), but it may still be required to explicitly include the numerical

errors in the error-indicator in other flows.

We also note that the error-indicator arguably measures the sensitivity of the solution at the test-filter level and not at the LES filter level $\overline{\Delta}$. This is perfectly fine for the final grid(s), but may not be ideal for the initial grids in the sequence that are far from resolving the inertial subrange of the turbulence. One possibility is to investigate approaches similar to that of Porte-Agel *et al.* [81] who revised the dynamic procedure to work better on underresolved grids.

And finally, we remember that $\overline{e}^{\text{DNS}}_{\text{QoI}}$ and $\overline{e}_{\text{surr}}$ had very different convergence behaviors (Figs. 5.13 and 5.15), to a point where $\overline{e}_{\text{surr}}$ remained nearly unchanged on a few of the intermediate grids in the sequence, and started decreasing again only when the DNS resolution was reached. This is while $\overline{e}^{\text{DNS}}_{\text{QoI}}$ was constantly decreasing on those grids (Fig. 5.13). We argued that a plausible explanation would be that the value of $\overline{\mathcal{G}}_{\text{tot}}(\mathbf{x})$ may not be a great representation of the value of $\overline{e}^{\text{ref}}_{\text{local}}(\mathbf{x})$, but their qualitative spatial distributions must clearly be close, to explain the convergence of $\overline{e}^{\text{DNS}}_{\text{QoI}}$ and the improved results over the grids generated by $\overline{\mathcal{A}}(\mathbf{x}, \mathbf{n})$ (that were already really good). This inconsistency between the magnitudes of $\overline{\mathcal{G}}_{\text{tot}}(\mathbf{x})$ and $\overline{e}^{\text{ref}}_{\text{local}}(\mathbf{x})$ did not seem to be an issue in any of the test cases considered here; however, such inconsistencies are always dangerous, since the same may happen qualitatively as well, i.e., that the relative change in the value of $\overline{\mathcal{G}}_{\text{tot}}(\mathbf{x})$ may become different from the relative change in the value of $\overline{e}^{\text{ref}}_{\text{local}}(\mathbf{x})$, leading to an inaccurate localization of the error source, and consequently, grids that are not optimal. This means that, despite the many advantages of the new error-indicator $\overline{\mathcal{G}}(\mathbf{x}, \mathbf{n})$ over the old one $\overline{\mathcal{A}}(\mathbf{x}, \mathbf{n})$, the problem of error-estimation in LES is still far from fully solved,

and more work still needs to be done. This motivates our third error-indicator in Chapter 8.

Chapter 6: Statistical convergence of the error-indicators and their target grids

Most quantities of interest in LES depend on the large scales of motion, which then require a relatively long averaging time for adequate convergence. In contrast, the error-indicators of Chapters 3 and 5 depend on the smallest resolved scales and should therefore converge more quickly. The implication is that one could in practice reduce the cost of the adaptation process by running only short simulations on many of the grids, and start collecting long averages only for the finer grids whose resolutions are deemed adequate to produce converged results. In this Chapter we study the sensitivity of the error-indicators proposed in Chapters 3 and 5 and their target grids to insufficient averaging in time.

The convergence assessment is done only for the backward-facing step flow, for which we have 400 snapshots spaced $2.5H/U_\infty$ apart in time. The error-indicators computed for grid $\overline{\Delta}(\mathbf{x},\mathbf{n})$ using all 400 snapshots are labeled $\overline{\mathcal{A}}_{\text{ref}}(\mathbf{x},\mathbf{n})$ and $\overline{\mathcal{G}}_{\text{ref}}(\mathbf{x},\mathbf{n})$, and the refinement level of their target grids, $\check{\Delta}(\mathbf{x},\mathbf{n})$, are labeled $\check{\mathcal{R}}_{\text{ref}}(\mathbf{x},\mathbf{n})$ (for both error-indicators), quantified as

$$\check{\mathcal{R}}(\mathbf{x},\mathbf{n}) = \log_2 \frac{\check{\Delta}(\mathbf{x},\mathbf{n})}{\Delta_0(\mathbf{x},\mathbf{n})}\,, \tag{6.1}$$

where $\Delta_0(\mathbf{x},\mathbf{n}) = 0.2$ for all $\mathbf{x}$ and $\mathbf{n}$ (this $\check{\mathcal{R}}(\mathbf{x},\mathbf{n})$ is what was plotted in Figs. 3.9, 4.9,

and 5.6). All target grids in this Chapter are such that the cell count is doubled from grid $\overline{\Delta}$ to $\check{\Delta}$.

We also consider averages over batches of m snapshots only, for which the resulting error-indicators and their target refinement levels are labeled $\overline{\mathcal{G}}_{m,j}(\mathbf{x},\mathbf{n})$, $\overline{\mathcal{A}}_{m,j}(\mathbf{x},\mathbf{n})$, and $\check{\mathcal{R}}_{m,j}(\mathbf{x},\mathbf{n})$, respectively, where j is the batch number. The errors due to insufficient averaging are then defined as

$$\begin{aligned}
\mathcal{E}_{\mathcal{G}}(m;j) &= \frac{\sum_i \iint_\Omega \left|\overline{\mathcal{G}}_{m,j}(\mathbf{x},\mathbf{n}_i) - \overline{\mathcal{G}}_{\text{ref}}(\mathbf{x},\mathbf{n}_i)\right| d\mathbf{x}}{\sum_i \iint_\Omega \overline{\mathcal{G}}_{\text{ref}}(\mathbf{x},\mathbf{n}_i) d\mathbf{x}} \\
\mathcal{E}_{\mathcal{A}}(m;j) &= \frac{\sum_i \iint_\Omega \left|\overline{\mathcal{A}}_{m,j}(\mathbf{x},\mathbf{n}_i) - \overline{\mathcal{A}}_{\text{ref}}(\mathbf{x},\mathbf{n}_i)\right| d\mathbf{x}}{\sum_i \iint_\Omega \overline{\mathcal{A}}_{\text{ref}}(\mathbf{x},\mathbf{n}_i) d\mathbf{x}} \\
\mathcal{E}_{\mathcal{R}}(m;j) &= \frac{\sum_i \iint_\Omega \left|\check{\mathcal{R}}_{m,j}(\mathbf{x},\mathbf{n}_i) - \check{\mathcal{R}}_{\text{ref}}(\mathbf{x},\mathbf{n}_i)\right| d\mathbf{x}}{\sum_i \iint_\Omega \left|\check{\mathcal{R}}_{\text{ref}}(\mathbf{x},\mathbf{n}_i)\right| d\mathbf{x}}
\end{aligned} \tag{6.2}$$

where $\Omega : \mathbf{x} = (x, y) \in [-20H, 25H] \times [-H, 5H]$ is taken as the full two-dimensional domain subject to grid selection/adaptation.

Since all three of $\overline{\mathcal{G}}_{m,j}(\mathbf{x},\mathbf{n})$, $\overline{\mathcal{A}}_{m,j}(\mathbf{x},\mathbf{n})$, and $\check{\mathcal{R}}_{m,j}(\mathbf{x},\mathbf{n})$ are random variables, their errors (Eqn. 6.2) are also random variables. A 90% two-sided prediction interval is computed for each of these variables using the sample mean and sample standard deviation of $\mathcal{E}_{\mathcal{G}}(m;j)$, $\mathcal{E}_{\mathcal{A}}(m;j)$ and $\mathcal{E}_{\mathcal{R}}(m;j)$ and the Student's t-distribution (cf. [65] for more details on prediction intervals). These prediction intervals are shown in Fig. 6.1 for $\overline{\mathcal{A}}(\mathbf{x},\mathbf{n})$ (using both the heuristic and modified grid selection criteria) and in Fig. 6.2 for $\overline{\mathcal{G}}(\mathbf{x},\mathbf{n})$ (using only the modified criterion).

To interpret the results, we need to decide what constitutes acceptable errors in $\mathcal{E}_{\mathcal{G}}$, $\mathcal{E}_{\mathcal{A}}$, and $\mathcal{E}_{\mathcal{R}}$. This was done by visually looking at different random realizations at different error levels: error levels of 0.05 in all three quantities were deemed to be definitely acceptable, meaning that the random variation between batches did not

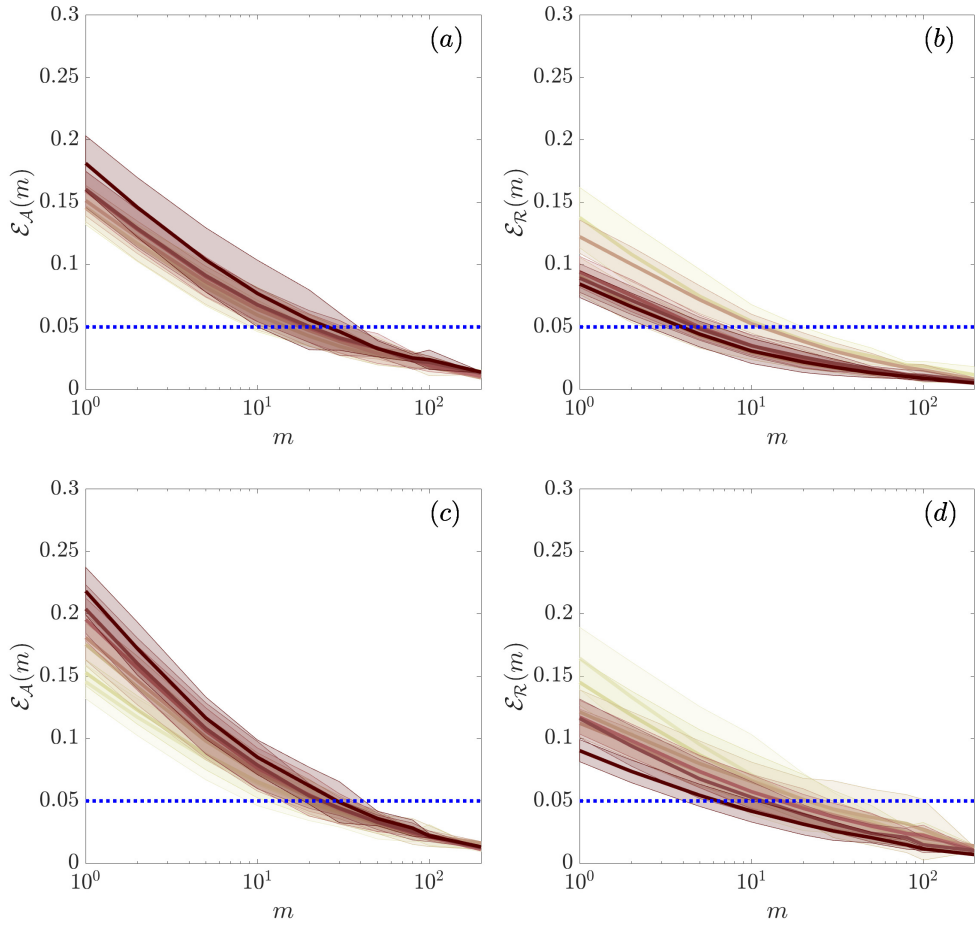

Figure 6.1: Convergence of the error-indicator $\overline{\mathcal{A}}(\mathbf{x}, \mathbf{n})$ (left column) and the refinement levels of the target grid $\check{\mathcal{R}}(\mathbf{x}, \mathbf{n})$ (right column) with the number of snapshots m used in the averaging. The top row corresponds to the sequence of "LES" grids in Table 3.4 (generated using the heuristic criterion of Chapter 3), while the bottom row corresponds to the sequence of "A" grids (Table 5.6) generated by the modified grid selection criterion. The grids are shown by the lightest color for LES-1 (or A-1) to the darkest for LES-6 (or A-7). The solid lines show the sample means of $\mathcal{E}_{\mathcal{A}}(m; j)$ and $\mathcal{E}_{\mathcal{R}}(m; j)$, while the shaded regions highlight the 90% prediction interval of the computed values. When the upper bound of the prediction interval goes below the horizontal dotted line there is a 95% chance that the error metric for a single realization is below 0.05. The required integration times can be computed as $2.5\, m_r\, H/U_\infty$ (m_r being the required number of snapshots) and are reported in Table 6.1.

significantly change the levels of $\overline{\mathcal{A}}$, $\overline{\mathcal{G}}$ or $\check{\mathcal{R}}$, and how they were distributed over the domain (compared to the reference). The 0.05 level is shown as a horizontal line in Figs. 6.1 and 6.2.

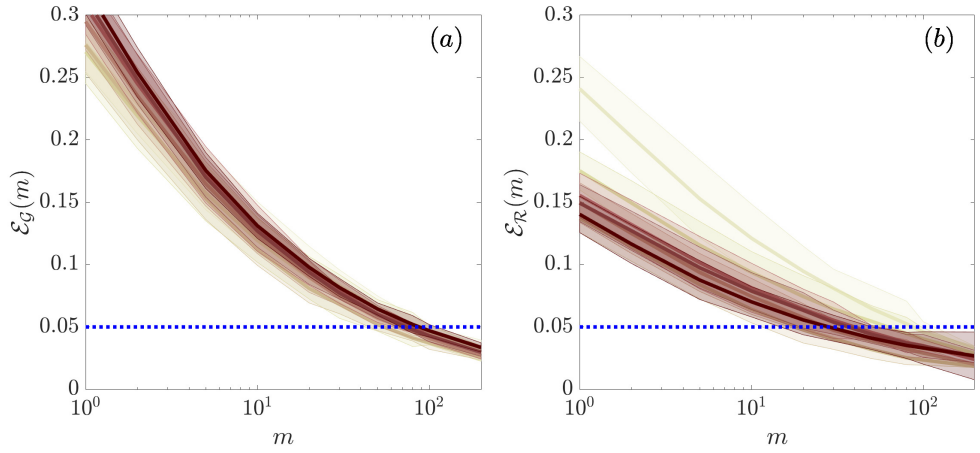

Figure 6.2: Convergence of (a) the error-indicator $\overline{\mathcal{G}}(\mathbf{x}, \mathbf{n})$ and (b) the refinement levels of the target grid $\check{\mathcal{R}}(\mathbf{x}, \mathbf{n})$ with the number of snapshots m used in the averaging. Results are for the "G" grids in Table 5.6. The grids are shown by the lightest color for G-1 to the darkest for G-7. See the caption of Fig. 6.1 for more details. Compare the results to Fig. 6.1.

When the upper bound of the prediction interval lies below the acceptable threshold, there is a 95% chance that the error metric in a single realization of the flow, averaged over m snapshots, is below the acceptable value of 0.05. The approximate integration times required for this to happen are summarized in Table 6.1 (for all grids), along with the simulation times used in Sections 3.3, 4.6, and 5.3 for plotting the QoI profiles.

We can make a few interesting observations from Table 6.1. First and foremost, it is quite clear that $t_{\mathcal{A}/\mathcal{G}}$ (run time required for sufficient convergence of either of the error-indicators) and $t_{\mathcal{R}}$ (run time required for sufficient convergence of their target grids) are significantly lower (by about one order of magnitude) compared to what is needed for sufficiently converged QoI profiles (t_{QoI}). This verifies what we discussed earlier about the faster convergence of the error-indicators.

The second interesting observation is that the target grids "A" in Table 6.1 (for

Grid	N_{tot}	$t_{\text{QoI}}U_\infty/H$	$t_{\mathcal{A}/\mathcal{G}}U_\infty/H$	$t_{\mathcal{R}}U_\infty/H$
LES-1	149k	1000	75	50
LES-2	293k	1000	50	15
LES-3	596k	1000	75	40
LES-4	1.28M	1000	85	20
LES-5	2.22M	1000	90	20
LES-6	3.59M	1000	100	20
A-1	149k	1000	75	95
A-2	297k	1000	75	110
A-3	599k	1000	95	250
A-4	1.35M	1000	90	75
A-5	2.17M	1000	100	75
A-6	3.70M	1000	80	50
A-7	7.26M	1000	110	30
G-1	149k	2000	260	290
G-2	297k	2000	280	250
G-3	611k	2000	150	80
G-4	1.32M	2000	220	100
G-5	2.13M	2000	240	140
G-6	3.41M	2000	210	140
G-7	6.72M	2000	280	130

Table 6.1: The simulation times used for sufficiently converged mean QoI profiles, t_{QoI}, (reported in results of Sections 3.3, 4.6, and 5.3) compared against the integration time required for accurate computation of the error-indicator, $t_{\mathcal{A}/\mathcal{G}}$, and the refinement levels of the target grid, $t_{\mathcal{R}}$. The required integration times are computed as $2.5\,m\,H/U_\infty$, where m is the number of snapshots required for the upper bound of the prediction intervals in Figs. 6.1 and 6.2 to go below the horizontal lines. The longer t_{QoI} for the "G" grids was to increase the accuracy of the results, and was not required.

which the modified grid selection criterion was used) need a longer $t_{\mathcal{R}}$ compared to the "LES" grids for which the heuristic criterion was used, while $t_{\mathcal{A}/\mathcal{G}}$ is very similar for both. This is actually consistent with the effect of the modified criterion on the target grids; in other words, a larger portion of the domain is selected for refinement, which means that (i) there are more degrees of freedom for how the computational cells are selected for refinement/coarsening, and (ii) most of these extended regions are areas that exhibit highly unsteady behavior, e.g., near the edge of the boundary

layer. Both of these result in a slower convergence of the target grids.

And the third observation is that the error-indicator $\overline{\mathcal{G}}$ of Chapter 5 requires a longer convergence time ($t_{\mathcal{A}/\mathcal{G}}$) compared to $\overline{\mathcal{A}}$ of Chapter 3 (compare grids "A" and "G" in Table 6.1). The exact reason for this is not fully clear, as both the error-indicators are small-scale quantities; however, we should point out that there is no need for them to converge at the same rate anyway. The slower convergence of the target grids generated by $\overline{\mathcal{G}}(\mathbf{x}, \mathbf{n})$ is presumably due to the slow convergence of the error-indicator itself.

We conclude this Chapter by emphasizing that the exact results presented here are specific to the flow over a backward-facing step, the sampling frequency, and other flow parameters; however, the conclusion about a much faster convergence of the error-indicator and target grids compared to the QoI profiles, the slower convergence of $\overline{\mathcal{G}}(\mathbf{x}, \mathbf{n})$ compared to $\overline{\mathcal{A}}(\mathbf{x}, \mathbf{n})$, and the slower convergence of the target grids predicted by the modified criterion are probably more general and valid for a broader set of flows.

Chapter 7: Towards robust convergence-verification and algorithmic grid selection/adaptation in LES

Any robust and systematic computational simulation should follow an algorithm that consists of three essential parts: (i) convergence-verification, to make sure that the results and their observed patterns come from the physics of the problem and not the unavoidable errors associated with almost any discretized simulation, (ii) error-estimation, to locate where the errors are introduced into the solution and its QoIs, (iii) grid-adaptation, to enable an efficient path towards the "optimal" grid−the grid that satisfies the convergence-verification criteria with the lowest computational cost. This systematic algorithm is shown in Fig. 7.1.

It is useful to study a more detailed example of such algorithms, namely, the adjoint-weighted residual method for RANS and laminar simulations. The algorithm is sketched in Fig. 7.2. In each iteration the algorithm

(i) estimates the local sources of error;

(ii) solves the adjoint equations to link the change in the QoIs to those local error sources;

(iii) estimates the error in all QoIs from the adjoint fields and the local error sources (convergence-verification);

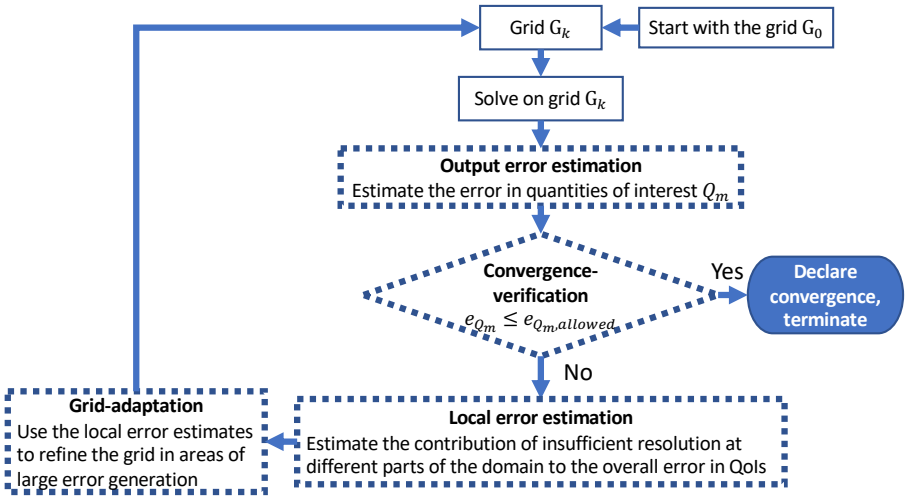

Figure 7.1: A typical grid-adaptation algorithm (same as Fig. 1.5). The boxes with dotted borders are those that are different between LES and other computational simulations, and have been the subject of study in this dissertation.

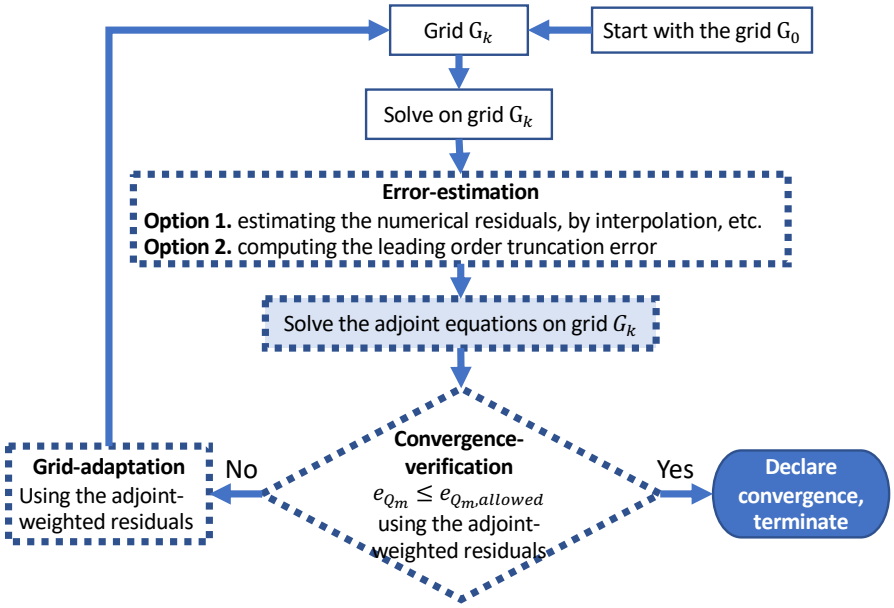

Figure 7.2: The standard adjoint-weighted residual method used for convergence-verification and grid-adaptation in RANS and laminar flows. Dotted borders mean that the process cannot be directly applied to LES. The shaded box shows the process that has a computational cost comparable to that of the original solution.

(iv) use the "adjoint-weighted residuals" to adapt the grid if the error in the QoIs is above an acceptable threshold.

Note that the order of different processes in the "adjoint-weighted residual"

algorithm is slightly modified (compared to Fig. 7.1) to increase the efficiency. Particularly, the error-estimation and adjoint solution processes are done before the convergence-verification step, since they are needed for robust convergence-verification (see Fig. 7.3). Unfortunately, based on what we have discussed in Chapters 1 and 2, the boxes with dotted borderlines in Fig. 7.2 are those parts of the algorithm that cannot be simply used or generalized for LES. Consequently, despite the efficiency and overall advantage of the adjoint-weighted residual method, it cannot be directly applied to LES, and we need a new algorithm. The order of different processes involved in the algorithm should also be modified consistent with these changes.

In this Chapter, we first address the problem of convergence-verification in LES, and then we propose an algorithm that is designed around that verification process.

7.1 Convergence-verification

Among the three possible convergence-verification methods available from the literature (Fig. 7.3), the adjoint-weighted residual method is the most robust and most efficient method; however, the presence of the modeling errors in LES introduce an inherent uncertainty to the estimated errors (see Section 2.2). This reasoning leads to the idea that convergence-verification based on estimated local error sources will always carry an uncertainty, and (crucially) that this uncertainty has nothing to do with the adjoint itself. Therefore, solving the "chaotic adjoint problem" is not

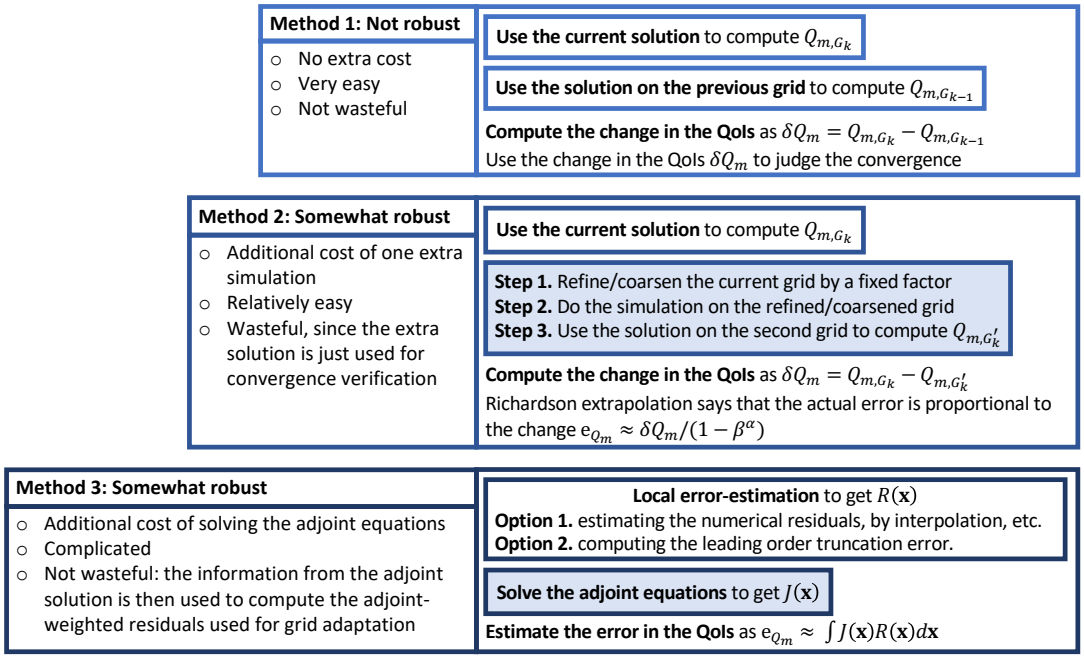

Figure 7.3: A review of different approaches to convergence-verification (same as Fig. 2.5). The shaded boxes denote the processes with computational costs that are of the same order of magnitude as the original simulation. Robustness of the methods are judged for laminar and RANS simulations. Methods 1 and 2 can be readily applied to both LES and DNS, while for application of method 3 to DNS we should first find a way to avoid the chaotic divergence of the adjoint fields for long time integrations. Having found a way to compute the adjoint fields, method 3 can be used for convergence-verification in LES as well; however, it is no longer fully robust, since error-estimation in LES cannot be fully robust (because of the projection errors).

sufficient, and we must also find a method to verify grid-convergence with greater confidence.

Given the uncertainties in estimating the local error sources in LES (due to the modeling errors and the uncertainty of our estimate of them because of the projection errors), it stands to reason that any robust convergence-verification test should essentially involve varying the uncertainty due to the effect of the projection errors. Assuming a constant ratio between filter-width and grid-size, we hypothesize that the only (?) way to verify grid-convergence with confidence is to compare actual

LES solutions from different grids with different projection errors.

The two grids used for such convergence-verification must be such that they do not produce the same error sources anywhere in the domain; otherwise, the two grids could produce similar solutions despite neither being grid-converged. This leads to the following criteria on the relation between the original LES grid (subject to convergence-verification) and the test grid (as the second LES solution):

(a) The two grids cannot be built based on the same assumptions about the necessary resolution requirements (e.g., the user expertise or an error-indicator). A corollary is that one cannot use two grids from a sequence of adapted grids to truly verify grid-convergence (cf. Venditti and Darmofal [40] for some examples).

(b) They cannot have any regions with the same grid spacing.

(c) They cannot have similar resolution in any one direction.

(d) At least one of the grids must produce a "meaningful" LES solution, i.e., have some reasonable amount of resolved turbulence.

One systematic way of generating a suitable "test" grid is to refine or coarsen the original grid uniformly (i.e., with the same factor everywhere) and isotropically (with the same factor in all directions). A distinct advantage of this uniform refinement/coarsening factor is that it allows us to use the Richardson extrapolation technique and have a better estimate of the error in the QoIs [22, 25, 26]. All of these arguments clearly favor "method 2" of Fig. 7.3 as the "best" choice for convergence-verification in LES.

Having access to the LES solutions from two grids, the convergence criterion

for each of the QoIs becomes

$$\overline{e}_{Q_m} \approx \left| \frac{\delta \overline{Q}_m}{1-\beta^\alpha} \right| \leq e_{Q_m,\text{allowed}} \,, \tag{7.1}$$

where β is the uniform refinement/coarsening factor between grids G_k and G'_k (i.e., $\beta = \overline{\Delta}'/\overline{\Delta}$, where $\overline{\Delta}'$ is the characteristic filter-width of grid G'_k), α is the assumed scaling of the results with the change in the filter-width, and $e_{Q_m,\text{allowed}}$ is the acceptable threshold. Note that in when the quantities of interest are defined as fields rather than scalars (e.g., mean velocity or Reynolds stress profiles) $\delta \overline{Q}_m$ should be defined as the volume average of absolute value of the local difference in the QoIs (e.g., Eqns. 3.9 and 3.11), and the above equation is modified slightly as

$$\overline{e}_{Q_m} \leq \left| \frac{\delta \overline{Q}_m}{1-\beta^\alpha} \right| \leq e_{Q_m,\text{allowed}} \,.$$

The coarsening of the grid ($\beta > 1$) is usually favored over its refinement, since the computational cost of solving the LES equations on the test grid $\overline{\Delta}' = \beta\overline{\Delta}$ is approximately a factor $(1/\beta)^4$ of the cost of the original LES solution on grid $\overline{\Delta}$. Note that the refinement can be theoretically done with almost any factor (although the computational cost may become prohibitive), while for coarsening the user may want to consider smaller factors such that the test is still meaningful. In other words, β is limited by the computational cost as its lower bound and by the meaningfulness of the test as its upper bound.

7.2 The proposed algorithm

The robust adaptation/verification algorithm of Fig. 7.1 consisted of four processes: output error-estimation, convergence-verification, local error-estimation, and

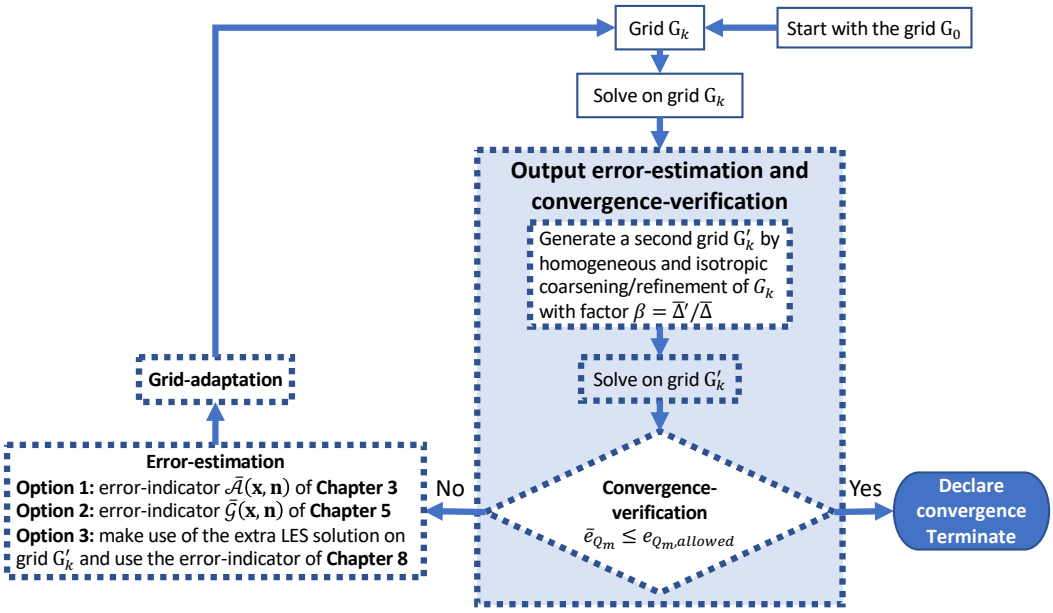

Figure 7.4: The proposed algorithm for convergence-verification and grid-adaptation in LES. Boxes with dotted borders correspond to the redesigned processes for LES. The shaded box corresponds to the process whose cost is comparable to the original LES solution.

grid-adaptation. Chapters 3 and 5 addressed the problem of local error-estimation in LES, while Chapter 4 focused on the grid selection/adaptation process of the algorithm. Section 7.1 of this Chapter addressed the convergence-verification process, and since the convergence-verification is done by running an extra simulation with a uniform refinement/coarsening factor β, the output error-estimation simply becomes the use of Eqn. 7.1 to approximate $\bar{e}_{Q_m}$. At this point, all the different processes involved in a robust adaptation/verification algorithm are discussed, and we can finally assemble a robust algorithm for LES. This is shown in Fig. 7.4.

7.3 Cost of the algorithm

There are two main factors contributing to the cost of the algorithm: (i) all the G_k simulations prior to the one that is declared converged (denoted by G_{final}), and (ii) all the simulations performed on grids G'_k, including G'_{final}.

In Section 3.5 we addressed the additional cost of the iterative adjustment of the LES grid/filter (i.e. the cost of performing LES on grids G_k). In summary we argued that:

- If the cell count is doubled between G_k and G_{k+1}, the additional cost of all simulations prior to G_{final} is only 66% of the cost of solving on G_{final} itself (this reduces to 19% if the cell count is quadrupled).

- There is no need to start from a very coarse grid: if we have a "good guess" of what G_{final} should look like we can start from that "best guess" and reach G_{final} in only a couple of iterations.

- The error-indicators and the target grids usually converge much faster than the QoI profiles (see Table 6.1 and Figs. 6.1 and 6.2); therefore, in practice one could cut the simulation time (and consequently the cost) for many of the grids prior to G_{final} and perform full simulations on the fine grids only.

- The additional cost of performing LES on a sequence of grids should of course be compared to the potential saving due to a more optimal G_{final}.

The additional cost of the convergence-verification process (i.e., performing LES on the G'_k grids) is a direct function of the refinement/coarsening factor $\beta \approx$

$\overline{\Delta}'/\overline{\Delta}$, and approximately scales as β^{-4}. If we take $\beta = 1.25$ (we usually favor coarsening to reduce the cost), the additional cost of running full simulations on all the G'_k grids is approximately 68% ($(1/1.25)^4 \times 1.66 \approx 0.68$) of the cost of the LES on G_{final}. We can make very similar remarks about this additional cost

- If the user starts from a "best guess" grid this additional cost is reduced.
- There is no need to perform convergence-verification on the initial grids that are too coarse to produce accurate results. These are the same grids for which the user could perform short simulations.
- Most of the additional cost of the G'_k grids comes from G'_{final} (around 60% if the cell count is doubled in each iteration, and 85% if it is quadrupled). This is the price that one has to pay to ensure the convergence of the results, and must not be subject to compromise.

The existence of the LES solution on G'_k grids also means that we have some extra *a posteriori* information available on the response of the LES solution on grid G_k to a (uniform) change in its filter-width $\overline{\Delta}(\mathbf{x}, \mathbf{n})$. Given that the error-estimation in LES has always involved some approximation, this extra information can actually be used to define a more accurate estimate of the local sources of errors. This can potentially lead to a more optimal G_{final}, which further reduces the cost of the algorithm. This "two-grid" error-indicator is defined in Chapter 8 with some preliminary assessments on the channel flow and the flow over a backward-facing step.

Chapter 8: Error-estimation using the solution on more than one grid

One major shortcoming of the error-indicator $\overline{\mathcal{A}}(\mathbf{x}, \mathbf{n})$ of Chapter 3 was the lack of its direct connection to the governing equations. This was addressed later in Chapter 5 by defining $\overline{\mathcal{G}}(\mathbf{x}, \mathbf{n})$, which was a measure of sensitivity of the governing equations to the filter-width. While a major theoretical improvement over $\overline{\mathcal{A}}(\mathbf{x}, \mathbf{n})$, this error-indicator was still based on the smaller scales of the motion and did not solve the disconnect between the value of the error-indicator and the error in the QoIs (as portrayed in Section 5.4). In this Chapter, we make another attempt to address this disconnect, and define an error-indicator that is more directly connected to both the governing equations and the error in the QoIs.

The other inspiration behind the developments of this Chapter is the algorithm proposed in Fig. 7.4 for convergence-verification and grid selection/adaptation in LES. Every time we perform the proposed convergence-verification test, we get access to two LES solutions: one on the original grid G_k, and the other on the slightly "perturbed" version of that grid, G'_k. Since accurate error-estimation has always been an issue in LES, the idea in this Chapter is that we may as well take advantage of this extra information and hopefully come up with a more accurate

estimate of the source of errors.

The chaotic nature of the LES solution means that a direct comparison between any two independent solutions is meaningless. The alternative is to either (i) synchronize the two solutions periodically, or (ii) to focus on the statistics of the two solutions instead. The first approach is not fully desirable since it may either alter the result of the convergence-verification test (if we only use statistics that are stored at a fixed time after synchronization), or require two separate LES runs on the same test grid (where one runs independently and is only used for convergence-verification, while the other one is periodically synchronized with the original LES solution and is used only for error-estimation). In this Chapter we take the second approach with an added distinct advantage that it can be later (as a subject for future research) complemented with the adjoint fields of those statistics [82] (that are no longer chaotic, and can be solved with minimal computational cost by solving the mean adjoint equations) to enable "output-based" grid-adaptation in LES.

We should emphasize that the results presented in this Chapter are somewhat preliminary and mostly a "proof of concept". In the same spirit, some of the target grids are not as "good" as what we have seen in Chapters 3 and 5 for the other two error-indicators $\overline{\mathcal{A}}(\mathbf{x}, \mathbf{n})$ and $\overline{\mathcal{G}}(\mathbf{x}, \mathbf{n})$; however, this should not be interpreted as an inherent deficiency of the new approach, but only that it is still under development.

8.1 The proposed error-indicator

The governing equation for implicitly filtered large eddy simulation (LES) of an incompressible, constant-viscosity, Newtonian fluid reads

$$\frac{\partial \overline{v}_i}{\partial t} + \frac{\partial}{\partial x_j}\overline{v}_i\overline{v}_j + \frac{1}{\rho}\frac{\partial \overline{q}}{\partial x_i} - \nu\frac{\partial^2 \overline{v}_i}{\partial x_j \partial x_j} + \frac{\partial \tau_{ij}}{\partial x_j} = 0\,, \tag{8.1}$$

where $\overline{v}_i$ and $\overline{q}$ are the "exact" resolved velocity and pressure fields at the LES filter level $\overline{\Delta}$, $\bar{\cdot}$ denotes the filtering process, and τ_{ij} is the exact SGS stress tensor $\tau_{ij} = \overline{v_i v_j} - \overline{v}_i\overline{v}_j$.

Denoting the discrete temporal and spatial differentiation by $\delta/\delta t$ and $\delta/\delta x_j$ respectively, the equation that the code actually solves reads

$$\frac{\delta \overline{u}_i}{\delta t} + \frac{\delta}{\delta x_j}\overline{u}_i\overline{u}_j + \frac{1}{\rho}\frac{\delta \overline{p}}{\delta x_i} - \nu\frac{\delta^2 \overline{u}_i}{\delta x_j \delta x_j} + \frac{\delta \tau_{ij}^{\mathrm{mod}}}{\delta x_j} = 0\,, \tag{8.2}$$

where $\overline{u}_i$ and $\overline{p}$ are the resolved velocity and pressure fields from the numerical simulation, and τ_{ij}^{mod} is computed based on the LES model used in the code. Equation 8.2 can be equivalently written (by replacing all numerical differentiations by their analytical version) as

$$\frac{\partial \overline{u}_i}{\partial t} + \frac{\partial}{\partial x_j}\overline{u}_i\overline{u}_j + \frac{1}{\rho}\frac{\partial \overline{p}}{\partial x_i} - \nu\frac{\partial^2 \overline{u}_i}{\partial x_j \partial x_j} + \frac{\partial \tau_{ij}^{\mathrm{mod}}}{\partial x_j} = -f_i^{\mathrm{num}}\,, \tag{8.3}$$

where all the difference between the numerical and analytical operators is included in the forcing term f_i^{num} that describes the direct effect of the numerical errors on the resolved fields.

An evolution equation for the error in the solution $\overline{e}_i = \overline{v}_i - \overline{u}_i$ can then be

derived (similar to Chapter 5) by taking the difference between Eqns. 8.2 and 8.3

$$\frac{\partial \overline{e}_i}{\partial t} + \frac{\partial}{\partial x_j}\left(\overline{u}_i\overline{e}_j + \overline{e}_i\overline{u}_j + \overline{e}_i\overline{e}_j\right) + \frac{1}{\rho}\frac{\partial \overline{\Pi}}{\partial x_i} - \nu\frac{\partial^2 \overline{e}_i}{\partial x_j \partial x_j} + \underbrace{\frac{\partial}{\partial x_j}\left(\tau_{ij}^{\text{mod}} - \tau_{ij}\right)}_{-f_i^{\text{mod}}} = f_i^{\text{num}}, \quad (8.4)$$

where $\overline{\Pi} = \overline{q} - \overline{p}$ is the error in the resolved pressure field.

We can identify two distinct source terms in Eqn. 8.4, f_i^{num} and f_i^{mod}, where f_i^{num} is completely of numerical nature, and we consider f_i^{mod} as the modeling error (τ_{ij}^{mod} is the numerical implementation of the LES model in the code, thus f_i^{mod} in fact contains some contribution from the numerical errors as well). The goal is then to estimate and minimize $f_i^{\text{tot}} = f_i^{\text{num}} + f_i^{\text{mod}}$.

The numerical contribution f_i^{num} can be easily computed by evaluating the left-hand side (lhs) of Eqn. 8.3, where the exact differentiations can be approximated by interpolating $\overline{u}_i$ and $\overline{p}$ onto a sufficiently fine grid using an appropriate interpolation operator (e.g. similar to the approach proposed by [27] for interpolating the LES fields) and computing the derivatives on that grid.

Estimating the modeling error f_i^{mod} requires estimation of the exact residual stress tensor τ_{ij} and is much more involved. Many researchers tried estimating τ_{ij} using the approximate deconvolution of the velocity fields (cf. [3,44,83,84]) or using the scale similarity models (cf. [32–34]). However, a significant part of τ_{ij} could be due to the completely unresolved scales (including their direct and indirect effects) that can never be recovered by an approximate deconvolution method, or in fact any method (cf. [83]). This means that an accurate estimate of the modeling errors in LES essentially involves comparing the solution to another LES or DNS (for the same reason as Chapter 7). This can be done in two ways: (i) comparing the

instantaneous fields, or (ii) comparing the mean fields. The error-indicator of this Chapter is developed based on the latter approach, which will require a more careful development and formulation compared to when one uses the instantaneous fields. This careful treatment is addressed in the rest of this Chapter.

The quantities of interest from an LES should all be only functions of the larger scales of the motion. For a quantity of interest Q_m this assumption can be expressed as

$$Q_m = Q_m(v_i, q) \approx \overline{Q}_m(\overline{v}_i, \overline{q}, \tau_{jk})\,. \tag{8.5}$$

Both Q_m and $\overline{Q}_m$ may have some type of averaging in their definition, such that the QoI is a statistic of the solution and not a single realization of it. In this Chapter, we only consider the statistically stationary flows with long-averaged QoIs, for which we can go one step further and assume that $\overline{Q}_m$ can be approximately described, with sufficient accuracy, by a number of statistics of the instantaneous LES fields; i.e.,

$$\begin{aligned} Q_m &\approx \overline{Q}_m(\overline{v}_i, \overline{q}, \tau_{jk}) \\ &\approx \overline{\mathcal{Q}}_m(\langle\overline{v}_i\rangle, \langle\overline{q}\rangle, \langle\tau_{jk}\rangle, \langle\overline{v}_i'\overline{v}_j'\rangle, \langle\overline{q}'\overline{q}'\rangle, \langle\tau_{ij}'\tau_{kl}'\rangle, \langle\overline{v}_i'\overline{q}'\rangle, \langle\overline{v}_i'\tau_{jk}'\rangle, \langle\overline{q}'\tau_{jk}'\rangle, ...)\,, \end{aligned} \tag{8.6}$$

where $\langle\cdot\rangle$ denotes a suitable averaging. Description of $\overline{Q}_m$ based on the statistics of the solution has the advantage that those statistics can be directly compared between two independent LES solutions; although, with a disadvantage that instead of estimating the error in a few instantaneous fields (i.e., $\overline{v}_i$, $\overline{q}$ and τ_{ij} for this specific flow) one might have to estimate the error in a large number of statistics.

The next question to answer becomes what statistics are most relevant and

what statistics in the expansion of $\overline{\mathcal{Q}}_m$ can be ignored without a significant loss of accuracy. In the present study we only keep the mean velocity, mean pressure, mean SGS stress, and the mean Reynolds stress; i.e., we assume that

$$Q_m \approx \overline{Q}_m \approx \overline{\mathcal{Q}}_m \approx \overline{\mathbb{Q}}_m(\langle \overline{v}_i \rangle , \langle \overline{q} \rangle , \langle \tau_{jk} \rangle , \langle \overline{v}_i' \overline{v}_j' \rangle) . \tag{8.7}$$

Here, we justify our approximation by "the principle of receding influence", stating that "the n-th moment correlations have markedly less effect on the mean flow than those of $(n-1)$-th order" [85]. This may seem as a limiting and perhaps inadequate assumption; however, we should note that this is the same assumption used in almost all RANS models and simulation, where decades of successful application of the RANS models in computing the QoIs in a wide range of flows of engineering interest (cf. [9]) suggests that one can reasonably assume that this assumption holds for most scenarios. The counter argument is that the most important application of LES is for cases where the RANS models fail to predict the correct values. However, we should emphasize that the failure of the RANS model does not necessarily mean that the underlying assumption (i.e. the principle of receding influence) has failed as well; instead, it could mostly be due to the inaccuracy of the RANS models in correct predictions of those moments. In LES we have direct access to the mean fields, Reynolds stresses, and many other statistics, and that should not be a problem.

The goal of the rest of this Section is to find the source of errors in any of the mean fields entering the definition of $\overline{\mathbb{Q}}_m$ in Eqn. 8.7; i.e., to find the error in the mean velocity and pressure fields, as well as the Reynolds and SGS stresses.

8.1.1 Source of error in the mean velocity and pressure fields

We can average Eqn. 8.4 to obtain an evolution equation for the error in the mean velocity field

$$\begin{aligned}\frac{\partial \langle \overline{e}_i \rangle}{\partial t} + \frac{\partial}{\partial x_j}\left(\overline{U}_i \langle \overline{e}_j \rangle + \langle \overline{e}_i \rangle \overline{U}_j + \langle \overline{e}_i \rangle \langle \overline{e}_j \rangle\right) + \frac{1}{\rho}\frac{\partial \langle \overline{\Pi} \rangle}{\partial x_i} - \nu \frac{\partial^2 \langle \overline{e}_i \rangle}{\partial x_j \partial x_j} = \\ - \frac{\partial}{\partial x_j} \underbrace{\left(\langle \overline{u}_i' \overline{e}_j' \rangle + \langle \overline{e}_i' \overline{u}_j' \rangle + \langle \overline{e}_i' \overline{e}_j' \rangle\right)}_{\langle \overline{e}_{ij}^{\mathrm{rs}} \rangle = \langle \overline{v}_i' \overline{v}_j' \rangle - \langle \overline{u}_i' \overline{u}_j' \rangle} + \langle f_i^{\mathrm{mod}} \rangle + \langle f_i^{\mathrm{num}} \rangle\end{aligned} \tag{8.8}$$

where $\overline{U}_i = \langle \overline{u}_i \rangle$ is the mean filtered velocity field, $\langle \cdot \rangle$ denotes a suitable time/ensemble averaging, and $\cdot'$ denotes the fluctuating part of each field. It is clear that $\langle \overline{e}_i \rangle = \overline{V}_i - \overline{U}_i$ is the error in the mean filtered velocity field.

The convective term is decomposed into six different terms, three of which describe the convection of $\langle \overline{e}_i \rangle$ by the mean velocity field or the mean error (kept on the left-hand side of the equation), while the remaining three are interactions between the fluctuating filtered velocity and the error in the fluctuating velocity. These latter three terms are in fact the error in the resolved part of the Reynolds stress, $\langle \overline{e}_{ij}^{\mathrm{rs}} \rangle$, and are moved to the right-hand side of the equation. The divergence of this term, i.e., $\langle f_i^{\mathrm{rs}} \rangle = \partial \langle \overline{e}_{ij}^{\mathrm{rs}} \rangle / \partial x_j$ is an erroneous forcing term that shows up in the mean momentum equation and introduces error into the mean velocity fields.

Based on Eqn. 8.8 there are three important factors in generation of error in the mean velocity fields in an LES: (i) the direct contribution of the numerical error that shows up as an averaged term $\langle f_i^{\mathrm{num}} \rangle$; (ii) the direct contribution of the modeling error, showing up as its average $\langle f_i^{\mathrm{mod}} \rangle$; and (iii) the indirect contribution of both the numerical and modeling errors, affecting the mean velocity field through

the error they introduce into the Reynolds stress $\langle \overline{e}_{ij}^{\text{rs}} \rangle$.

The direct contribution of numerical errors $\langle f_i^{\text{num}} \rangle$ can be easily computed by access to the numerical mean fields and interpolating these mean fields onto a sufficiently fine grid. Nevertheless, a reasonable LES grid is usually sufficiently fine for resolving the mean velocity field, and the resolution requirements are usually imposed by the fluctuating scales (e.g., the Reynolds stress and the subgrid stress). In other words, the direct effect of the numerical error on the mean momentum equation is secondary to the errors in the turbulent field

$$\langle f_i^{\text{num}} \rangle \ll \left\langle \overline{f}_i^{\text{rs}} + f_i^{\text{mod}} \right\rangle . \tag{8.9}$$

This means that obtaining an accurate LES solution of the mean velocity field requires the minimization of

$$\left\langle \overline{f}_i^{\text{rs}} + f_i^{\text{mod}} \right\rangle = \frac{\partial}{\partial x_j} \left[\langle \overline{e}_{ij}^{\text{rs}} + e_{ij}^{\text{mod}} \rangle \right] . \tag{8.10}$$

We can combine the error in the resolved Reynolds stress $\langle \overline{e}_{ij}^{\text{rs}} \rangle$ with the errors in the modeled subgrid stress tensor $\langle e_{ij}^{\text{mod}} \rangle$. This is done by defining the total Reynolds stress as the sum of the resolved and modeled stresses [19, 86] as

$$\overline{T}_{ij}^{\text{tot}} = \langle \overline{v}_i' \overline{v}_j' \rangle + \langle \tau_{ij} \rangle ,$$

with a similar definition for its numerical version as

$$\overline{R}_{ij}^{\text{tot}} = \langle \overline{u}_i' \overline{u}_j' \rangle + \langle \tau_{ij}^{\text{mod}} \rangle ,$$

where we can express the right-hand side of Eqn. 8.10 as

$$\langle \overline{e}_{ij}^{\text{rs}} + e_{ij}^{\text{mod}} \rangle = \langle \overline{e}_{ij}^{\text{RS}} \rangle = \overline{T}_{ij}^{\text{tot}} - \overline{R}_{ij}^{\text{tot}} . \tag{8.11}$$

Note that our definition of $\overline{R}_{ij}^{\text{tot}}$ implies that in an eddy viscosity model the full subgrid stress tensor should be recovered by approximating the SGS kinetic energy (usually absorbed in the modified pressure) using a method similar to Vreman [19, 86].

Equations 8.9 and 8.10 suggest that the source of error in the mean velocity can be recovered by finding the source of error in the total Reynolds stresses. As a corollary, we do not have to directly consider the mean momentum equations anymore, since reducing the error in $\overline{R}_{ij}^{\text{tot}}$ automatically reduces the error in the mean velocity field (similar to our reasoning in Section 5.6 for excluding the mass conservation equation from our analysis).

The Poisson equation for the mean pressure $\langle \overline{q} \rangle$ reads

$$\frac{\partial^2 \langle \overline{q} \rangle}{\partial x_k \partial x_k} = -\rho \frac{\partial^2}{\partial x_i \partial x_j} \left(\overline{V}_i \overline{V}_j + \overline{T}_{ij}^{\text{tot}} \right) , \tag{8.12}$$

which again suggests that we automatically minimize the error in the mean pressure by minimizing the error in the mean velocity field and the total Reynolds stress (assuming negligible effect from the numerical errors).

Therefore, the problem of error-estimation in LES really narrows down to finding the error in the total Reynolds stress.

8.1.2 Source of error in the total Reynolds stress

The source of error in $\overline{R}_{ij}^{\text{tot}}$ can be carefully studied by deriving an evolution equation for $\langle \overline{e}_{ij}^{\text{RS}} \rangle$. This equation can be obtained by subtracting the evolution equation of $\overline{R}_{ij}^{\text{tot}}$ from that of $\overline{T}_{ij}^{\text{tot}}$. The governing equation of the exact field $\overline{T}_{ij}^{\text{tot}} =$

$\left\langle \overline{v}_i' \overline{v}_j' \right\rangle + \langle \tau_{ij} \rangle$ can be derived by either adding the evolution equations of $\left\langle \overline{v}_i' \overline{v}_j' \right\rangle$ and τ_{ij}, or in an algebraically less involved way, by subtracting the evolution equation of $\overline{V}_i \overline{V}_j$ from that of $\langle \overline{v_i v_j} \rangle = \left\langle \overline{v_i' v_j'} \right\rangle + \overline{V_i V_j}$. This equation reads

$$\frac{\partial \overline{T}_{ij}^{\text{tot}}}{\partial t} + \frac{\partial}{\partial x_k}(\overline{V}_k \overline{T}_{ij}^{\text{tot}}) - \nu \frac{\partial^2 \overline{T}_{ij}^{\text{tot}}}{\partial x_k \partial x_k} + \left[\overline{T}_{ik}^{\text{tot}} \frac{\partial \overline{V}_j}{\partial x_k} + \overline{T}_{jk}^{\text{tot}} \frac{\partial \overline{V}_i}{\partial x_k} \right] = \overline{\Phi}_{ij} + \overline{\phi}_{ij} \,, \tag{8.13}$$

where $\overline{\Phi}_{ij}$ contains all the unclosed terms arising from the unfiltered mean fields,

$$\begin{aligned} \overline{\Phi}_{ij} = & - \frac{\partial}{\partial x_k} \left[\left(\overline{V_i T_{jk}} - \overline{V}_i \overline{T}_{jk}^{\text{tot}} \right) + \left(\overline{V_j T_{ik}} - \overline{V}_j \overline{T}_{ik}^{\text{tot}} \right) + \left(\overline{V_k T_{ij}} - \overline{V}_k \overline{T}_{ij}^{\text{tot}} \right) + \left(\overline{V_i V_j V_k} - \overline{V}_i \overline{V}_j \overline{V}_k \right) \right] \\ & - \frac{1}{\rho} \left[\left(\overline{V_j \frac{\partial \langle q \rangle}{\partial x_i}} - \overline{V}_j \frac{\partial \overline{\langle q \rangle}}{\partial x_i} \right) + \left(\overline{V_i \frac{\partial \langle q \rangle}{\partial x_j}} - \overline{V}_i \frac{\partial \overline{\langle q \rangle}}{\partial x_j} \right) \right] \\ & - 2\nu \left[\overline{\frac{\partial V_i}{\partial x_k} \frac{\partial V_j}{\partial x_k}} - \frac{\partial \overline{V}_i}{\partial x_k} \frac{\partial \overline{V}_j}{\partial x_k} \right] , \end{aligned} \tag{8.14}$$

and $\overline{\phi}_{ij}$ contains the unclosed fluctuating fields,

$$\overline{\phi}_{ij} = - \frac{\partial}{\partial x_k} \overline{\left\langle v_i' v_j' v_k' \right\rangle} - \frac{1}{\rho} \left[\frac{\partial \left\langle \overline{q' v_j'} \right\rangle}{\partial x_i} + \frac{\partial \left\langle \overline{q' v_i'} \right\rangle}{\partial x_j} \right] - \frac{1}{\rho} \overline{\left\langle q' \left(\frac{\partial v_j'}{\partial x_i} + \frac{\partial v_i'}{\partial x_j} \right) \right\rangle} - 2\nu \overline{\left\langle \frac{\partial v_i'}{\partial x_k} \frac{\partial v_j'}{\partial x_k} \right\rangle} . \tag{8.15}$$

Note that the first two terms in the definition of $\overline{\phi}_{ij}$ describe the turbulent transport (velocity and pressure fluctuations), the third term is the pressure-strain tensor, and the last term is the viscous dissipation.

The term $\overline{\Phi}_{ij}$ expresses the residual due to estimating an unclosed term containing the unfiltered mean fields by its expansion based on the filtered mean fields which is presumably small (here we have also assumed that the filtering and differentiation commute). On the other hand, $\overline{\phi}_{ij}$ contains the total effect of the fluctuating fields (and not the residual), which is quite significant in general. As a result, we can generally assume that

$$\overline{\Phi}_{ij} \ll \overline{\phi}_{ij} \,. \tag{8.16}$$

It is important to note that the dissipation and all the other terms in $\overline{\phi}_{ij}$ only show up as the filtered part of their exact definition. This is to emphasize that the change in both $\overline{\Phi}_{ij}$ and $\overline{\phi}_{ij}$ should be minimal from one grid to the other: even though by changing the grid we change the characteristic length scale of the filter, that filter acts only on the mean fields which are presumably smooth and should not be significantly affected by application of any reasonable filter (this involves some approximation).

A similar expression for the evolution of the numerical total Reynolds stress $\overline{R}_{ij}^{\text{tot}} = \left\langle \overline{u}_i' \overline{u}_j' \right\rangle + \left\langle \tau_{ij}^{\text{mod}} \right\rangle$ can be derived as

$$\frac{\partial \overline{R}_{ij}^{\text{tot}}}{\partial t} + \frac{\partial}{\partial x_k}(\overline{U}_k \overline{R}_{ij}^{\text{tot}}) - \nu \frac{\partial^2 \overline{R}_{ij}^{\text{tot}}}{\partial x_k \partial x_k} + \left[\overline{R}_{ik}^{\text{tot}} \frac{\partial \overline{U}_j}{\partial x_k} + \overline{R}_{jk}^{\text{tot}} \frac{\partial \overline{U}_i}{\partial x_k} \right] = \overline{\Psi}_{ij} + \overline{\psi}_{ij} \,. \quad (8.17)$$

where $\overline{U}_i$ denotes the average of the numerically solved resolved velocity fields $\overline{u}_i$.

The exact form of the unclosed terms $\overline{\Psi}_{ij}$ and $\overline{\psi}_{ij}$ depends on the specific LES model used in the code. Nevertheless, $\overline{\Psi}_{ij}$ and $\overline{\psi}_{ij}$ are equivalents of their exact counterparts $\overline{\Phi}_{ij}$ and $\overline{\phi}_{ij}$, and have a generally similar form; i.e., $\overline{\psi}_{ij}$ essentially contains terms due to the transport properties (fluctuating velocity and pressure fields, as well as transport due to the subgrid stresses), terms for redistribution of the Reynolds stresses (the resolved pressure-strain term as well as the contribution of the subgrid kinetic energy), and dissipative terms (both molecular and LES dissipation).

The evolution equation for the error in the total Reynolds stress $\left\langle \overline{e}_{ij}^{\text{RS}} \right\rangle = \overline{T}_{ij}^{\text{tot}} - \overline{R}_{ij}^{\text{tot}}$ can then be obtained by subtracting the evolution equations of $\overline{R}_{ij}^{\text{tot}}$ and

$\overline{T}_{ij}^{\text{tot}}$. This yields

$$\begin{aligned}
&\frac{\partial \left\langle \overline{e}_{ij}^{\text{RS}} \right\rangle}{\partial t} + \frac{\partial \overline{U}_k \left\langle \overline{e}_{ij}^{\text{RS}} \right\rangle}{\partial x_k} + \frac{\partial}{\partial x_k}(\langle \overline{e}_k \rangle \overline{R}_{ij}^{\text{tot}} + \langle \overline{e}_k \rangle \left\langle \overline{e}_{ij}^{\text{RS}} \right\rangle) - \nu \frac{\partial^2 \left\langle \overline{e}_{ij}^{\text{RS}} \right\rangle}{\partial x_k \partial x_k} \\
&\quad + \left[\left\langle \overline{e}_{ik}^{\text{RS}} \right\rangle \frac{\partial \overline{U}_j}{\partial x_k} + \left\langle \overline{e}_{jk}^{\text{RS}} \right\rangle \frac{\partial \overline{U}_i}{\partial x_k} \right] + \left[\overline{R}_{ik}^{\text{tot}} \frac{\partial \langle \overline{e}_j \rangle}{\partial x_k} + \overline{R}_{jk}^{\text{tot}} \frac{\partial \langle \overline{e}_i \rangle}{\partial x_k} \right] + \left[\left\langle \overline{e}_{ik}^{\text{RS}} \right\rangle \frac{\partial \langle \overline{e}_j \rangle}{\partial x_k} + \left\langle \overline{e}_{jk}^{\text{RS}} \right\rangle \frac{\partial \langle \overline{e}_i \rangle}{\partial x_k} \right] \\
&\quad = \underbrace{\overline{\Psi}_{ij} - \overline{\Phi}_{ij}}_{\overline{\Gamma}_{ij}} + \underbrace{\overline{\psi}_{ij} - \overline{\phi}_{ij}}_{\overline{\gamma}_{ij}} .
\end{aligned} \tag{8.18}$$

The first line in the evolution equation of $\left\langle \overline{e}_{ij}^{\text{RS}} \right\rangle$ describes the material derivative $\left\langle \overline{e}_{ij}^{\text{RS}} \right\rangle$ (first and second terms), the convection of the errors by the errors in the mean velocity fields as well as the erroneous convection of the total Reynolds stress by the errors in the mean velocity (third term), and the viscous diffusion of $\left\langle \overline{e}_{ij}^{\text{RS}} \right\rangle$ (fourth term). The second line of Eqn. 8.18 arises from the production term in the evolution equation of the total Reynolds stress, and describes the production of errors in the total Reynolds stress due to the mean velocity gradients (the first term), erroneous production of Reynolds stress due to the errors in the mean velocity fields (the second term), and production of Reynolds stress errors due to errors in the mean velocity fields (the third term).

Based on the same reasoning we used in Chapter 5, (i.e., that the terms that are vanishing in the absence of errors in the solutions, $\left\langle \overline{e}_{ij}^{\text{RS}} \right\rangle$ and $\langle \overline{e}_i \rangle$ in this formulation, are not innate sources of errors) we can assume that none of the terms on the left-hand side of the equation should be considered in local error-estimation. This means that we should only look at the unclosed terms

$$\begin{aligned}
\overline{\Gamma}_{ij} &= \overline{\Psi}_{ij} - \overline{\Phi}_{ij} \\
\overline{\gamma}_{ij} &= \overline{\psi}_{ij} - \overline{\phi}_{ij} ,
\end{aligned} \tag{8.19}$$

to find the source of error.

Equation 8.16 suggests that the mean unclosed terms $\overline{\Psi}_{ij}$ and $\overline{\Phi}_{ij}$ are relatively smaller in magnitude compared to the terms arising from the fluctuating fields ($\overline{\psi}_{ij}$ and $\overline{\phi}_{ij}$). Here, we further assume that their difference is also smaller, i.e.,

$$\overline{\Gamma}_{ij} = \overline{\Psi}_{ij} - \overline{\Phi}_{ij} \ll \overline{\psi}_{ij} - \overline{\phi}_{ij} = \overline{\gamma}_{ij} \,. \tag{8.20}$$

This assumption is only made as a guide for us to focus more on $\overline{\gamma}_{ij}$ and less on $\overline{\Gamma}_{ij}$, while in the final definition of our error-indicator we will include $\overline{\Gamma}_{ij}$.

We can decompose the unclosed term $\overline{\gamma}_{ij} = \overline{\psi}_{ij} - \overline{\phi}_{ij}$ into three physically different terms:

(i) The part arising from the turbulent transport $\overline{\gamma}^t_{ij} = \overline{\psi}^t_{ij} - \overline{\phi}^t_{ij}$: this term contains transport due to the fluctuating velocity and pressure fields as well as the modeled subgrid stresses. $\overline{\gamma}^t_{ij}$ would then mostly describe the transport of errors by the fluctuating fields and is most probably *not* a source of error. Perhaps, this could also be learned by looking at the form of $\overline{\phi}^t_{ij}$ in the Reynolds stress equation, i.e. only the divergence of the mean fields $\langle \overline{v'_i v'_j v'_k} \rangle$ and $\langle \overline{q' v'_i} \rangle$ show up in its definition. Similarly, $\overline{\psi}^t_{ij}$ and thus $\overline{\gamma}^t_{ij}$ have the same form and describe the same process.

(ii) The term describing the error in the pressure-strain term $\overline{\gamma}^p_{ij} = \overline{\psi}^p_{ij} - \overline{\phi}^p_{ij}$. The main role of the pressure-strain tensor is to redistribute the Reynolds stresses; therefore, we hypothesize that $\overline{\gamma}^p_{ij}$, which describes the error in this term, can be decomposed into two major contributions: the part that is due to the error already present in the solution (i.e. because Reynolds stresses are erroneous

and so their redistribution), and the part that is due to the insufficiencies in the grid resolution or the LES model. This could also be seen in the shape of the pressure-strain tensor that is a multiplication of the large-scale field q' and the strain rate $\partial v_i'/\partial x_j + \partial v_j'/\partial x_i$ that is biased towards the smaller scales.

(iii) The contribution from the errors in the dissipation rate $\overline{\gamma}_{ij}^d = \overline{\psi}_{ij}^d - \overline{\phi}_{ij}^d$, which can also be decomposed into the part that is due to the error in the turbulent field, and the part that is due to the inability of the grid and the LES model to dissipate energy at the correct rate.

We can continue our quest for finding the source of error by considering the evolution equation for all three different terms in the definition of $\overline{\gamma}_{ij} = \overline{\gamma}_{ij}^t + \overline{\gamma}_{ij}^p + \overline{\gamma}_{ij}^d$ (i.e. the turbulent transport, pressure-strain and dissipation terms) to further isolate the local source of error from the errors showing up in the solution ($\overline{e}_i = \overline{v}_i - \overline{u}_i$). However, instead of directly looking at the evolution equations for each of these terms we truncate our analysis here and employ the available knowledge from the RANS literature. In other words, due to decades of experience and the many models that are available for describing each of these terms, their general behavior is known and the different processes involved in them are also rather well-known. This means that we do not need to directly look at their governing equation to understand how and where the errors are generated: the same can be known by relying on the RANS models.

8.1.3 Identifying the source of error in the unclosed term $\overline{\gamma}_{ij}$

The source of error in the total Reynolds stress equation (and therefore the mean velocity and mean pressure) is the error in $\overline{\phi}_{ij}$ (denoted by $\overline{\gamma}_{ij}$) that does not come from the error in the solution itself.

Error in the turbulent transport: based on our discussion, the error in the turbulent transport $\overline{\gamma}^t_{ij}$ is almost entirely due to the solution errors. Therefore, this term should be completely excluded from what we define as the source of error.

Error in the pressure-strain tensor: the pressure-strain term has been identified as one of the most important and difficult terms to model [17, 85, 87, 88] and the models proposed for describing it vary, sometimes significantly, from each other. For the purpose of this study the important point is that this term (and thus $\overline{\gamma}^p_{ij}$) can be decomposed into three separate parts: the "rapid" part, the "slow" part, and the "harmonic" part [17, 85, 89]. The rapid part, as seen in most models [17, 85], is based on the large-scale fields (i.e. mean velocity, Reynolds stress, production, etc.), while the slow part is mostly described based on the small-scale dominated fields like dissipation; and, the harmonic part is only active near the walls. If we simply assume that the larger scales of the solution are mostly affected by the errors already present in the solution, while the smaller scales of the solution are mostly affected by the source of error (i.e. insufficient grid resolution and inaccurate LES models) then we can hypothesize that the change in the "rapid" part of the pressure-strain term should not a part of our error estimate, while the "slow" part should be included. Therefore, as a first approximation we can exclude the effect

of the "rapid" part $\overline{\gamma}_{ij}^{p,\text{rapid}}$ from the error source and keep the slow part. The error in the "harmonic" part probably should not included in our estimate of the error; however, this term is usually small and can be neglected anyway (the "harmonic" term is different from the effect of wall reflection, which is included in the "rapid" and "slow" parts). We should emphasize that this was a very simplified reasoning; while, the actual behavior of the pressure-strain term is much more complicated, as can be seen in more sophisticated models of the pressure-strain term (cf. [17] and references therein).

Error in the dissipation rate: The dissipation tensor is a non-local, transported quantity, and so is its error $\overline{\gamma}_{ij}^{d}$. In a large eddy simulation the errors in the dissipation rate happen when the LES model is incapable of accurately accounting for the effect of the smaller scales in dissipating the resolved energy, or when the grid resolution is too coarse to accurately describe the resolved fields (that enter the LES model). Both the insufficient grid resolution and an inaccurate LES model are considered as an error source. The erroneous field (with higher or lower turbulent intensity) is then convected and transported to other parts of the domain, where it will cause more error in the dissipation term due to the wrong turbulent field (not part of the error source), as well as a possibly new source of error due to the insufficient resolution or the deficient LES model at that new location (part of the error source). Since the dissipation is a small-scale quantity of the solution, we roughly assume that the contribution from the transported erroneous fields is secondary to the local error due to coarse resolution of the grid or inaccurate LES models. Thus, we include the entire term $\overline{\gamma}_{ij}^{d}$ in what we will define as the error source.

8.1.4 How to isolate the source of error from the rest of the unclosed term $\overline{\gamma}_{ij}$

In an LES one has access to the instantaneous fields, and therefore, some of the terms that are to be excluded (e.g., the transport term) can be directly computing and subtracted from the total $\overline{\gamma}_{ij}$. However, terms like the rapid part of the pressure-strain tensor are not directly available from the LES solution, and one has to somehow estimate them. Additionally, the final goal of the proposed methodology of this Chapter is to supplement it with the adjoint fields, to link the errors in the QoIs to the estimated error sources, and to define an output-based grid-adaptation framework for LES. This justifies an alternative approach for approximating the parts of $\overline{\gamma}_{ij}$ that we want to exclude (rather than direct computation).

Looking at the governing equation for the error in the Reynolds stress (Eqn. 8.18) we realize that any term that contains the error in the mean velocity or the Reynolds stress is automatically excluded from what we considered as the source of error (since it reduces to zero when the error in the solution goes to zero). This means that the effect of the turbulent transport for example can be eliminated by replacing it with a model that describes it using only the Reynolds stress and the mean velocity and pressure fields. This is where the RANS modeling comes into play, i.e. when replacing an unclosed term by its RANS model to exclude it from the local error estimate. We note that this description cannot be exact, due to the errors in the RANS models as well as the inherent deficiency involved in describing an unclosed term based on a

few fields in the closed form. Therefore, when we use a RANS model to exclude the effect of a term from the error source we in fact only exclude the effect of the part that the RANS model captures, while a residual part (due to the inaccuracies in the RANS model) still remains in our definition of the error source. In other words,

$$\overline{\gamma}_{ij} = \overline{\gamma}_{ij}^{\text{mod}} + \overline{\gamma}_{ij}^{\text{res}} + \overline{\mathcal{F}}_{ij}^{\gamma} = \overline{\gamma}_{ij}^{\text{mod}} + \overline{\mathcal{E}}_{ij}^{\gamma}$$

where $\overline{\mathcal{F}}_{ij}^{\gamma}$ is the actual error source in $\overline{\gamma}_{ij}$, $\overline{\gamma}_{ij}^{\text{mod}} = \overline{\psi}_{ij}^{\text{mod}} - \overline{\phi}_{ij}^{\text{mod}}$ is the part of $\overline{\gamma}_{ij}$ that we have modeled, and $\overline{\gamma}_{ij}^{\text{res}} = \overline{\psi}_{ij}^{\text{res}} - \overline{\phi}_{ij}^{\text{res}}$ is the part of $\overline{\gamma}_{ij}$ that in fact is not a part of the error source but we could not include in $\overline{\gamma}_{ij}^{\text{mod}}$ due to the imperfect description of the unclosed terms by the RANS model. Finally, the term $\overline{\mathcal{E}}_{ij}^{\gamma}$

$$\begin{aligned}\overline{\mathcal{E}}_{ij}^{\gamma} &= \overline{\gamma}_{ij} - \overline{\gamma}_{ij}^{\text{mod}} \\ &= \overline{\gamma}_{ij}^{\text{res}} + \overline{\mathcal{F}}_{ij}^{\gamma} \approx \overline{\mathcal{F}}_{ij}^{\gamma},\end{aligned}$$

is our best estimate of $\overline{\mathcal{F}}_{ij}^{\gamma}$.

The other unclosed term $\overline{\Gamma}_{ij}$ in the evolution equation of the Reynolds stress error is due to a filtering residual (see Eqn. 8.14) and is typically insignificant compared to $\overline{\gamma}_{ij}$. Therefore, no further effort has been made to distinguish between its different terms and their contribution to the source of error.

Finally, we define the estimated total source of error, denoted by $\overline{\mathcal{E}}_{ij}$, as

$$\overline{\mathcal{E}}_{ij} = \overline{\Gamma}_{ij} + \overline{\mathcal{E}}_{ij}^{\gamma} = \overline{\Gamma}_{ij} + \overline{\gamma}_{ij} - \overline{\gamma}_{ij}^{\text{mod}}\,. \tag{8.21}$$

There is some additional benefit to keeping the term $\overline{\Gamma}_{ij}$ in our definition of the error source that is discussed in the next Section.

8.1.5 Estimating $\overline{\mathcal{E}}_{ij}$ without the exact solution

The direct computation of $\overline{\gamma}_{ij} = \overline{\psi}_{ij} - \overline{\phi}_{ij}$ and $\overline{\Gamma}_{ij} = \overline{\Psi}_{ij} - \overline{\Phi}_{ij}$ involves both the numerical fields ($\overline{\psi}_{ij}$ and $\overline{\Psi}_{ij}$) and the exact fields $\overline{\phi}_{ij}$ and $\overline{\Phi}_{ij}$. While the numerical fields are available from the LES solution the exact fields are (of course) not. The problem is then to find a way to estimate $\overline{\mathcal{E}}_{ij}$ without having access to the exact fields.

In our derivation of the governing equation for $\overline{T}_{ij}^{\text{tot}}$ we have intentionally formulated the exact unclosed term $\overline{\phi}_{ij}$ in a way that its definition only includes filtering of the exact mean fields, e.g., $\overline{\langle v_i' v_j' v_k' \rangle}$ instead of $\langle \overline{v}_i' \overline{v}_j' \overline{v}_k' \rangle$. In other words, the filter only acts on the mean fields that are presumably smooth, and as a result, changing the filter-width slightly should not change this term significantly,

$$\overline{\phi}_{ij} \approx \widetilde{\phi}_{ij} \,,$$

where $\widetilde{\cdot}$ denotes a different filtering process with a characteristic filter-width $\widetilde{\Delta}$. The same argument can be made for $\overline{\Phi}_{ij}$, i.e. $\overline{\Phi}_{ij} \approx \widetilde{\Phi}_{ij}$. Therefore,

$$\overline{\Gamma}_{ij} - \widetilde{\Gamma}_{ij} = \overline{\Psi}_{ij} - \widetilde{\Psi}_{ij} - \left[\overline{\Phi}_{ij} - \widetilde{\Phi}_{ij} \right] \approx \overline{\Psi}_{ij} - \widetilde{\Psi}_{ij}$$

$$\overline{\gamma}_{ij} - \widetilde{\gamma}_{ij} = \overline{\psi}_{ij} - \widetilde{\psi}_{ij} - \left[\overline{\phi}_{ij} - \widetilde{\phi}_{ij} \right] \approx \overline{\psi}_{ij} - \widetilde{\psi}_{ij} \,.$$

Similarly, we assumed that we use a RANS model in describing $\overline{\gamma}_{ij}^{\text{mod}} = \overline{\psi}_{ij}^{\text{mod}} - \overline{\phi}_{ij}^{\text{mod}}$, where the term $\overline{\phi}_{ij}^{\text{mod}}$ contains only the filtered exact mean fields $\overline{V}_k$, $\langle \overline{q} \rangle$, $\overline{T}_{ij}^{\text{tot}}$. Thus, with a similar arguement

$$\overline{\gamma}_{ij}^{\text{mod}} - \widetilde{\gamma}_{ij}^{\text{mod}} = \overline{\psi}_{ij}^{\text{mod}} - \widetilde{\psi}_{ij}^{\text{mod}} - \left[\overline{\phi}_{ij}^{\text{mod}} - \widetilde{\phi}_{ij}^{\text{mod}} \right] \approx \overline{\psi}_{ij}^{\text{mod}} - \widetilde{\psi}_{ij}^{\text{mod}} \,.$$

This means that even though a direct computation of $\overline{\mathcal{E}}_{ij}$ is not possible, we can directly compute how $\mathcal{E}_{ij}$ changes from one grid to the other

$$\begin{aligned}\overline{\mathcal{E}}_{ij} - \widetilde{\mathcal{E}}_{ij} &= \left[\overline{\Gamma}_{ij} + \overline{\gamma}_{ij} - \overline{\gamma}_{ij}^{\text{mod}}\right] - \left[\widetilde{\Gamma}_{ij} + \widetilde{\gamma}_{ij} - \widetilde{\gamma}_{ij}^{\text{mod}}\right] \\ &\approx \left[\overline{\Psi}_{ij} + \overline{\psi}_{ij} - \overline{\psi}_{ij}^{\text{mod}}\right] - \left[\widetilde{\Psi}_{ij} + \widetilde{\psi}_{ij} - \widetilde{\psi}_{ij}^{\text{mod}}\right] .\end{aligned} \tag{8.22}$$

Note that we can simply compute the left-hand side of Eqn. 8.17 to compute $\overline{\Psi}_{ij} + \overline{\psi}_{ij}$, i.e.

$$\overline{\Psi}_{ij} + \overline{\psi}_{ij} - \overline{\psi}_{ij}^{\text{mod}} = \frac{\partial \overline{R}_{ij}^{\text{tot}}}{\partial t} + \frac{\partial}{\partial x_k}(\overline{u}_k \overline{R}_{ij}^{\text{tot}}) - \nu \frac{\partial^2 \overline{R}_{ij}^{\text{tot}}}{\partial x_k \partial x_k} + \left[\overline{R}_{ik}^{\text{tot}} \frac{\partial \overline{u}_j}{\partial x_k} + \overline{R}_{jk}^{\text{tot}} \frac{\partial \overline{u}_i}{\partial x_k}\right] - \overline{\psi}_{ij}^{\text{mod}} \tag{8.23}$$

where $\overline{\psi}_{ij}^{\text{mod}}$ is from a RANS model and expressed in terms of $\overline{U}_k$ and $\overline{R}_{ij}^{\text{tot}}$. Computing $\widetilde{\Psi}_{ij} + \widetilde{\psi}_{ij} - \widetilde{\psi}_{ij}^{\text{mod}}$ is done in the exact same way, by using the numerical fields $\widetilde{U}_k$ and $\widetilde{R}_{ij}^{\text{tot}}$ from the actual LES solution on a different grid with characteristic filter-width $\widetilde{\Delta}$. This second grid can in general be any other grid solving the same flow; for instance, a previous grid in a sequence of adapted grids, or more favorably the test grid used in the proposed robust convergence-verification of Chapter 7.

We should emphasize that the formulation of Eqn. 8.23 uses exact differentiation operators. The major advantage of this formulation is that it makes the method almost agnostic to the order of accuracy of the code, whether the filtering was implicit or explicit, etc. In other words, the implementation is theoretically the same for all codes. Despite the relative advantage of Eqn. 8.23 in computing $\overline{\Psi}_{ij} + \overline{\psi}_{ij} - \overline{\psi}_{ij}^{\text{mod}}$, the computed values may contain significant time averaging errors and those averaging errors may adversely affect the estimated errors, especially in flows with significant unsteady motions. This can be overcome by directly including

the average of the term $\partial \overline{R}_{ij}^{\text{tot}} / \partial t$ (by storing this field exported from the code), or by directly computing $\overline{\psi}_{ij}$.

At this point, the only part that remains for our error-estimation is to find a way to approximate $\overline{\mathcal{E}}_{ij}$ from the knowledge we have on how it changes from one grid to the other. This can be achieved by a model that relates $\overline{\mathcal{E}}_{ij}$ to the grid-resolution $\overline{h}$ and filter-width $\overline{\Delta}$. The simplest model that describes this dependence would take the form

$$\overline{\mathcal{E}}_{ij}(\mathbf{x}) = \overline{c}_{ij}(\mathbf{x}) \overline{\Delta}_{\text{vol}}^{\alpha}(\mathbf{x}) \,, \tag{8.24}$$

where $\overline{\Delta}_{\text{vol}}(\mathbf{x})$ is the cube-root of the cell volume. Similar to the models used in Chapters 3 and 5 the scaling exponent is flow and code dependent and may take any value up to the nominal order of accuracy of the code (e.g. $\alpha \leq 2$ in a second-order accurate code).

In this simple model of Eqn. 8.24 the dependence of the error on the filter-width is explicitly included by the term $\overline{\Delta}_{\text{vol}}^{\alpha}$, where $\overline{c}_{ij}$ is meant to be only a function of the solution and not $\overline{\Delta}_{\text{vol}}$. However, this assumption is not strictly satisfied in reality, since the solution itself implicitly depends on the filter and changes from one grid to the other. Nevertheless, if the characteristic size of the filter does not change by much, the coefficient $\widetilde{c}_{ij}$ (on a grid with characteristic filter-width $\widetilde{\Delta}_{\text{vol}}$) could be approximated using the Taylor expansion of $\widetilde{c}_{ij}$ about $\overline{c}_{ij}$ such that

$$\widetilde{\mathcal{E}}_{ij} = \widetilde{c}_{ij} \widetilde{\Delta}_{\text{vol}}^{\alpha} = \overline{c}_{ij} \widetilde{\Delta}_{\text{vol}}^{\alpha} + \mathcal{O}(\widetilde{\Delta}_{\text{vol}}^{\alpha+1}) \,. \tag{8.25}$$

In that case, we can use the computed $\overline{\mathcal{E}}_{ij} - \widetilde{\mathcal{E}}_{ij}$ to approximate $\overline{c}_{ij}$ as

$$\overline{c}_{ij}(\mathbf{x}) \approx \frac{\overline{\mathcal{E}}_{ij}(\mathbf{x}) - \widetilde{\mathcal{E}}_{ij}(\mathbf{x})}{\overline{\Delta}_{\text{vol}}^{\alpha}(\mathbf{x}) - \widetilde{\Delta}_{\text{vol}}^{\alpha}(\mathbf{x})}$$

and thus the error on an arbitrary grid with a characteristic filter-width $\check{\Delta}_{\text{vol}}$ can be approximated as

$$\check{\mathcal{E}}_{ij}(\mathbf{x}) \approx \overline{c}_{ij}(\mathbf{x})\check{\Delta}^{\alpha}_{\text{vol}}(\mathbf{x}) \approx \left[\frac{\overline{\mathcal{E}}_{ij}(\mathbf{x}) - \widetilde{\mathcal{E}}_{ij}(\mathbf{x})}{\overline{\Delta}^{\alpha}_{\text{vol}}(\mathbf{x}) - \widetilde{\Delta}^{\alpha}_{\text{vol}}(\mathbf{x})}\right]\check{\Delta}^{\alpha}_{\text{vol}}(\mathbf{x})\,. \tag{8.26}$$

The estimated value of $\check{\mathcal{E}}_{ij}(\mathbf{x})$ is our best estimate of the source of errors on grid $\check{\Delta}_{\text{vol}}(\mathbf{x})$ and can be used to drive the grid selection/adaptation process. Note that this error estimate is only a function of space $\mathbf{x}$; as a result, it must be complemented by a measure of directional resolution to enable fully anisotropic adaptation. This can be done by either of the anisotropic error-indicators of Chapters 3 or 5, and is explained in Section 8.2 below.

8.2 Finding the optimal filter-width

The optimal filter width $\check{\Delta}_{\text{opt}}(\mathbf{x}, \mathbf{n})$ can be found by solving the constrained optimization problem that minimizes the quantity

$$\check{e}^{\text{ref}}_{\text{QoI}} = \int_{\Omega} \check{e}^{\text{ref}}_{\text{local}}(\mathbf{x})\, d\mathbf{x}$$

on a grid $\check{\Delta}$ with a desired number of cells N_{tot},

$$N_{\text{tot}} = \int_{\Omega} \frac{d\mathbf{x}}{\check{V}_c}\,.$$

Note that this is exactly equivalent to finding the least expensive grid (grid with lowest N_{tot}) that satisfies a set threshold on the acceptable value of $\check{e}^{\text{ref}}_{\text{QoI}}$.

If we follow the same approach taken in Sections 4.1 and 4.4 and assume that

$$\check{e}^{\text{ref}}_{\text{local}}(\mathbf{x}) \propto \sqrt{\check{\mathcal{E}}_{ij}(\mathbf{x})\check{\mathcal{E}}_{ij}(\mathbf{x})} = \sqrt{\overline{c}_{ij}(\mathbf{x})\overline{c}_{ij}(\mathbf{x})}\check{\Delta}^{\alpha}_{\text{vol}}(\mathbf{x}) \tag{8.27}$$

the optimization problem takes a closed form solution

$$\overline{C}(\mathbf{x})\check{\Delta}_{\text{vol,opt}}^{\alpha+3}(\mathbf{x}) = \Lambda = \text{const.}\,, \tag{8.28}$$

where

$$\overline{C}(\mathbf{x}) \equiv \sqrt{\overline{c}_{ij}(\mathbf{x})\overline{c}_{ij}(\mathbf{x})}\,. \tag{8.29}$$

In other words, the optimal $\check{\Delta}_{\text{vol}}(\mathbf{x})$ results in an equidistribution of the cell-integrated error defined in Eqn. 8.27.

Equation 8.28 determines the optimal distribution of $\check{\Delta}_{\text{vol}}$ (the cube root of the cell volume), but it does not provide any information about the optimal anisotropy of the filter. In fact the whole error-estimation technique of this Chapter is in general incapable of distinguishing between insufficient resolution in different directions (unless the grid $\widetilde{\Delta}$ is generated by refinement/coarsening of $\overline{\Delta}$ in a single direction $\mathbf{n}$). As a simple solution, we can take advantage of either of our anisotropic error-indicators $\overline{\mathcal{A}}(\mathbf{x},\mathbf{n})$ (Chapter 3) or $\overline{\mathcal{G}}(\mathbf{x},\mathbf{n})$ (Chapter 5) to determine the optimal aspect ratio. For example, using $\overline{\mathcal{A}}(\mathbf{x},\mathbf{n})$ we can define $\check{\Delta}(\mathbf{x},\mathbf{n})$ as

$$\check{\Delta}_{\text{opt}}(\mathbf{x},\mathbf{n}_i) = \left(\frac{\overline{a}_{\text{vol}}(\mathbf{x})}{\overline{a}(\mathbf{x},\mathbf{n}_i)}\right)^{1/\alpha'} \check{\Delta}_{\text{vol,opt}}(\mathbf{x})\,, \tag{8.30}$$

where α' is the scaling exponent of $\overline{\mathcal{A}}(\mathbf{x},\mathbf{n})$ and

$$\begin{aligned} \overline{a}(\mathbf{x},\mathbf{n}_i) &= \frac{\overline{\mathcal{A}}(\mathbf{x},\mathbf{n}_i)}{\overline{\Delta}^{\alpha'}(\mathbf{x},\mathbf{n}_i)} \\ \overline{a}_{\text{vol}}(\mathbf{x}) &= \left(\overline{a}(\mathbf{x},\mathbf{n}_1)\overline{a}(\mathbf{x},\mathbf{n}_2)\overline{a}(\mathbf{x},\mathbf{n}_3)\right)^{1/3}\,. \end{aligned} \tag{8.31}$$

Equations 8.28 and 8.30 define the optimal filter $\check{\Delta}_{\text{opt}}$ as a function of both $\mathbf{x}$ and $\mathbf{n}$.

We have to admit that $\overline{\mathcal{G}}$ is a more advanced error-indicator compared to $\overline{\mathcal{A}}$, and we should have used that instead to determine the aspect ratio of the cells; however, at the time we were developing $\overline{\mathcal{E}}_{ij}$, we had not yet fully tested $\overline{\mathcal{G}}$, and therefore, all of our preliminary tests were performed using $\overline{\mathcal{A}}$. That is actually why the formulations of this Section are based on this older error-indicator.

An interesting result of using two grids in error-estimation is that we can now directly compute the scaling exponent $\alpha'(\mathbf{x}, \mathbf{n})$ of $\overline{\mathcal{A}}(\mathbf{x}, \mathbf{n})$. For the example of a uniformly refined/coarsened grid with a factor β, i.e., $\widetilde{\Delta}(\mathbf{x}, \mathbf{n}) = \beta\overline{\Delta}(\mathbf{x}, \mathbf{n})$, we have

$$\alpha'(\mathbf{x}, \mathbf{n}) = \log_\beta \frac{\widetilde{\mathcal{A}}(\mathbf{x}, \mathbf{n})}{\overline{\mathcal{A}}(\mathbf{x}, \mathbf{n})},$$

where $\overline{\mathcal{A}}$ and $\widetilde{\mathcal{A}}$ are the values of the error-indicator computed on grids $\overline{\Delta}$ and $\widetilde{\Delta} = 1.25\overline{\Delta}$, respectively. However, despite the theoretical advantage of using the computed value of α', to increase the robustness of the method we have used $\alpha'(\mathbf{x}, \mathbf{n}) \equiv 2$ throughout this Chapter.

8.3 Algorithm and implementation

In this Chapter we directly follow the proposed algorithm and guidelines of Chapter 7 for convergence-verification and grid selection/adaptation in LES. This is shown in Fig. 8.1.

At each iteration of the algorithm a new test grid (labeled G'_k) is generated for convergence-verification of grid G_k, which is constructed by uniform coarsening of G_k by 25%, i.e. $\overline{\Delta}'(\mathbf{x}, \mathbf{n}) = 1.25\overline{\Delta}(\mathbf{x}, \mathbf{n})$. This was a compromise between the computational cost (which appeals larger coarsening factors) and the meaningfulness

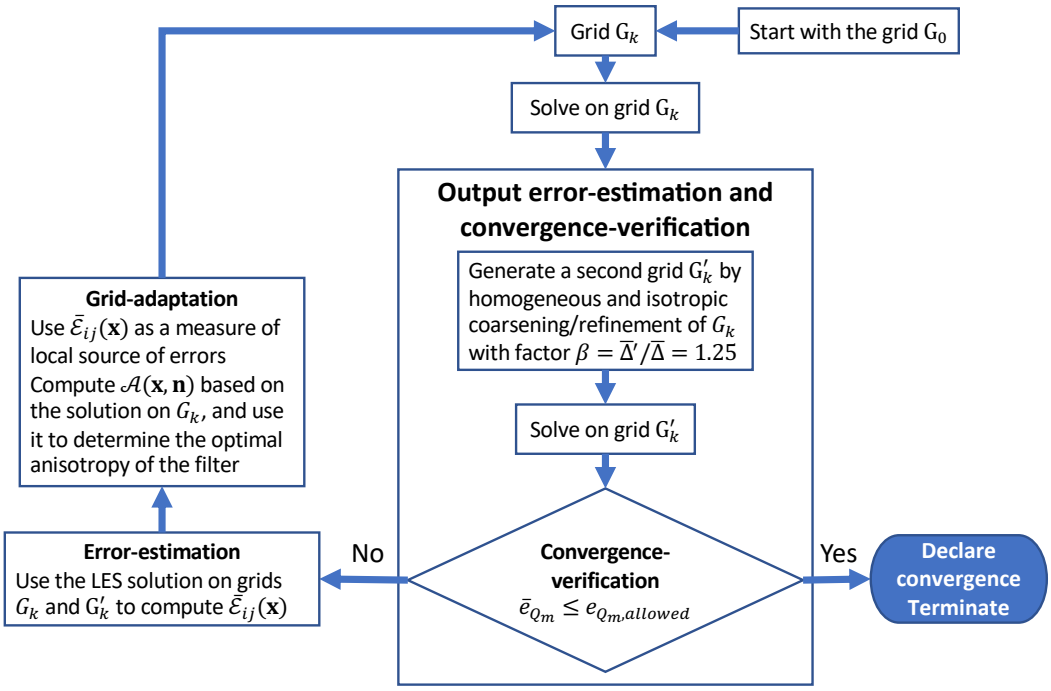

Figure 8.1: The convergence-verification and grid selection/adaptation algorithm followed in this Chapter. See text for more details about each process.

of the test (requiring sufficiently small factors).

Due to the approximations involved in the use of the Richardson extrapolation, i.e.,

$$\bar{e}_{Q_m}^{\mathrm{DNS}} \approx \frac{\delta\overline{Q}_m^{G_k,G'_k}}{1-\beta^{\alpha''}} \tag{8.32}$$

where the exponent α'' is not exactly known, the verification tests of this Chapter are reported by $\delta\overline{Q}_m^{G_k,G'_k}$. The reader can assume some value for α'' and approximate $\bar{e}_{Q_m}^{\mathrm{DNS}}$ accordingly.

The error-estimation is done using G'_k as the second solution, i.e., $\widetilde{\Delta}(\mathbf{x},\mathbf{n}) = \overline{\Delta}'(\mathbf{x},\mathbf{n}) = 1.25\overline{\Delta}(\mathbf{x},\mathbf{n})$. Note that the coarsening factor is presumably small enough to satisfy the assumption of nearly constant $\bar{c}_{ij}$ between the two grids. Also, we have simply used a constant exponent $\alpha(\mathbf{x},\mathbf{n}) \equiv 2$ in the model, $\check{\mathcal{E}}_{ij} = \bar{c}_{ij}\check{\Delta}^{\alpha}$, without

any attempt at finding the optimal value.

The formulation of Eqn. 8.23 uses exact differentiation, which implies that we need to interpolate the mean fields onto a sufficiently fine grid with negligible numerical errors. However, interpolation onto extremely fine grids introduces interpolation errors that can become dominant and negatively affect our estimation of the source of errors. To have a bound on the interpolation error and overcome this issue, we interpolate the fields onto a grid that is generated by refining the original grid G_k by a fixed factor. We tried factors of 2 and 4, i.e., $\overline{h}^f = \overline{h}/2$ and $\overline{h}^f = \overline{h}/4$ and found almost no difference between the results for the test cases presented in this paper (and using linear interpolation). Therefore, from now on we use $\overline{h}^f = \overline{h}/2$ when computing Eqn. 8.23 for grid G_k (and similarly $\widetilde{h}^f = \overline{h}'^f = \overline{h}'/2$ for G'_k grids).

Another important factor in error-estimation is the definition of $\overline{\gamma}_{ij}^{\text{mod}}$, i.e. the part of $\overline{\gamma}_{ij}$ that we model: preferably, the entire turbulent transport should be excluded from our definition of the error source, as well as the rapid part of the pressure-strain tensor (as a first approximation). However, for the test cases of this paper (the turbulent channel flow and the flow over a backward-facing step) we saw inconsistent results on improvement of the error-estimation when the rapid pressure-strain term was excluded from our definition of $\check{\mathcal{E}}_{ij}$. More specifically, we tried both the LRR [17, 87] and the SSG [17, 85, 88] models of the pressure-strain tensor, and while for the turbulent channel flow we saw slightly improved results, for the flow over a backward-facing step both models led to less accurate error-estimation and thus less optimal adapted grids. Both the LRR and SSG models were also strongly affected by the time averaging errors. Hence, we decided to

include the entire pressure-strain tensor in our definition of $\check{\mathcal{E}}_{ij}$ until a more careful study can be made on the effect of the pressure-strain term and the adequacy of the current RANS models. Therefore, we have only modeled the effect of the turbulent transport using the gradient-diffusion model of Daly & Harlow [90]

$$\overline{\psi}_{ij}^{\text{mod}} = -C_s \frac{\partial}{\partial x_k}\left[\frac{\overline{R}_{mm}^{\text{tot}}}{\overline{\epsilon}_{nn}^{\text{tot}}}\overline{R}_{kl}^{\text{tot}}\frac{\partial \overline{R}_{ij}^{\text{tot}}}{\partial x_l}\right]$$

where $\overline{\epsilon}_{ij}^{\text{tot}}$ is the total dissipation tensor, including both the molecular and LES dissipations). We have used $C_s = 0.22$ which is the value recommended by Launder [17, 91].

8.4 Assessment on LES of the channel flow at $Re_\tau \approx 545$ using the dynamic Smagorinsky model

The proposed error-estimation and convergence-verification methods are first assessed on the canonical problem of turbulent channel flow.

The code used for this problem is the *Hybrid* code (used is Sections 3.2, 4.5, and 5.2), which solves the compressible implicitly filtered Navier-Stokes equations using explicit LES modeling and a calorically perfect gas formulation on structured Cartesian grids using sixth-order accurate central differencing schemes with a split form of the convective term, and the classical Runge-Kutta method for time integration.

The bulk Reynolds number $Re_b = \rho_b U_b H/\mu_w$ (based on the channel half-width H) is 10,000, which leads to a friction Reynolds number of about $Re_\tau \approx 545$. The bulk Mach number is 0.2. These numbers are identical to the setup used in

Sections 4.5 and 5.2. The rest of the parameters used in the computational setup are also identical to those Sections and are not repeated here.

Because of the structured nature of the girds the grid-spacing in the wall-parallel directions is taken as the smallest predicted value across the channel. However, the wall-normal resolution is directly matched to the target values by giving the code a list of y coordinates.

Quantities of interest are taken to be the streamwise mean velocity and the four non-zero Reynolds stresses (same as Sections 3.2, 4.5, and 5.2). The actual error in the QoIs $\overline{e}_{\text{QoI}}^{\text{DNS}}$ is again computed by comparison to the DNS solution of del Alamo & Jimenez [18], while instead of $\overline{e}_{\text{QoI}}^{\text{prev}}$ (change in the QoIs from the previous grid G_{k-1}) we use our new convergence-verification test and report $\delta\overline{Q}^{G_k,G'_k}$, defined as

$$\delta\overline{Q}^{G_k,G'_k} = \frac{1}{5}\sum_{m=1}^{5} \delta\overline{Q}_m^{G_k,G'_k}, \tag{8.33}$$

quantifying the change in the QoIs from the uniformly coarsened grid G'_k. Assuming that the underlying assumptions of the Richardson extrapolation hold the actual error $\overline{e}_{\text{QoI}}^{\text{DNS}}$ can be computed from $\delta\overline{Q}^{G_k,G'_k}$ using $\overline{e}_{\text{QoI}}^{\text{DNS}} \approx \delta\overline{Q}^{G_k,G'_k}/(1-\beta^{\alpha''})$ (as a result of Eqn. 8.32); however, due to the unknown value of α'' (scaling of the QoIs errors with $\check{\Delta}$) only $\delta\overline{Q}^{G_k,G'_k}$ itself is reported in the results.

This first grid (labeled G_1) has a uniform resolution of $(\overline{\Delta}_x, \overline{\Delta}_y, \overline{\Delta}_z)/H = (0.20, 0.10, 0.20)$, corresponding to $(\overline{\Delta}_x^+, \overline{\Delta}_{y_w}^+/2, \overline{\Delta}_z^+) \approx (110, 28, 110)$ if one uses the fully converged friction units. Note that $\overline{\Delta}_{y_w}^+$ is the wall-normal filter width at the wall. This is the same initial grid used previously for channel flow assessments in

Sections 4.5 and 5.2. The finer $\overline{\Delta}_y$ is required for the error-indicator of this Chapter, since it is defined based on the assumption of turbulent flows (where we assumed that the source of error in the mean momentum equation comes from the error in the total Reynolds stress and not the numerical errors).

The solution on this grid is shown in Fig. 8.2 with some details given in Table 8.1. Another grid (G_1') is then generated by coarsening the grid G_1 by 25%. Convergence of the grid is tested by directly comparing the solution on the two grids, i.e., $\delta\overline{Q}^{G_k,G_k'}$ (see Table 8.1). Since the solution is not converged ($\delta\overline{Q}^{G_k,G_k'} \approx 5\%$), grids G_1 and G_1' are used to estimate the source of error using the proposed error-indicator $\overline{\mathcal{E}}_{ij}$. The constant Λ in Eqn. 8.28 is chosen such that it leads to an increase in the cell count by approximately a factor of 5. Directional small-scale energy $\mathcal{A}(\mathbf{x},\mathbf{n})$ is computed based on the solution on grid G_1, which is then used to determine the anisotropy of the optimal filter based on Eqn. 8.30. This leads to the next grid, labeled G_2, with $\overline{\Delta}_x = 0.13H$, $\overline{\Delta}_y = 0.011H \rightarrow 0.12H$ ($\overline{\Delta}_{y_w}^+/2 \approx 5.8$ at the wall, based on the converged solution) and $\overline{\Delta}_z = 0.091H$. Note that we have used the minimum values of the target $\overline{\Delta}_x$ and $\overline{\Delta}_z$ in order to ensure a structured grid.

The process continues in the same manner, generating the 7 grids listed in Table 8.1. At each iteration N_{tot} is matched, as closely as possible, with the grids in Table 5.5 generated by error-indicators $\overline{\mathcal{A}}(\mathbf{x},\mathbf{n})$ and $\overline{\mathcal{G}}(\mathbf{x},\mathbf{n})$.

The solution clearly converges as the grid is refined. The fact that it takes a few iterations is partly due to the change in the resolved turbulence as the grid is refined (particularly from the exceedingly coarse initial grid used here), partly

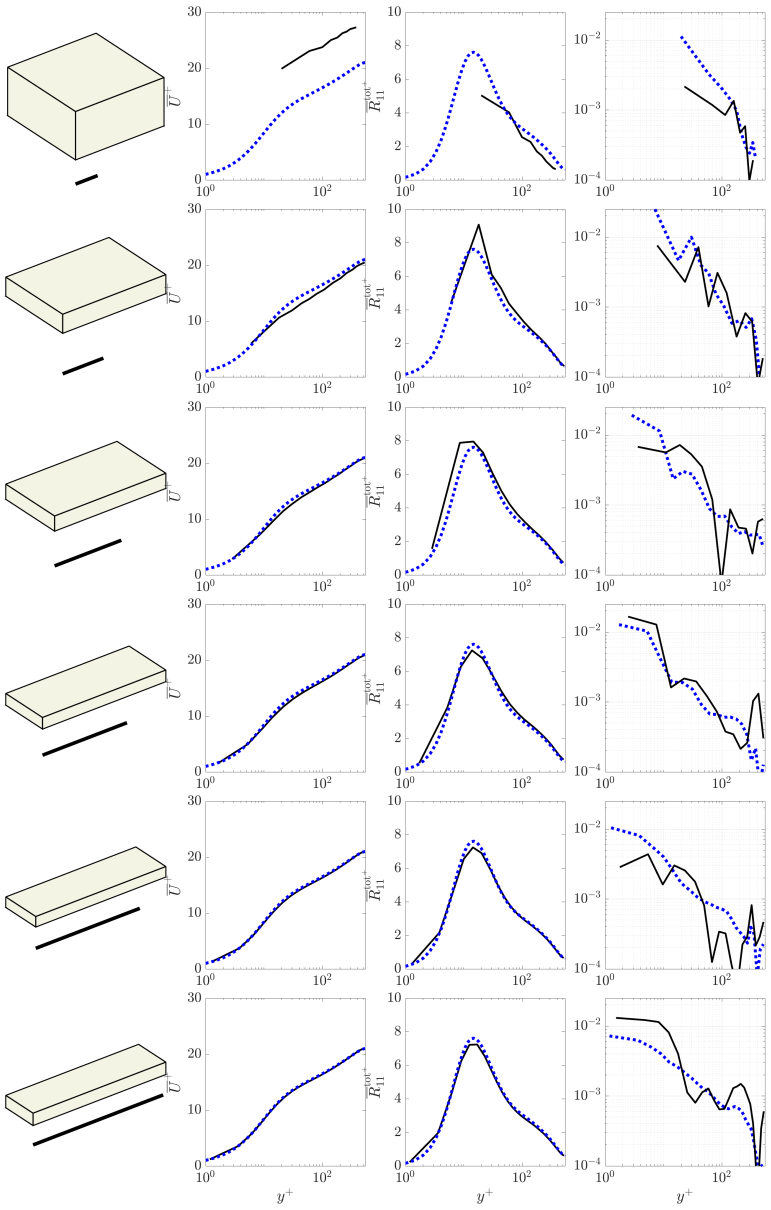

Figure 8.2: Sequence of grids generated by $\overline{\mathcal{E}}_{ij}(\mathbf{x})$ for LES of the channel flow at $Re_\tau \approx 545$. The rows show the progression of grids from G_1 (top row) to G_6 (bottom row). Key quantities are listed in Table 8.1. The left column shows the shape of a wall-adjacent cell, while the right column shows the streamwise, wall-normal, and spanwise error-indicators by the brightest to the darkest colors. In the right column the dotted blue line shows the actual value of $\overline{\mathcal{E}}_{ij}(\mathbf{x})$ (computed by comparing to DNS solution), while the black solid lines show the estimated value based on the change in the quantity (used for grid selection). The dotted blue lines in the middle columns show the reference DNS solution of del Alamo and Jimenez [18].

Grid	N_{tot}	N_y	$(\overline{\Delta}_x^+, \overline{\Delta}_{y_w}^+/2, \overline{\Delta}z^+)$	$(\overline{\Delta}_x, \overline{\Delta}_{y_c}, \overline{\Delta}_z)/H$	Re_τ	$\delta\overline{Q}^{G_k,G'_k}$ (%)	$\overline{e}_{\text{QoI}}^{\text{DNS}}$ (%)
G_1	$15k$	20	$(80, 20, 80)$	$(0.2, 0.1, 0.2)$	398	5.4	32
G_2	$73k$	28	$(70, 6.0, 51)$	$(0.13, 0.12, 0.091)$	562	3.6	11.3
G_3	$242k$	32	$(46, 2.8, 26)$	$(0.083, 0.15, 0.048)$	549	3.3	5.6
G_4	$523k$	36	$(40, 1.7, 16)$	$(0.073, 0.13, 0.028)$	550	2.9	3.1
G_5	$1.18M$	46	$(34, 1.3, 10)$	$(0.063, 0.11, 0.019)$	546	1.3	1.5
G_6	$2.59M$	60	$(28, 1.2, 7.4)$	$(0.051, 0.078, 0.014)$	544	0.9	1.3
G_7	$5.86M$	76	$(21, 1.0, 5.6)$	$(0.038, 0.056, 0.010)$	542	0.9	0.7

Table 8.1: Sequence of grids generated for LES of channel flow at $Re_\tau \approx 545$ using the dynamic Smagorinsky model. N_{tot} is the total number of grid points, while N_y denotes the number of points across the channel. $\overline{\Delta}_{\mathbf{n}} = \overline{\Delta}(\mathbf{x}, \mathbf{n})$ is both the filter-width and the grid-resolution. Friction resolutions $\overline{\Delta}_{\mathbf{n}}^+$ are computed based on grid-specific values. $\overline{\Delta}_{y_c}$ is the wall-normal filter-width at the center of the channel, while $\overline{\Delta}_{y_w}$ is its value at the wall. The actual error in the QoIs, $\overline{e}_{\text{QoI}}^{\text{DNS}}$, is defined by Eqns. 3.9 and 3.10, while $\delta\overline{Q}^{G_k,G'_k}$ (defined is Eqn. 8.33) shows the change in the QoIs between grids G_k and G'_k.

due to the simple model used for connecting $\check{\mathcal{E}}$ and $\check{\Delta}$, or more generally due to the inaccuracies involved in the error-estimation process, and partly due to the fact that the true scaling exponents α and α' are different from the assumed values of 2.

Looking at the plots in Fig. 8.2 the solution is sufficiently accurate on grid G_4 and afterwards. The computed value of $\delta\overline{Q}^{G_k,G'_k}$ also confirms this conclusion with values that are all arguably small enough for an LES. We also notice that the convergence-verification based on $\delta\overline{Q}^{G_k,G'_k}$ generally leads to the same conclusion as the validation test based on $\overline{e}_{\text{QoI}}^{\text{DNS}}$. However, for the initial grids $\delta\overline{Q}^{G_k,G'_k}$ has a lower value compared to $\overline{e}_{\text{QoI}}^{\text{DNS}}$ (also α'' is probably lower for these grids), while it starts to increase in its relative magnitude to $\overline{e}_{\text{QoI}}^{\text{DNS}}$ (where the LES model is getting deactivated and α'' is approaching the nominal value of the code); to a point that in the final grid we have $\delta\overline{Q}^{G_k,G'_k} > \overline{e}_{\text{QoI}}^{\text{DNS}}$.

The G_4 and G_5 grids have filter widths $(\overline{\Delta}_x^+, \overline{\Delta}_{y_w}^+/2, \overline{\Delta}_z^+)$ of $(40, 1.7, 16)$ and

$(34, 1.3, 10)$ at the wall. These resolutions are commensurate with the literature and experience on high quality wall-resolved LES. The wall normal filter-width at the center of the channel, $\overline{\Delta}_{y_c}$, is $0.13H$ and $0.11H$ for grids G_4 and G_5, respectively, which are arguably too coarse judging by the LES standards. However, these coarse resolutions did not seem to negatively impact the accuracy of our quantities of interest (note that this may not be necessarily true for other QoIs, especially those that are more sensitive to the resolution level).

Grids G_6 and G_7 are generated to make sure that the grid-adaptation method keeps improving the solution and does not drive the grid away from optimality.

8.5 Assessment on the flow over a backward-facing step at $Re_H = 5100$

The convergence-verification and grid selection/adaptation algorithm of Fig. 8.1 is next tested on the flow over a backward-facing step. The geometry and flow conditions are identical to what we used is Sections 3.3, 4.6, and 5.3, and are not explained here.

The OpenFOAM code version 2.3.1 (which is a second-order finite-volume solver; cf. [60]) is used for this test case in order to allow for fully unstructured adapted grids. The PISO algorithm is used for the pressure-velocity coupling, with the dynamic k_{sgs}-equation eddy viscosity model [61, 62] as the SGS model and the cube root of the cell volume as the filter-width.

At each iteration of the algorithm the LES equations are solved on two grids

(i.e. the primary grid G_k and the test grid G'_k generated by uniform coarsening of G_k by 25% used for our convergence-verification test) and the change in the quantities of interest is computed. The quantities of interest are chosen to be the two non-zero mean velocity and the four non-zero Reynolds stress profiles, as well as the friction and pressure coefficient profiles on the horizontal wall. The error in each of the QoIs is computed using Eqn. 3.11. The computed $\delta\overline{Q}_m$ are then scaled by their representative values to make them comparable and then weighting together as 1/3 each of the mean velocities, the Reynolds stress, and the wall quantities, to define $\overline{e}^{\text{DNS}}_{\text{QoI}}$ based on Eqn. 3.12, and $\delta\overline{Q}^{G_k,G'_k}$ as

$$\delta\overline{Q}^{G_k,G'_k} = \frac{1}{3}\sum_{m=1}^{2}\frac{\delta\overline{Q}_m^{G_k,G'_k}}{2} + \frac{1}{3}\sum_{m=3}^{6}\frac{\delta\overline{Q}_m^{G_k,G'_k}}{4} + \frac{1}{3}\sum_{m=7}^{8}\frac{\delta\overline{Q}_m^{G_k,G'_k}}{2}\,. \tag{8.34}$$

The convergence-verification results of this Section are reported by both of $\overline{e}^{\text{DNS}}_{\text{QoI}}$ and $\delta\overline{Q}^{G_k,G'_k}$. Note that in a practical grid selection/adaptation case one only has access to $\delta\overline{Q}^{G_k,G'_k}$, while $\overline{e}^{\text{DNS}}_{\text{QoI}}$ is reported to make sure that our conclusions from $\delta\overline{Q}^{G_k,G'_k}$ is consistent with the actual error in the QoIs, and to enable a direct comparison between the results of this Section and the sequences of grids generated by either of $\overline{\mathcal{A}}(\mathbf{x},\mathbf{n})$ and $\overline{\mathcal{G}}(\mathbf{x},\mathbf{n})$ for the flow over a backward-facing step in Sections 4.6 and 5.3.

In the same spirit as for the channel tests, the initial grid is chosen to have very coarse cells of size $\overline{\Delta}_x = \overline{\Delta}_y = \overline{\Delta}_z = 0.2H$ everywhere, except for a distance H from the walls where the grid is refined in the wall-normal direction by a factor of two. This initial grid is labeled G_1 in this Section, which is identical to the initial grid used in Table 5.4 (labeled G-1), and in Table 3.4 (labeled LES-1). A test grid G'_1 is also

generated for convergence-verification, which has the exact same structure as grid G_1, but is coarser everywhere and in all directions by 25%, $\overline{\Delta}'(\mathbf{x},\mathbf{n}) = 1.25\overline{\Delta}(\mathbf{x},\mathbf{n})$. Note that the grid G_1' has half the number of computational cells of the grid G_1, and the cost of solving on this grid is about 41% the cost of LES on the primary grid G_1.

After computing the convergence-verification criteria ($\delta\overline{Q}^{G_k,G_k'}$ and $\overline{e}_{\text{QoI}}^{\text{DNS}}$), and since the change in the QoIs is above the acceptable threshold, the algorithm of Fig. 8.1 tells us that we need to estimate $\check{\mathcal{E}}_{ij}$ (Eqn. 8.26), computed $\overline{\mathcal{A}}(\mathbf{x},\mathbf{n})$ on grid G_1 (Eqns. 3.2 and 3.3), and adapt the grid based on Eqns. 8.28 and 8.30. The two grid-scaling exponents required for error-estimation and grid-adaptation, α and α', are again assumed constant throughout the domain and independent of direction, $\alpha(\mathbf{x},\mathbf{n}) = \alpha'(\mathbf{x},\mathbf{n}) = 2$, without any attempt at finding the optimal values. First, the optimal $\check{\Delta}_{\text{vol,opt}}$ is found by solving Eqn. 8.28 with Λ selected such that the next grid G_2 has twice as many cells as G_1, and then the optimal anisotropic filter $\check{\Delta}_{\text{opt}}(\mathbf{x},\mathbf{n})$ is found from Eqn. 8.30. All target resolutions are then converted to the refinement regions. Since OpenFOAM's *refineMesh* utility can only refine hexahedral cells by factors of $2^{\check{\mathcal{R}}}$ in any direction (where $\check{\mathcal{R}}(\mathbf{x},\mathbf{n})$ in the refinement level defined in Eqn. 6.1), a cell is cut in half until the grid-spacing is less than or equal to the target grid-spacing in that location and direction. These target refinement regions are illustrated in Fig. 8.3 for grid G-2.

The process suggests a single level of refinement (i.e., by a factor of 2) of $\overline{\Delta}_y$ almost everywhere within the boundary layer downstream of the step, a large portion of the incoming boundary layer, the shear layer, and the recirculation bubble, with

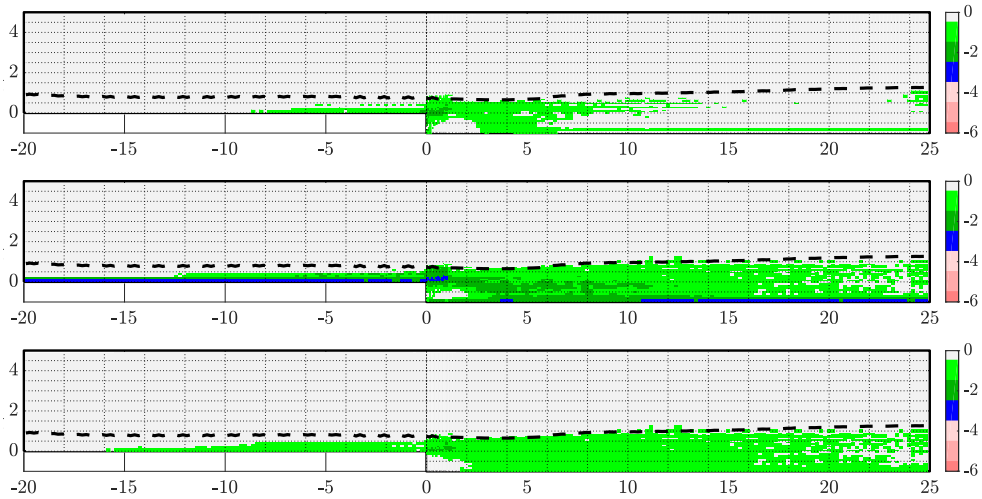

Figure 8.3: The grid G_2 from Table 8.2 illustrated by its refinement levels in x (top), y (middle), and z (bottom). Refinement levels are computed based on a skeletal grid with $\Delta_0(\mathbf{x}, \mathbf{n}) = 0.2H$ for all $\mathbf{x}$ and $\mathbf{n}$. The light green, dark green and blue colors illustrate regions with one ($\overline{\Delta}_\mathbf{n}/H = 0.1$), two ($\overline{\Delta}_\mathbf{n}/H = 0.05$), and three ($\overline{\Delta}_\mathbf{n}/H = 0.025$) refinement levels, respectively. The white regions show areas of the domain that are left untouched (i.e. $\overline{\Delta}_\mathbf{n}/H = 0.2$). The dashed line highlights the δ_{95} boundary layer thickness. The refinement regions are then converted to an input file to OpenFOAM's *refineMesh* utility. Same refinement regions are used for generating the test grid G_2'. The irregularities in the target refinement regions encountered towards the end of the computational domain $x/H \geq 15$ are result of slow convergence of the error-indicator $\check{\mathcal{E}}_{ij}$ in time.

an additional level of refinement (i.e., a factor of 4) near the horizontal wall in the entire domain and the shear layer, as well as a third level of refinement (a factor of 8) in the incoming boundary layer upstream of the step, the recovering boundary layer downstream of the step, and at the initial part of the shear layer. The spanwise resolution $\overline{\Delta}_z$ is refined by a single level throughout most of the upstream and downstream boundary layers and the shear layer, but not in the recirculation region where the turbulent activity is small. The streamwise grid-spacing $\overline{\Delta}_x$ is refined at the approaching boundary layer close to the step, the vertical step wall where the recirculation bubble causes shear, the entire free shear layer formed after the step, and the region close to the impingement/reattachment point. These refinement

regions are quite consistent with what the other error-indicators $\overline{\mathcal{A}}(\mathbf{x},\mathbf{n})$ and $\overline{\mathcal{G}}(\mathbf{x},\mathbf{n})$ produced, and also with the experience and "common practice" in LES of such flows.

The adapted grid G_2 is then generated by using the target refinement regions to produce an input file to the *refineMesh*. The test grid G_2' is generated by using the same refinement regions (i.e. same *refineMesh* input file) but applied on the uniformly coarser test grid G_1' (with minimal change made in the input file to ensure proper performance of the *refineMesh* utility). The LES is solved on these two grids and the algorithm repeats until the solution converges.

At each iteration of the algorithm the constant Λ in Eqn. 8.28 is chosen such that the next target grid has an approximately equal number of cells, N_{tot}, to its equivalent grids generated by error-indicators $\overline{\mathcal{A}}(\mathbf{x},\mathbf{n})$ and $\overline{\mathcal{G}}(\mathbf{x},\mathbf{n})$ (Table 5.6). This approximation was done before the actual construction of the adapted grid using the *refineMesh* utility, by estimating the number of cells from the target grid-spacings, and therefore, the actual adapted grids may have slightly different number of cells.

The sequence of grids generated by this method is reported in Table 8.2 with some key resolutions reported for reference. The convergence of the QoI profiles is plotted in Fig. 8.4 for friction and pressure coefficients, and in Figs. 8.5, 8.6, and 8.7 for the mean velocity and Reynolds stresses at some of the more interesting locations.

The computed values for the the solution error is reported in Table 8.2 for both our convergence-verification criterion, $\delta\overline{Q}^{G_k,G_k'}$, and the validation test by comparison to the DNS solution, $\overline{e}_{\text{QoI}}^{\text{DNS}}$. For all grids G_k in the sequence the computed values of $\delta\overline{Q}^{G_k,G_k'}$ and $\overline{e}_{\text{QoI}}^{\text{DNS}}$ result in the same conclusion about the convergence of the grid;

Grid	N_{tot}	$(\overline{\Delta}_x^+, \overline{\Delta}_{y_w}^+/2, \overline{\Delta}_z^+)$	$(\overline{\Delta}_x, \overline{\Delta}_y, \overline{\Delta}_z)/\delta_{\text{shear}}$	$\delta\overline{Q}^{G_k,G_k'}$ (%)	$\overline{e}_{\text{QoI}}^{\text{DNS}}$ (%)
G_1	149k	$(42, 10, 42)$	$(0.21, 0.17, 0.33)$	9.4	11
G_2	292k	$(20, 2.6, 20)$	$(0.078, 0.049, 0.16)$	7.9	12
G_3	596k	$(22, 1.4, 11)$	$(0.16, 0.078, 0.078)$	6.8	7.3
G_4	1.31M	$(23, 0.71, 5.7)$	$(0.073, 0.036, 0.073)$	6.3	7.4
G_5	2.13M	$(23, 0.73, 5.8)$	$(0.068, 0.017, 0.034)$	6.4	4.5
G_6	3.78M	$(25, 0.39, 6.2)$	$(0.068, 0.017, 0.034)$	3.8	4.5
G_7	6.69M	$(13, 0.42, 3.3)$	$(0.034, 0.017, 0.034)$	3.6	4.5
DNS	54M	$(6.0, 0.38.3.0)$	$(0.017, 0.0086, 0.017)$	–	0

Table 8.2: Sequence of grids generated for LES of flow over a backward-facing step. $(\overline{\Delta}_x^+, \overline{\Delta}_{y_w}^+/2, \overline{\Delta}_z^+)$ correspond to the boundary layer resolutions at $x/H = -3$ upstream of the step, δ_{shear} is the approximate shear layer thickness at $(x, y)/H = (1, 0)$, and $(\overline{\Delta}_x, \overline{\Delta}_y, \overline{\Delta}_z)$ is the resolution at that location. See Fig. 8.8 for more details. $\overline{e}_{\text{QoI}}^{\text{DNS}}$ and $\delta\overline{Q}^{G_k,G_k'}$ are defined in Eqns. 3.12 and 8.34.

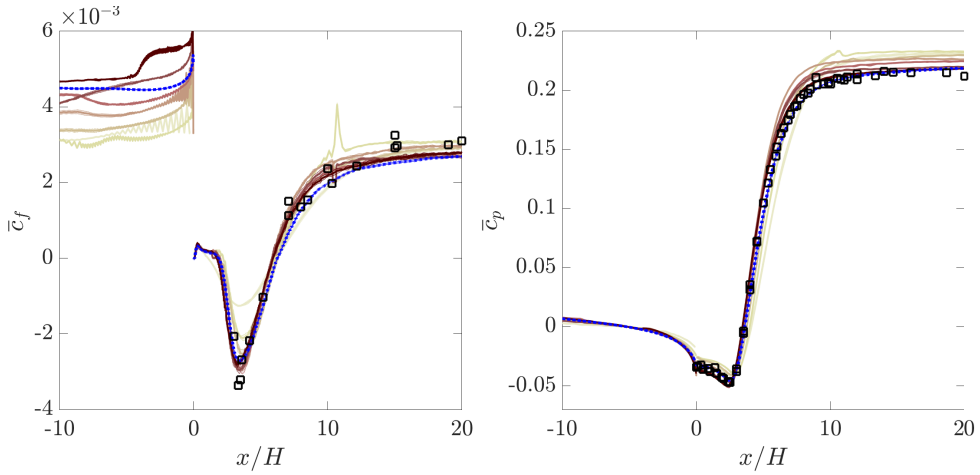

Figure 8.4: Convergence of (a) friction coefficient $\overline{c}_f$ and (b) pressure coefficient $\overline{c}_p$ for LES of flow over a backward-facing step. Grids in Table 8.2 are shown by the lightest color for G_1 to the darkest for G_7. Solid lines denote the sample means, while the shaded regions correspond to the approximate confidence intervals (computed locally). The dotted blue lines and their shaded regions denote our DNS results and their confidence intervals. Symbols correspond to the experimental data of Jovic & Driver [57, 58] with slightly different setup (error bars on the experimental data are not shown). Experimental measurements of $\overline{c}_f$ and $\overline{c}_p$ are not available upstream of the step.

in other words, $\delta\overline{Q}^{G_k,G_k'}$ takes larger values when $\overline{e}_{\text{QoI}}^{\text{DNS}}$ is large and becomes smaller as $\overline{e}_{\text{QoI}}^{\text{DNS}}$ decreases. This is a critical property for a convergence-verification test, as

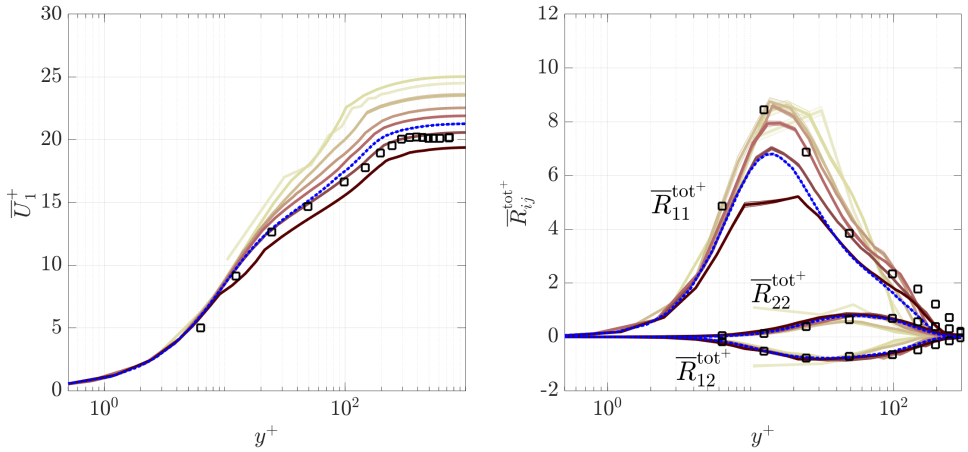

Figure 8.5: Convergence of the mean velocity and Reynolds stress profiles for the sequence of grids in Table 8.2 at the incoming boundary layer at $x/H = -3$. Grids in the sequence are shown by the lightest color for G_1 to the darkest for G_7. Solid lines denote the sample means, while the shaded regions correspond to the approximate confidence intervals (computed locally). The dotted blue lines and their shaded regions denote our DNS results and their confidence intervals. Symbols correspond to the experimental data of Jovic & Driver [57, 58] (error bars on the experimental data are not shown).

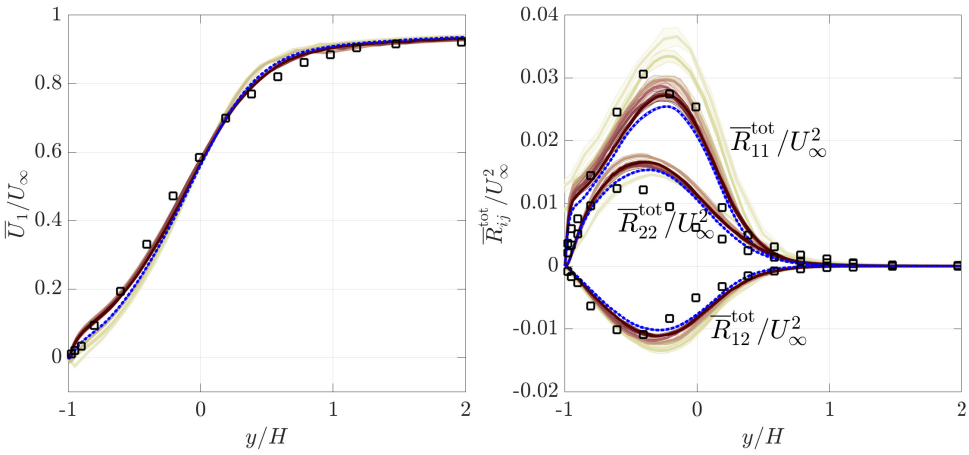

Figure 8.6: Convergence of the mean velocity and Reynolds stress profiles for grids in Table 8.2 at $x/H = 6$ near the reattachment point. See Fig. 8.5 for more details.

in reality there is no DNS solution to judge the accuracy of the solution and the convergence-verification test is the only tool we have.

The generated grid G_6 is shown in Fig. 8.8 for comparison with the grids generated by $\overline{\mathcal{A}}(\mathbf{x}, \mathbf{n})$ (Fig. 5.14) and $\overline{\mathcal{G}}(\mathbf{x}, \mathbf{n})$ (Fig. 5.11). Note how complicated

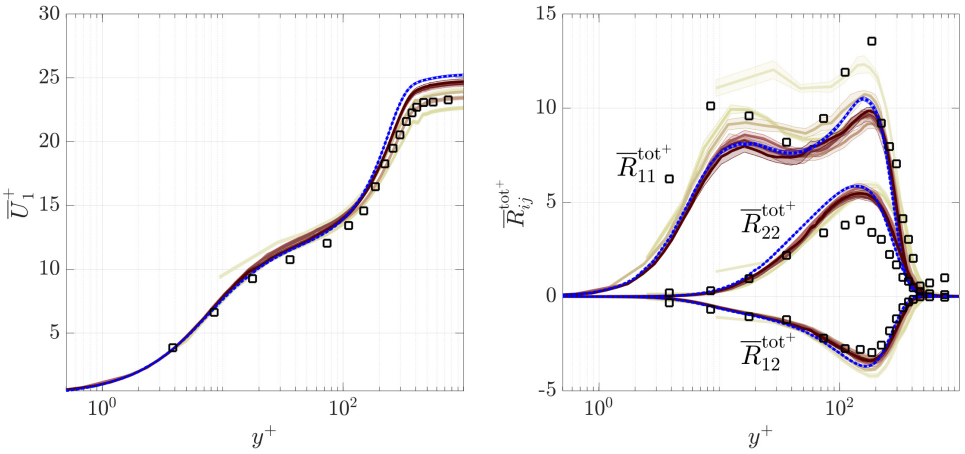

Figure 8.7: Convergence of the mean velocity and Reynolds stress profiles for the recovering boundary layer at $x/H = 15$ for the sequence of grids in Table 8.2. See Fig. 8.5 for more details.

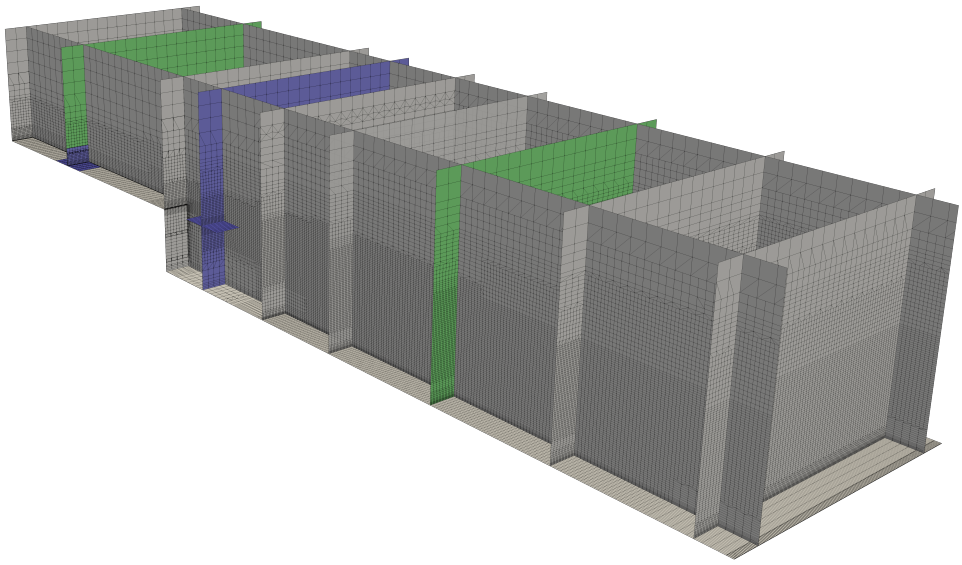

Figure 8.8: The generated grid G_6 of Table 8.2 with 3.78M cells. Intersections of the blue planes denote locations whose resolutions are reported in Table 8.2, while the green planes correspond to $x/H = -3$ and $x/H = 6$ whose velocity and Reynolds stress profiles are plotted in Figs. 8.5 and 8.6. The grid is resulted from computation of the proposed error-indicator and applying the grid selection criteria of Eqns. 8.28 and 8.30 with no user experience involved.

the structure of the grid has become, with highly anisotropic cells and so many transitions in cell anisotropy as well as resolution throughout the domain.

Looking more closely at how the computed $\overline{e}^{\text{DNS}}_{\text{QoI}}$ changes in Table 8.2 from one grid to the next we notice a slower convergence compared to the turbulent channel flow. Specifically, the reported values of $\overline{e}^{\text{DNS}}_{\text{QoI}}$ suggest that the convergence is nearly stalled (at 4.5%) for grids G_5 and afterwards. The exact reason for this is not known, but a closer study of the convergence of each of the QoIs in Fig. 8.9 identifies the friction coefficient as the main limiting quantity that prevents further convergence of $\overline{e}^{\text{DNS}}_{\text{QoI}}$. This could also be seen from the sudden jump in $\overline{c}_f$ upstream of the step (Fig. 8.4) which, in turn, shows up as an underprediction of the normalized mean velocity and Reynolds stresses in the friction units at $x/H = -3$ (Fig. 8.5). A further examination of $\overline{\Delta}(\mathbf{x}, \mathbf{n})$ in that region (see the third column of Table 8.2 for filter resolution at $x/H = -3$) shows that the spanwise friction resolution $\overline{\Delta}_z^+$ (grid G_7 for instance) is much finer than what is known as "optimal" based on the streamwise and wall-normal resolutions of the grid at that location. In fact, the situation is even worse, since the streamwise resolution of $\Delta x^+ \approx 13$ is only achieved very close to the wall (say $y^+ < 15$), meaning that the effective boundary layer resolution is probably closer to $(26, 0.42, 3.3)$. It is somewhat well-known that LES grids that are too fine in the spanwise direction (especially when the dynamic procedure is used) tend to overpredict the resolved shear stress, which can lead to an underpredicted mean velocity profile (in friction units). This helps us hypothesize a few potential factors to be contributing to this misbehavior of the adapted grids:

(i) The error-indicator $\overline{\mathcal{E}}_{ij}(\mathbf{x})$, under the current assumptions and implementation, could become somewhat insufficient in describing the local sources of errors. Note that a similar behavior was seen before in the case of channel

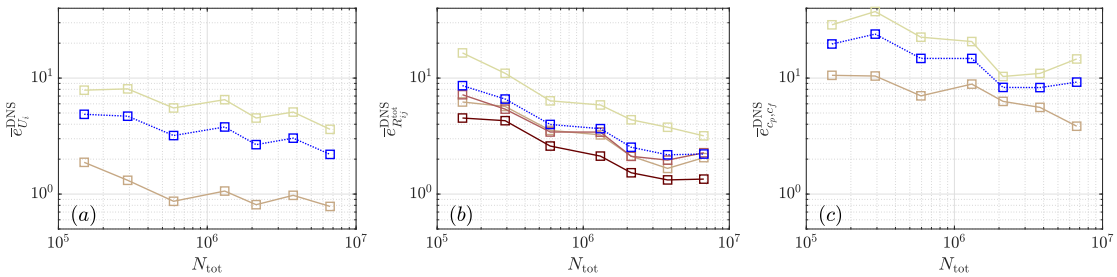

Figure 8.9: The error in each of the quantities of interest in the backward-facing step for (a) the two non-zero mean velocity fields in the x and y directions (lighter and darker colors, respectively) and their total contribution to $\overline{e}^{\mathrm{DNS}}_{\mathrm{QoI}}$ (dotted blue), (b) the four non-zero Reynolds stresses $\overline{R}^{\mathrm{tot}}_{11}$, $\overline{R}^{\mathrm{tot}}_{22}$, $\overline{R}^{\mathrm{tot}}_{33}$, $\overline{R}^{\mathrm{tot}}_{12}$ (from the lightest color to the darkest) as well as their total contribution to $\overline{e}^{\mathrm{DNS}}_{\mathrm{QoI}}$ (dotted blue), and (c) the friction (lighter color) and pressure (darker color) coefficients and their total contribution to $\overline{e}^{\mathrm{DNS}}_{\mathrm{QoI}}$ (dotted blue). The nearly constant value of $\overline{e}^{\mathrm{DNS}}_{\mathrm{QoI}}$ on grids G_5, G_6, and G_7 in Table 8.2 can be mostly attributed to the increase in the error in the friction coefficient on these grids.

flow where the wall-normal resolution of the target grids were too coarse towards the center of the channel.

(ii) The model we have used to describe the change in $\check{\mathcal{E}}_{ij}$ with $\check{\Delta}_{\mathrm{vol}}$ (and thus to estimate $\overline{\mathcal{E}}_{ij}$ from its change between grids $\overline{\Delta}$ and $\widetilde{\Delta}$) is insufficient.

(iii) The assumption of full separation between the tasks of finding $\check{\Delta}_{\mathrm{vol,opt}}(\mathbf{x})$ based on $\check{\mathcal{E}}_{ij}$ and finding $\check{\Delta}_{\mathrm{vol}}(\mathbf{x},\mathbf{n})$ based on $\overline{\mathcal{A}}(\mathbf{x},\mathbf{n})$ was inadequate.

(iv) The adjoint fields could be more important for the success of $\overline{\mathcal{E}}_{ij}$ in optimal grid selection/adaptation in LES compared to the other two error indicators.

The error-indicator of this Chapter is still under development and the resolution of these issues is the subject of future research.

Chapter 9: Summary, conclusion, and future directions

With the huge increase in computing power over the past few decades, large eddy simulation has become one of the most promising tools for simulation of turbulence in academic research and industrial applications. However, the accuracy of an LES, and consequently its success, depends directly on (i) the model used to account for the effect of the unresolved scales, (ii) the computational grid used for discretization of the filtered equations, and (iii) the accuracy of numerics used in solving the discretized equation. While there has been extensive research on items (i) and (iii), systematic identification of the computational grid is a relatively unexplored field.

The current practice in grid selection/adaptation in LES is to have the user generate a computational grid that is deemed suitable based on prior experience with LES of that specific flow and its resolution requirements. This gives rise to a variety of issues, from the non-systematic nature of the process (e.g., different users end up with different grids and hence different results), to the possibility of failing to resolve some of the important features of the flow, and to the problem of suboptimal application of LES to new flows where limited prior experience and knowledge is available. This dissertation was aimed at addressing this issue.

The three error-indicators $\overline{\mathcal{A}}(\mathbf{x}, \mathbf{n})$, $\overline{\mathcal{G}}(\mathbf{x}, \mathbf{n})$ and $\overline{\mathcal{E}}_{ij}(\mathbf{x})$ were described and

tested in Chapters 3, 5, and 8, respectively. The optimal grid selection criterion in space and direction was introduced in Chapter 4, followed by a detailed study of its impact on the generated grids and the overall error in the solution and its quantities of interest (QoIs). The statistical convergence of $\overline{\mathcal{A}}(\mathbf{x},\mathbf{n})$ and $\overline{\mathcal{G}}(\mathbf{x},\mathbf{n})$ with time averaging was studied in Chapter 6, where it was shown that they exhibited a much faster convergence compared to the QoI profiles. Introduction of the proposed convergence-verification method and the proposed systematic algorithm for convergence-verification and grid selection were delayed until Chapter 7, in order to also motivate the "two-grid" error-estimation method of Chapter 8. The cost of an iterative and systematic grid selection/adaptation process was first discussed in Section 3.5, and later in Section 7.3 for the full convergence-verification and grid-adaptation algorithm.

All the error-indicators were tested for their ability in automatic grid selection in the canonical problem of turbulent channel flow and in the more complex case of flow over a backward-facing step (BFS). It was shown that the heuristic-based error-indicator $\overline{\mathcal{A}}(\mathbf{x},\mathbf{n})$ was able to produce grids that were remarkably close to what is known as "best practice" in LES of such flows; however, we identified and acknowledged a few shortcomings in the definition of the error-indicator and its target grids (discussed in some detail in Section 3.6). These issue were then solved by introducing the second error-indicator $\overline{\mathcal{G}}(\mathbf{x},\mathbf{n})$, which could outperform $\overline{\mathcal{A}}(\mathbf{x},\mathbf{n})$ in terms of its theoretical background and the optimality of its target grids. We then argued that a possible shortcoming of $\overline{\mathcal{G}}(\mathbf{x},\mathbf{n})$ (which measures the sensitivity of the governing equations to a change in the filter-width) could be in cases where

the sensitivity of the grid at a certain length scale $\overline{\Delta}$ was not a direct measure of its overall error generation (even though we did not see this in our assessments).

The third error-indicator $\overline{\mathcal{E}}_{ij}(\mathbf{x})$ was introduced as a more comprehensive treatment of error-estimation in LES, where it directly targeted the local source of errors in the governing equation. The underlying assumption in development of $\overline{\mathcal{E}}_{ij}(\mathbf{x})$ was that the source of error in the instantaneous governing equations of LES could be found by studying their ensemble/time averaged version and employing our knowledge of turbulence modeling. While the grids generated by $\overline{\mathcal{E}}_{ij}(\mathbf{x})$ had the same level of accuracy as those generated by $\overline{\mathcal{G}}(\mathbf{x}, \mathbf{n})$ for the channel flow, its BFS grids (Table 8.2) were in fact worse. This led to a more careful study of the convergence of each of the QoIs, where we argued that the evidence (presented at the end of Section 8.5) pointed us more towards the suboptimal implementation of the method as the primary cause (an interaction of the simplified model used for computing $\overline{\mathcal{E}}_{ij}(\mathbf{x})$ based on its change between the two grids, the suboptimal prediction of aspect ratio of the filter, and the spurious sensitivity of the LES models to extra refined resolutions in the spanwise direction), and less to a fundamental flaw in our underlying assumptions. Nevertheless, the final decision on the suitability of this error-indicator requires a more comprehensive assessment.

9.1 Future directions

The most important subject for future research is arguably the improvement of the proposed error-indicator $\overline{\mathcal{E}}_{ij}(\mathbf{x})$. Due to the complicated implementation of this

error-indicator and the many different components involved in it, this must be done by isolating each process and finding the exact cause of the issue. For instance, the effect of the model and the approximations associated with it can be easily excluded by direct computation of $\overline{\mathcal{E}}_{ij}(\mathbf{x})$ from the reference DNS solution. This will be the focus of our research in the immediate future.

The present work can be also extended in a few different directions.

(a) Throughout this dissertation we only considered static grids for statistically stationary flows. Application of $\overline{\mathcal{A}}(\mathbf{x}, \mathbf{n})$ and $\overline{\mathcal{G}}(\mathbf{x}, \mathbf{n})$ to turbomachinary flows and flows with strong unsteady effects (vortex shedding, flutter, etc.) is quite natural and can be easily pursued; however, changing the grid resolution may change the frequency of these unsteady motions, and thus, application of $\overline{\mathcal{E}}_{ij}(\mathbf{x})$ to such flows appears to be more involved.

(b) We only assessed our error-indicators on relatively simple flows, while in reality their main benefit would be in their capability in accurate error-estimation and optimal grid selection of more complex flowfields. A more comprehensive assessment of their performance (e.g., in transitional flows, turbulent jets, high Reynolds number flows, etc.) will be instructive and quite beneficial.

(c) Most of the developments of this dissertation were for the implicitly-filtered LES of single-phase, incompressible, Newtonian fluids with constant density and viscosity. There is still much potential in extending the proposed error-indicators to more complex problems, including aeroacoustic and noise prediction, supersonic and hypersonic flows, combustion, two phase flows, etc. In the same spirit, our error-indicators can be combined with the feature-based

indicators used to locate and follow a strong physical feature (shock, flame, etc.) in adaptive mesh refinement (AMR) and enable fully adaptable grids.

(d) All of our error-indicators are deterministic measures of error generation in LES. A more consistent approach is to define stochastic error-indicators that can also provide a lower and upper bound (due to the uncertainties in estimating the modeling errors) on the estimated values. This could be the next huge improvement in error-estimation in LES, and can also remove the need for a second LES solution to verify convergence.

(e) Despite the promising results from the proposed convergence-verification method (using the LES solution on two grids and employing the Richardson extrapolation) there might be more optimal ways of using the second solution, or possibly, other methods (with the same level of robustness) without the need for a second LES solution.

(f) A huge improvement of the optimality of the girds could be achieved by "output-based" grid-adaptation enabled by the adjoint fields. However, this will first require a computationally tractable method of estimating the adjoint fields in chaotic problems. A possible solution could be to solve the adjoint fields of the mean equations (cf. the method proposed by Larsson [82]). Note that in the case of output-based adaptation, the proposed algorithm of Fig. 7.4 can be modified and rearranged to take a more efficient form similar to Fig. 9.1.

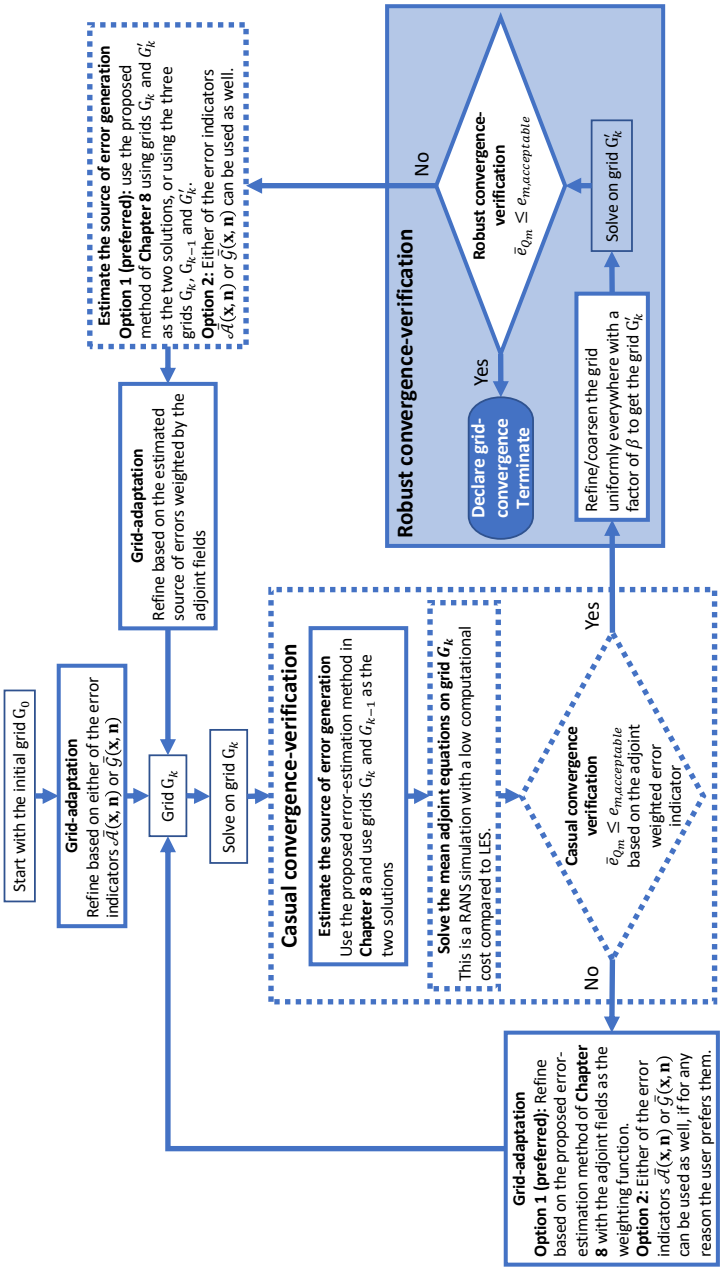

Figure 9.1: The envisioned algorithm for output-based filter/grid-adaptation and convergence-verification in LES. Note that the problem of chaotic divergence of the adjoint fields needs to be solved before we can use this algorithm. The current algorithm uses the adjoint of the mean equations combined with $\overline{\mathcal{E}}_{ij}(\mathbf{x})$ defined based on the mean equations. More research on "two-grid" error-estimation, $\overline{\mathcal{E}}_{ij}(\mathbf{x})$, is also necessary, including models that work on partially unchanged grids (encountered when the two grids used for estimation of $\overline{\mathcal{E}}_{ij}(\mathbf{x})$ are taken from the same sequence of adapted grids). Addition of stochastic error-indicators can potentially make the "casual convergence-verification" process more robust and remove the need of running a second LES for the "robust convergence-verification" process.

Bibliography

[1] P. R. Spalart, W.-H. Jou, M. Strelets, and S. R. Allmaras. Comments on the feasibility of LES for wings, and on a hybrid RANS/LES approach. In C. Liu and Z. Liu, editors, *Advances in DNS/LES*, Greyden, Columbus, OH, 1997.

[2] G. A. Bres, V. Jaunet, M. Le Rallic, P. Jordan, T. Colonius, and S. K. Lele. Large eddy simulation for jet noise: the importance of getting the boundary layer right. AIAA Paper 2015-2535, 2015.

[3] P. Sagaut. *Large eddy simulation for incompressible flows*. Springer Heidelberg, 2006.

[4] S. Ghosal. An analysis of numerical errors in large-eddy simulations of turbulence. *J. Comput. Phys.*, 125:187–206, 1996.

[5] F. G. Kravchenko and P. Moin. On the effect of numerical errors in large eddy simulations of turbulent flows. *J. Comput. Phys.*, 131:310–322, 1997.

[6] R. Mittal and P. Moin. Suitability of upwind-biased finite difference schemes for large-eddy simulation of turbulent flows. *AIAA J.*, 35(8):1415–1417, 1997.

[7] T. Brandt. A posteriori study on modelling and numerical error in LES applying the Smagorinsky model. In *Complex effects in large eddy simulations. Lecture notes in computational science and engineering, vol 56.* Springer, Berlin, Heidelberg, 2007.

[8] N. Park and K. Mahesh. Analysis of numerical errors in large eddy simulation using statistical closure theory. *J. Comput. Phys.*, 222:194–216, 2007.

[9] K. J. Fidkowski and D. L. Darmofal. Review of output-based error estimation and mesh adaptation in computational fluid dynamics. *AIAA J.*, 49(4):673–694, 2011.

[10] NRC. Assessing the reliability of complex models: Mathematical and statistical foundations of verification, validation, and uncertainty quantification. Technical report, National Research Council, 2012.

[11] S. Toosi and J. Larsson. Anisotropic grid adaptation in large eddy simulations. *Computers and Fluids*, 156:146–161, 2017.

[12] S. Toosi and J. Larsson. Towards systematic grid selection in LES: iterative identification of the coarse-graining length scale by minimizing the solution sensitivity. *J. Fluid Mech.*, under review.

[13] S. Toosi and J. Larsson. Grid-adaptation and convergence-verification in large eddy simulation: A robust and systematic approach. In *AIAA Aviation Forum, Atlanta, GA*, 2018.

[14] I. Babuška and W. C. Rheinboldt. Analysis of optimal finite-element meshes in R^1. *Math. of Comp.*, 33:435–463, 1979.

[15] A. R. Diaz, N. Kikuchi, and J. E. Taylor. A method of grid optimization for finite element methods. *Comput. Methods Appl. Mech. Engrg.*, 41:29–45, 1983.

[16] G. Lapenta. Variational grid adaptation based on the minimization of local truncation error: time-independent problems. *J. Comput. Phys.*, 193:159–179, 2003.

[17] S. B. Pope. *Turbulent Flows*. Cambridge University Press, 2000.

[18] J. C. del Alamo and J. Jimenez. Spectra of the very large anisotropic scales in turbulent channels. *Phys. Fluids*, 15(6):L41–L43, 2003.

[19] A. W. Vreman. An eddy-viscosity subgrid-scale model for turbulent shear flow: Algebraic theory and applications. *Phys. Fluids*, 16(10):3670–3681, 2004.

[20] B. J. Geurts and J. Fröhlich. A framework for predicting accuracy limitations in large-eddy simulation. *Phys. Fluids*, 14:L41, 2002.

[21] S. B. Pope. Ten questions concerning the large-eddy simulation of turbulent flows. *New Journal of Physics*, 6:35, 2004.

[22] I. Celik, M. Klein, M. Freitag, and J. Janicka. Assessment measures for URANS/DES/LES: an overview with applications. *J. Turbul.*, 7:1–27, 2009.

[23] S. T. Bose. Explicitly filtered large-eddy simulation: with application to grid adaptation and wall modeling. PhD thesis, Stanford University, 2012.

[24] I. Celik, M. Klein, and J. Janicka. Assessment measures for engineering LES applications. *J. Fluids Engr.*, 131:031102–1, 2009.

[25] M. Klein. An attempt to assess the quality of large eddy simulations in the context of implicit filtering. *Flow Turb. Comb.*, 75:131–147, 2005.

[26] M. Freitag and M. Klein. An improved method to assess the quality of large eddy simulations in the context of implicit filtering. *J. Turbul.*, 7:N40, 2006.

[27] N. Legrand, G. Lartigue, and V. Moureau. Adaptive multi-resolution large eddy simulation with control of modeling and numerical errors. In *56th AIAA Aerospace Sciences Meeting*, 2018.

[28] I. B. Celik, Z. N. Cehreli, and I. Yavuz. Index of resolution quality for large eddy simulations. *J. Fluids Engr.*, 127:939–958, 2005.

[29] J. Jimenez and R. D. Moser. Large-eddy simulations: Where are we and what can we expect? *AIAA J.*, 38(4):605–612, 2000.

[30] M. Klein, J. Meyers, and B. J. Geurts. Assessment of LES quality measures using the error landscape approach. In *Quality and reliability of large-eddy simulations. Ercoftac series, vol 12*. Springer, Dordrecht, 2008.

[31] M. Klein, G. Scovazzi, and M. Germano. On the Richardson extrapolation of the Reynolds stress with the Systematic Grid and Model Variation method. In *Direct and Large-Eddy Simulation XI. Ercoftac series, vol 25*. Springer, Cham, 2019.

[32] J. Hoffman and C. Johnsson. Adaptive DNS/LES: a new agenda in cfd. Preprint, Chalmers Finite Element Center, 2003.

[33] J. Hoffman. On duality-based a posteriori error estimation in various norms and linear functionals for large eddy simulation. *SIAM J. Sci. Comput.*, 26(1):178–191, 2014.

[34] T.J. Barth. Space-time error representation and estimation in Navier-Stokes calculations. In *Complex effects in large eddy simulations. Lecture notes in computational science and engineering, vol 56*. Springer, Berlin, Heidelberg, 2007.

[35] Q. Wang. Forward and adjoint sensitivity computation of chaotic dynamical systems. *J. Comput. Phys.*, 235:1–13, 2013.

[36] Q. Wang. Convergence of the least squares shadowing method for computing derivative of ergodic averages. *SIAM J. Num. Anal.*, 52(1):156–170, 2014.

[37] Y. Addad, U. Gaitonde, D. Laurence, and S. Rolfo. Optimal unstructured meshing for large eddy simulations. In *Quality and reliability of large-eddy simulations. Ercoftac series, vol 12*. Springer, Dordrecht, 2008.

[38] S. T. Bose, P. Moin, and D. You. Grid-independent large-eddy simulation using explicit filtering. *Phys. Fluids*, 22:105103, 2010.

[39] J. Gullbrand and F. K. Chow. The effect of numerical errors and turbulence models in large-eddy simulations of channel flow, with and without explicit filtering. *J. Fluid Mech.*, 495:323–341, 2003.

[40] D. A. Venditti and D. L. Darmofal. Anisotropic grid adaptation for functional outputs: application to two-dimensional viscous flows. *J. Comput. Phys.*, 187:22–46, 2003.

[41] L. Temmerman, M. Hadziabdic, M. Leschziner, and K. Hanjalic. A hybrid two-layer URANS-LES approach for large eddy simulation at high Reynolds numbers. *Int. J. Heat Fluid Flow*, 26:173–190, 2005.

[42] M. Germano. Differential filters for large eddy numerical simulation of turbulent flows. *Phys. Fluids*, 29:1755, 1986.

[43] P. H. van Cittert. *Z. Phys.*, 69:298, 1931.

[44] S. Stolz and N. A. Adams. An approximate deconvolution procedure for large-eddy simulation. *Phys. Fluids*, 11(7):1699–1701, 1999.

[45] J.-F. Remacle, X. Li, M. S. Shephard, and J. E. Flaherty. Anisotropic adaptive simulation of transient flows using discontinuous Galerkin methods. *Int. J. Num. Meth. Engr.*, 62:899–923, 2005.

[46] P. J. Frey and F. Alauzet. Anisotropic mesh adaptation for cfd computations. *Comput. Methods Appl. Mech. Engrg.*, 194:5068–5082, 2005.

[47] K. J. Fidkowski and D. L. Darmofal. A triangular cut-cell adaptive method for high-order discretizations of the compressible navier-stokes equations. *J. Comput. Phys.*, 225:1653–1672, 2007.

[48] M. A. Park. Three-dimensional turbulent rans adjoint-based error correction. *AIAA Paper*, page 3849, 2003.

[49] R. D. Moser and S. Haering. An anisotropic subgrid stress model for high aspect ratio grids. In *APS/DFD 69th Annual Meeting*, 2016.

[50] S. W. Haering and R. D. Moser. Treating anisotropy in LES subgrid models. In *XXIV ICTAM*, 2016.

[51] S. W. Haering. Anisotropic hybrid turbulence modeling with specific application to the simulation of pulse-actuated dynamic stall control. PhD thesis, UT Austin, 2015.

[52] S. K. Lele. Compact finite difference schemes with spectral-like resolution. *J. Comput. Phys.*, 103(1):16–42, 1992.

[53] F. Ducros, F. Laporte, T. Souleres, V. Guinot, P. Moinat, and B. Caruelle. High-order fluxes for conservative skew-symmetric-like schemes in structured meshes: application to compressible flows. *J. Comput. Phys.*, 161:114–139, 2000.

[54] M. Germano, U. Piomelli, P. Moin, and W. H. Cabot. A dynamic subgrid-scale eddy viscosity model. *Phys. Fluids*, 3(7):1760–1765, 1991.

[55] D. K. Lilly. A proposed modification of the Germano subgrid-scale closure method. *Phys. Fluids*, 4(3):633–635, 1992.

[56] A. G. Kravchenko, P. Moin, and R. Moser. Zonal embedded grids for numerical simulations of wall-bounded turbulent flows. *J. Comput. Phys.*, 127:412–423, 1996.

[57] S. Jovic and D. M. Driver. Backward-facing step measurements at low Reynolds number, $Re_h = 5000$. Tech. Mem. 108807, NASA, 1994.

[58] S. Jovic and D. M. Driver. Reynolds number effects on the skin friction in separated flows behind a backward facing step. *Exp. Fluids*, 18:464–467, 1995.

[59] H. Le, P. Moin, and J. Kim. Direct numerical simulation of turbulent flow over a backward-farcing step. *J. Fluid Mech.*, 330:349–374, 1997.

[60] OpenFOAM Foundation. *OpenFOAM* description. `http://www.openfoam.org`, 2019.

[61] A. Yoshizawa. Bridging between eddy-viscosity-type and second-order models using a two-scale DIA. In *9th Symposium on Turbulent Shear Flows*, 1993.

[62] W. Kim and S. Menon. A new dynamic one-equation subgrid-scale model for large eddy simulations. In *33rd AIAA Aerospace Sciences Meeting*, 1995.

[63] S. Menon and W. W. Kim. High Reynolds number flow simulations using the localized dynamic subgrid-scale model. *AIAA Paper*, 96:0425, 1996.

[64] X. Chai and K. Mahesh. Dynamic k-equation model for large-eddy simulation of compressible flows. *J. Fluid Mech.*, 699:385413, 2012.

[65] D. C. Montgomery and G. C. Runger. *Applied statistics and probability for engineers*. "Wiley & Sons", 2011.

[66] M. B. Giles and N. A. Pierce. An introduction to the adjoint approach to design. *Flow Turb. Comb.*, 65:393–415, 2000.

[67] D. Barkley, H. M. Blackburn, and S. J. Sherwin. Direct optimal growth analysis for timesteppers. *Int. J. Num. Meth. Fluids*, 57:14351458, 2008.

[68] Q. Wang and J. Gao. The drag-adjoint field of a circular cylinder wake at Reynolds numbers 20, 100 and 500. *J. Fluid Mech.*, 730:145–161, 2013.

[69] M. Nemec, M. J. Aftosmis, and M. Wintzer. Adjoint-based adaptive mesh refinement for complex geometries. In *46th AIAA Aerospace Sciences Meeting*, 2008.

[70] J. Peraire, M. Vahdati, K. Morgan, and O. C. Zeinkiewicz. Adaptive remeshing for compressible flow computations. *J. Comput. Phys.*, 72:449–466, 1987.

[71] F. Alauzet and A. Loseille. A decade of progress on anisotropic mesh adaptation for computational fluid dynamics. *Comp.-Aided Design*, 72:13–39, 2016.

[72] F. E. Ham, F. S. Lien, and A. B. Strong. A fully conservative second-order finite difference scheme for incompressible flow on nonuniform grids. *J. Comput. Phys.*, 177:117–133, 2002.

[73] X. D. Zhang, M. G. Vallet, J. Dompierre, P. Labbe, D. Pelletier, J. Y. Trepanier, R. Camarero, J. V. Lassaline, L. M. Manzano, , and D. W. Zingg. Mesh adaptation using different error indicators for the euler equations. In *40th AIAA Aerospace Sciences Meeting*, 2002.

[74] K. J. Fidkowski and P. L. Roe. An entropy adjoint approach to mesh refinement. *SIAM J. Sci. Comp.*, 32:12611287, 2010.

[75] D. J. Lea, M. R. Allen, and T. W. N. Haine. Sensitivity analysis of the climate of a chaotic system. *Tellus*, 52:523–532, 2000.

[76] M. Germano. Differential filters of elliptic type. *Phys. Fluids*, 29:1757, 1986.

[77] C. Meneveau and J. Katz. Scale-invariance and turbulence models for large-eddy simulation. *Annu. Rev. Fluid Mech.*, 32:1–32, 2000.

[78] Y. Morinishi and O. V. Vasilyev. A recommended modification to the dynamic two-parameter mixed subgrid scale model for large eddy simulation of wall bounded turbulent flow. *Phys. Fluids*, 13(11):3400–3410, 2001.

[79] E. Garnier, N. Adams, and P. Sagaut. *Large Eddy Simulation for Compressible Flows*. Springer, 2009.

[80] S. T. Bose, B. C. Wang, and M. Saeedi. Prediction of unsteady heat transfer from a cylinder in crossflow. In *Proceedings of the Summer Program*, pages 107–116. Center for Turbulence Research, 2012.

[81] F. Porte-Agel, C. Meneveau, and M. B. Parlange. A scale-dependent dynamic model for large-eddy simulation: application to a neutral atmospheric boundary layer. *J. Fluid Mech.*, 415:261–284, 2000.

[82] J. Larsson. Grid-adaptation for chaotic multi-scale simulations as a verification-driven inverse problem. In *56th AIAA Aerospace Sciences Meeting*, 2018.

[83] D. Carati, G. S. Winckelmans, and H. Jeanmart. On the modeling of the subgrid-scale and filtered-scale stress tensors in large-eddy simulation. *J. Fluid Mech.*, 441:119–138, 2001.

[84] S. Stolz, N. A. Adams, and L. Kleiser. The approximate deconvolution model for large-eddy simulations of compressible flows and its application to shock-turbulent-boundary-layer interaction. *Phys. Fluids*, 13(10):2985–3001, 2001.

[85] K. Hanjalić and B. Launder. *Modeling turbulence in engineering and the environment*. Cambridge University Press, 2011.

[86] B. Vreman, B. Geurts, and H. Kuerten. Large-eddy simulation of the turbulent mixing layer. *J. Fluid Mech.*, 339:357–390, 1997.

[87] B. E. Launder, G. J. Reece, and W. Rodi. Progress in the development of a reynolds-stress turbulence closure. *J. Fluid Mech.*, 68:537–566, 1975.

[88] C.G. Speziale, S. Sarkar, and T. B. Gatski. Modeling the pressure-strain correlation of turbulence: an invariant dynamical systems approach. *J. Fluid Mech.*, 227:245–272, 1991.

[89] R. L. Panton, M. Lee, and R. D. Moser. Correlation of pressure fluctuations in turbulent wall layers. *Phys. Rev. Fluids*, 2:094604, 2017.

[90] B. J. Daly and F. H. Harlow. Transport equations in turbulence. *Phys. Fluids*, 13:2634–2649, 1970.

[91] B. E. Launder. *Phenomenological modelling: Present... and future?*, volume 357. Springer, Berlin, Heidelberg, 1990.